

Adaptive Robust Interaction Control for Low-cost Robotic Grasping



University of
Salford
MANCHESTER

Saber Mahboubi Heydarabad

University of Salford

This dissertation is submitted in partial fulfilment
of the requirements for the degree of
Doctor of Philosophy

School of Computing, Science & Engineering
Autonomous Systems and Robotics

March 2018

Contents

1	Introduction	1
1.1	Motivation.....	1
1.1.1	Gripper with Fixed Gain Motion Control	1
1.1.2	Grip Force Control	5
1.1.3	Gripper/hand with Serial Elastic Element (SEE)	7
1.1.4	Gripper/hand with Variable Stiffness Mechanism	11
1.2	End effectors in industry	13
1.3	Aim and Objectives	15
1.4	List of Contributions	16
1.5	Organisation of Thesis	18
2	Background.....	20
2.1	Introduction.....	20
2.2	Variable stiffness mechanisms.....	21
2.2.1	Series Elastic Actuator	21
2.2.2	Force Controllable Hydro-Elastic Actuator	21
2.2.3	Compact Rotational Soft Actuator	22
2.2.4	Compact Rotary Series Elastic Actuator (cRSEA).....	22
2.2.5	Selective Compliant Actuator	23
2.2.6	Pulley-belt driven variable stiffness actuator (VSA)	24
2.2.7	Series Elastic Actuator for a Biomimetic Walking Robot	24
2.2.8	Antagonistically-twisted round-belt actuator	25
2.2.9	Controllable Equilibrium Position Actuator	26
2.2.10	MACCEPA2	27
2.2.11	Cam-based variable stiffness actuator.....	27
2.2.12	Adjustable moment arm	28
2.2.13	A leaf spring-based variable stiffness joint.....	29
2.2.14	Antagonistic VSM.....	30
2.2.15	McKibben muscle	31
2.2.16	Artificial muscles	31
2.2.17	Quasi-antagonistic variable stiffness actuator.....	32
2.2.18	VSM for prosthetic limbs.....	32
2.2.19	VSA-Cube	33

2.2.20	Variable physical damping actuator (VPDA)	33
2.3	Compliant grasp	35
2.3.1	Parallel passive joint	36
2.3.2	Adaptive SDM Hand	37
2.3.3	HEU Hand II	39
2.3.4	Bio-mechatronic anthropomorphic artificial hand	39
2.3.5	Modular hand	39
2.3.6	MR actuated variable impedance gripper	40
2.3.7	Three-finger hand with a new stiffness control method	40
2.3.8	DLR-HIT hand	40
2.3.9	Composite robot end-effectors	41
2.3.10	Octopus inspired arm	41
2.3.11	Reconfigurable gripper for flexible assembly tasks	42
2.3.12	Capstan brake mechanism for tendon-driven hands	42
2.3.13	TUAT/Karlsruhe humanoid hand	43
2.3.14	PAM-based anthropomorphic robotic hand	43
2.3.15	RAMA-1	43
2.4	Robust grasp, Dexterous hand and in-hand manipulation	44
2.4.1	Grasp synthesis	44
2.4.1	Adaptive grasp with an under-actuated hand	52
2.4.2	Iterative learning control (ILC)	52
2.4.3	RL-based impedance control	53
2.4.4	Grasp simplifier	53
2.4.5	Impedance control in a flexible joint	54
2.4.6	Adaptive slip prevention control	55
2.5	Discussion	56
3	Passive Controllable Stiffness Gripper for Advanced, Flexible Handling	59
3.1	Introduction	59
3.2	VSG ₁	65
3.2.1	Design Explanation	65
3.2.2	Working Principle and Simulation	67
3.2.3	Experimental Results and Discussion	69
3.3	VSG ₂	74
3.3.1	Design Explanation	75

3.3.2	Modelling the stiffness function.....	77
3.3.3	Experimental results.....	84
3.4	Discussion.....	88
4	Robust grasp control.....	89
4.1	Introduction.....	89
4.2	Gripper test platform.....	89
4.3	Proportional-Derivative position control.....	91
4.4	First-Order Sliding Mode Control Design.....	93
4.4.1	Disturbance rejection.....	101
4.4.2	Quasi-Sliding Mode Control Design.....	104
4.4.3	Error space-based sliding mode control.....	109
4.4.4	Impedance control for the VSGs.....	111
4.5	Super-Twisting Sliding Mode Control (STSMC).....	113
4.6	Robust Interaction Control for Robotic Grasping.....	116
4.6.1	Gripper Test Platform.....	118
4.6.2	Gripper Model.....	120
4.6.3	Grasp Model.....	122
4.6.4	Control Design.....	124
4.6.5	Experimental Results and Discussion.....	126
4.7	Discussion.....	135
5	High-Performing Adaptive Grasp Control.....	136
5.1	Introduction.....	136
5.2	Gripper Design Explanation.....	137
5.2.1	The 8 kg payload gripper.....	137
5.2.2	The 45 kg payload gripper.....	142
5.3	Grasp Model.....	146
5.4	Hybrid SMC-PI Control Design.....	150
5.4.1	Quasi-sliding Mode grasp control.....	151
5.4.2	Control Design and Robustness Analysis.....	153
5.4.3	Adaptive SMC grasp control.....	155
5.5	Super Twisting Sliding Mode Control.....	157
5.6	Experimental Results and Discussion.....	158
5.7	Discussion.....	178
6	Conclusions and Future Work.....	179

6.1 Summary.....	179
6.2 List of contributions.....	181
6.3 Limitations and Future Work.....	183
Appendix A	186
References	187

Publications and patent

- From the work presented in this thesis, there is a patent.
- Mahboubi, S., Milella, F., Davis, S.T. and Nefti-Meziani, S., 2017. High-performing adaptive grasp for a robotic gripper using super twisting sliding mode control, IEEE International Conference on Robotics and Automation (ICRA), 2017.
- Mahboubi, S., Davis, S.T. and Nefti-Meziani, S., VSG: A Novel Variable Stiffness Gripper for Advanced, Flexible Handling in Industrial Applications. Journal of IEEE Access accepted with minor correction.
- Mahboubi, S., Davis, S.T. and Nefti-Meziani, S., A Robust Interaction Control for Robotic Grasping Based on Gripping Force and Slip Feedback. Pending for the patent application.

List of Figures

1.1	Schematic model of a two-finger gripper.....	2
1.2	Position control of the fingers using a linear PI control. The blue and purple lines in this figure illustrate the desired and the actual position of the fingers, respectively	2
1.3	Schematic model of the gripper with an object between the fingers.....	3
1.4	Schematic model of the gripper with the held object.....	4
1.5	Position control of the finger using fixed-gain PI control. The blue and purple lines in this figure illustrate the desired position and the actual finger position, respectively.	5
1.6	A schematic model of a two-finger gripper and its DC motor.....	6
1.7	Root locus plot for the gripper-object model as K_b increases.....	6
1.8	Adding a Serial Elastic Element (SEE) between the fingers and actuator can allow the grasp of an unknown object to be more stable	7
1.9	The dexterous 24-joint Bielefeld Shadow hand (162).....	8
1.10	The granular jamming universal gripper proposed by Brown et al. (163)..	8
1.11	Universal jamming gripper proposed in (164). (b) The gripper was able to grip objects without the need for a grasp planning or sensory feedback.	9
1.12	(a) Festo flexshape and (b) Festo adaptive gripper fingers, DHAS, provide fixed compliance solutions for industrial graspings (165).	10
1.13	(a) The solidification principle of the proposed magnetic fluid in (166). (b) An example of the gripper that used the MR α fluid in its actuation system.	10
1.14	Inclusion of a parallel damper with the SEE can stabilise the grasping action	11
1.15	A two-finger gripper with a VSM to stabilise the grasp.....	12
1.16	The dexterous, variable stiffness DLR-HIT hand (117), (167).	13
1.17	Some examples of the industrial electric grippers (168).	14
1.18	Some examples of the industrial hydraulic grippers (168).	14
1.19	Vacuum gripper and its suction cups (169).	15
1.20	Electromagnet grippers provide a simple and low-cost solution for lifting ferrous materials (170).	15
2.1	Series elastic actuator proposed by Pratt et al. (51).....	21
2.2	Hydro-elastic actuator proposed in (54).....	21
2.3	Compact rotational series stiffness actuator introduced by N.G. Tsagarakis et al. (55).	22
2.4	Selective compliant actuator proposed by Sugar (59).....	23-24
2.5	(a) Real and (b) Schematic model of the pulley-belt-spring system	24

	suggested by Tonietti et al. (60, 61).	
2.6	Schematic model of the SEA designed for a biomimetic walking robot (62).	25
2.7	Antagonistically-twisted round-belt actuator proposed by Inoue et al. (63)	25
2.8	Controllable Equilibrium Position Actuator (MACCEPA1) (64).....	26
2.9	Schematic model of Maccepa2 (66).....	27
2.10	Schematic representation of a cam-based variable stiffness actuator introduced in (67, 68).	28
2.11	Schematic representation of the cam-based variable stiffness actuator (69)..	29
2.12	Schematic model of the leaf spring-based variable stiffness actuator. Sliding the rollers along the leaf springs would change the effective length of the springs and consequently change the output stiffness (70).	30
2.13	Antagonistic VSM used in DLR hand (71-73).....	30
2.14	Schematic representation of a McKibben artificial muscle (74, 75).....	31
2.15	Two-artificial muscles in an antagonistic layout can control both the stiffness and position of the robot joints.	32
2.16	The VSA-Cube is made of four springs, two driven pulleys and one main shaft (92).	33
2.17	Schematic model of the parallel passive joint suggested in (107).....	36
2.18	Schematic model of the Adaptive SDM Hand (108-110).....	37
2.19	Schematic model of a robotic joint with an added parallel spring (101).....	38
2.20	The simulated robot successfully mimicked human grasps using imitation technique (176).	45
2.21	Using the deep learning method introduced in (177), the robot could successfully perform a grasp synthesis.	45
2.22	A 3-finger, 6 DOF hand, performing form (left) and force (right) closure.	47
2.23	(a) point contact without friction (b) point contact with friction and (c) soft-finger contact models (Figure recreated from (191)).	49
2.24	Friction cone (left) and polyhedral friction cone (right) (Figure recreated from (191)).	50
3.1	The VSG ₁ introduced in this section.....	65
3.2	Schematic representation of the actuation system of VSG ₁	66
3.3	The combination of the motions of M ₁ and M ₂ provides the ability to change the stiffness and position in VSG ₁ .	67
3.4	The output stiffness of the gripper, δ_o , is a function of α	68
3.5	VSG ₁ in its maximum (red) and minimum (blue) stiffness configurations...	69
3.6	Force-displacement curves for the VSG ₁	69
3.7	Different objects with different sizes and stiffnesses, as lifted by the VSG.	70

3.8	Experimental results (solid lines) versus simulation results (dashed lines) for the force-displacement test.	71
3.8b	The rack and pinion mechanism of VSG1.	72
3.9	Hardware setup for the trajectory tracking experiment.....	73
3.10	(a, b, c, d) Finger's motion (solid lines) versus desired trajectory (dashed lines) for the sinusoidal trajectory tracking experiment for $\theta = 0^\circ, 10^\circ, 20^\circ$ and 30° respectively. (e) FSR sensor measurements of the impedance force exerted by the fingers on the brick.	74
3.11	The hysteresis curves of VSG ₁ for different values of the rod angle.....	74
3.12	(a) CAD model of the modified shaft of M ₁ used in VSG ₂ . (b) Schematic model of M ₁ used in VSG ₁ (left) versus M ₁ with the modified shaft used in VSG ₂ (right)	75
3.13	The three-finger variable stiffness gripper, as introduced in this section.....	76
3.14	A CAD model and a schematic representation of the second variable..... stiffness design.	77
3.15	Schematic model of VSG ₂	78
3.16	The tendon is pulled by F and the spring is compressed due to this force.....	78
3.17	VSG ₂ at maximum and minimum stiffness.....	79
3.18	Position of the rod and tendon before and after application of force F	80
3.19	Stiffness of the gripper δ_o for different values of θ	82
3.20	Stiffness of the gripper δ_o for different values of K and B	83
3.21	Different objects with different sizes and flexibilities lifted by VSG ₂	84
3.22	Experimental measurements of the displacement d for different values of applied force and rod angles ($\theta = 5^\circ, 10^\circ, 15^\circ, 20^\circ, 25^\circ, 30^\circ, 40^\circ$)	85
3.23	Trajectory and force tracking for a stiffness-controlled gripper colliding with a physical rigid brick.	86
3.24	The spring hysteresis curves for different rod angles.....	87
3.25	Magnitude bode plot for VSG ₂ for $\theta = 5^\circ, 10^\circ, 20^\circ, 30^\circ$ and 40°	88
4.1	The two-finger gripper mounted on the KUKA robot.....	90
4.2	Schematic model of the gripper and the coordinate frames used.....	90
4.3	When the gripper is isolated from the environment, the conventional proportional-derivative position control will drive the state variables to the origin in a finite time.	92
4.4	System response for a bounded disturbance $F_{du}(X_1, X_2, t) = \cos(2t)$ in the presence of a proportional-derivative control law.	93
4.5	System response for a bounded square wave disturbance in the presence of a proportional-derivative control law.	93
4.6	Results of the gripper system controlled by a first-order sliding mode	97

	controller in the presence of a sinusoidal external disturbance.	
4.7	Results of the gripper system controlled by a first-order sliding mode control in the presence of a square wave pulse external disturbance.	98
4.8	The effect of convergence rate on the response of the gripper controlled by an SMC.	99
4.9	Effect of different values of Ω on the (a) states' responses and (b) sliding variable.	100
4.10	Chattering phenomenon in a system controlled by an FSMC.....	101
4.11	Zoomed plot of the Figure 4.6.....	101
4.12	A grasp case study to test the robustness of the embedded FSM in the gripper.	103
4.13	Schematic model of the gripper and held object moving together in an accelerated and decelerated manner.	103
4.14	Schematic model of the gripper-FSMC system used in this test.....	103
4.15	Experimental results for the T-shaped object lifted by the gripper.....	104
4.16	(a) $\text{sign}(\sigma)$ (b) $\text{Sigm}(\sigma, \epsilon)$ and (c) $\text{Tanh}(\sigma, \epsilon)$ for different values of ϵ	105
4.17	Schematic model of the gripper-QSMC system used in this test.....	106
4.18	Results of the gripper system controlled by a Quasi-FSMC (sigmoid function) controller in the presence of a sinusoidal external disturbance.	107
4.19	Results for the gripper system controlled by a Quasi-FSMC (sigmoid function) controller for the test, as explained in Example 4. 2.	108
4.20	Schematic model of the gripper-SMC.....	111
4.21	Schematic model of the gripper-SMC.....	112
4.22	Reference trajectory tracking.....	112
4.23	Reference trajectory tracking.....	116
4.24	The two-finger gripper mounted on the ABB robot.....	119
4.25	(a) Flexible absolute potentiometer (b) Force Sensing Resistor used for the tests.	119
4.26	VSO, Variable Stiffness Object used in this chapter.....	120
4.27	Dropping weights on the base of the slide to simulate disturbance.....	120
4.28	Uncertainty about the mechanical properties of the object to be grasped makes the grasp model inaccurate.	122
4.29	Schematic model of the gripper with the held object and the coordinate frames used.	123
4.30	Schematic model of the object and fingers.....	123
4.31	Block diagram of HSMC.....	125
4.32	Block diagram of HSTSMC.....	126

4.33	Four-stage experiment used to evaluate the performance of the designed controllers.	127
4.34	Experimental results of the FSMS for the VSO with stiffness K_1	128
4.35	Experimental results for the FOSMS with a VSO of stiffness K_2	129
4.36	Experimental results for the STSMC with a VSO of stiffness K_1	129
4.37	Experimental results for the STSMC with a VSO of stiffness K_2	130
4.38	Angular velocity of the motor ω_m . The yellow line is the related velocity for FSMC whilst the purple line is the velocity for STSMC.	130
4.39	Using the gripper and STSMC design, the robot was able to grasp and lift objects of different mechanical properties.	131
4.40	The gripper increases the applied force on the egg and apple to stop them from slipping after lifting. Dashed lines refer to the apple.	132
4.41	A four finger, 8 DOF hand designed and developed as part of this research in order to evaluate the possibility of integrating the slip prevention control designs with high-level, in-hand manipulation algorithms.	132
4.42	The robot grasps and lifts different objects (an egg in this figure) and starts to move along a pre-programmed trajectory in an accelerating and decelerating manner in order to test the robustness of the designed STSMC.	134
5.1	The 8 kg payload gripper mounted on the KUKA KR10 robot.....	138
5.2	The 8 kg payload gripper in its open and closed states.....	138
5.3	Schematic model of the gripper illustrating a held object and the coordinate frames used.	139
5.4	Optical flow sensor used in the 8 kg payload gripper in order to measure the grasped objects' slippages.	141
5.5	Operation explanation of the optical flow sensor.....	141
5.6	The 45 kg payload gripper mounted on a KUKA robot.....	142
5.7	A Cad model and the side view of the 45 kg payload gripper in both open and closed states.	143
5.8	The servo motor used in the 45 kg payload gripper.....	144
5.9	Front and back view of the ultrasonic sensor used in the 45 kg payload gripper	144
5.10	Frequency range used for the ultrasonic sensors.....	145
5.11	Diagram of the ultrasonic sensor operation.....	145
5.12	Diagram of the send and receive comments of the ultrasonic sensor.....	146
5.13	Hybrid position, velocity and force feedback control with an anti-windup layout.	147
5.14	Grasp response of the gripper controlled by the hybrid position-force controller to the step inputs with increasing amplitude (dashed green curve).	148

5.15	Uncertainty about the mechanical properties of the object to be grasped makes the grasp model inaccurate.	149
5.16	Hybrid sliding mode-PI force controller design.....	149
5.17	Force tracking test with the 45 kg payload gripper for (a) foam block (b) piece of wood and (c) RSJ steel beam. The dashed blue lines, solid orange and solid red lines are the reference trajectory, the response of the fixed gain PI control and the response of hybrid sliding mode-PI controller to the reference trajectory input, respectively.	150
5.18	A schematic model of the gripper and object in its grasp (left) and lift (right) mode.	152
5.19	Block diagram of FSMC.....	153
5.20	Schematic model of the gripper with the held object	153
5.21	The control block diagram of the designed ASMC.....	156
5.22	ASTSMC block diagram.....	158
5.23	The robot grasps and lifts different objects (an egg in this figure) and starts to move along a pre-programmed trajectory in an accelerating and decelerating manner.	159
5.24	Motion trajectory profile of the gripper used in the experiment.....	159
5.25	Experimental results using the ASMC for the Coca-Cola bottle.....	160
5.26	Experimental results using the ASMC for the metal block.....	161
5.27	Experimental results using the ASMC for the wood.....	162
5.28	Experimental results using the ASMC for the egg.....	163
5.29	Experimental results using the STSMC for the Coca-Cola bottle.....	165
5.30	Experimental results using the STSMC for the metal block.....	166
5.31	Experimental results using the STSMC for the wood.....	167
5.32	Experimental results using the STSMC for the egg.....	168
5.33	Pick and place tasks with the 45 kg payload gripper and STSMC.....	170
5.34	Experimental results for the Pick and place tests shown in Figure 6.33.....	171
5.35	Many lifting tests with several different objects has been performed in order to test the robustness of the system in real-world scenarios.	171
5.36	Experimental results for the test shown in Figure 6. 35. Purple curves for chairs and red curves for glass of wine.	172
5.37	Using the gripper and STSMC the robot performs very robust grasp.	172
5.38	Experimental results of the ASMC (blue line) and FSMC (pink line) for the Coca-Cola bottle.	173
5.39	(a) The way in which a human picks up a business card or any thin object from a desk by sliding it across the surface of the desk (b) The way that the	176

- robot slides the card across the surface using ASTSMC.
- 5.40 Using two sensors provides the capability to measure the deviation of the object. 177
- 5.41 Rotation of the gripper about z_0 axis generates an extra force, F_d acting on the fingers. However, the proposed controllers can satisfactorily compensate this force. 177

List of Tables

3.1.a	The mechanical properties of all the objects used for the experiments reported in this thesis.....	62 63
3.1	Mechanical and electrical specification of the servos used in VSG ₁	66
4.1	Specification of the slip sensor used in the gripper.....	119
4.2	Specification of the force sensor used in the gripper.....	119
5.1	Specification of the servo motors.....	140
5.2	Specifications of the slip (optical flow) sensor.....	140
5.3	Specification of the servo motors used in the 45 kg payload gripper.....	140
5.4	Specification of the ultrasonic distance sensor used to measure the slippage of the object in the 45 kg payload gripper.	140

Acknowledgments

I would like to take this opportunity to extend my heartfelt gratitude to my supervisors, Dr. Steve Davis and Prof. Samia-Nefti Meziani, for their constructive feedback, patient guidance, encouragement, and more specially for giving me the chance to be part of a great European project over the last three years.

I am particularly grateful for all the help and support received from Mr. Andrew Baker and Mr. Michael Clegg during these years.

Many thanks to my family for their boundless love, care and support. Although we have lived apart for years now, they were there when I needed them, and I am very lucky to have them in my life.

I would like to thank my love, my wife, my everything, Dr. Neda Dadbakhsh, for her constant support, her patience and for all the late nights and early mornings. I owe her my life.

Finally, I would like to mention that the research leading to these results has received funding from the People Programme (Marie Curie Actions) of the European Union's Seventh Framework Programme FP7/2007-2013/ under REA grant agreement number 608022.

Abbreviations

VSG ₁	Variable Stiffness Gripper 1
VSG ₂	Variable Stiffness Gripper 2
PID	Proportional Integral Derivative
DC	Direct Current
SEE	Serial Elastic Element
VSM	Variable Stiffness Mechanism
ASTSMC	Adaptive Super Twisting Sliding Mode Control
ASMC	Adaptive First-Order Sliding Mode Controller
CHPH	Chattering Phenomenon
cRSEA	Compact Rotary Series Elastic Actuator
MACCEPA	Mechanically Adjustable Compliance and Controllable Equilibrium Position Actuator
VPDA	Variable Physical Damping Actuator
SDM	Shape Deposition Manufacturing
MR	Magnetorheological
FPGA	Field Programmable Gate Array
PPSeCo	Point-to-Point Serial Communication
ILC	Iterative learning control
RL	Reinforcement Learning
DOF	Degree of Freedom
QSMC	Quasi-Sliding Mode Control
FSR	Force Sensing Resistor
VSO	Variable Stiffness Object
fps	Frame per second
CAD	Computer-aided Design
USB	Universal Serial Bus
RPM	Revolutions Per Minute
CEMF	Counter-electromotive Force
OBS	Observer

Symbols

M_F	finger mass
x	fingers displacements along their DOF
F_a	actuator force
B	damping constant
X	Laplace transform of the finger position x
G_P	proportional gain
G_I	integral gain
X_d	Laplace transform of the desired position of the finger
M_b	mass of the object
K_b	stiffness coefficient of the object
B_b	damping coefficient of the object
F_b	resistive force of the object
M_R	rotor mass of the DC motor
K_J	stiffness of the shaft
B_J	frictional loss of the motor shaft
G_P^F	proportional gain in the force controller
X^R	actual position of the shaft
X_d^R	desired position of the shaft
G_D	derivative gain
K_V	stiffness coefficient of the serial elastic element
Y_F^S	Laplace transforms of the admittance of the fingertip
Y_a^S	Laplace transforms of the admittance of the actuation system
Y_V^S	Laplace transforms of the admittance of the stabiliser
Θ_f	rotation angle of the position frame
l_{sb}	length of the moment arm
k_j	apparent stiffness of the output shaft
τ_{ext}	external torque applied to the output shaft
Θ	rotation of the output shaft due to the external torque
k_s	spring constant
S	torsional output stiffness

l	effective length of the springs
D	diameter of the output axis
E	Young's modulus
δ_o	apparent stiffness of the fingers in VSGs
α	the angle between the rod and tendon in VSGs
$Z's$	the amount of co-contraction in the spring due to the force
K	spring constant
d	displacement of the tendon due to the external force in VSG
D_0	the distance between rod's end point (tendon-rod fixing point) and the wrist of the gripper in VSGs
Z'	the length between rod's end point and the centre of the shaft of M1 before applying the force.
D_1	the distance between rod's end point and gripper wrist after applying force.
$f_d(x,t), F_{du}$	external disturbance
$\Gamma(x_f, v_f)$	any un-modelled resistance force
x_f	the finger displacement
v_f	the finger velocity
X_1, X_2	state variables
σ	sliding variable
η	convergence rate
Λ_σ	Lyapunov function
ζ	positive constant
T_s	reaching time
R_{ph}	reaching phase
S_{ph}	sliding phase
ε	positive small constant
$\text{sign}(\cdot)$	Sign function
$\text{sigm}(\cdot)$	sigmoid function
$\text{Tanh}(\cdot)$	hyperbolic tangent function
$\sigma_{(e,\dot{e})}^t$	error-based sliding variable
e	error of the finger in following the desired trajectory
y_d	fingers' desired position
y	fingers' actual (measured) position
$\mathcal{F}(y, \dot{y}, t)$	disturbance term

\hat{D}	boundary condition of disturbance term
$\dot{\sigma}$	time derivative of the sliding variable
Ω	Control gain of the FSMC
F_{grip}	grip force
B_v	damping coefficient in VSM
$\hat{\Omega}$	positive constant
U	positive constant
T	disturbance follower
I	the equivalent moment of inertia for the fingers and the motor armature
k_T	DC motor's torque constant
V_s	DC motor's operating voltage
V_{CEMF}	DC motor's counter-electromotive force (CEMF)
$R_{armature}$	DC motor's terminal resistance (ohms)
I_m	DC motor's operating current
T_m	motor's output torque
K_e	counter-electromotive force constant
$A_{I,\tilde{B},K,D}$	a function of state variables that contains the I , \tilde{B} , K and F_{du} terms
\tilde{k}_{TR}	quotient of I and K
B_{obj}	damping coefficient of the object
m	mass of the object
g	gravitational acceleration
ψ_c	yaw angle
u	the input to the system
V_c	velocity of the contact point along the X_c axis
ω_f	angular velocity of the fingers around their joints
ω_m	rotational velocity of the motor
ω_{md}	desired value of the motor shaft speed
κ	a constant related to the stiffness of the grasped object
μ	coefficient of friction
λ	constant
γ	the angle between the gripping link and the link connected to the motor
$T(t)$	torque of the motor

d_{so}	distance between the sensor and object
TOF	Time-of-Flight
K_P	proportional gain for the velocity control
K_I	integral gain for the velocity control
K_{aw}	anti-windup gain
K_β	conversion constant of the shaft's position and angular velocity
S_l	slippage of the object
x_0	the position of the fingers when they make contact with the object's surface without applying any force to it
S_w	control switch
\dot{S}_l	the speed of the slippage
$A(X_1, \dots)$	cumulative uncertainty-disturbance
D_A	upper bound of the cumulative uncertainty-disturbance
\tilde{D}	control gain
K_{RC4}	feedback from the manipulator's control cabinet
H_1, H_2	control gains

Abstract

Robotic grasping is a challenging area in the field of robotics. When a gripper starts interacting with an object to perform a grasp, the mechanical properties of the object (stiffness and damping) will play an important role. A gripper which is stable in isolated conditions, can become unstable when coupled to an object. This can lead to the extreme condition where the gripper becomes unstable and generates excessive or insufficient grip force resulting in the grasped object either being crushed, or falling and breaking.

In addition to the stability issue, grasp maintenance is one of the most important requirements of any grasp where it guarantees a secure grasp in the presence of any unknown disturbance. The term grasp maintenance refers to the reaction of the controller in the presence of external disturbances, trying to prevent any undesired slippage. To do so, the controller continuously adjusts the grip force. This is a challenging task as it requires an accurate model of the friction and object's weight to estimate a sufficient grip force to stop the object from slipping while incurring minimum deformation.

Unfortunately, in reality, there is no solution which is able to obtain the mechanical properties, frictional coefficient and weight of an object before establishing a mechanical interaction with it. External disturbance forces are also stochastic meaning they are impossible to predict.

This thesis addresses both of the problems mentioned above by:

- Creating a novel variable stiffness gripper, capable of grasping unknown objects, mainly those found in agricultural or food manufacturing companies. In addition to the stabilisation effect of the introduced variable stiffness mechanism, a novel force control algorithm has been designed that passively controls the grip force in variable stiffness grippers. Due to the passive nature of the suggested controller, it completely eliminates the necessity for any force sensor. The combination of both the proposed variable stiffness gripper and the passivity based control provides a unique solution for the stable grasp and force control problem in tendon driven, angular grippers.
- Introducing a novel active multi input-multi output slip prevention algorithm. The algorithm developed provides a robust control solution to endow direct drive parallel jaw

grippers with the capability to stop held objects from slipping while incurring minimum deformation; this can be done without any prior knowledge of the object's friction and weight. The large number of experiments provided in this thesis demonstrate the robustness of the proposed controller when controlling parallel jaw grippers in order to quickly grip, lift and place a broad range of objects firmly without dropping or crushing them. This is particularly useful for teleoperation and nuclear decommissioning tasks where there is often no accurate information available about the objects to be handled. This can mean that pre-programming of the gripper is required for each different object and for high numbers of objects this is impractical and overly time-consuming. A robust controller, which is able to compensate for any uncertainties regarding the object model and any unknown external disturbances during grasping, is implemented.

This work has advanced the state of the art in the following two main areas:

- Direct impedance modulation for stable grasping in tendon driven, angular grippers.
- Active MIMO slip prevention grasp control for direct drive parallel jaw grippers.

Chapter 1

INTRODUCTION

1.1 Motivation

Robotic grasping is a challenging area in the field of Robotics. The difficulties inherent to grasping arise for two main reasons: firstly, any interaction with the object to be grasped has the potential to destabilise the gripper and, consequently, can cause the grasped object to be either crushed, or to fall and break; secondly, any interaction with an unknown object can cause (undesired and sometimes dangerous) errors in the performance of the motion or force control. When interacting with an object, the dynamic properties of the object will play an important role where a gripper (as a system), which has been shown to be stable as per appropriate stability criteria, can become unstable when coupled to an object. The two following sections illustrate the effect of gripper-object interaction on a particular primary motion and force control, respectively.

1.1.1 Gripper with Fixed Gain Motion Control

Figure 1.1 depicts a schematic model of a two-finger gripper, where M_F and x represent the fingers' masses and displacements along their DOF, respectively. In this model, the two identical fingers are mechanically interconnected and thus that their displacements are equal. As shown in this figure, the fingers are subject to an actuator force, F_a . The damping constant, B , shown in this figure represents the total frictional losses between the fingers and palm of the gripper.

The dynamical model of the fingers is as follows:

$$M_F \ddot{x} + B \dot{x} = F_a \quad (1.1)$$

where the Laplace transform of Eq. 1.1 is:

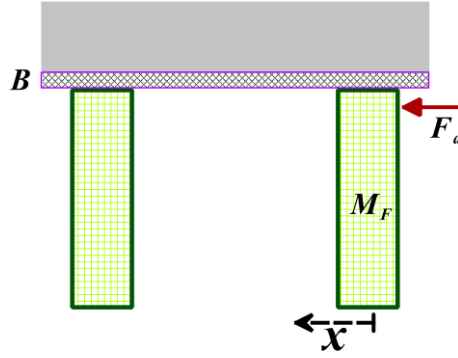


Figure 1.1: Schematic model of a two-finger gripper.

$$(M_F S^2 + BS)X = F_a \quad (1.2)$$

where X is the Laplace transform of the finger position x . Assuming G_P and G_I to be the proportional and integral gain of the control, respectively, we can write:

$$F_a = G_P(X_d - X) + \frac{G_I}{S}(X_d - X) \quad (1.3)$$

where Eq. 1.3 shows a proportional-integral (PI) motion controller for the finger and X_d represents the Laplace transform of the desired position of the finger. From Eq. 1.3, the transfer function for the closed-loop system can be written as Eq. 1.4:

$$\frac{X}{X_d} = \frac{G_P S + G_I}{M_F S^3 + BS^2 + G_P S + G_I} \quad (1.4)$$

The solid blue line and purple dashed line in Figure 1.2 show the desired position and real position of the fingers in the presence of the designed controller.

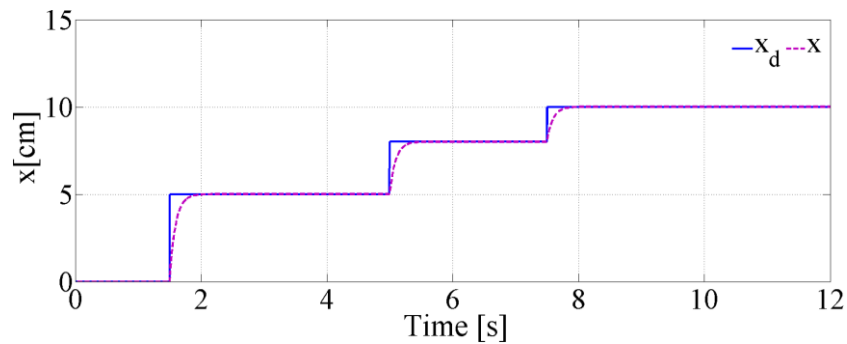


Figure 1.2: Position control of the fingers using a linear PI control. The blue and purple lines in this figure illustrate the desired and the actual position of the fingers, respectively.

From the Routh-Hurwitz criterion, the closed-loop system (Eq. 1.4) has a stability condition that can be defined as follows (1, 2):

$$G_I < \frac{BG_P}{M_F} \quad (1.5)$$

It is worth noting that to design the motion control described, it is assumed that the finger has no interaction with its environment (the gripper simply closes its fingers, even though there is no object between them). However, this is not the case in real-world scenarios, where we use the grippers to grasp and lift objects. In the presence of a finger-object interaction, the criterion described in Eq. 1.5 cannot guarantee the stability of the grasp; even the simple act of grasping an object may be destabilizing (3, 4). Let us assume that there is an object between the two fingers that is positioned in such a way that the geometrical centre of the object and gripper are not co-aligned. In this case, from Figure. 1.3, it may be noted that the right finger will have a physical interaction with the object during its movement along the x -direction. This is equivalent to increasing the finger's mass from M_F to $(M_F + M_b)$, where M_b is the mass of the object. In this case, the new stability condition of the system is described by:

$$G_I < \frac{BG_P}{(M_F + M_b)} \quad (1.6)$$

From Eq. 1.5 and 1.6, it may be noted that a sufficiently small integral gain can guarantee the stability of the grasp of an unmodeled object with bounded inertial properties. However, even with a small value of G_I , any interaction between the fingers and a heavy object can change the stability condition of the motion controller.

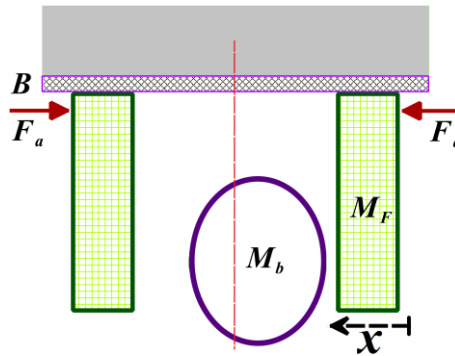


Figure 1.3: Schematic model of the gripper with an object between the fingers.

It should also be noted that, in addition to the stability issue, steady-state error is also one of the difficulties encountered with fixed gain controllers. As an example, consider an object being held by the gripper in the manner shown in Figure 1.4.

In this figure, the mechanical properties of the object, its mass, stiffness and damping coefficient, are shown by M_b , K_b and B_b , respectively. The fingers are subject to actuator force, F_a , and resistive force, F_b , where the latter is a function of the deformation of the object. For clarity, only one resistive force is shown in this figure. From this figure, the resistive force can be calculated as

$$F_b = K_b x + B_b \dot{x} \quad (1.7)$$

By adding the resistive force to the model and from Eq. 1.1, the new dynamical model of the fingers is given by:

$$M_F \ddot{x} + B \dot{x} = F_a - F_b \quad (1.8)$$

Using the same control gains as Figure 1.2, the resultant motion control for the system with a specific K_b and B_b is shown in Figure 1.5.

This figure clearly illustrates a steady-state error in the finger position. From this figure, it can be concluded that although the external object does not change the stability of the system, it does, however, result in an undesired error in the controller response.

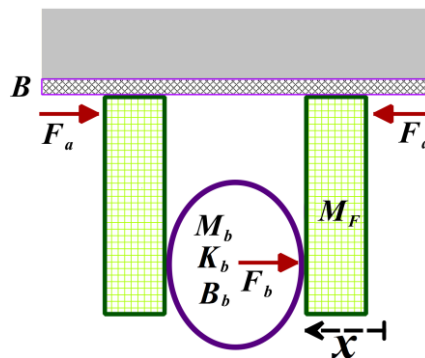


Figure 1.4: Schematic model of the gripper with the held object.

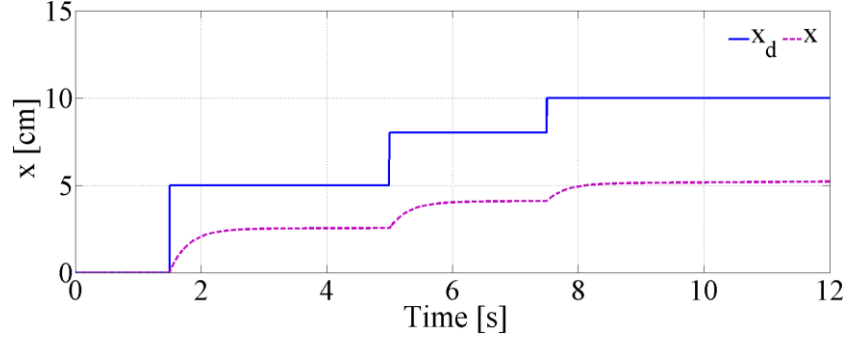


Figure 1.5: Position control of the finger using fixed-gain PI control. The blue and purple lines in this figure illustrate the desired position and the actual finger position, respectively.

1.1.2 Grip Force Control

This section explains the difficulties in using a linear fixed-gain controller to control the grip force. A schematic model of a two-finger gripper and its DC actuator is illustrated in Figure 1.6. For clarity, the mechanical connections for only one finger and the DC motor are shown in this figure. Two masses, M_F and M_R , depict the mass of the finger and rotor mass of the DC motor, respectively. The spring and damper, K_J and B_J , in this figure are used to model the joint and shaft coupling between the DC motor and finger. The two dampers, B_F and B_R , are used to model the friction between the fingers and palm and the friction between the rotor and the motor stator (the friction due to the shaft bearings, and between the commutator and brushes), respectively. As shown in the figure, the rotor is driven by the motor magnetic field force, F_a . The fingers are subject to the resistive force of the object, F_b .

A linear motion controller with proportional-derivative gains of G_P and G_D , respectively, acting on the position error of the shaft is shown in Eq. 1.9. In this equation, the actual position of the shaft and the desired position are shown by X^R and X_d^R , respectively. A force sensor is mounted on the fingertips to measure the grip force. A proportional controller with a gain of G_P^F is applied to this force feedback.

$$F_a = G_P^F \left(F_b + G_P (X_d^R - X^R) + G_D (\dot{X}_d^R - \dot{X}^R) \right) + G_P (X_d^R - X^R) + G_D (\dot{X}_d^R - \dot{X}^R) \quad (1.9)$$

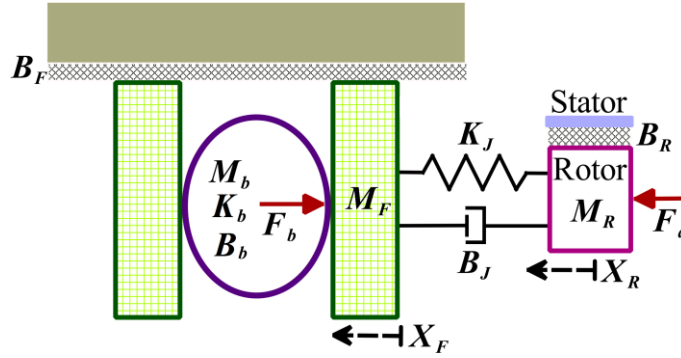


Figure 1.6: A schematic model of a two-finger gripper and its DC motor.

In this equation, the PD gains (G_P and G_D) are equivalent to the passive mechanical components, spring and damper, and it can be demonstrated that any active PD position control can be used to emulate a passive Mass-Spring-Damper system. In Eq. 1.9, a proportional gain is chosen for the force feedback so as to not change this analogy because, as can be seen from Eq. 1.9, this equation is equivalent to a spring and damper system with stiffness and damping ratios of $G_P(1 + G_P^F)$ and $G_D(1 + G_P^F)$, respectively. From the Routh-Hurwitz criterion, it can be shown that this closed-loop system is stable as long as the force measured by the force sensor is zero (K_b and $B_b \rightarrow 0$ and $F_b = 0$). However, in the presence of an external force applied to the fingers, (that is, K_b and $B_b \neq 0$ and $F_b = K_b X_F + B_b \dot{X}_F \neq 0$), there are certain situations where the some of the poles of the system can be in the open right half plane. Some examples of such unstable situations can be found in (1, 5). Figure 1.7 depicts the root locus plot for this example. In this figure, the stiffness of the object varies from 1 to 120 N/mm; as can be seen, increasing the stiffness of the object will destabilise the system.

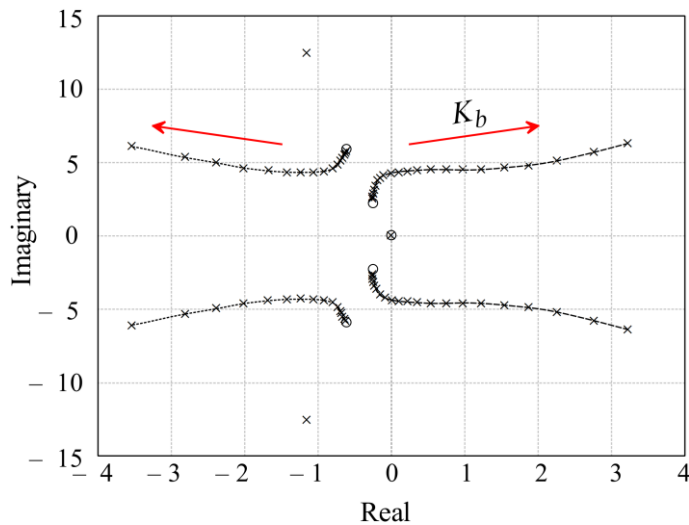


Figure 1.7: Root locus plot for the gripper-object model as K_b increases.

1.1.3 Gripper/hand with Serial Elastic Element (SEE)

As shown in Section 1.1.2, the grip force control described by Eq. 1.9 is prone to uncertainty due to the object's mechanical properties. Indeed, from Figure 1.7, although the suggested control design with fixed gains is stable in isolated conditions ($K_b = 0$), it can be driven to instability when the fingers interact with a sufficiently stiff object ($K_b \gg 0$). One of the solutions to stabilising the force controller is to add a Serial Elastic Element (SEE) between the finger and actuator (6-9). In Figure 1.8, the variable K_V is used to represent this SEE. From this figure, the passive elements K_b and K_V are connected in series, hence the apparent stiffness that the controller experiences cannot exceed K_V . Therefore, the stability condition for grasping any object with any stiffness can be satisfied by appropriately selecting the magnitude of K_V .

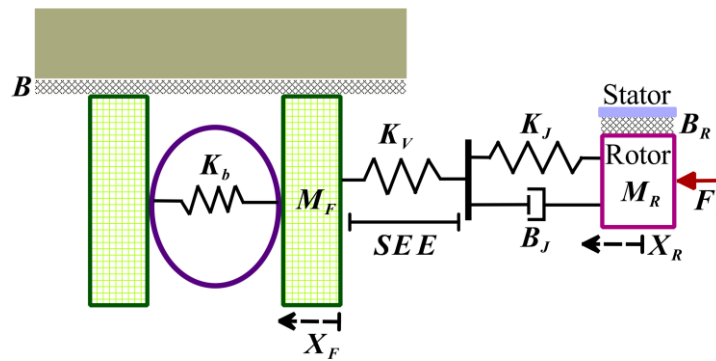


Figure 1.8: Adding a Serial Elastic Element (SEE) between the fingers and actuator can allow the grasp of an unknown object to be more stable.

The Bielefeld Shadow hand, shown in Figure 1.9, was one of the most popular dexterous robotic hands to use a serial elastic mechanism in its actuation system. The hand was made by the Shadow Robot company and has been available on the market since 2004 (161,162). In total, the hand was made of 20 active and four passive joints. Each joint was actuated by a pair of McKibben pneumatic muscles in an antagonistic manner. Thanks to the lightweight properties of this muscle, the hand had a high force to mass ratio. All the artificial muscles were packed in the hand's forearm. The hand used tendons to transfer the actuation forces of the muscles to the fingers. It used 80 solenoid valves to control the air flow and consequently motion of the hand. The McKibben based actuators used in this hand provided inherent serial elastic properties in the fingers, allowing a stable grasp and safe operation; however, the stiffness variability and maximum payload achieved by this hand was limited. The high cost,

weight (4.3 kg), complexity of design, durability and limited payload (5 kg max) were amongst its most obvious issues.



Figure 1.9: The dexterous 24-joint Bielefeld Shadow hand (162).

Figure 1.10 shows the granular jamming universal gripper proposed by Brown et al. (163). The gripper was made of granular material surrounded by an elastic membrane making a single spherical universal gripper. The gripper generated a simple grasp by surrounding the object to determine its shape, after which a vacuum pump was activated, reducing the inner pressure and hence jamming the filled granular material. This increased the rigidity of the gripper and provided enough grip force to compensate for the weight of the object. The gripper was then able to lift the object. Interestingly the proposed gripper was capable of grasping objects with unknown and odd shapes without any feedback from the gripper. This mechanism could also be considered a sensor free, passive serial elastic gripper due to the compliant properties of the elastic material. This compliance provided a stable grasp and safe interaction with objects to be grasped. However, the gripper was unable to lift heavy objects, with a maximum payload of only 2 kg. The maximum size and volume of the object that could be grasped by this gripper was also somewhat limited.



Figure 1.10: The granular jamming universal gripper proposed by Brown et al. (163).

Figure 1.11 depicts the passive universal gripper suggested in (164). The gripper was made of a mass of granular material encased in a membrane. The membrane was made of an elastic material. Using both positive and negative air pressure, the gripper could rapidly lift and place objects with very different shapes. As shown in Figure 1.11.b, and in order to firmly grasp the objects, the gripper first conformed to the body shape of the object to be grasped, after which the elastic membrane was hardened using an air vacuum pump. This generated a lifting force that was large enough to lift the object. Using a positive pressure would then reverse this procedure, meaning the elastic membrane would return to its deformable condition and hence release the object being grasped. Using both negative and positive pressure, it was demonstrated experimentally that the performance of the gripper increased by up to 85% in reliability and 25% in error tolerance. The capability of the gripper to shoot objects by fast ejection was also demonstrated.

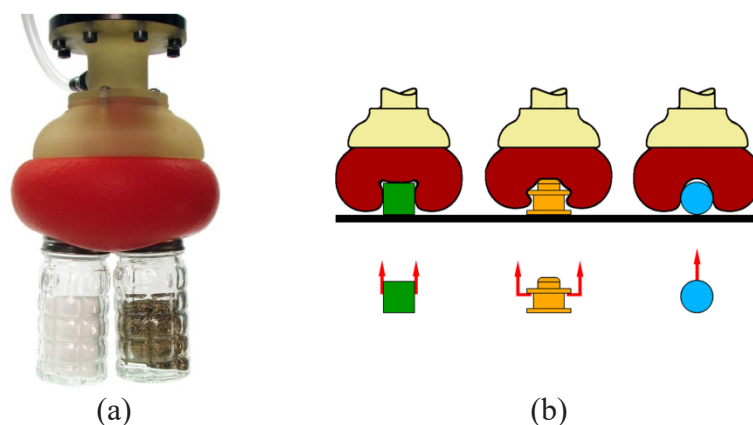
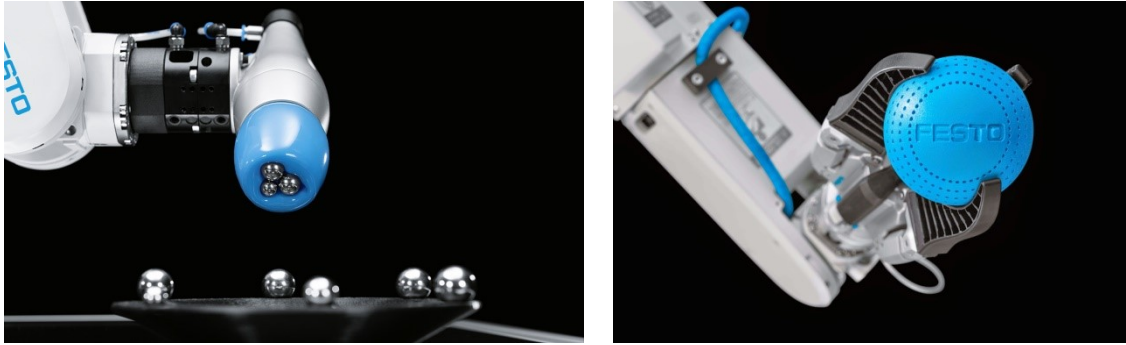


Figure 1.11: (a) Universal jamming gripper proposed in (164). (b) The gripper was able to grip objects without the need for a grasp planning or sensory feedback.

Figure 1.12 depicts two pneumatic grippers, the so-called Festo flexshape (left) and Festo adaptive gripper fingers DHAS (right) as two examples of commercially available grippers with SEE (165). The Festo flexshape is very similar to the granular jamming gripper in terms of its working concept where it utilises a flexible membrane shell and air vacuum pump to grasp and lift the object. Festo's adaptive gripper fingers, DHAS, provides a multi-choice gripper solution that can be mounted on both parallel and centric grippers without requiring additional conversion. Festo's SEE gripper can handle objects with different shapes and flexibilities without the need for additional sensors or complex control. Limited payload, grasp accuracy and repeatability and uncontrollable stiffness are the main shortcoming of these grippers.

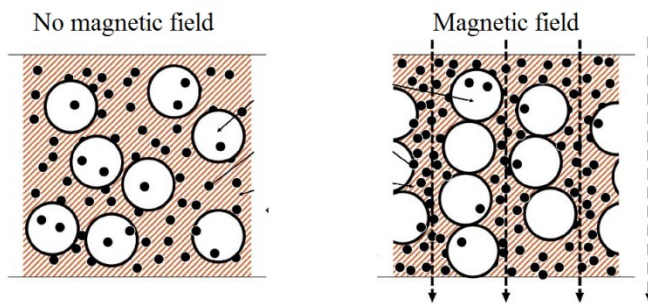


(a)

(b)

Figure 1.12: (a) Festo flexshape and (b) Festo adaptive gripper fingers, DHAS, provide fixed compliance solutions for industrial grasplings (165).

A smart magnetic fluid, $MR\alpha$, was proposed in (166) for use in jamming grippers. The specific gravity of the proposed magnetic fluid was half, whilst its hardness in its solid mode was double, compared to the ordinary MR fluid. Figure 1.13.a depicts how a magnetic field solidifies the $MR\alpha$. This fluid was made of nonmagnetic particles mixed into conventional MR fluid. When a magnetic field was applied, the iron particles of the MR fluid, as well as the nonmagnetic particles, aligned themselves along the magnetic flux lines. This generated a strong shear force acting against any external force.



(a)



(b)

Figure 1.13: (a) The solidification principle of the proposed magnetic fluid in (166). (b) An example of the gripper that used the $MR\alpha$ fluid in its actuation system.

They also developed a universal jamming gripper using the proposed $MR\alpha$ fluid, as shown in Figure 1.13.b. The gripper was made of an electromagnet and an elastic membrane. The

elastic membrane was made of a silicone rubber and it was filled with the MR α fluid, and an external collar used to fix the membrane to the electromagnet. They mounted their gripper on a 6-DOF robotic arm. To lift objects using the robotic arm, the gripper was pressed onto a target object, after which the electromagnet was powered using a DC power supply and the object gripped and lifted using the gripper and arm. The capability of the gripper to lift objects with a maximum weight of 5.17 kg was shown experimentally.

Although the SEE can, to some extent, increase the stability of the grasp by reducing the apparent stiffness observed by the controller, including a parallel damper to the SEE, the output energy of this active system can be negated, hence effectively increasing the stability of the system (10-14). A schematic model of the gripper with the recommended parallel passive stabiliser is shown in Figure 1.14.

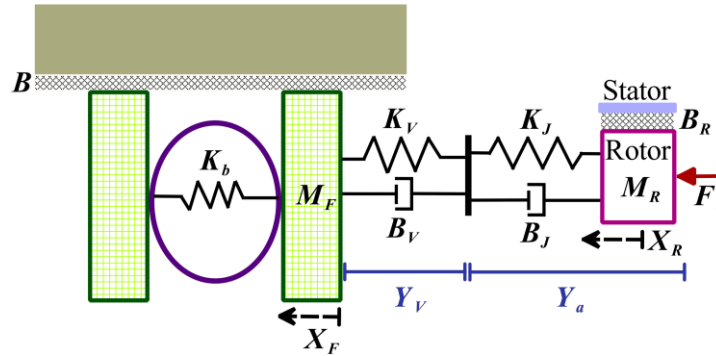


Figure 1.14: Inclusion of a parallel damper with the SEE can stabilise the grasping action.

From this figure, the apparent mechanical admittance, when measured at the fingertips, can be calculated as:

$$Y_F^S = Y_a^S + Y_V^S = Y_a^S + \frac{S}{B_V S + K_V} \quad (1.10)$$

where Y_F^S , Y_a^S and Y_V^S represent the Laplace transforms of the admittance of the fingertip, actuation system and the stabiliser, respectively.

1.1.4 Gripper/hand with Variable Stiffness Mechanism

It is worth noting that despite the above-mentioned advantage of the SEE, there is a drawback to it; this passive element may compromise fine motion control. To benefit from the stabilisation effect of the SEE and maintain the fine motion control, a Variable Stiffness

Mechanism (VSM) can be used as an appropriate replacement for the SEE. Figure 1.15 demonstrates a schematic model of a gripper with a VSM. Using such an adjustable stiffness system will help the controller to stabilise the grasp (by reducing the stiffness) in the presence of any uncertainty, while fine motion control can be achieved by increasing the stiffness of the system.

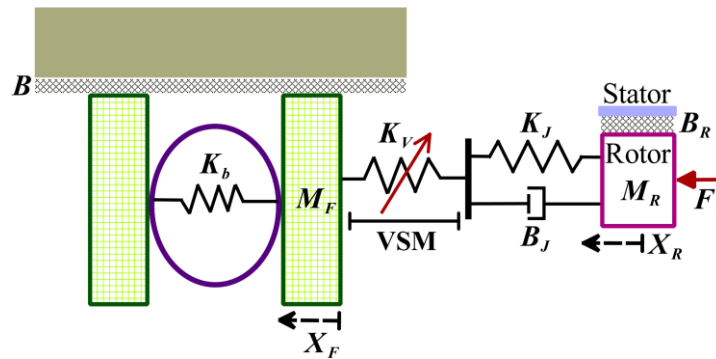


Figure 1.15: A two-finger gripper with a VSM to stabilise the grasp.

Figure 1.16 shows one of the most famous variable stiffness dextrous hands designed and fabricated by the German aerospace centre (117, 118). The hand consisted of four identically shaped fingers connected to a palm, which itself incorporated an extra degree of freedom. The hand utilised a Field Programmable Gate Array (FPGA) board to collect the feedback data in each joint. Point-to-Point Serial Communication (PPSeCo) connected the brushless DC motors to the palm's FPGA. A PCI-based high-speed floating-point Digital Signal Processor (DSP) was used as the kernel of the hardware system for data processing purposes. The FPGA boards provided a high speed (up to 25 Mbps) real-time serial control communication for the system. In order to control the stiffness and positions of the fingers and achieve a compliant grasp, the hand used an antagonistic variable stiffness mechanism. Each joint in this hand was actuated by two DC motors where a pulley-tendon system and a slider-spring mechanism connected each DC motor's shaft to the relevant joint. The slider-spring mechanisms were made of a linear compression spring, which was used to push the tendon in its rest position, forming the tendon into a triangle. The height of each triangle determined the stiffness of the tendon and its relevant joint. In order to achieve independent position and stiffness controllability in each joint, they used a pair of the mechanisms detailed above in an antagonistic manner for each joint. However, complexity of control, expensive and delicate sensors, requirement for continuous maintenance, limited achievable force, weight, and high cost are just some of the reasons for the limited use of this hand in automated lines.

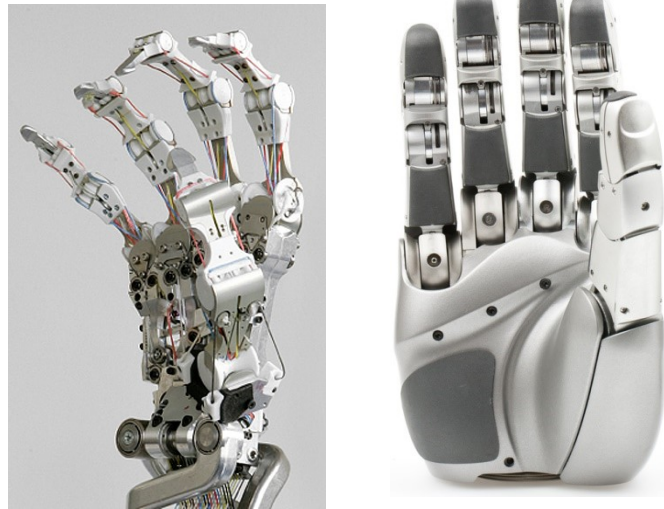


Figure 1.16: The dexterous, variable stiffness DLR-HIT hand (117), (167).

1.2 End effectors in industry

In industry, usually an end effector refers to a device at the end of a manipulator, designed to interact with the environment (168). The type and shape of the end effector mainly depends on the required tasks. Industrial end effectors can be classified either by their gripping methods or by the methods by which they close and open the fingers. In terms of the gripping methods, an industrial gripper can be classified as electromagnetic, vacuum cup or mechanical grippers. According to the closing/opening methods, a mechanical gripper can be either parallel jaw fingers or angular fingers. A synchronous gripper is referred to as a mechanical gripper that can centralise the grasped object during grasp. Usually, parallel finger grippers have the capability of centralising the objects.

❖ Mechanical Grippers

These types of grippers grasp objects by generating clamping forces using their fingers. The mechanical grippers can be further classified into electric and pneumatic grippers.

Figure 1.17 depicts some commercially available electric grippers. These types of grippers utilise an electromotor in order to move the fingers and generate the grip force. The main advantages of these grippers are that both speed and force can be precisely controlled using a sufficient active control algorithm. Adaptive actively controlled electric grippers are a good choice for many industrial applications such as in the food industry and teleoperation in harsh environments.



Figure 1.17: Some examples of the industrial electric grippers (168).

Pneumatic grippers on the other hand utilise air pressure to actuate the fingers. Usually compressed air inside a pneumatic actuator is used to generate a motion to move the fingers and generate a grip force. Such pneumatic grippers are found in both parallel and angular versions as shown in Figure 1.18.

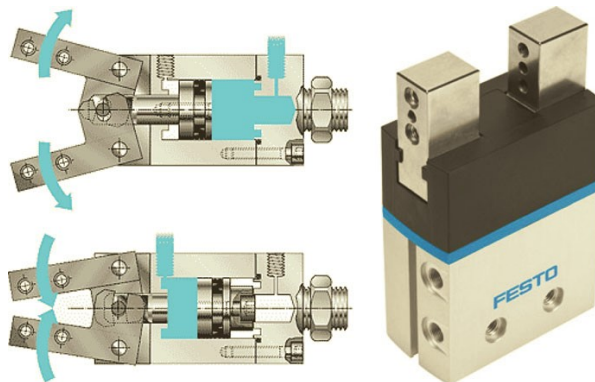


Figure 1.18: Some examples of the industrial hydraulic grippers (168).

❖ Vacuum Grippers

Figure 1.19 depicts a specific type of end effector, the so called vacuum gripper. These grippers utilise a vacuum force to hold and lift objects. In the presence of objects with a smooth, flat and clean surface, these grippers provide a low cost and durable grasp solution. As mentioned, the main problem of this type of gripper is that the grip performance is highly depended on the surface properties of the object being grasped.



Figure 1.19: Vacuum gripper and its suction cups (169).

❖ Magnetic Gripper

Magnetic grippers are used to lift ferrous materials and can be classified into electromagnets and permanent magnets. Figure 1.20 shows an electromagnet gripper used to lift steel pipes and rebars. The electromagnet grippers consist of a DC power supply and an active current control in order to control the magnetic field. The main advantages of magnetic grippers are that they provide an easy, efficient and powerful solution for grasping and lifting very heavy objects in industrial environments. However, as mentioned, their applications are very narrow as they only can grasp ferrous materials.



Figure 1.20: Electromagnet grippers provide a simple and low-cost solution for lifting ferrous materials (170).

1.3 Aim and Objectives

Sections 1.1.1 and 1.1.2 show that to achieve a promisingly robust robotic grasp, the dynamical model and mechanical properties (stiffness and damping ratio) of the object to be grasped needs to be considered in the system model. Any miscalculation or neglect of the object's mechanical properties can bring the poles of the system into the instability zones,

even if the system is stable in isolation. However, in the majority of instances, the mechanical properties of the objects are not available. Although some vision-based AI algorithms can, at least to some extent, recognise the objects and allocate pre-learned dynamics (of the object) into the dynamical model of the system (15-19), to date, these methods are not sufficiently reliable to that extent that they can be confidently used in industrial environments.

Clearly, the easiest way to identify the object's properties is via mechanical interaction with it (20-26). Thus, stable mechanical interaction might be required before one can design an appropriate grasp controller; however, a stable grasp cannot be guaranteed without knowing the properties of the object.

In short, the main objectives of this work are:

- ❖ To develop a passive grasp control method to overcome the following uncertainties of the grasping tasks:
 - Uncertainty or miscalculation of the gripper model.
 - Uncertainty of objects to be grasped with unknown mechanical properties.
 - Stochastic perturbations and unpredictable/deterministic external disturbances.
- ❖ To develop an active slip prevention method to allow robotic grasping of unknown objects whilst ensuring the grasp does not result in damage to the object being handled.

1.4 List of Contributions

As mentioned previously, in grasping scenarios there is no system or technique available which allows the weight, mechanical properties or frictional coefficients of an unknown object to be determined without physically interacting with it. For example a vision systems can be used to determine the geometry of an object but is unable to establish the mass distribution; the frictional coefficient of the material that an object is made of may be known but if the part is wet this would significantly change its frictional properties. Furthermore any external disturbance forces that are applied to the object whilst it is handled are impossible to predictable or anticipate in advance as they are stochastic.

This thesis addresses the two problems mentioned above by advancing the state of the art in both passive and active grasping, as follows:

❖ **Direct impedance modulation for stable grasping in tendon driven, angular grippers:**

- ✓ It has been demonstrated how a novel variable stiffness gripper is capable of grasping unknown objects commonly found in the agricultural and food processing sectors. Furthermore it has been shown that the introduction of a variable stiffness mechanism enhances the stability of the grasp achievable with an angular gripper.
- ✓ A novel force control algorithm that passively controls the grip force in a variable stiffness gripper has been designed, developed and proven. Due to the passive nature of the controller, it eliminates the need to use force sensors. The combination of the proposed variable stiffness gripper design and the passivity based controller provides a novel solution to the force control and stable grasp challenge in tendon driven angular grippers.

❖ **Active MIMO slip prevention grasp control for direct drive parallel jaw grippers:**

- ✓ A novel multi input-multi output slip prevention algorithm has been demonstrated which allows direct drive parallel jaw grippers to prevent grasped objects from slipping whilst minimising the amount the object is deformed by the gripper. The system developed does not require any prior knowledge of the object's friction, geometry or weight in order to operate. It has been shown how the system allows a broad range of unknown objects to be grasped, manipulated and placed without dropping, crushing or otherwise damaging them. It has been demonstrated how this novel technique can be applied to the task of nuclear decommissioning where there is either no accurate description of the objects to be handled or where pre-programming the gripper for each object manually would be impracticable and overly time-consuming.

This work has advanced the state of the art in the following two areas:

- Direct impedance modulation (passive based control) for stable grasping in tendon driven, angular grippers.

- Active MIMO slip prevention grasp control for direct drive parallel jaw grippers.

1.5 Organisation of Thesis

This thesis is organised into six chapters as follows:

Chapter 2:

Describes the different approaches to variable compliance mechanisms traditionally utilised in robotic systems and points out the shortcomings of such technologies to date. This chapter provides a further literature review of the history, design and development of variable stiffness and variable compliance mechanisms. A number of compliant actuation systems are described, with particular attention given to variable stiffness robotic grasper systems. The operational similarity between the human body's sensorimotor and the compliant gripper/hands is discussed through a basic study of the function of metacarpophalangeal joints.

Chapter 3:

Deals with two innovative robotic variable stiffness gripper designs, VSG₁ and VSG₂, for industrial pick and place applications. This chapter proposes two novel variable stiffness actuators designed to drive the tendon-driven underactuated grippers. To control the compliance of the fingers, a mathematical model of the stiffness is derived and presented. The experimental results provided will show how, despite the relatively simple implementation of the first prototype, the gripper performs extremely well in terms of both stiffness and grasping control. The two passive, adjustable compliance, serial elastic actuators introduced in this chapter are suitable for industrial applications, both of which greatly reduce the limitation of the maximum achievable stiffness.

Chapter 4:

This chapter explains the theory of sliding mode control (SMC), which is a particular method of robust controller theorem. It is shown how, in the presence of unknown external disturbances, an SMC can robustly and in a finite time converge the state variables to the desired values. The performance of a tendon-driven underactuated gripper controlled by a high-order sliding mode control with feedback on gripping force and slippage is presented and evaluated. More specifically, a Hybrid Super Twisting Sliding Mode Control (HSTSMC) is compared with a Hybrid First-Order Sliding Mode Control (HSMC).

Chapter 5:

This chapter addresses the uncertainty inherent to robotic grasping by evaluating the performance of a 8 kg and a 45 kg payload grippers (designed and fabricated as part of this research) which use a novel Adaptive PI-Super Twisting Sliding Mode Control (ASTSMC) and an new Adaptive First-Order Sliding Mode Controller (ASMC) that are designed to prevent slippage whilst minimising any deformation of the grasped object. The experimental results presented in this chapter show that when grasping unknown objects, the controllers are sufficiently robust to overcome external nonlinear disturbances and inaccuracies in the system model, preventing slippage and minimising any deformation of the objects. Furthermore, the proposed ASMC and ASTSMC, eliminate the major drawback of the SMC (which is called the Chattering Phenomenon (CHPH)), whilst preserving the robustness of the control.

Chapter 6:

Provides the final discussion and conclusions. The inherent limitation of the work presented and a number of suggestions to further optimise it, as well as potential areas for future work in the field of the robotic grasping, are suggested in this chapter.

Chapter 2

BACKGROUND

2.1 Introduction

For decades, robotics researchers have been influenced by the dexterity of the human hand, and have shown great interest in designing and controlling robotic hands (27-37). As discussed earlier in chapter one, the uncertainty associated with miscalculated grasp model and/or objects with unknown mechanical parameters create difficulties in performing a stable grasp. Traditional approaches to eliminating this problem involve robotic hands that are expensive, delicate, complex and difficult to control. However, as explained previously, including a sufficiently compliant element within the actuation system of the robotic hand can provide an alternative solution to this challenge. Integrating such a passive component into a robotic system will increase the stability of the grasp in the presence of uncertainties. This is also true in the human hand, as it has been demonstrated that the passive nonlinear dynamics of the joints in the human hand play a vital role in providing a stable grasp (38-44).

The passive behaviour of the human body, and more specifically the human hand, is the result of a combination of both parallel and series compliance. This form of behaviour at the metacarpophalangeal joints is largely due to the elasticity of the capsular ligament of the joints and muscle-tendon units (43), where the latter contributes to the stiffness of the joints by generating force when the muscle or tendon is under some form of tension (44).

Most of the existing research on robotic systems with variable stiffness/compliance take inspiration from the human body, mainly because of the aim of developing artificial limbs (45-52). However, certain fundamental concepts and ideas that arise from this line of research can be exploited in order to create a new generation of industrial robots, and more specifically industrial grippers, which feature controllable stiffness for demanding industrial applications requiring flexibility in grasping tasks. In-depth discussions about human hand grasping and human body impedance modulation can be found in (38-45), to mention but a few.

Following these and other similar studies, a plethora of variable stiffness/compliance designs have been proposed for robotic systems over the last decade (46-55).

2.2 Variable stiffness mechanisms

The main objective of this section is to provide a brief explanation of the most popular variable stiffness-impedance actuators and compliant hands that are, for the most part, used in the field of robotics.

2.2.1 Series Elastic Actuator

One of the earliest attempts to produce compliant actuators was accomplished by Pratt et al. (51). They suggested an elastic element should be placed between the conventional rigid actuators and external loads, as shown in Figure 2.1. They also developed one of the earliest impedance control methods for their serial elastic actuator. They showed some of the benefits of using such actuators, which include shock resistance, smaller sensible inertia, more precise and robust force control, safer interaction with the environment and energy storage properties. This actuator was used as the actuation system in the arms of the MIT humanoid robot “COG” (52, 53).

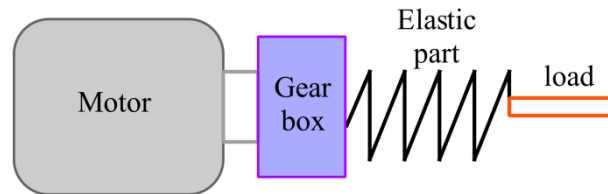


Figure 2.1: Series elastic actuator proposed by Pratt et al. (Figure recreated from (51)).

2.2.2 Force Controllable Hydro-Elastic Actuator

Figure 2.2 depicts a force controllable hydro-elastic actuator proposed by Robinson et al. (54). Similar to the series elastic actuator discussed above, this system used an elastic element to achieve compliance. This elastic element was located in a series configuration between the rigid shaft of a hydraulic piston and external shaft. Adding an elastic part to the conventional hydraulic actuator provided an easier way to control the output force by controlling the length of the spring, as demonstrated in (54).

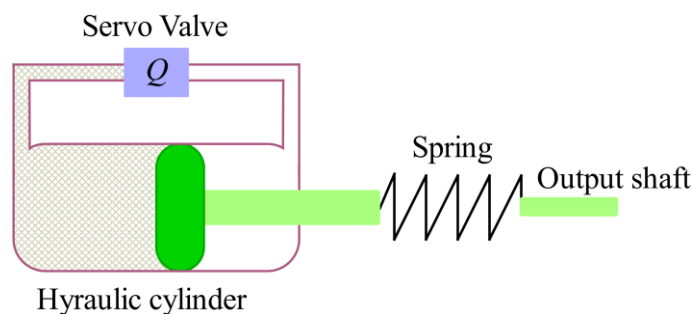


Figure 2.2: Hydro-elastic actuator proposed in (Figure recreated from (54)).

2.2.3 Compact Rotational Soft Actuator

A compact rotational series elastic actuator was introduced in (55, 56) for use in multi-DOF small-scale humanoid robots. A schematic model of this actuator is shown in Figure 2.3. As can be seen, the design consists of six identical linear mechanical springs, K , and a conventional DC motor. In this figure, the rotational motion of the DC motor is shown by M . There were three rigid spoke elements connecting the central bearing (output shaft) of the actuator to the springs. This connection was used to transfer the elasticity of the springs to the main shaft and hence provide compliance at the shaft. In order to measure the rotational angle of the output shaft, as well as the deflection of the compliant module, they used three encoders in their design. The feedback signals from these sensors also have been used to calculate the external torque applied to the shaft.

They suggested an angular velocity control in order to control the apparent output stiffness (virtually control the impedance). To do so, they used the desired virtual stiffness and the springs' states to calculate the desired velocity of the DC motor. The experimental results obtained from their prototype illustrate the ability of the actuator to generate a relatively wide range of impedance.

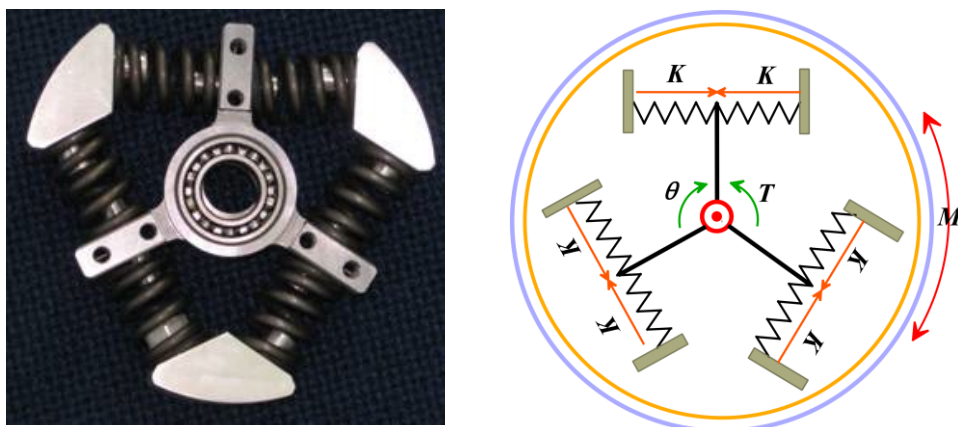


Figure 2.3: Compact rotational series stiffness actuator introduced by N.G. Tsagarakis et al. (Figure recreated from (55)).

2.2.4 Compact Rotary Series Elastic Actuator (cRSEA)

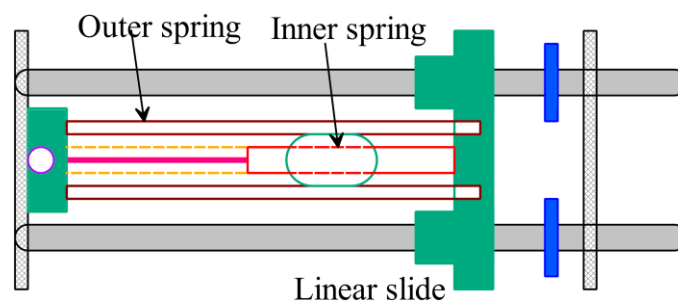
The Compact Rotary Series Elastic Actuator (cRSEA) was suggested by Kong et al. (57, 58) to be used in human assistive limbs. They used a combination of a torsion spring and a chain of worm and spur gears in this design to reduce size and achieve precise torque control. To control the output torque of the actuator (assistive torque) they used real-time feedback of the

joint angle and environmental contact force. The gear-spring mechanism in their system isolates the motor from the environment and hence could potentially be used as a shock absorber.

2.2.5 Selective Compliant Actuator

A selective compliant actuator has been proposed by Sugar (59) in order to control the applied force and the apparent stiffness of the robots. Similar to most of the series elastic actuators mentioned above, and as shown in Figure 2.4, the design is one of a mechanical spring serially connected to a linear DC motor. Due to this elastic component, and as explained in chapter one, the actuator could potentially guarantee the environment-robot interaction stability and subsequently safe interaction between the robot and any unknown/unmodeled environment.

As shown in the figure, the actuator was made of a DC servo motor. A ball screw mechanism transfers the torque of the motor to the spring. The spring system was made of a parallel configuration of an extension spring (inner spring) and a compression spring (outer spring). These two coaxial springs allowed the actuation force to be transmitted in both directions. Feedback as to the spring's deflection was used to control the interaction force between the environment and the actuator with a maximum bandwidth of 24 Hz. Due to the inertia of the moving parts, this control bandwidth dropped dramatically in the presence of large disturbances. Due to noisy feedback of the integrated accelerometer and the high inertial ratio of the gearbox DC motor, the system was not able to compensate for the effects of large disturbances. As may be noted from the figure, the output stiffness of the actuator in this system was fixed and equal to the stiffness of the integrated spring. However, the designed controller was able to control the interaction force by controlling the equilibrium position of the spring.



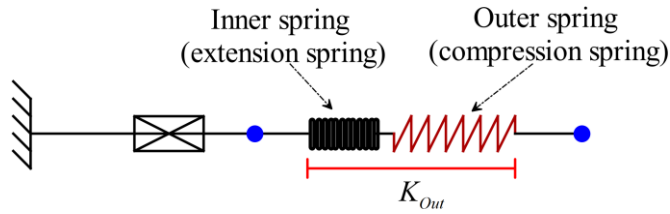


Figure 2.4: Selective compliant actuator proposed by Sugar (Figure recreated from (59)).

2.2.6 Pulley-belt driven variable stiffness actuator (VSA)

Tonietti et al. proposed a variable stiffness actuator designed for use in robotic systems as well as any mechanical devices which require some form of physical interaction with their surrounding environment (60, 61). Figure 2.5 depicts a schematic model of their suggested actuation system. The actuator consists of two DC motors. The shaft of each DC motor is connected to a pulley. A timing belt connects the two DC motors and their associated pulleys to the output shaft. Three compression springs were used so as to create tension on the belt in their rest positions, as shown in the figure. In order to control the position of the output shaft, both DC motors were rotated in the same direction (and at the same speed), whereas the rotation of the motors in the opposite direction changed the apparent stiffness of the output shaft.

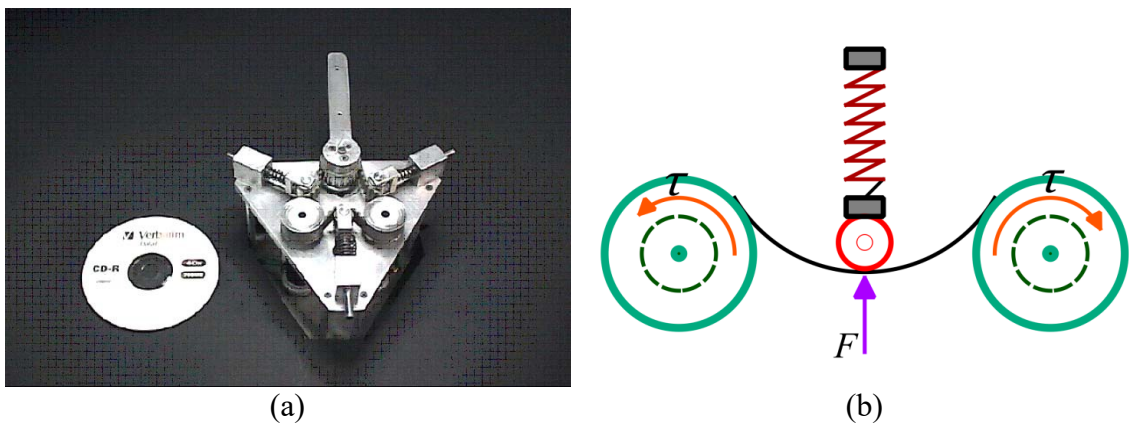


Figure 2.5: (a) Real and (b) a schematic model of the pulley-belt-spring system suggested by Tonietti et al. ((60, 61)).

2.2.7 Series Elastic Actuator for a Biomimetic Walking Robot

Figure 2.6 depicts the series elastic actuator designed by Robinson et al. (62), and that is used in a seven-link, twelve DOF biomimetic walking robot. As shown in the figure, the actuator consisted of a brushless DC motor. There was a ball screw mechanism to transfer the rotational motion of the DC motor to a linear motion. Four compression springs were placed

between the ball screw nut and the output shaft. As shown, they used a linear encoder to measure the compression of the spring system and hence control the actuators' output forces. The maximum output force achieved by this design was 1350 N.

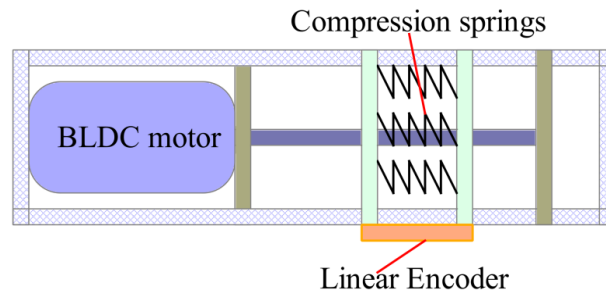


Figure 2.6: Schematic model of the SEA designed for a biomimetic walking robot (Figure recreated from (62)).

2.2.8 Antagonistically-twisted round-belt actuator

Figure 2.7 shows a compliant joint actuated by an antagonistically-twisted round-belt actuator, as proposed by Inoue et al., (63). As shown in this figure, the design comprised two DC motors, one pulley, and a link connected to this pulley. Two twisting elastic and flexible round-belts connect the pulley to the shaft of the DC motors in an antagonistic setup. The contraction generated by twisting the belts was used to create a moment, and consequently rotational motion on the pulley. Due to twisting mechanism of this design, the rotational speed of the revolute joint (pulley) was lower than rotational speed of the motors, which provided a means of speed reduction for the actuator. This design also had the advantage of increasing the output torque, which was beneficial for lifting heavy loads. They illustrated through experiment that a simple proportional control design was sufficiently robust to control the contraction force, as well as contact force (63). They also claimed that the poor material properties of the twisted strings did not affect the performance of the proportional force control.

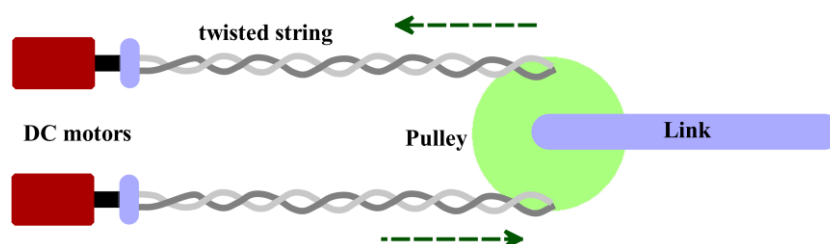


Figure 2.7: Antagonistically-twisted round-belt actuator proposed by Inoue et al. (Figure recreated from (63)).

2.2.9 Controllable Equilibrium Position Actuator

In order to achieve a compliant leg for the bipedal robots, a mechanically adjustable compliance and controllable equilibrium position actuator (MACCEPA1) was suggested in (64, 65), where a schematic model of their design is shown in Figure 2.8. As depicted in this figure, the MACCEPA consists of three links and one common revolute joint (knee joint), where the links pivot around the knee joint. In this figure, the left and right links are the upper and lower links of the leg, respectively. There was also a lever link (shown by the smallest link in the figure) connected to the knee. A linear tension spring was attached to the lever link and a string connected this spring to the lower link. The angle between the upper link and lever link is denoted by φ in the figure. This angle could be changed by an electrical motor connected to the lever link. The angle α in the figure corresponds to the angle between lever link and the lower link. Clearly, when α was not zero any elongation of the spring would generate a resistive torque, trying to line up the lower link with the lever link. When α was zero (the equilibrium position) the spring would not apply any resistive torque to the lower link.

To generate an elongation on the spring and consequently a resistive torque, they used an electro-motor. This electro-motor was used to pull on the cable connected to the spring, which resulted in the pre-tensioning of the latter. This pre-tension changed the resistive torque for a given angle α , consequently changing the apparent stiffness of the system. They modelled the stiffness as a function of α and elongation of the spring due to the pre-tension, after which they validated the model generated through a number of experiments performed using the prototype.

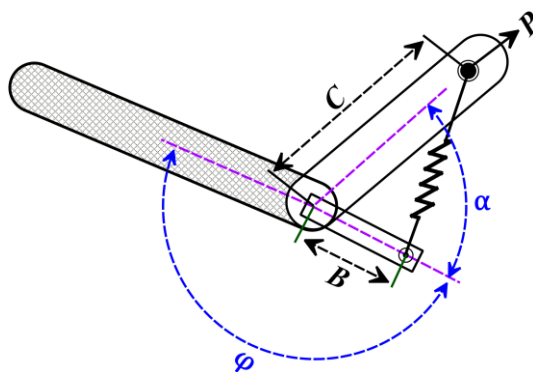


Figure 2.8: Controllable Equilibrium Position Actuator (MACCEPA1)

(Figure recreated from (64)).

2.2.10 MACCEPA2

MACCEPA2 was a modified version of MACCEPA1 with improved torque-angle and stiffness-angle curves, as proposed by the designer of MACCEPA1 (66). In order to improve the functionality of the actuator, they replaced the lever link in MACCEPA1 with a profile disk, as shown in Figure 2.9.

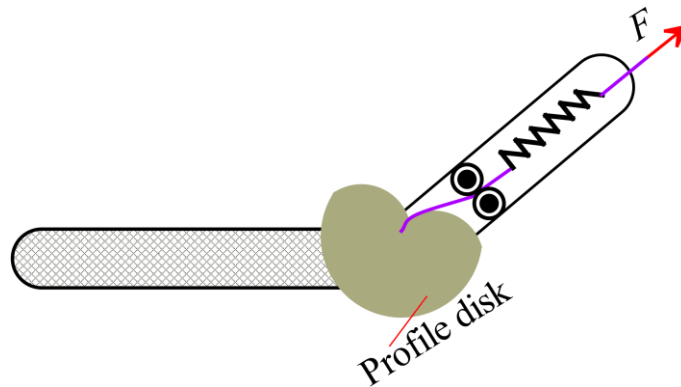


Figure 2.9: Schematic model of Maccepa2 (Figure recreated from (66)).

They used two actuators in MACCEPA2 in order to independently control the position and compliance of the joint. The first servo motor was used to generate a pre-tensioning force (depicted by F in the figure) on the spring and hence change position, whereas the second motor was used to rotate the profile disk to change the stiffness of the joint (66).

2.2.11 Cam-based variable stiffness actuator

Another relatively similar approach to the variable stiffness actuator was introduced in (67, 68). Figure 2.10 depicts a schematic model of the actuator. As shown in this figure, the model consisted of a linear compression spring connected to a low-friction roller on one side and a linear actuation mechanism on the other. Similar to MACCEPA, the role of the linear actuation system in this model was to generate a pre-tension on the linear spring by compressing it. The output link of the system was connected to a concave nonlinear cam and a revolute joint was used to connect this cam to the main chassis. The roller was able to move inside the concave surface of the cam with a very low friction, with the associated motion used to generate the apparent stiffness of the output link. In this figure, q denotes the output position of the system, whereas x represents the control input (the position of the motor's shaft). To change the apparent stiffness of the system, the linear motor was used to change the length of the spring and, consequently, the stiffness of the joint. The apparent stiffness of the

system was a nonlinear function of the stiffness constant of the spring K , the cam transmission ratio, and the offset of the output link P_2 . As mentioned, the design used a single actuator to change the output stiffness; however, the system was unable to control the output position (position of the output link). It should be mentioned that due to the roller-cam mechanism used in this system, the design could be prone to the collection of dust inside the concave surface of the cam which might increase the friction and consequently increase the apparent damping ratio of the system.

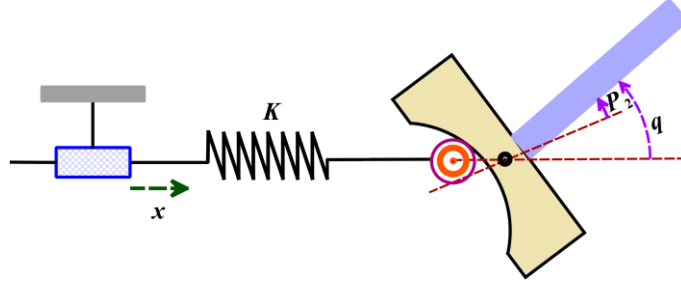


Figure 2.10: Schematic representation of a cam-based variable stiffness actuator introduced in (67, 68). (Figure recreated from (68)).

2.2.12 Adjustable moment arm

Figure 2.11, depicts a schematic model of a variable stiffness mechanism introduced by Kim et al. (69). The design was based on an adjustable moment arm. The model consisted of a position frame and an output shaft which was fixed to a guide and two spring blocks. Each of the spring blocks consisted of a linear compression spring. The springs were used to push the guide on each side and hence limit the rotation of the output shaft. Unlike the two previous models, in this mechanism the position and apparent stiffness of the output shaft were independently controllable. The rotation angle θ_f of the position frame was used to control the position of the output shaft, whilst the length of the moment arm l_{sb} was used to adjust the output stiffness. They modelled the apparent stiffness of the output shaft as below:

$$k_j = \partial \tau_{ext} / \partial \theta = k_s l_{sb}^2 \tan^2 \theta \quad (2.1)$$

Where k_j , τ_{ext} , θ and k_s denote the apparent stiffness of the output shaft, the external torque applied to the output shaft, the rotation of the output shaft due to this external torque and the spring constant, respectively. From Eq. 2.1, the output stiffness is proportional to the spring constant and l_{sb}^2 . From this equation, it may also be noted that the output stiffness is also

proportional to the deflection angle θ , and varies as this angle is changed. The position of the output shaft Θ can be calculated as below (69):

$$\theta_o = \theta_f + \theta = \theta_f + \tau_{ext}/k_j \quad (2.2)$$

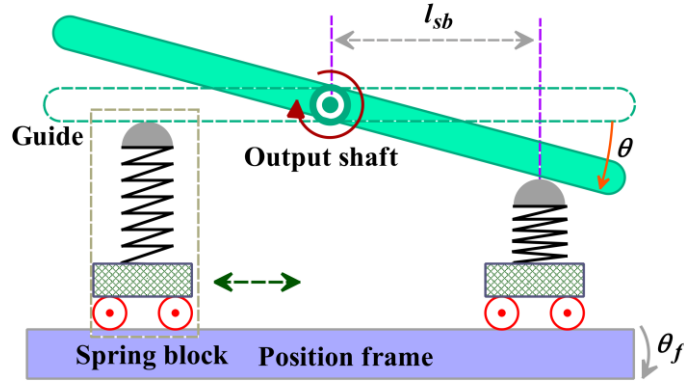


Figure 2.11: Schematic representation of the cam-based variable stiffness actuator (Figure recreated from (69)).

2.2.13 A leaf spring-based variable stiffness joint

A leaf spring-based variable stiffness joint was suggested in (70) for use in a manipulators' joint. Their proposed system utilized four leaf springs to achieve compliance. As shown in Figure 2.12, the springs were symmetrically fixed to the output axis. The mechanism consisted of four pairs of rollers, where each pair slides along the axis of the relevant spring. The distance between the axis and the rollers determines the effective length of the spring. In order to control the position of the output joint, as well as the output stiffness, independently, they used two actuators to change the effective length of the springs by moving the rollers (subsequently changing the output stiffness). The same actuators also were used to change the position of the output shaft by rotating all the springs and rollers around the main axis of the shaft. ψ shows this rotation in the figure. They experimentally illustrated the ability to independently control the stiffness and position in their actuator. The output torsional stiffness was modelled as:

$$S = (l + D/2)^2 \frac{E\omega t^3}{l^3} \quad (2.3)$$

where S , l , D , E , ω , and t denoted the torsional output stiffness, effective length of the springs, diameter of the output axis, Young's modulus, width, and thickness of the leaf springs, respectively (70).

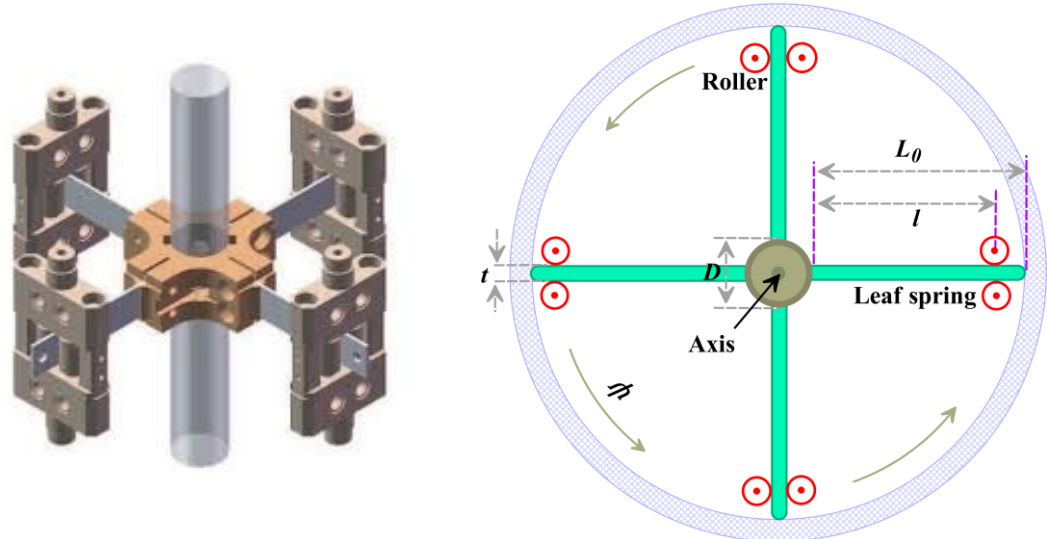


Figure 2.12: Schematic model of the leaf spring-based variable stiffness actuator. Sliding the rollers along the leaf springs would change the effective length of the springs and consequently change the output stiffness (Figure recreated from (70)).

2.2.14 Antagonistic VSM

A simplified model of the variable stiffness design discussed in section 2.1.6 was suggested by Grebenstein et al. (71, 72), and has been used as the actuation system in the DLR hand (73). Figure 2.13, depicts a schematic model of their design. As this figure shows, the model consisted of a DC motor, a pulley-tendon system and a slider-spring mechanism. The slider-spring mechanism was made of a linear compression spring, which was used to push the tendon in its rest position, forming the tendon into a triangle. The variable h shown in the figure determined the stiffness of the tendon. In order to achieve an independent position and stiffness controllability in each joint, they used a pair of the mechanism detailed here in an antagonistic manner for each joint.

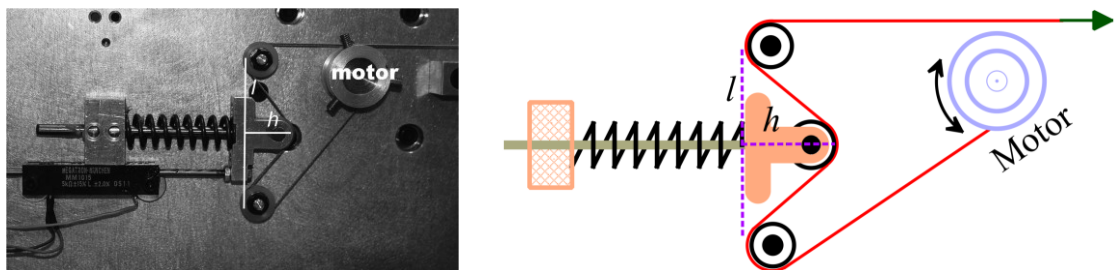


Figure 2.13: Antagonistic VSM used in DLR hand (71-73).

2.2.15 McKibben muscle

McKibben is a relatively low cost, lightweight, small, soft and flexible actuator with a high power-to-weight ratio (74, 75).

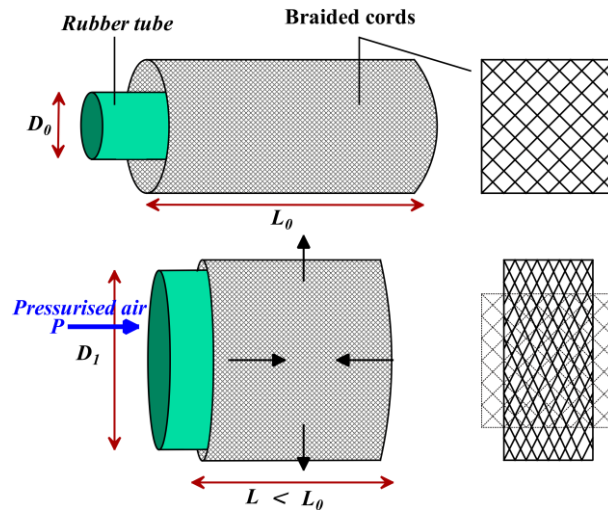


Figure 2.14: Schematic representation of a McKibben artificial muscle (74, 75).

This type of actuator saw its first use in the early 1950s for the purposes of prosthetic limb research (76). The actuator, as shown in Figure 2.14, is commonly made of an inflatable bladder (generally made of rubber tube) covered by a braided mesh shell (77-80). The braided shell is made of non-stretchable threads. The behaviour of this actuator is similar to that of muscles in the human body. To actuate this artificial muscle, a high-pressure air supply, as provided by a pneumatic compressor, is required. As shown in the figure, the applied air pressure will inflate the internal bladder; consequently, the pressurized air pushes against its inner surface and the surrounding sleeve, thus increasing its volume. As the sleeve is made of non-extensible threads, the actuator starts to become shorter, thus generating force.

2.2.16 Artificial muscles

Pneumatic artificial muscles, e.g., McKibben muscles (74, 75) or PAMs (Pneumatic Artificial Muscles) (81-87), could be considered as an alternative to the mechanical spring and damper in designing variable stiffness, variable compliance systems. PAMs can generate a high power-to-weight ratio (82). These actuators also provide satisfactory compliance due to gas compressibility and the flexibility of the inflatable bladder. In an antagonistic layout, as shown in Figure 2.15, these actuators can be used to control both the stiffness and position of

the robot joints. To solve the limitation of the requirement for heavy compressors, which is an inevitable part of all pneumatic actuators, Vitale et al. proposed an energy transduction method that could be used to lead propellant-based chemical actuators (88, 89). The actuator was able to transform chemical energy into mechanical energy as an alternative to the use of a compressor. They used this method for a prosthetic under-actuated hand with 21 degrees of freedom and nine actuators. The fuel cartridge carried 200 mL of hydrogen peroxide, which could provide 55 kJ based on a 70% concentration. In-depth discussion about artificial muscles and their application in robotics can be found in (81-87).

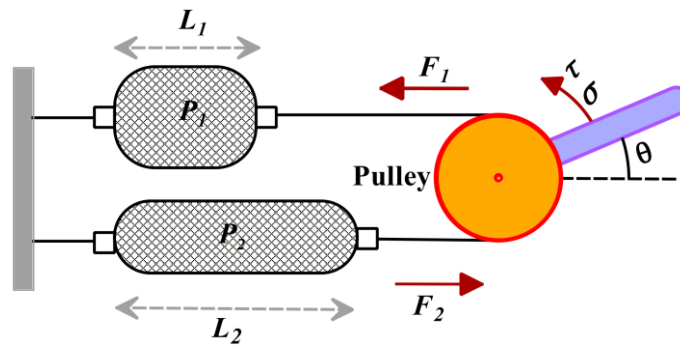


Figure 2.15: Two-artificial muscles in an antagonistic layout can control both the stiffness and position of the robot joints.

2.2.17 Quasi-antagonistic variable stiffness actuator

AMASC was proposed by Hurst et al (90) in order to generate the motion and control the impedance of the legs of a quadruped robot. The variable stiffness actuator was made of two DC motors which were coupled in a quasi-antagonistic configuration using two pulleys and a cable. The first actuator was used to rotate the first pulley J_1 , and provide the rotational motion in the joint of the legs, whereas the second motor was used to change the length of the springs and consequently the output stiffness of the legs. To get the nonlinear effect from the linear springs, which were linked with floating pulleys, the robot's legs were connected to the second pulley J_2 . Instead of designing a mechanism to change the linear function of the spring, they used two nonlinear elastic elements.

2.2.18 VSM for prosthetic limbs

English et al. proposed a new variable stiffness structure for prosthetic limbs. To achieve the linear relationship between actuator co-contraction and joint stiffness, they suggested two quadratic springs in an antagonistic configuration (91). As long as the torques generated from

the two motors had the same magnitude in opposing directions, the output shaft would be placed in a fixed position. When the two motors rotated at the same speed but in different directions, the stiffness of the output shaft was changed due to the contraction of the two nonlinear springs. Therefore, if torques of different magnitudes were to be applied, the difference between the magnitudes would generate a torque, thus resulting in a rotation of the output shaft.

2.2.19 VSA-Cube

The VSA-Cube was based on a bidirectional antagonistic design which consisted of two driven pulleys, P_1 and P_2 , and a main shaft, P_{sh} , in the centre. The main shaft was connected to the pulleys via four tendons and four non-linear springs in the symmetrical arrangement shown in Figure 2.16.

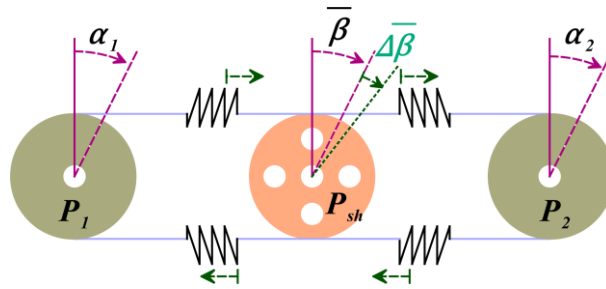


Figure 2.16: The VSA-Cube is made of four springs, two driven pulleys and one main shaft (Figure recreated from (92)).

The rotation of the pulleys, α_1 and α_2 , in opposite directions causes the elongation of the two of the springs and hence increases the output stiffness, whilst rotating the pulleys in the same direction and same speeds caused a rotation on the output shaft with a fixed stiffness (92, 93).

2.2.20 Variable physical damping actuator (VPDA)

A semi-active friction-based variable physical damping actuator (VPDA) was introduced in (94). The VPDA consisted of a variable damping element. In order to induce a desired oscillation to the response of the actuator, they also used a passive torsion spring connected in parallel to the damping element. To produce an appropriate friction and to control the damping coefficient of the output shaft, they used three piezo stack actuators connected in parallel to apply a normal force to a rotating disk. This normal force generated friction and hence increased the damping ratio of the system. The output damping was a function of the piezos' generated force.

Finally, Visser et al. (95, 96) proposed a variable stiffness actuator to provide a mechanical solution for independently controlling the position and stiffness. Similar to MACCEPA, they used a mechanical spring mounted on the lever arm of a variable effective length. The effective length of the lever arm, which was controlled via a servo motor, was used to change the output stiffness.

2.3 Compliant grasp

It has been shown that the inherent passive properties of the human hand, in both serial and parallel combinations, play an important role in grasp stabilization (97-101). Various studies into the grasp of the human hand shows that as a preliminary response, to achieve a robust grasp, humans tighten their fingers by co-contracting antagonistic muscles and consequently increase the stiffness of the fingers just before perceiving impact (97). In-depth discussions into the effect of human hand impedance modulation in grasping stability can be found in (99-101). Inspired by human hand, Kuo et al. designed a finger that was used to mimic the human index finger. Each three joints of their robotic finger had internal pulleys for tendon routing and joint rotation. To achieve a parallel stiffness, they used nonlinear stiffness elastomer materials which were inserted between two pulleys. The pulleys were connected to the rotating shaft of the joints and were rotated with the joints. The elastomer part was fixed to the housing case by two pairs of spacers and was deformed due to joint rotation (100).

Kajikawa et al. designed a four finger, twelve joint variable stiffness robotic hand for human care service tasks. To reduce the number of the actuators in the hand, they suggested a linkage mechanism which coupled the distal and proximal interphalangeal joints and actuated these two joints via a single motor. To achieve compliance in the joints, they used silicon made from deformable cushions called SRC_{trans}. An expandable cushion, SRC_{stiff}, has been used to compress the SRC_{trans} and consequently change the stiffness of the fingers. They used air pressure to inflate the SRC_{stiff} (102).

A three-joint variable stiffness robotic finger was introduced by Yang et al. (103). Their design consisted of a soft pneumatic muscle and three pin heaters which were embedded in a shape memory polymer (SMP). The finger could bend by selectively heating the SMPs and due to internal air pressure of the pneumatic muscle. Additionally, the finger exhibited variable stiffness in different SMP's temperatures.

Yap et al. introduced a soft wearable exoskeleton glove for assistive and rehabilitation applications. They used embedded pneumatic actuators to actuate the exoskeleton. They showed that the stiffness of the fingers could be changed in different locations; however, this stiffness was not controllable (104).

IRobot-Harvard-Yale (iHY) was an underactuated tendon driven, three-fingered, six joint compliant hand which utilized five DC motors to actuate the fingers. A circular magnetic base

was used to connect the fingers to the hand. This high-force breakaway coupler was used to prevent any damage due to collisions. The hand consisted of compliant flexure joints on the fingers' joints to provide passive adaptability to the shape of the grasped object, three-dimensional fingertip motions, as well as low-stiffness fingertip grasps. However, the stiffness of the joint could not be altered (105). A three-fingered, pneumatically actuated hand, PBO, was introduced by Deimel et al. in (106). The reinforced silicone rubber-made fingers in this hand used air pressure to actuate a bending motion. Each finger consisted of an active and a passive layer of silicon. The fingers were bent by applying air pressure in conjunction with the different mechanical properties of these two layers. The hand did not use any rigid materials in the fingers, which increased the robustness of the grasp in the instance of a collision. Small grip force and payload were the main disadvantages of this hand (106).

2.3.1 Parallel passive joint

Inspired by the human hand's tendon routings, and with the aim of improving the grasp stability and dexterity in manipulation tasks, a parallel compliant joint has been suggested for robotic fingers in (107). A schematic model of this compliant joint is shown in Figure 2.17. As shown in this figure, the design consisted of a rectangular-shaped compliant material which was fixed between a pair of pulleys. The pulleys were fixed to the rotating shaft of the joints in such a way as to allow them to rotate with the fingers about the fingers' revolute joints. In order to fix the compliant part, they used two fixed pairs of pins, as shown in the figure. To prevent the compliant part from undergoing any undesired displacement, they used two clamps at the top of the pins. The rotation of the joint induced a tension on the compliant material, and consequently the compliant material created a passive torque due to its intrinsic properties.

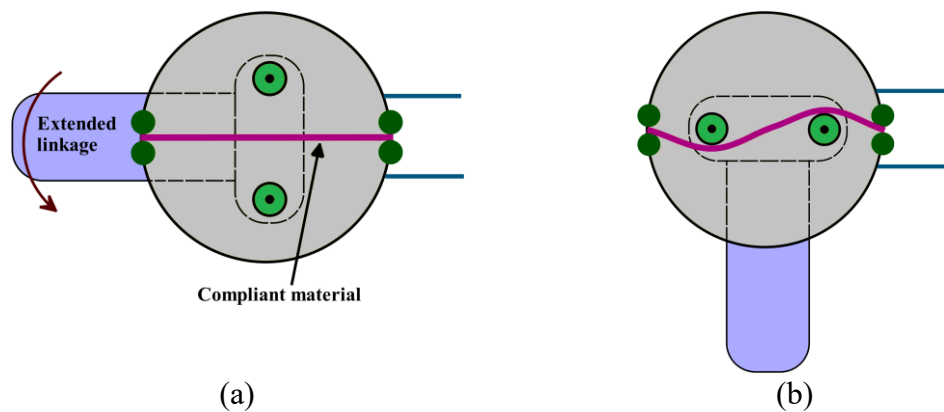


Figure 2.17: Schematic model of the parallel passive joint suggested in (107). (Figure recreated from (107)).

To achieve appropriate mechanical impedance properties for the wide range of joint angles inherent to the human hand, they suggested a design optimization method. They used this method to optimise the design variables (radius of joints, pulley and pins, the distance between centre of pulleys and joint and the thickness of the compliant component). Using an open-loop motion control to execute certain grasps, they proved experimentally that adding a parallel compliant component to the finger joints could improve the quality of the grasp.

2.3.2 Adaptive SDM Hand

Using polymer-based Shape Deposition Manufacturing (SDM), Dollar et al. designed and fabricated an under-actuated, adaptive and compliant grasper, as shown in Figure 2.18 (108, 109, 110). In order to increase the friction and prevent undesired slippage, the grasp side of each link contained a soft finger pad.

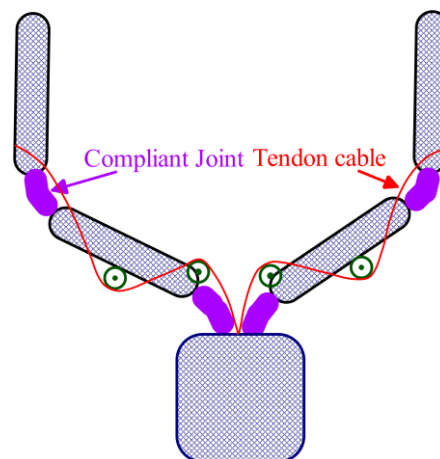


Figure 2.18: Schematic model of the Adaptive SDM Hand (108-110).

A compliant joint flexure with a stiffness range between 0.0421 and 0.224 Nm/rad was used in the proximal and distal joints to connect the finger links, as shown in the figure. An embedded Hall Effect sensor in each joint was used to provide feedback regarding joint angle. A pre-stretched, nylon-coated, stainless-steel cable anchored into the distal link was used to transfer the actuation force from the actuator to the fingers and hence provide the motion. In zero actuation mode, the tendons, which were parallel with the flexible joints, remained slack, and hence the fingers remained in their maximum compliant mode. In actuation mode, however, the inelastic tendons reduced the flexibility of the fingers (increasing the fingers' stiffness), consequently increasing the accuracy of the grasp. The stiffness constant of the joints was 0.19 Nm.deg for both proximal and distal joints, as based on the optimization

studies they developed to create a functional grasper. They showed that this stiffness enables the grasping of the widest range of object sizes with the greatest amount of uncertainty in object position (110). They also showed that the uncertainty of the grasping tasks can be satisfactorily accommodated by having optimal compliance and adaptability in the mechanical design of the hand. The experimental results provided demonstrated the robustness of the SDM hand in grasping objects in the presence of large positional errors.

Inspired by the outstanding effect of the parallel compliance behaviour of human body joints, and more specifically the important role of this compliance in metacarpophalangeal joints, a two-finger, four DOF underactuated, tendon-driven gripper prototype was developed in (101). Two antagonistic compliant parts were used in this model to provide a parallel stiffness effect for each joint. A schematic model and motion equation for a single joint are shown in Figure 2.19 and Eq. 2.4, respectively; M_{Link} and B in this equation are the equivalent mass and damping ratio, K_p is the suggested parallel compliance part and u is the control input.

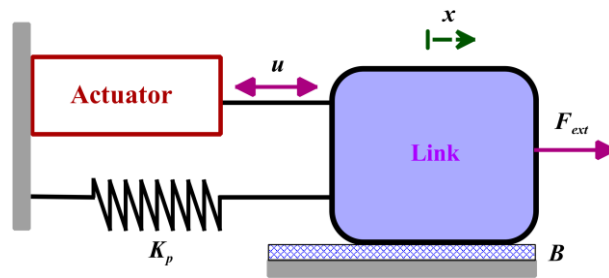


Figure 2.19: Schematic model of a robotic joint with an added parallel spring (Figure recreated from (101)).

$$M_{Link}\ddot{x} + B\dot{x} + K_p x = u + F_{ext} \quad (2.4)$$

From Eq. 2.4, it may be noted that increasing the stiffness constant of the parallel spring K_p does not change the apparent stiffness of the fingers and hence the grasp impedance will not change with changing K_p (101). However, on the other hand, the introduced parallel stiffness can be used to replace the software-based passivity of the joints with a real mechanical stiffness; clearly, such a replacement can increase the stability of the system (101). To emphasise the role of the suggested parallel stiffness, they first demonstrated that the feedback delay can destabilise the grasping task. Afterwards they concluded mathematically, as well as experimentally, that adding parallel compliance part to the gripper's joint can reduce the sensitivity of the gripper to this delay and consequently increase the stability of the grasp.

2.3.3 HEU Hand II

HEU Hand II was a non-anthropomorphic underwater robot hand presented by Meng et al. with the aim of grasping objects of different shapes, sizes and weights (111). The hand consisted of three identical fingers, where each finger was made of three joints, providing three degrees of freedom. Similar to the human hand, the two nearest joints axes to the palm orthogonally crossed at one point. A six-axis FT sensor at each fingertip and encoder in every joint were embedded in HEU Hand II. They designed and used a neural network-based impedance control and the hand force tracking was achieved using the PBNNIC scheme. The HEU Hand II, which was a modified version of HEU Hand, consisted of a new optimized mechanism for power transmission, and a new design to prevent corrosion, and the sealing design, sensor system and control system were improved, so it was considerably improved compared to the first version.

2.3.4 Bio-mechatronic anthropomorphic artificial hand

The bio-mechatronic anthropomorphic artificial hand was proposed by Zollo et al. (112). The hand was able to mimic the human hand. They addressed biomechatronics to harmonize the mechanical design of the hand with the control system. They used a conventional PD control law to obtain humanlike kinematics and dynamics, and refined the design of the hand after evaluating it by simulation. Due to some constraints coming from prosthesis hands, such as weight and size, they optimized the structure and the number of the actuators used. Their anthropomorphic hand consisted of three articulated fingers driven by four DC motors. The proposed under-actuated transmission system had the advantage of an adaptive grasp as well as passive compliance in distal joints which was achieved with a relatively small number of actuators.

2.3.5 Modular hand

A modular design for a robotic hand-assisted laparoscopic surgery was proposed in (113). They suggested this hand as an alternative for a human hand. The design had three fingers which provided nine degrees of freedom in a modular platform. The centre finger was mounted to the operational side from its end, whereas the right and left finger units were connected to the operational side outside the abdominal cavity. A similar design has been introduced by Park et al. The hand had no wrist joint and the role of wrist was performed by

three finger joints. The hand had four active fingers with sixteen joints driven by a DC motor and spur gear arrangement. The design represented a relatively lightweight (900 g in total) solution for a robotic hand. The hand provided only positional feedback from the joints, and the control design was a simple kinematic control. Experimental results for grasping under disturbances can be found in (114).

2.3.6 MR actuated variable impedance gripper

Pettersson et al. proposed a gripper mechanism that utilized the magnetorheological (MR) fluid in its variable impedance actuation mechanism. The gripper was designed for pick and place tasks in natural food product companies where the objects have different shapes and can be easily squashed. Reducing the risk of bruising through variable impedance gripping was the main advantage of the design, as claimed in (115).

2.3.7 Three-finger hand with a new stiffness control method

Maekawa et al. developed a three-fingered robot hand with a new method of controlling stiffness. Briefly, the hand was formed from three fingers, each of which included three joints. A tendon-sheath actuated by D.C. servo motor was the driver mechanism for each joint. An embedded potentiometer and a new tension differential-type torque sensor was used to provide torque feedback from each joint. They proposed a stiffness control scheme to control the apparent stiffness of the hand. Using the joints' positions and torque feedback, the controller was conjointly controlling the position and stiffness of the joints in order to achieve the desired grasp impedance. Finally, they validated the proposed mechanism and designed a position-stiffness control method by conducting various grasping experiments (116).

2.3.8 DLR-HIT hand

The DLR-HIT hand is one of the more popular dextrous hands designed and fabricated by DLR laboratory (117, 118). The hand consists of four identically shaped fingers connected to the palm of the hand. There is also an extra degree of freedom in the palm. The hand utilises a Field Programmable Gate Array (FPGA) board to collect the feedback data in each joint. Point-to-Point Serial Communication (PPSeCo) connects the brushless DC motors to the palm's FPGA. A PCI-based high-speed floating-point Digital Signal Processor (DSP) is used

as the kernel of the hardware system for data processing purposes. The FPGA boards provide a high speed (up to 25 Mbps) real-time serial control communication for the system. The hand uses the antagonistic variable stiffness mechanism explained in section 2.2.14 in order to control the stiffness and positions of the fingers and achieve a compliance grasp.

2.3.9 Composite robot end-effectors

A composite robot end-effector that incorporated optical fibre force sensors has been developed by Park et al. (119). Inspired by the receptors in arthropod exoskeletons, the proposed force sensor was able to estimate the contact locations in the fingertips. They also introduced a fabrication process that allowed them to build hollow multi material structures with embedded fibres. They used the experimental results collected from an industrial robot and a two-fingered dexterous hand to calibrate the sensors and to control contact forces in their hand. They also developed an optical interrogation method which helped them to collect the data from more than one sensor along a single fibre. Using this method helped them to achieve a closed-loop force control method with a baud rate in the kilohertz range (119).

2.3.10 Octopus inspired arm

Animal body embodiment is a dynamical coupling structure between sensorimotor brain-body control, muscular tissue materials, body anatomy and the dynamics of the body's surrounding environment.

The octopuses arm is a good example of a highly compliant arm embodied with an incredible dexterity. This omnidirectional, fully flexible arm has the capability to grasp objects and control stiffness along their entire length.

Guglielmino et al. carried out in-depth neurophysiology and biomechanics analyses of the octopus arm (120). They also proposed an octopus-based continuum arm and a relevant control design in light of embodiment theory. The analyses they provided could be used to design and control an embodied soft robotic arm. They also demonstrated the capability to reproduce the motions performed by live octopus, such as contraction, elongation, bending, and grasping, in an experimental setting. In addition to its fully functional and flexible arm, for daily tasks this creature also use a sucker mechanism inside its arm, which provides the ability to achieve a sufficient reversible wet adhesion on different surfaces.

Inspired by the octopus suction mechanism, a suction cup was designed and developed by Tramacere et al. (121). As a benchmark for these suction cups, they performed a non-invasive technique-based investigation into the sucker's morphology that allows octopi to stick to various wet surfaces. To make a 3D reconstruction CAD model of the octopus sucker of a similar size and anatomical proportion, they used images of contiguous sections of octopus suckers. They used this 3D information to develop their first silicone-made passive prototype of the artificial suction cups.

A similar approach to the octopus-based suction cup was undertaken by Kier et al. (122). They proposed an octopus adhesion design, where to obtain suction, they tensioned the water volume inside the interior chamber of the suction cup. To model the suction of the cup, they measured the differential pressure between the external and internal water volume of the cup. The maximum pull-off force measured for their suction cups was 8 N (122).

2.3.11 Reconfigurable gripper for flexible assembly tasks

A reconfigurable gripper with six degrees of freedom was proposed by Yeung et al. for flexible assembly tasks. Their gripper had the capability to grasp the different geometric parts, rigidly holding them, and change the grasping points (123). The gripper consisted of three fingers. Each finger had two movable joints and two point contacts. Deflections of the gripper had been simulated by the finite element analysis to determine critical design parameters. The workspace and the kinematic model of the gripper were developed and the experimental results were performed and tested in grasping automotive body panels.

2.3.12 Capstan brake mechanism for tendon-driven hands

To improve the efficiency of tendon-driven hands, Kang et al. proposed a passive brake mechanism, a capstan brake, which consisted of a capstan and two one-way clutches (124). To gain sufficient braking force, the friction between the capstan and the cable amplifies a small resisting force. Generation of the brake force did not consume any energy in this design due to there being no additional actuator in the mechanism. The capstan was able to rotate in the winding direction using one-way clutches. Therefore, the brake force was exerted only when it was needed, so the brake did not affect the performance of the whole device. In order to evaluate the performance of the brake mechanism, they conducted a number of experiments, whereby the maximum brake force achieved by their mechanisms was about 55

N, which was suitable for a tendon-driven wearable robotic hand. However, the maximum brake force could be increased by increasing the number of windings.

2.3.13 TUAT/Karlsruhe humanoid hand

The TUAT/Karlsruhe humanoid hand was developed by Fukaya et al. (125) in order to achieve a similar performance to the human hand in grasping various objects and dealing with different environments. To eliminate the need for a touch sensor and feedback control, the hand was designed in such a way as to automatically adjust the grasp shape and grip force.

2.3.14 PAM-based anthropomorphic robotic hand

Inspired by human hand, Lau et al. designed a low cost, variable stiffness anthropomorphic robotic hand using pneumatic artificial muscles. Their proposed anthropomorphic design consisted of 16 DOFs in which 14 pneumatic air muscles were used to actuate the tendon-driven fingers. They used an open-loop control scheme to control the fingers' positions and stiffnesses. The hand was able to perform some basic grasps (126).

2.3.15 RAMA-1

RAMA-1 was a highly dexterous 48 DOF robotic hand designed by Rasakatla et al. (127). The robot consisted of joints which were based on magnetic sliding and spherical spheres and used tendons to actuate the fingers. It provided more degrees of freedom than the human hand. The new six DOF thumb in this hand had a greater range of motion than the ordinary thumb and improved the overall dexterity and manipulability of the hand. They tried to simplify the process and control task for robust grasping. They demonstrated through experiment that using an optimized passive compliant joint and adaptive coupling in the hand increases the adaptability of the large positioning errors that can occur in unstructured grasping tasks.

2.4 Robust grasp, Dexterous hand and in-hand manipulation

2.4.1 Grasp synthesis

Grasp quality measure (also is called grasp synthesis) is a criterion for measuring the quality of grasp required in order to obtain a secure grasp. Indeed, it is used to automatically obtain a secure grasp by determining proper contact points on the object to be grasped as well as the correct finger configuration (171). Also, grasp planning refers to the decision making algorithms that establish the desired contact points on the surface of the object based on predefined criteria. Grasp planning is also used to generate the motion trajectory for the fingers in order to achieve an appropriate gripper configuration (172). Finding an appropriate grasp synergy, among the theoretically infinite number of candidates is a challenging task that requires a huge amount of calculation and processing time (173). There are two main approaches to solve the grasp synthesis problem, as follows (174).

2.4.1.1 Empirical grasp synthesis

The Empirical approach determines the most appropriate hand synergy for the defined grasp task using different methods such as learning by demonstration. This type of synthesis relies on the behaviour of the human hand and tries to mimic the human hand grasp (175). As an example, the robot can imitate the human grasp using some learning techniques such as imitation learning (176). Figure 2.20 depicts an example in which a simulated robot successfully grasped unknown objects using the imitation learning technique. In this example, the robot was trained to grasp random objects using its arms, torso and hands. To teach the robot a human-like grasp (demonstration mode) using a combination of three predefined primitives, they were grasping and lifting some simulated objects using a teleoperation haptic device. Afterwards, and in exploitation mode, the robot compared the target objects (the objects to be grasped) against the recorded information in its database trying to identify suitable motion primitives. The trained robot successfully lifted 92 out of 100 unknown objects randomly generated by the simulation environment.

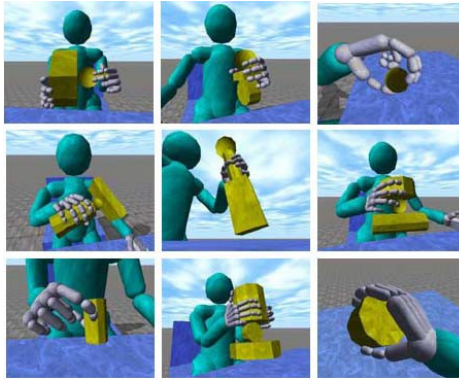


Figure 2.20: The simulated robot successfully mimicked human grasps using imitation technique (176).

A similar approach was developed by Lenz et al. (177) using an artificial intelligence algorithm. They developed a deep learning system for empirical grasp synthesis which used data collected from an RGB-D camera. Using a deep learning method eliminated the necessity for hand engineering features as the system was able to learn them directly. Furthermore, their learning methods outperformed the pre-modeled hand-engineered features as demonstrated in (177) in which they illustrate through experiment (using both offline and real platforms) that their proposed deep learning method was capable of performing a robust grasp synthesis for a wide range of unknown and random objects, including unknown objects, please see Figure 2.21.

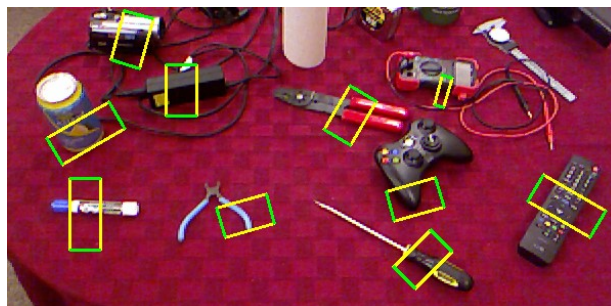


Figure 2.21: Using the deep learning method introduced in (177), the robot could successfully perform a grasp synthesis.

2.4.1.2 Analytical grasp synthesis

This approach relies on mathematically modelling the physical interaction between the gripper (fingers) and object for achieving dexterity, stability, equilibrium and desired dynamic

behaviour. This synthesis needs to consider all the physical constraints and mechanical properties involved in the grasp (178).

The dextrous hand must be controlled in such a way as to autonomously achieve the required grasp properties and consequently perform any required grasp tasks in a similar manner as a human does. All the grasp synthesis algorithms need to satisfy the following grasp properties:

a) Stability

The gripper has to be stable in isolated conditions and remain stable when interacting with an unknown object. Although any uncertainty in the grasp model can cause some errors, a stable grasp should remove the steady state errors from the grasp and limit the responses' overshoot (transient errors) to within acceptable boundaries (179-181).

As will be discussed in the upcoming chapters, the main problem in achieving a stable grasp lies in the estimation of the exact mechanical properties of the objects to be grasped. As shown in chapter 1, these mechanical properties are some of the main requirements for designing a stable grasp. Any miscalculation of the object's mechanical properties can bring the poles of the system into the instability zone, even if the system is stable in isolation. In the presence of such uncertainties during grasping tasks, utilising any ordinary control methods will be difficult if not impossible. Despite all research in the field of vision-based AI algorithms used for object recognition, (15-19), these methods still require a lot of modification to become reliable enough for industrial applications.

b) Disturbance resistance

A promising mathematical model of a grasp must satisfactorily predict the outcome of the grasp under all the possible scenarios that might happen during grasp tasks. This outcome consists of the behaviour of the gripper and grasped object during the moment that the grasp takes place and after lifting the object. The term grasp maintenance refers to the reaction of the gripper and control in the presence of any disturbance, trying to prevent contact (between fingers and object), separation and undesired slippage. To do so, the grasp control continuously adjusts the grip force (37).

Clearly, grasp maintenance is one of the most important requirements of any grasp, and it guarantees a secure grasp in the presence of any model uncertainty in the grasp and any unknown disturbance. As will be discussed in the upcoming chapters, most of the disturbances in grasping tasks arise from inertial, centripetal and gravitational forces.

Determining correct contact points and appropriate grasp type to robustly overcome the disturbance are the main difficulties of the disturbance resistance problem (182, 183). A disturbance can be cancelled in any DOF by either form or force closure (Figure 2.22).

❖ *Form closure*

Figure 2.22 (left) depicts a specific type of grasp, the so called closure grasp. As can be seen from this figure, the gripper performs this grasp by wrapping the fingers around the held object and pulling it towards its palm. Let us assume that the hand shown in the left side of the figure grasped the object and afterward all the finger joints are locked and the palm is fixed in place. We call the object form closed if this assumption reduces the degree of freedom of the object to zero; this means that the object cannot move, even infinitesimally. As long as the actuators of the gripper provide enough torque to compensate the external disturbances, the gripper can maintain the grasp (184, 185).

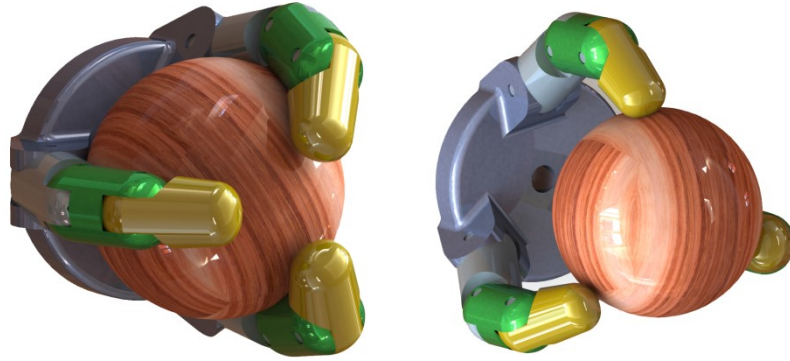


Figure 2.22: A 3-finger, 6 DOF hand, performing form (left) and force (right) closure.

❖ *Force closure*

A simplified grasp model can be written as shown below:

$$\begin{aligned} I_h(q)\ddot{q} + B_h(q, \dot{q}) + J^T \lambda &= \tau_{app} \\ I_o(u)\dot{v} + B_o(u, v) - G\lambda &= g_{app} \end{aligned} \quad (2.5)$$

where I_h and I_o are inertia matrices, B_h and B_o denote the velocity product terms, g_{app} is a force vector applied to the object due to gravity and other external sources and τ_{app} is a vector of actuation forces and any external perturbations. $G\lambda$ is the resultant wrench on the object by

the hand. Under the same assumption mentioned in the previous section, a grasp achieves force closure (the object is force-closed) if for any moment/force experienced by the held object there exist contact wrenches that satisfy equations (1). Clearly, from this explanation, a form closure grasp can be considered also as a force closure grasp.

It is worth mentioning that despite the robustness of the form closure grasp, it is out of the scope of this thesis as form closure requires a grasp with many numbers of DOFs. Force closure on the other hand, can be achieved by even one degree of freedom which provides a low cost, simple grasp solution for industrial grasping tasks.

c) Dexterity

Generally, we call a grasp a dexterous grasp if the hand moves the grasped object in a manner compatible with the required task. When there is no specific grasp requirement, a dexterous grasp should theoretically be capable of moving the grasped object in any direction (178). A dexterous motion planning algorithm therefore has to achieve two main objectives (186):

- Planning the motion of the object to achieve a desired configuration, or accomplish a desired task.
- Planning the grasp or motion of the fingers required to impart this motion.

In-hand manipulation (also called: dexterous manipulation) is a higher level of grasp planning and grasp control which involves changing the position of the held object with respect to the gripper by using only the fingers and without any external support. Rus developed a new method for efficient in-hand manipulation tasks (187). He suggested an algorithm to independently use the fingers to cooperatively manipulate an object between the fingers. In his experiments, he used some mobile robots to emulate the fingers. He illustrated through experiment that the differential control of an object's reorientation can be formulated by tracking the fingers as individual linear systems. Finally, he demonstrated that in order to perform global one- and multistep reorientations he could iterate a single differential control. Donald et. al. used Rus's proposed method for manipulation of heavy and large objects as described in (188,189).

d) Equilibrium

When the resultant of the applied forces and torques (by fingers and/or perturbations) applied on the grasped object is null, the grasp is in its equilibrium condition (171). The main

difficulty is to determine and control the grip force in order to continuously maintain the equilibrium conditions.

❖ *Contact model*

A taxonomy of eight contact models was proposed in (190) namely, point contact without friction, line contact without friction, point contact with friction, planar contact without friction, line-line contact without friction, soft finger contact, line-line contact with friction and planar contact with friction. Figure 2.23 depicts the most frequently used contact models in the field of robotic grasping. The shown contact models are: (a) point contact without friction (b) point contact with friction and (c) soft-finger contact models (191).

The point contact models (also called rigid-body contact model Fig. 2.23. a and b) assume a solid body for both finger and grasped object. In these models any collision between the fingers and object is assumed to be a discontinuous and instantaneous phenomenon where the kinematic and dynamic equations of the system are derived when the system is in stable conditions before and after the collision.

In the soft finger contact model (also named compliant models, shown in Figure 2.23.c) we assume a flexible body property for the fingertips that are interacting with a solid body (grasped object). Unlike the former contact models, this model continuously describes the compliance of the contact in both normal and tangential directions.

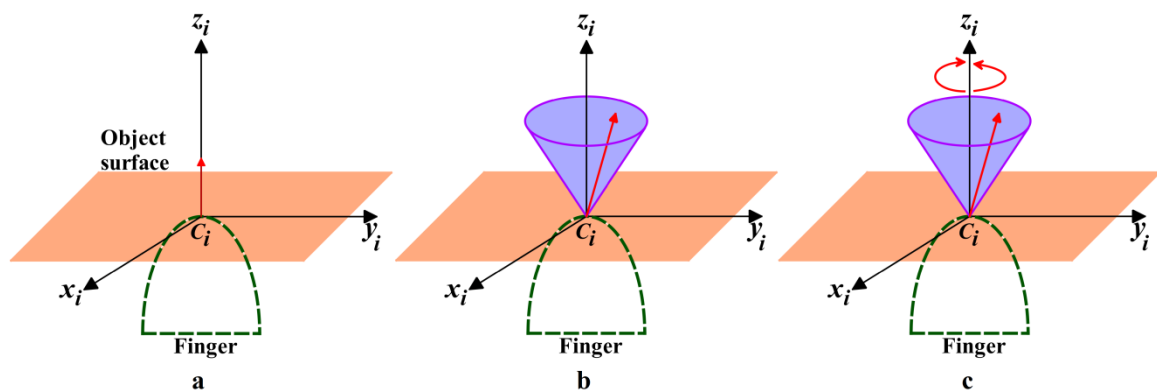


Figure 2.23: (a) point contact without friction (b) point contact with friction and (c) soft-finger contact models (Figure recreated from (191)).

➤ *Point contact without friction*

A point contact without friction is usually used to model the small and slippery contact surfaces between the fingertips and object. In this model, the contact point can only transmit

normal forces (the force that is perpendicular to the object surface at the contact point). This model assumes that both object and fingers are entirely rigid and imposes a no deformation constraint to the contact model. Although this model simplifies the grasp model and hence reduces the processing time of the grasp synthesis, it does not represent the precise contact properties of real grasp scenarios. Furthermore, in the case of grasps with multiple contact points, the frictionless point contact model does not distinguish a specific contact force from the others (192).

➤ **Point contact with friction**

This model is usually used to model a small contact surface with large (non-negligible) values of friction. Due to the very small contact surface in this model, and as shown in Figure. 1. b, the finger can only generate normal and tangential forces at the contact point and the frictional moments are assumed to be zero in this model (193).

A plethora of research has been conducted attempting to model the complex friction phenomena (194). The most popular friction model, so called Coulomb friction, simply models the friction as a vector that opposes the relative motion between two surfaces where (regardless of the contact area and velocity of the motion) the magnitude can be calculated as shown below:

$$|f_f| \leq \mu |f_n| \tag{2.6}$$

where f_f , f_n and μ in this equation denote the tangential friction force, applied normal force and friction coefficient of the contact respectively. Figure 2.24 depicts a geometrical representation of a point contact with friction.

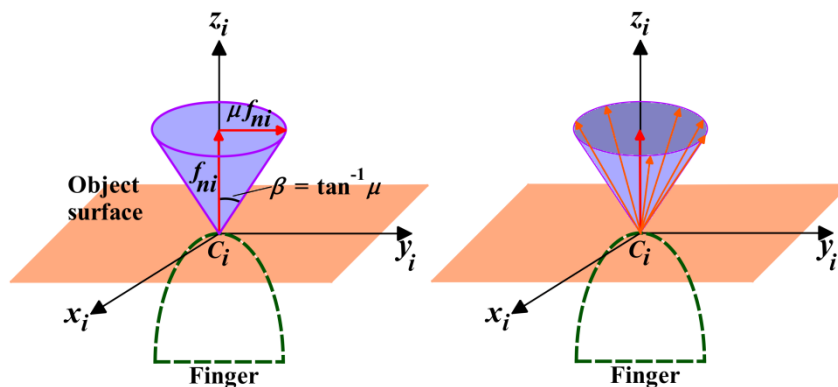


Figure 2.24: Friction cone (left) and polyhedral friction cone (right) (Figure recreated from (191)).

As shown in this figure, the friction forces are usually shown by a friction cone where all of the possible frictional forces are constrained to be inside this cone. As shown in this figure, the cone is centred about the normal surface of the contact point with half angle $\beta = \tan^{-1}(\mu)$. In some specific conditions, the friction cone becomes a circular cone with the following geometry:

$$(f_{xi}^2 + f_{yi}^2)^{1/2} \leq \mu f_{ni} \quad (2.7)$$

As shown in Figure 2.24 and in order to reduce the processing time, we usually replace the friction cone with a polyhedral cone with n faces. This will reduce the accuracy of the model, which is the price we are paying to eliminate the high processing time. It is also worth noting that the accuracy of the model can be improved by increasing the number of faces of the polyhedral cone which clearly slows down the processing time (191).

➤ *Soft fingertip contact*

This model is usually used to model the contact between a flexible fingertip and a solid object that is in frictional contact with a larger contact surface. The contact surface should be large enough to generate noticeable frictional force and moment (191, 195). The generated force and moments are always about the vertical axis shown by z_i in Figure 2.24 . It should be noted that a limit surface that includes the frictional moment is replacing the friction cone in this type of contact model. In-depth discussion about grasp synthesis and contact modelling can be found in (193, 190).

2.3.3 Optimal Contact Forces Computation

The applied grip forces for a given grasp can be calculated by considering the dynamic equilibrium conditions of the grasped object. As in most cases, there are more contact points than the number required for a stable grasp and therefore there are sometimes more than one solution to the equilibrium problem. Therefore, the grasp controllers usually follow some pre-defined optimisation criteria in order to achieve single or finite solutions. For example minimising the magnitude or inclination angles of contact forces are popular optimisation criteria (196). There have been a number of algorithms suggested in the last decades aimed at achieving a general grasp algorithm that satisfies a variety of general optimisation methods (191). Zheng et al. proposed an algorithm to improve computation efficiency since it was desirable to obtain the contact force distribution in real-time (196). To solve the slip

prevention problem with minimum deformation of the object, a novel active optimal force controller is proposed in this thesis

2.4.1 Adaptive grasp with an under-actuated hand

A multi-task myoelectric under-actuated hand is presented in (129). Adaptive grasp, as well as adaptable fingers-phalanges, are the main advantages of the design. The embedded self-lock metacarpophalangeal joints in the design were used to mechanically prevent the fingers to back drive in the presence of any external forces acting on the fingers. They also suggested an intermittent rotary motion in the carpometacarpal joint in the thumb finger. The adaptive hand used two actuators to perform different grasping motions. The adaptability of the hand reduced the necessity for electromyogram pattern recognition.

Another good example of adaptive hands is the Matahand, which gained its inspiration from artwork and origami. The hand consisted of a metamorphic palm with a novel multi-fingered hand. They used a foldable and flexible palm to make the hand adaptable and reconfigurable. Adding additional motion to the palm enhanced the workspace of the hand, and the fingers were complemented with the palm motion. In order to examine the orientation and pose change of the hand, they used a 4-D ruled surface. They also developed an orientation–pose manifold from this pose–orientation ruled surface (130).

2.4.2 Iterative learning control (ILC)

The iterative learning control (ILC) algorithm was introduced by Chen et al. to solve the synchronous problem in multi-finger dexterous hands. They also claimed that they were able to guarantee that the system performed well by synchronizing the finger joints. They suggested a semi-Lyapunov composite energy function to analyse the stability of the system as controlled by their ILC control method (131).

In order to imitate the synergistic behaviour of human hand, they also suggested an under-actuated robotic hand for which they designed a torque control method. By controlling the number of hand synergies and using the null space, even the mechanical coupling properties could be assigned to some extent. Using the suggested controller and a low-level user interface, they could reduce their grasp-training time significantly. They also demonstrated that 74% of the database grasps were executable by using just two actuators among twelve.

They also demonstrated that to grasp objects with a dexterous robot hand, just two set points were sufficient.

2.4.3 RL-based impedance control

Inspired by the human body, a reinforcement learning method to control the mechanical impedance of the robot was proposed by Stulp et al. (132). In the presence of environmental disturbances, the human body uses a combination of two strategies to adapt its impedance to environmental perturbations. In fact, this adaption is used to minimize muscular energy consumption as well as positional error.

- 1) In the presence of unpredictable disturbances, subjects attempt to increase their body impedance by co-contracting their muscle
- 2) In the case that the environmental disturbances are deterministic, subjects attempt to learn a feed-forward sensorimotor command to compensate for the perturbation.

They conducted a robot simulator platform to validate their learning method. Using their suggested model-free reinforcement learning algorithm, their 7-DOF simulated robot demonstrated human-like behaviour in the presence of both deterministic and stochastic disturbance fields.

2.4.4 Grasp simplifier

With the aim of reducing the processing time of the grasp control, grasp simplifier methods were introduced in (133). The authors demonstrated experimentally that using adaptive couplings and optimized compliant joints in robotic hands can increase the robustness of the grasp in the presence of relatively large positional errors. In the case of positioning error with a maximum offset of 100%, through the use of the proposed simplification method, they could satisfactorily grasp objects up to a maximum diameter of 5 cm, whereas the hand was able to grasp objects with a maximum diameter of 10 cm when the offset of the positioning errors was up to 33% of the object size. Their achieved grasp autonomy, however, could be increased using the feedback data from angle of the joints and tactile sensor on the fingertips (133).

2.4.5 Impedance control in a flexible joint

To control the mechanical impedance of the fingers in a flexible joint hand, two new control designs were proposed in (9). The target impedance in the authors' grasp model was based on the desired stiffness and damping, though they neglected the inertia term of the impedance in their model. The two suggested cascade controllers consisted of one inner torque-feedback loop, and an outer impedance control loop. They used a physical interpretation of the rotor inertia to estimate the torque in the inner loop of the controllers. They then designed two different outer impedance controllers. The first controller used a combination of the motor shaft's position and the system's stiffness and damping term to control the impedance of the grasp, while in the second controller these parameters were merged such that under steady-state conditions the desired equilibrium position could be satisfied. They also demonstrated that both controllers could be adapted to the visco-elastic properties of the joints. They experimentally verified the concept of the controllers using a DLR lightweight hand.

Some complex tasks, such as unscrewing and screwing objects using a dexterous robotic hand, have been conducted by Karnati et al. in two different scenarios (128). First, they used a first finger and thumb to perform a given task, whilst in the second test they changed the first finger to the little finger. In order to develop an anthropomorphic solution, they recorded nine test subjects' finger synergies when they were unscrewing and screwing a threaded cap. The results collected from their tests showed periodic motions in the joints with same frequency but differing amplitudes and phases. The collected data showed that the human hand's joint motions during unscrewing are a mirror image of the screwing a lid back on. They suggested a set of sinusoidal trajectories to model this motion and a set of sinusoids with a common time vector for screw-unscrew tasks. For the screwing task, they decreased the time vector, and to produce the unscrewing task they increased the time vector; the computational cost, as well as complexity of the task, were significantly reduced through this method. Cartesian and joint space error analyses have been used to prove that the suggested sinusoidal motion trajectory closely follows the human hand's motion profile. Using forward kinematics equations, and by relating joint angle offsets of the hand to object diameter size, they extended their bio-inspired sinusoidal trajectory to objects with different widths. They used a sliding mode motion control algorithm to ensure the stability of the grasp. The experimental results have been performed using four different objects with different diameters, and through these

experiments they showed that the robotic hand successfully unscrewed and screwed the objects.

2.4.6 Adaptive slip prevention control

In many applications, a robot must be able to grip a broad range of objects quickly and firmly without dropping or crushing them (134). Grasping an object in the presence of unpredictable external disturbances and/or a lack of any precise estimation of the geometry and mass distribution of the object itself represents a significant challenge. The main problem is that of the estimation of the exact gripping force required to prevent slippage whilst not damaging or deforming the object.

A control scheme inspired by the human sensorimotor system is presented in (135), which shows how tactile feedback can be used as a primary means of completing a manipulation task. However, in this control architecture there is no direct sensing of object slippage and the initial grip force necessary to lift an object depends solely on the hardness information gathered during contact. Four different methods of hand prosthesis control with slip prevention were developed and examined in (136-138), three of which were based on sliding mode control (one open-loop and two closed-loop) and one on a closed-loop PD control, the latter being very similar to commercially available ones. The two closed-loop SMCs and the PD controller made use of strain gauges to detect forces along the normal and shear directions relative to the thumb motion. They used the derivative of the shear force as a feedback to prevent slippage. Results showed how the two closed-loop SMC-based architectures outperform the PD controller in terms of both slip prevention and object deformation.

As will be explained in chapter four, the sliding mode control methods provide robustness against unmodeled variables of the system and any uncertainty within the model (e.g., friction) (139). Indeed, friction is one of the most important factors in maintaining a static grasp, but at the same time it is quite difficult to estimate the friction between the fingertip and grasped object before slippage occurs.

A slightly different strategy, based on a fuzzy SMC and a disturbance observer, was used in (140), where only a slip sensor is used. No force feedback is implemented, and the grip is achieved through the combined control of finger angular position and slippage. The proposed control has the advantage of being compatible with a wide range of slip sensors and gripper

configurations, but the so-called chattering phenomenon introduced by the first-order SMC proved difficult to reduce or eliminate without compromising controller performance. On the other hand, it is well-known that High-Order Sliding Mode Controls (HOSMCs) have the advantage of reducing or removing chattering altogether while preserving robustness under uncertain conditions (141). However, at the time of this thesis, there are no relevant studies dealing with HOSMCs as applied to robot adaptive grasping.

Chapter four and five of this thesis evaluate the robotic grasping performance using a HOSMC with feedback on gripping force and slippage. More specifically, a Hybrid adaptive Super Twisting Sliding Mode Control (HASTSMC) is compared to an adaptive First-Order Sliding Mode Control (AFSMC). Force and slip feedback are provided by low-cost, off-the-shelf components.

2.5 Discussion

Research in the field of actuators with (passive) adjustable compliance and controllable stiffness grasping has been mainly driven by the development of effective, artificial hands for rehabilitation robotics, prosthetics and wearable robotics. In industry, however, there is a growing need for grippers with a high degree of (controllable) compliance, especially in food handling (given the wide variety of possible objects in terms of shape, weight, softness, fragility, etc. that might be encountered), where flexible and effective gripping is essential. And yet, in the industry, although there is an increasing demand for automation and robotized production lines, most robot grippers still rely on traditional mechanisms actuated by rigid pneumatic or electric actuators or are otherwise based on vacuum technology, which greatly limits handling capabilities, whereas compliance in such systems could potentially improve productivity and boost profits.

Complexity of design, limited achievable force, weight, durability and cost issues are some of the reasons for the limited use of compliant grippers to date which have forced industry to continue with the use of traditional, rigid gripper mechanisms in automated lines.

Most of the existing research on robotic grippers/hands with variable compliance/stiffness takes its inspiration from the human hand, mainly because its aim is to develop artificial hands. However, some fundamental concepts and ideas arising from this line of research can be exploited in order to create a new generation of industrial grippers that feature controllable stiffness for demanding industrial applications requiring flexibility in grasping tasks.

Following these and other similar studies, a plethora of variable stiffness/compliance designs have been proposed for robotic hands. The drawback of most of the proposed solutions is that “variability” does not necessarily involve full “controllability”. Commonly, the stiffness term in most variable stiffness actuators is coupled (and therefore changes) with finger posture. Whereas this could be sufficient to provide better functionality for prosthetic limbs during normal human activities compared to similar non-variant compliant systems, this is not the case in industrial scenarios, where, in order to implement effective grasping with a wide variety of soft (and rigid) objects, wide stiffness variability must be assured and achieved in real time (and therefore be fully tunable) in all possible gripper configurations.

Fortunately, in designing industrial grippers there is not any typical morphological and physical constraints required for human prosthetics, hence it is easier to elaborate more effective solutions. Indeed, the possibility of realizing a very large interval of stiffness variability (theoretically from full compliance to perfect rigidity) depends on how stiffness variability is conceived and implemented in the gripper actuator design.

For example, in (142) and (143), a 7 DOF multi-joint gripper comprising serially connected differential gear boxes uses two independent motors to control position and stiffness; therefore, stiffness can be controlled independently via gripper configuration. In this system, however, the variability of the stiffness is limited by the maximum elongation that the springs directly connected to each element of the chain can achieve within the range of their possible elastic deformation. A wider stiffness variability is achieved in (144), where variable (controllable) stiffness is implemented through an adjustable moment arm mechanism consisting of two spring blocks with an adjustable symmetrical position with respect to the gripper output shaft. As the spring blocks move outwards from the centre of the gripper towards the periphery, the contact point between the output shaft and springs defines a larger reactive torque (the moment arm increases) and the overall stiffness increases. This gripper is able to achieve wider stiffness variability than the previous one (in the range of 0.07 to 2.2 Nm/deg), but the maximum achievable stiffness is still limited insofar as it depends on the gripper diameter (maximum moment arm) for the same type of spring.

From a control point of view, a successful controller must be able to quickly grip a broad range of objects firmly without dropping or crushing them (134). Although there is a huge body of the literature available on robotic grasping, both detection and prevention of object slippage is still considered an open challenge for robotic manipulation. One of the main

reasons that it has been difficult to achieve human-like grasping for robots to date is the lack of a promising uncertainty/disturbance canceller grasp control, as well as any accurate tactile sensors with slip perception similar to that of human skin.

In many applications, a robot must be able to grip a broad range of objects quickly and firmly without dropping or crushing them (134). Grasping an object in the presence of unpredictable external disturbances and/or a lack of any precise estimation of the geometry and mass distribution of the object itself represents a significant challenge. The main problem is estimation of the exact gripping force required to prevent slippage whilst not damaging or deforming the object (new). However, the presence of unpredictable disturbances and model uncertainty, SMC (Sliding Mode Control) has been shown to be entirely robust in solving control problems for a variety of tasks and experiments (145). Robustness to system model miscalculations, high responsiveness to bounded disturbances, a competitive simple computation process and an easily implemented algorithm are just some of the advantages of SMC when compared to other robust controller methods (146). Briefly, the task of the SMC is to drive the error states to a sliding surface and maintain them (that is, the error states) on the sliding surface thereafter.

Despite all the mentioned advantages, there is nevertheless an inherent disadvantage to this method. The so-called chattering phenomenon introduced by the first-order SMC has proven difficult to reduce or eliminate without compromising controller performance. On the other hand, it is well-known that High-Order Sliding Mode Controls (HOSMCs) have the advantage of reducing or removing chattering altogether while preserving robustness under uncertain conditions (141). However, at the time of this thesis, there are no relevant studies dealing with HOSMCs as applied to robot adaptive grasping.

Chapter 3

PASSIVE CONTROLLABLE STIFFNESS GRIPPER FOR ADVANCED, FLEXIBLE HANDLING

3.1 Introduction

As previously explained in Section 1.1.2, any uncertainty inherent to the grasp model can easily destabilise the port (fingers-object contact point) behaviour of the gripper when controlled by a conventional fixed gain control method. Figure 1.7 depicted an example that illustrates how the mechanical properties of the object (different stiffness) can move the system's poles to the right side of the root locus plot, which leads to destabilising the grasp. As explained in the same section, one of the traditional approaches to eliminating this undesired destabilising effect is to include a passive elastic element between the finger and actuator. This passive element can increase the stability of the system in the presence of such uncertainties. In chapter two of this thesis, a range of variable stiffness/compliance designs have been reviewed and discussed. Although the actuators reviewed can still, to some extent, increase the stability of the system in interacting with the environment, their application in real-world industrial scenarios is still somewhat lacking.

As far as grippers are concerned, complexity of design, small operational force and stiffness range, weight, durability and cost issues are amongst the various reasons that might cause industry to insist on the continued use of traditional stiff mechanisms.

This chapter deals with two innovative robotic variable stiffness gripper designs, VSG₁ and VSG₂, for industrial applications. The main objective of this work is to realize an affordable, as well as durable, adaptable, and compliant gripper for industrial environments with a larger interval of stiffness variability than similar existing systems. This chapter proposes two novel variable stiffness actuators designed to drive the tendon-driven under-actuated grippers. The driving systems of the proposed actuators consist of two servo motors and one linear spring arranged in a relatively simple fashion. Having just a single spring in the actuation system helps us to achieve a very small hysteresis band and represents a means by which to rapidly control the stiffness. It will be proven, both mathematically and experimentally, that the proposed models are characterized by a broad range of stiffness. To control the compliance of the fingers, a mathematical model of the stiffness is derived and presented.

The experimental results provided will show how, despite the relatively simple implementation of the first prototype, the gripper performs extremely well in terms of both stiffness and grasping control.

The two passive, adjustable compliance, serial elastic actuators introduced in this chapter are suitable for industrial applications, both of which greatly reduce the limitation of the maximum achievable stiffness. As mentioned, the designs consist of only two servo motors, the combined motion of which are used to actuate the fingers and change the compliance of the joints. Non-stretchable tendons are used to transfer the force to the fingers. The designs provide a fast response solution by which to control the grip impedance; simplicity of design, small hysteresis band and affordability, as well as durability, are amongst their advantages. The overall concept's architecture is based on the principle that a simple mechanism provides inherent robustness and reliability and, therefore, is able to withstand the severe working conditions inherent to the long and repetitive tasks typical of production lines.

The remainder of this chapter is organized as follows: Section 3.2.1 provides an overall explanation of the first proposed variable stiffness gripper, called VSG₁, followed in Section 3.2.2, by a discussion of the stiffness model in both stiff and compliant status. Section 3.3 reports experimental results on the first gripper performance for different stiffness values. Section 3.3.1 provides a discussion about the design optimisation used to enhance the performance of the design in the second prototype, VSG₂, followed, in Section 3.3.2 by the mathematical modelling of the gripper's apparent stiffness and its associated force-displacement function. Section 3.3.3 reports experimental results on VSG₂'s performance for different stiffness values. The chapter will end with final discussion and conclusion in Section 3.3. Note that the terms "stiffness" and "compliance" and related adjectives ("compliant", "stiff") are used herein to indistinctly characterize, as opposing terms, the non-rigid behaviour of the gripper actuation system.

It is worth noting that there is no benchmark (or international standard) list of test objects for testing grippers. However, table 3.1.a provides the mechanical properties of all the objects used for the experiments reported in this thesis. This was a sample group of objects that was produced for testing based on a range of typical objects found in food manufacturing and nuclear decommissioning which were the application areas chosen to demonstrate the systems developed. It should be noted that it is not the intention that each gripper design presented in

this work be able to grasp all of the objects detailed below, however, each item should be able to be grasped by at least one of the grippers developed.

Table. 3.1.a: The mechanical properties of all the objects used for the experiments reported in this thesis.

Object	Size (mm)	Material	Shape	Weight (g)	Deformable	Stiffness (N/mm)	Texture	COM	Damping N.s/mm	Impact resistance	$\mu_{s^{**}}$
Kiwi	64×57×83	Fruit	ellipsoid	115	Small	14.28	Prickly	Fixed	26.8	Absorb	0.63
Bell pepper	110×95×123	Fruit	cylinder	47	Yes	2.7	Smooth	Fixed	8.3	Absorb	0.54
Strawberry	25×31×43	Fruit	cone	18	Yes	3.4	Smooth	Fixed	2.2	Absorb	0.48
Lettuce	209×193×178	Vegetable	sphere	493	Small	13.0	Rough	Fixed	34.7	Absorb	0.56
Orange	112×106×109	Fruit	sphere	180	Small	12.4	Smooth	Fixed	30.1	Absorb	0.58
Apple	99×101×89	Fruit	sphere	94	No	23.6	Smooth	Fixed	21.4	Absorb	0.49
Bread	149×114×94	Food	cylinder	356	Small	8.6	Rough	Fixed	5.4	Brittle	0.72
Tomato	73×68×70	Vegetable	sphere	85	Small	9.2	Smooth	Fixed	18.7	Absorb	0.47
Egg	55×56×68	CaCO ₃	ellipsoid	63	No	solid	Smooth	Fixed	–	Brittle	0.38
Coffee canister	88×72×82	Glass	cubic	725	No	solid	Smooth	Variable	–	Rigid	0.55
Beer can	85×85×69	Al	cylinder	682	Yes	5.25	Smooth	Variable	6.2	Deform	0.60
Coke bottle	118×118×32	PET*	cylinder	1746	Yes	2.0	Smooth	Variable	9.3	Deform	0.74
Cubic Piece	224×193×564	Wood	cubic	3376	No	solid	Rough	Fixed	–	Rigid	0.68
Cubic Block	125×125×140	Steel	cubic	800	No	solid	Smooth	Fixed	–	Rigid	0.41
Empty bottle	99×97×184	PET	cylinder	14	Yes	1.4	Smooth	Fixed	2.6	Deform	0.66
Foam	82×123×198	PLE	cubic	91	Yes	1.8	Rough	Fixed	5.3	Absorb	0.63
Pipe	88×88×51	Galvanized iron	cylinder	2800	No	solid	Smooth	Fixed	–	Rigid	0.39

Pipe	68×68×29	Cardboard	cylinder	42	Yes	3.1	Smooth	Fixed	3.8	Absorb/Deform	0.42
Wine glass	12×12×52	Glass	cone	112	No	solid	Smooth	Fixed	_	Brittle	0.35
Full sunflower oil	95×95×22	PLA	cubic	1820	Small	3.8	Smooth	Variable	14.4	Absorb	0.61
Block	550×380×220	Concrete	cubic	13,500	No	solid	Rough	Fixed	_	Rigid	1.12
Pipe	300×300×1780	Steel	cylinder	20,000	No	solid	Smooth	Fixed	_	Rigid	0.30
Chair	250×90×920	Foam, fabric, plastic	unsymmetric	16,000	Yes	7.7	Rough	variable	16.1	Deform	1.4
Pipe	215×215×523	PVC	cylinder	4230	No	126	Smooth	Fixed	85	Hardly deform	0.32
Empty box	340×232×470	cardboard	cubic	137	Yes	4.4	Smooth	Fixed	3.4	Deform	0.38
Caution cone	760×320×320	P	cone	135	Yes	45.6	Smooth	Fixed	28.2	Absorb	0.11
Foam	300×180×125	EPS	cubic	187	Small	6.1	Rough	Fixed	12.6	Absorb	0.74

PET: Polyethylene terephthalate

PLE: Polyurethane

PLA: Polylactic acid

EPS: Expanded Polystyrene

PVC: Polyvinyl chloride

** Static frictional coefficient between fingers and grasped objects (clean and dry surface).

The product list above allows the creation of a design specification for the gripper as follows:

Maximum dimensions of product to be grasped = $300 \times 300 \times 1780$ mm

Minimum dimension of product to be grasped = $25 \times 31 \times 43$ mm

Maximum weight of product to be grasped = 20,000 g

Minimum weight of product to be grasped = 14 g

3.2 VSG₁

This section introduces the design of a novel variable stiffness gripper (VSG₁) for industrial robotic manipulators, which can be used for stable interaction (as discussed in Chapter 1) with the environment, as well as to control the applied grip force in the absence of any accurate force sensor.

3.2.1 Design Explanation

Similar to the majority of variable stiffness mechanisms that are referenced in this thesis, the proposed design consists of two rotational electric actuators. The actuators are two identical back-drivable 7 Nm servo motors whose mechanical and electrical details are reported in Table 3.1. A side view of VSG₁ can be seen in Figure 3.1.

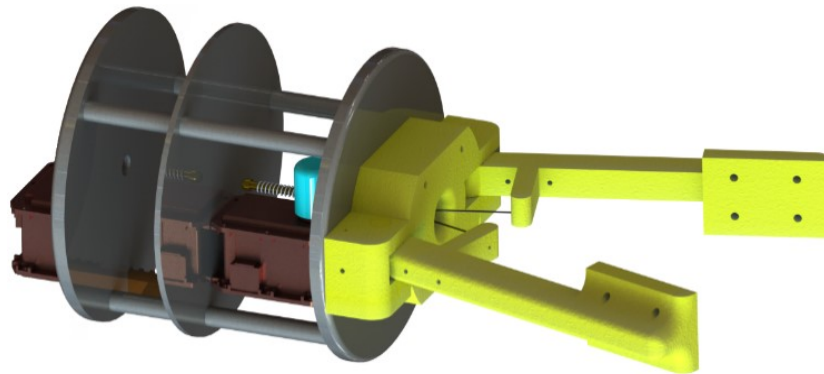


Figure 3.1: The VSG₁ introduced in this section.

The two servo motors also can be seen in this figure. One of the servos, M_1 , provides rotational motion θ , whilst the second is used to produce a linear displacement, ΔB , along the wrist axis of the gripper. Figure 3.2.a depicts these servos and their corresponding motions. As can be seen from this figure, a rack and pinion gear arrangement is used to transform the rotational motion of M_2 to achieve linear displacement. This linear motion has been used to move a slider along the wrist axis of VSG₁ as shown in this figure. Motor M_1 is mounted on this slider and follows the slider's movements. As shown in the figure, there is a linear compression spring connected to the shaft of M_1 through a rigid rod. Figure 3.2.a depicts a hole drilled in the centre of the shaft.

Model MX-64T			
Torque	5.5N.m (11.1V,3.9A)	6N.m (12V,4.1A)	7.3N.m (14.8V,5.2A)
Speed	58rpm (11.1V)	63rpm (12V)	78rpm (14.8V)
Communication Protocol	TTL		
Baud rate	8000 bps ~ 4.5Mbps		
Controller	PID		
Resolution	0.088 Degree		
Weight 126 g	Dimension	40.2 × 61.1 × 41 mm	

Table 3.1: Mechanical and electrical specification of the servos used in VSG₁.

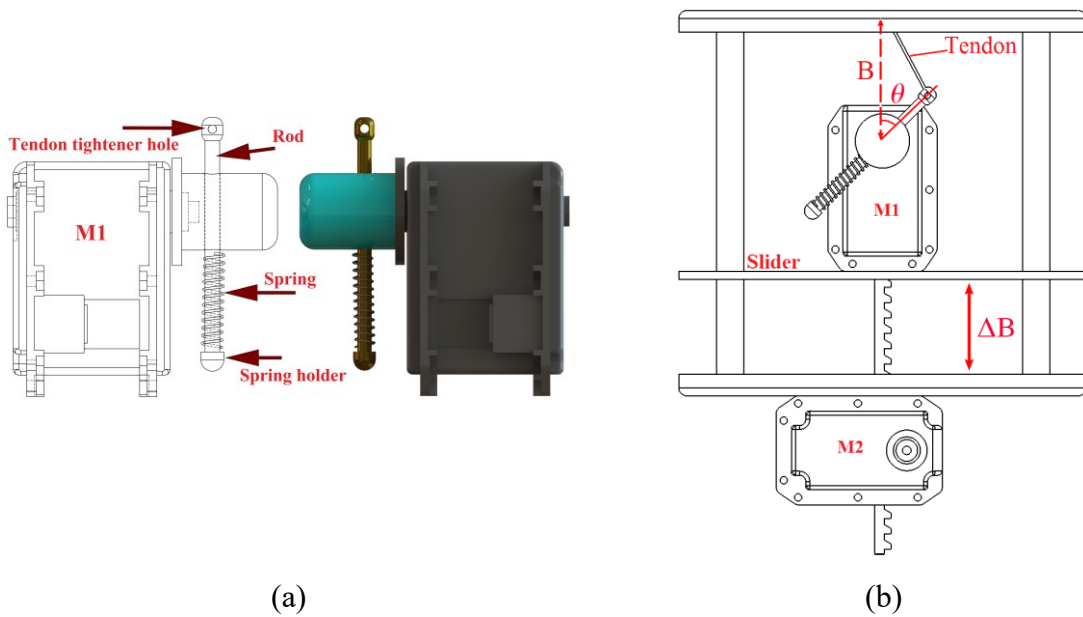


Figure 3.2: Schematic representation of the actuation system of VSG₁.

The rod slides through this hole and across the shaft's axis. The linear compression spring is placed around the rod, also as shown. A spring holder pin in the bottom of the rod holds the spring in place. To transfer the driving force from the actuator to the gripper, a tendon establishes the connection between the rod and gripper, as shown in Figure 3.2.b, which also shows the tendon-fixing hole on the rod. The subsequent tendon-rod-spring configuration generates a compliance behaviour for the gripper which will be explained in the upcoming sections. Any external force on the gripper's fingers will generate a tensile force which will be transferred to the rod-spring system via the tendon. The force transferred to the rod will pull it, and consequently compress the spring where, as will be explained in the following section, the magnitude of this compression is a function of the force and θ .

3.2.2 Working Principle and Simulation

This section, will explain the working principle of the variable stiffness mechanism. To do so, as depicted in Figure 3.3, there are two coordinate frames: (a) the reference coordinate frame OXYZ, and (b) the shaft coordinate frame $o'x'y'z'$ which is parallel to the reference coordinate frame. By assuming that the shaft coordinate frame is fixed to the shaft of M_1 in such a way that o' is in this shaft's geometric centre, as shown in the Figure. Here, the green, purple, and blue springs represent different angles of θ due to the rotation of the shaft of M_1 around the x' axis. From this figure, the linear motion of M_2 is along the Y direction of OXYZ. The combination of motions of M_1 and M_2 provide the ability to independently control the stiffness and position of the fingers, as will be explained below.

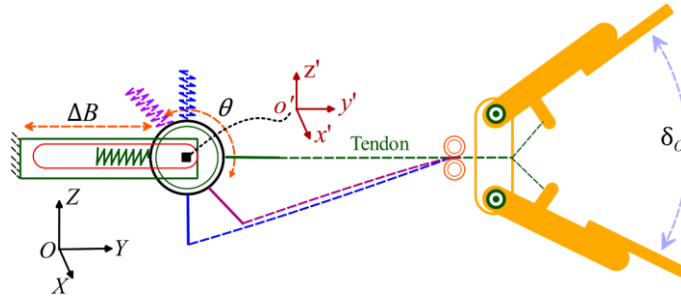


Figure 3.3: The combination of the motions of M_1 and M_2 provides the ability to change the stiffness and position in VSG₁.

In Figure 3.3, the dashed lines represent the tendon that establishes the connection between the rod and gripper. As already mentioned, this tendon is used to transfer the driving force from the variable stiffness mechanism to the gripper. The apparent stiffness of the fingers, δ_o , is dependent on the angle between the rod and tendon, and this stiffness changes according to this angle. M_1 is used to change this angle, and hence control the stiffness of the gripper.

Now let us remove the gripper from its actuation system and assume that the tendon is pushed by an external force, F , as shown in Figure 3.4. Hence, we can write:

$$|F \cos \alpha| = Kz'_s \quad (3.1)$$

Where α , as shown in the figure, is the angle between the rod and tendon, Z'_s is the amount of co-contraction in the spring due to the force F , and K denotes the spring constant. From Eq. 3.1 we can write:

$$z'_s = \frac{|F \cos \alpha|}{K} \quad (3.2)$$

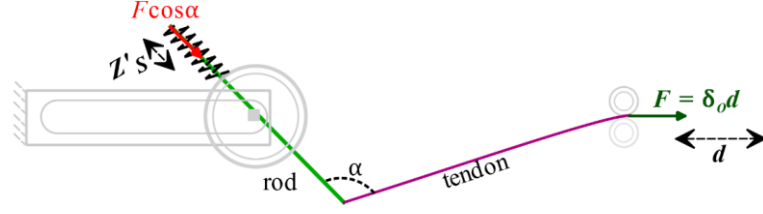


Figure 3.4: The output stiffness of the gripper, δ_o , is a function of α .

the rotation of the servo motor M_1 is assumed to be bounded as below:

$$0 \leq \theta \leq \frac{\pi}{2} \quad (3.3)$$

From Eq. 3.3 and 3.2 we can write:

$$\begin{aligned} \pi \leq \alpha \leq \frac{\pi}{2} \\ 0 \leq |z'_s| \leq \frac{F}{K} \end{aligned} \quad (3.4)$$

Equation Eq. 3.4 illustrates the minimum and maximum co-contraction of the spring (which is equal to the displacement of the rod) due to the external force F on the tendon. In this equation, zero co-contraction corresponds to $|\alpha| = \frac{\pi}{2}$; assuming the tendon is inelastic, and the shear deformation of the rod is negligible, we can thus write:

$$|\alpha| \rightarrow \frac{\pi}{2} \quad \delta_o \rightarrow \infty \quad (3.5)$$

and

$$\min \delta_o = K \text{ for } \alpha = \pi \quad (3.6)$$

where δ_o is the output stiffness of the VSM. Figure 3.5, depicts the gripper at both its minimum and maximum stiffnesses. In this figure, the red gripper corresponds to the stiff gripper with infinite stiffness (zero compliance), whilst the blue corresponds to the gripper with minimum stiffness ($\delta_o = K$). As shown in the figure, in the infinite stiffness configuration, the angle between the tendon and spring, α , is a right angle, whereas in the minimum stiffness configuration, the tendon is along the spring ($\alpha = \pi$). Figure 3.6 depicts the force-displacement curves collected from a simulated VSG₁ in MSC Adams multibody dynamics simulation software integrated with MATLAB simulink.

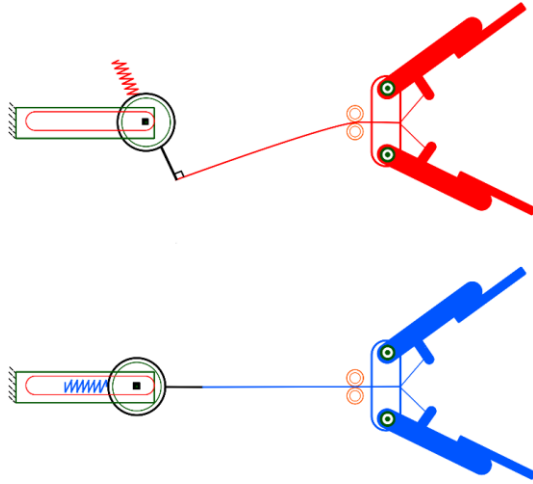


Figure 3.5: VSG₁ in its maximum (red) and minimum (blue) stiffness configurations.

In this simulation, a spring with a stiffness constant of 10 N/cm has been used. The Young's modulus, diameter and density of the tendon have been set 20 GPa, 0.3 mm and 4 g/cm³, respectively. In this figure, the slope of the curves at each point represents the output stiffness, δ_o , at that point. As expected from Eq. 3.5 and 3.6, the lowest stiffness δ_o occurs for the largest angle of α (in this figure 175°) and the highest stiffness takes place at the smallest value of α (135°). As this figure shows, the output stiffness between the green and black curves increases steadily, with each curve associated with α angles of 170°, 165°, 160°, 155°, 150°, 145° and 140°, respectively.

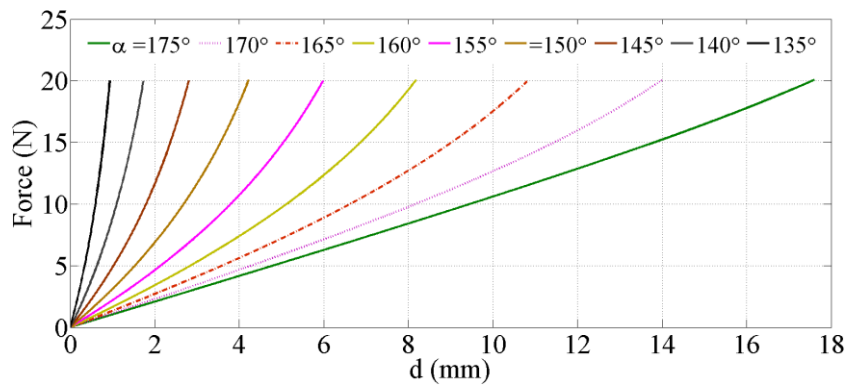


Figure 3.6: Force-displacement curves for the VSG₁.

3.2.3 Experimental Results and Discussion

To validate the concept of the proposed variable stiffness mechanism, a gripper prototype (Figure 3.7) characterized by two fingers has been developed. This figure shows the gripper and its capability to grasp and lift objects of different stiffnesses and weights. Figure 3.8

reports actual measurements of the displacement d for different values of applied force in the presence of different rotations of M_1 ($\theta = 5^\circ, 10^\circ, 15^\circ, 20^\circ, 25^\circ, 30^\circ, 40^\circ$ and 55°).

To collect these data, a spring with a stiffness constant of 0.3 N/mm has been used. The solid lines in this figure correspond to experimental results, whereas the dashed lines have been collected from the associated simulation model. To collect the experimental results, the gripper has been removed from the actuation system and, by hanging different weights on the tendon, the associated elongation of the tendon, d has been measured. The fact that the experimental results do not perfectly coincide with the equivalent simulation results shows that there are unmodeled features (e.g., the variable friction of the rod inside the shaft hole and the friction between the tendon and pulleys) which could be reduced by improving the gripper design. The upcoming section will introduce VSG₂, which is a modified version of VSG₁, and explain how enhancing the shaft of M_1 can reduce friction and improve the functionality of the VSM.



Figure 3.7: Different objects with different sizes and stiffnesses, as lifted by the VSG.

In order to test the capability of the fingers to follow a desired trajectory in the presence of different stiffnesses, a trajectory tracking experiment was performed using a $\sin(5t)$ motion input applied to M_2 . Figure 3.9 depicts the hardware setup of this experiment. The output of this experiment was the rotation of the fingers (left finger in the figure) about the fingers' joint. This rotation has been measured by a rotational encoder mounted on the joint of the right finger. Figure 3.9, also depicts a rigid object (fire brick) placed between the fingers. It is not important what this object is as long as it satisfies the infinite stiffness condition ($K \rightarrow \infty$)

and so a brick was chosen as one of the potential objects that can be found in the industrial application environments. This brick was used to stop the fingers in their movement at a certain position. An FSR (Force Sensitive Resistor) sensor was mounted on this brick to measure the grip force.

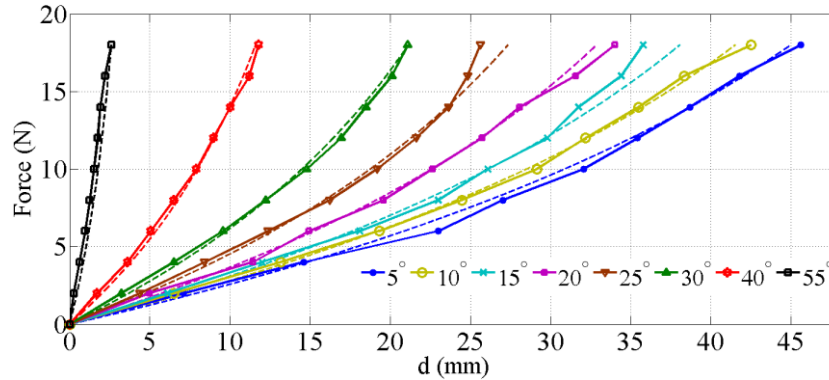


Figure 3.8: Experimental results (solid lines) versus simulation results (dashed lines) for the force-displacement test.

Figure 3.10 shows the experimental results collected from this experiment. To perform this test, the angle θ was set to 0° , 10° , 20° and 30° where the subplots a, b, c and d show the finger trajectories associated to these angles, respectively. The green dashed lines in this figure depict the desired input trajectory (applied to M_2), whereas the solid blue lines show the actual motion of the fingers measured by the encoder. As shown in this figure, the increased stiffness of the fingers acts to stabilize the system where the finger with higher stiffness ($\theta = 30^\circ$) follows the sinusoidal trajectory with a reduced error.

Figure 3.10.e depicts the grip force applied by the gripper to the fire brick, as measured through the FSR sensor. The figure shows that the applied force increases by increasing the value of θ and, consequently, the stiffness. The smallest force (the black line in the figure) measured for the test was for the smallest θ , which corresponds to the smallest stiffness. As this figure shows, the grip force was increased with increasing θ . This was expected, as larger θ corresponds the greater stiffness of the finger, so for a given displacement, the larger stiffness must generate the greater force.

Figure 3.8.a depicts the rack and pinion mechanism used in the VSG1 in order to convert the rotation of M_2 to a linear motion used to move the sliding mechanism.

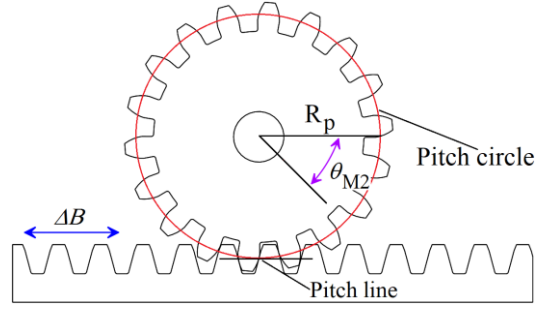


Figure 3.8.a: The rack and pinion mechanism of VSG1.

Eq. 3.7.a shows the relationship between the angular rotation of M2 and the linear displacement of the slider where ΔB in this equation depicts this linear displacement.

$$\Delta B = 2\pi R_p \theta_{M2} \pm B_{sh} \quad (3.7.a)$$

In this equation, θ_{M2} and R_p denote the angular rotation of M2 and the radius of the pitch circle of the gear in the rack and pinion mechanism and B_{sh} is the backlash of the system. The maximum backlash of the system is measured as ± 0.04 mm. This backlash can be reduced in the future by increasing the accuracy of the machining in the fabrication process.

From Eq. 3.7.b the resolution of the linear motion can be calculated as bellow:

$$r^{\Delta B} = 2\pi R_p r^{\theta_{M2}} \pm B_{sh} \quad (3.7.b)$$

Where $r^{\Delta B}$ and $r^{\theta_{M2}}$ denote the resolution of the linear motion and the resolution of the motor M2 respectively. From Table 3.1, for the resolution of M2 is $r^{\theta_{M2}} = 0.088^\circ$. By knowing the radius of the pitch circle of the gear $R_p = 2.4$ mm, and from Eq. 3.7.b the resolution of the linear motion of the slider can be calculated as below:

$$r^{\Delta B} = 2\pi \times 2.4 \times 0.088 \pm 0.04 = 1.32 \pm 0.04 \text{ mm} \quad (3.7.c)$$

Finally, Figure 3.11 depicts the hysteresis that occurs in the displacement-force curves for different values of θ . These results were obtained by gradually applying an external force and measuring the associated displacement, d (as previously undertaken for the force-displacement curves) and then gradually removing this force. To perform this experiment, a spring with a spring constant of 0.55 N/mm has been used. It is worth noting that the hysteresis shows a well-known phenomenon in Variable Stiffness Actuators (VSAs) (93), and this is particularly evident in this case for low stiffness values. The curves in this figure show

small variations in displacement of the order of only 2 mm as introduced by the largest hysteresis band, which could be further narrowed down through a better variable stiffness mechanism design aimed at reducing friction and damping in mechanical couplings.

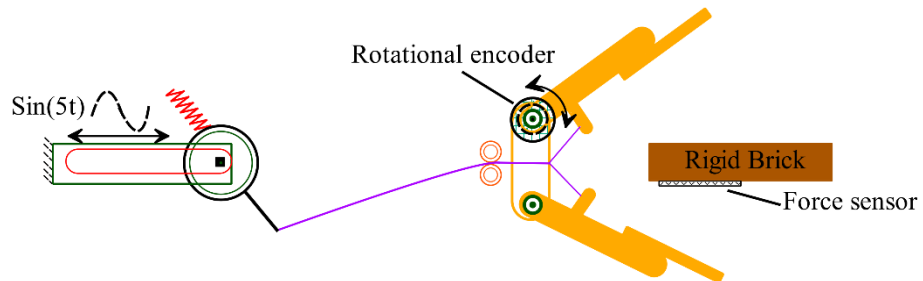
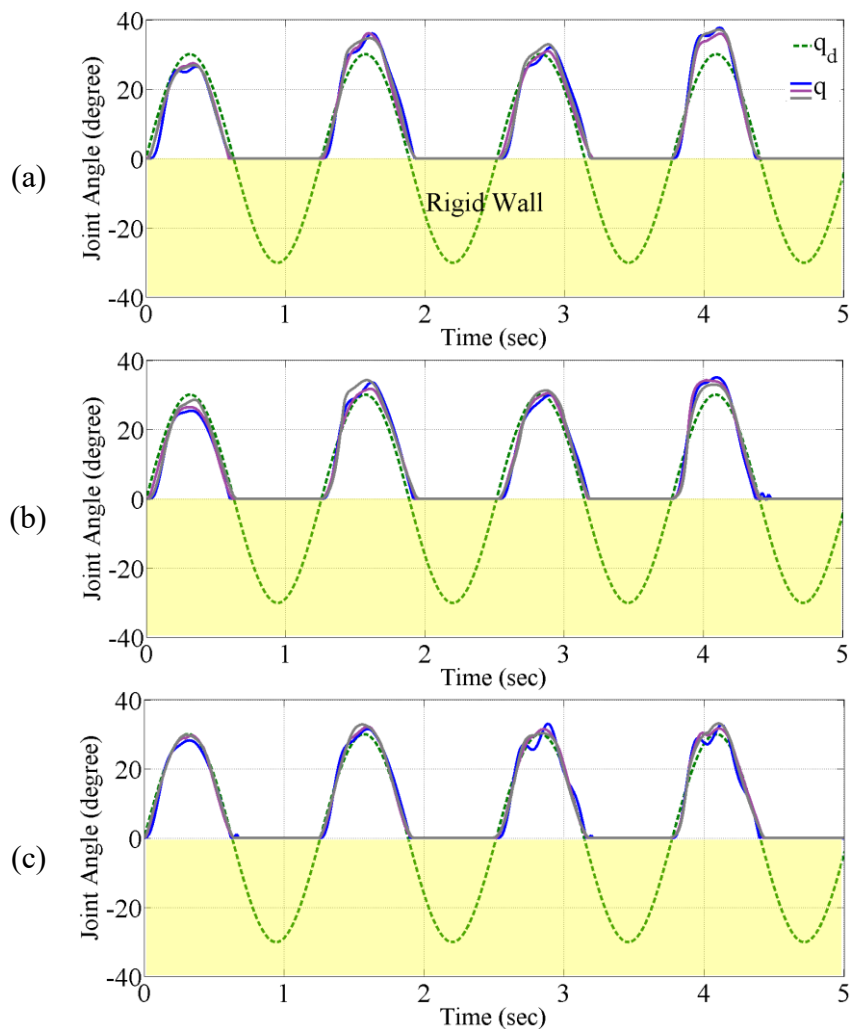


Figure 3.9: Hardware setup for the trajectory tracking experiment.



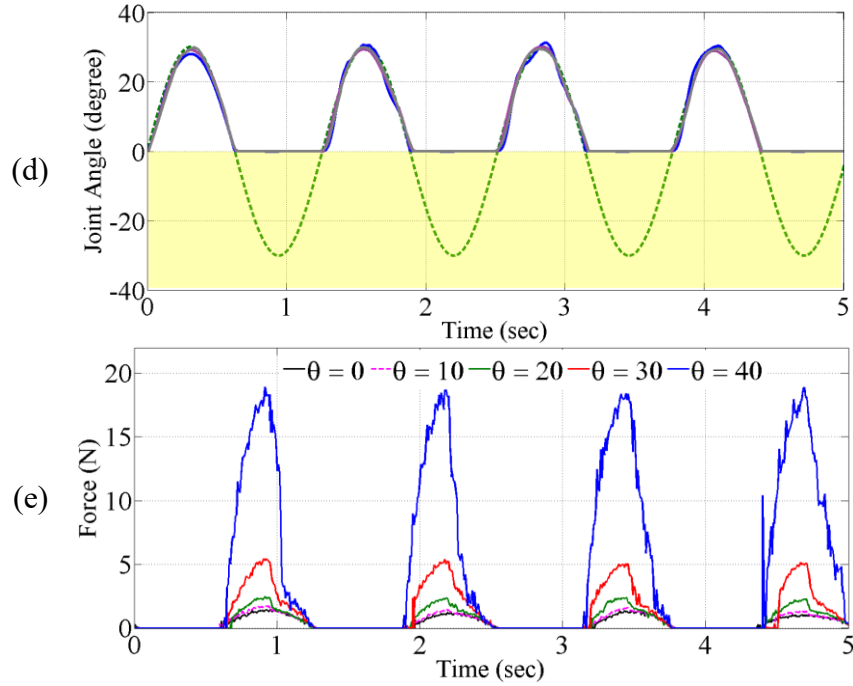


Figure 3.10: (a, b, c, d) Finger's motion (solid lines) versus desired trajectory (dashed lines) for the sinusoidal trajectory tracking experiment for $\theta = 0^\circ, 10^\circ, 20^\circ$ and 30° respectively. (e) FSR sensor measurements of the impedance force exerted by the fingers on the brick.

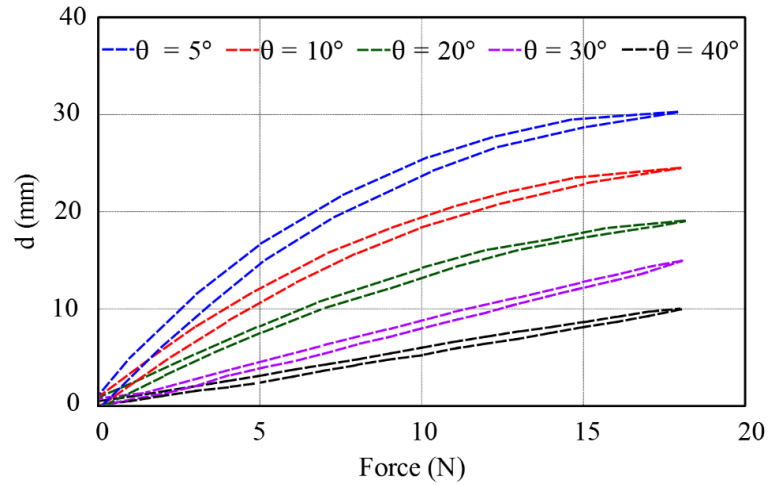


Figure 3.11: The hysteresis curves of VSG₁ for different values of the rod angle.

3.3 VSG₂

A novel variable stiffness mechanism was introduced in the previous sections of this chapter. As explained the proposed mechanism provides a low cost, fast and durable solution to the control of both of position and stiffness of the fingers. As explained previously, the mechanism has been used to drive a two-finger tendon-driven gripper, VSG₁. Unlike most of the variable stiffness mechanisms referenced in this thesis (which provide relatively small force/torque and hence can only be used in robots with a small range of payloads), the

proposed variable stiffness mechanism can be used for both low and heavy payload grippers. There is, however, a limitation on using this mechanism in the heavy payload grippers. The upcoming sections will explain this limitation and the modification method to overcome such limitation.

3.3.1 Design Explanation

Despite all the explained advantages, there is, however, a limitation on using the proposed variable stiffness mechanism as an actuation system for heavy payload grippers. This limitation arises from the relatively high dry friction between the shaft hole and rod. This is due to the large contact surface between the inner side of the hole and the rod. In order to reduce this friction, the shaft of M_1 is modified in the second prototype. Instead of using a hole, in the new design the shaft of M_1 utilises a pair of pins to hold the rod in place. Figure 3.12.a shows a CAD model of the modified shaft, whereas Figure 3.12.b depicts M_1 and both designs of its shaft. The left side of this figure shows M_1 in the first prototype, VSG₁, whilst the right side shows the motor and its enhanced shaft as used in VSG₂. This figure also shows the rod and spring configuration for both designs. The contact surface between the shaft and rod are shown

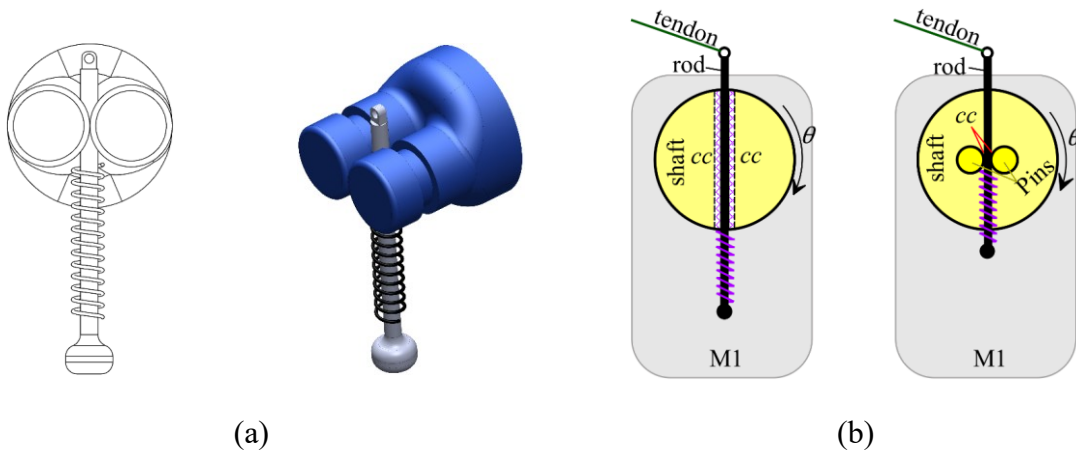


Figure 3.12: (a) CAD model of the modified shaft of M_1 used in VSG₂. (b) Schematic model of M_1 used in VSG₁ (left) versus M_1 with the modified shaft used in VSG₂ (right)

by cc . From this figure, it may be noted that the contact surface in VSG₂ is decreased dramatically and, as a result, the friction between the rod and shaft in VSG₂ is lower than in VSG₁. It is worth noting that the lower friction in VSG₂ causes a smaller hysteresis in the force-displacement curves, as will be discussed in the upcoming sections. Similar to VSG₁,

VSG₂ utilises two identical 7 N.m servo motors, M₁ and M₂, whose mechanical and electrical specifications are reported in Table 2.1. The gripper system of VSG₂ is a three finger, six degrees of freedom tendon-driven gripper that was designed and fabricated as a part of this work. A side view of the gripper and its actuation system is shown in Figure 3.13. The two servo motors are also shown in the figure. Alike VSG₁, one of the servos, M₁, is used to rotate the rod-spring system, whilst the second servo motor, M₂, is used to generate a linear motion. In order to reduce the size of the actuation system, the rack and pinion gear arrangement of VSG₁ is replaced with a 3D printed tendon-driven slider mechanism in VSG₂. A tendon connects the shaft of M₂ to the slider and transfers the motor's torque to the sliding force. Using this force, the slider can slide up and down along the wrist axis of the gripper. A CAD model and a schematic model of the new variable stiffness actuator are shown in Figure 3.14. As shown in this figure, the first motor, M₁, is fixed on this slider and follows the slider's movements. Similar to the first model, a tendon-pulley arrangement is used to transfer the driving force from the actuator to the gripper. As previously explained, the gripper utilises a linear compression mechanical spring that is mounted to the shaft of M₁ through a rigid rod, as shown in Figure 3.14. The rod slides perpendicular to the shaft of M₁ through a pair of pins across the shaft's axis. A spring holder in the bottom of the rod holds the spring in place and a tendon fixing hole is used to fasten the tendon to the rod.

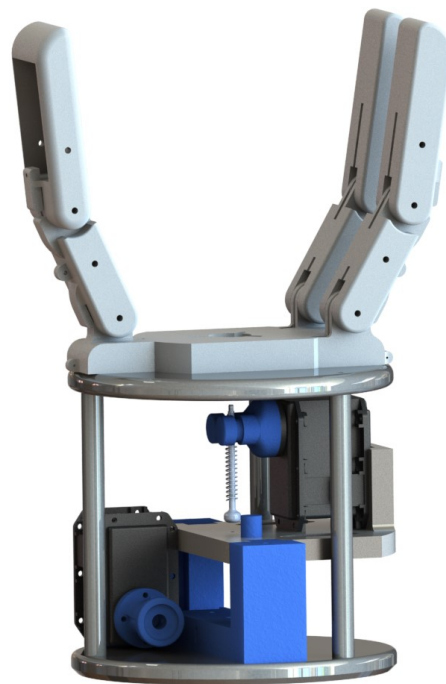


Figure. 3.13: The three-finger variable stiffness gripper, as introduced in this section.

3.3.2 Modelling the stiffness function

The output stiffness of the variable stiffness mechanism is modeled in this section. To derive the stiffness function as depicted in Figure 3.15, there are two coordinate frames: (a) the reference coordinate frame, OXYZ, and (b) the shaft coordinate frame, o'x'y'z', which is parallel to the reference coordinate frame and whose origin lies at the geometric centre of the shaft of M₁, as shown in the figure. In this same figure, the purple line shows the tendon making the connection between end of the rod and the gripper. The linear motion generated by the slider and M₂ is along the Y-axis of OXYZ. The combination of the motions of servos M₁ and M₂ provides the ability to change the stiffness of the gripper. Alike VSM₁, the apparent stiffness of the gripper in this system is related to θ , the angle between the rod and the Y-axis, and this stiffness changes according to this angle. The first motor, M₁, is used to change this angle and control the stiffness of the gripper. To model the output stiffness, let us assume that there is an external force from the environment acting on the fingers. This external force is shown by F_e in Figure 3.15. Clearly, the tendon transfers this force from the finger to the actuator; the tensile force F in Figure 3.16 represents the transferred force. For clarity, the gripper is not shown in this figure. From the above we can write:

$$|F \cos \alpha_1| = Kz'_s \quad (3.7)$$

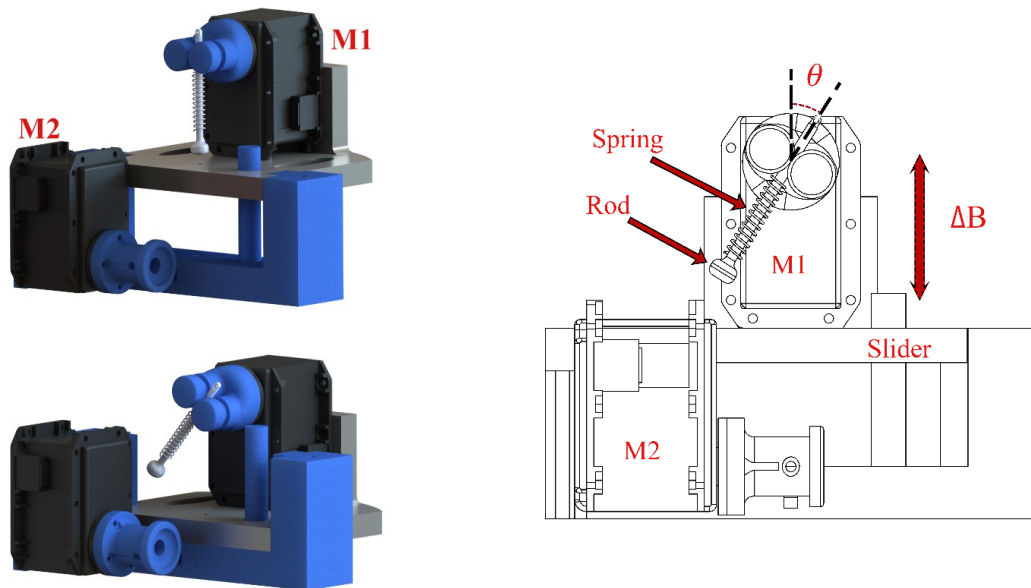


Figure 3.14: A CAD and a schematic representation of the second variable stiffness design.

where α_l is the angle between the rod and tendon, K is the stiffness constant of the spring and z'_s is the displacement of the rod (which is equal to the co-contraction of the spring) due to the pulling force F . From Eq. 3.7 we can write:

$$z'_s = \frac{|F \cos \alpha_1|}{K} \quad (3.8)$$

Similar to VSG₁, the maximum rotation of M₁ is assumed to be bounded as $\theta \leq \frac{\pi}{2}$. Thus, for α_l we have:

$$\pi \leq \alpha_1 \leq \frac{\pi}{2} \quad (3.9)$$

So, from Eq. 3.8 and 3.9 we can write:

$$0 \leq z'_s \leq \frac{|F|}{K} \quad (3.10)$$

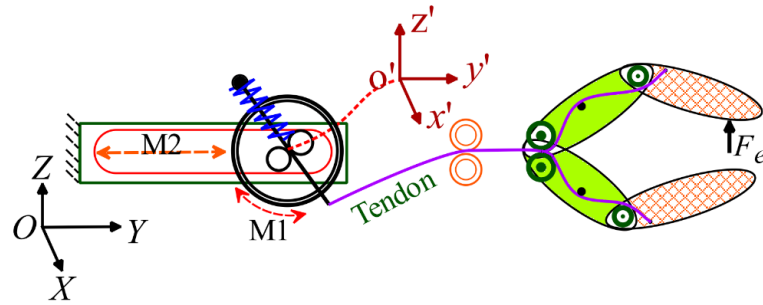


Figure 3.15: Schematic model of VSG₂.

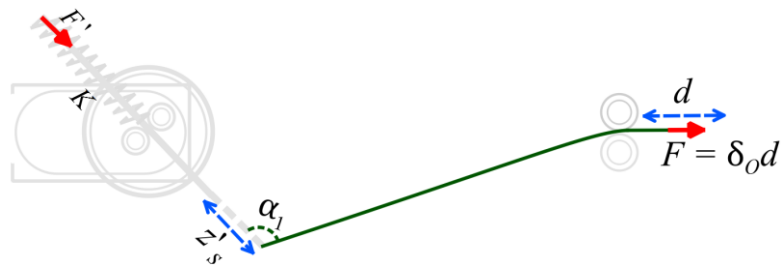


Figure 3.16: The tendon is pulled by F and the spring is compressed due to this force.

where, similar to VSG₁, this equation shows the minimum and maximum co-contraction of the spring due to the external force, F . From Eq. 3.10, it may be noted that $z'_s = 0$ when $\alpha_1 = \pi/2$ and, assuming that the tendon is inelastic and the shear deformation of the rod is negligible, we can write:

$$\alpha_1 \rightarrow \frac{\pi}{2} \quad \delta_0 \rightarrow \infty \quad (3.11)$$

and

$$\min \delta_0 = K|_{\alpha_1=\pi} \quad (3.12)$$

where δ_0 is the apparent stiffness of the gripper. Figure 3.17 shows the gripper in both its open and closed states with minimum and maximum stiffness. In this figure, the red grippers correspond to the stiff gripper with the maximum (ideally infinite) stiffness, whilst the blue grippers correspond to the gripper with minimum stiffness, which is equal to the stiffness of the spring, K . As shown in Figure 3.17, in both states related to the gripper with maximum stiffness, the angles between the tendon and rod are perpendicular, and for the blue grippers, which correspond to the minimum stiffness, the tendon lies along the rod and spring ($\alpha_l = \pi$).

In order to derive the stiffness function of the gripper, let us assume that the displacement of the tendon due to the above-mentioned external force is equal to d .

Figure 3.18 depicts this force and its associated displacement. For clarity, the gripper have not shown in this figure. D_0 represents the distance between rod's end point (tendon-rod fixing point) and the wrist of the gripper. Z' is the length between rod's end point and the centre of the shaft of M_1 before applying the force. D_l is the distance between rod's end point and gripper wrist after applying the force. z'_s shows the displacement of the rod's end point due to co-contraction of the spring after applying the force. Using the law of sines, we can write:

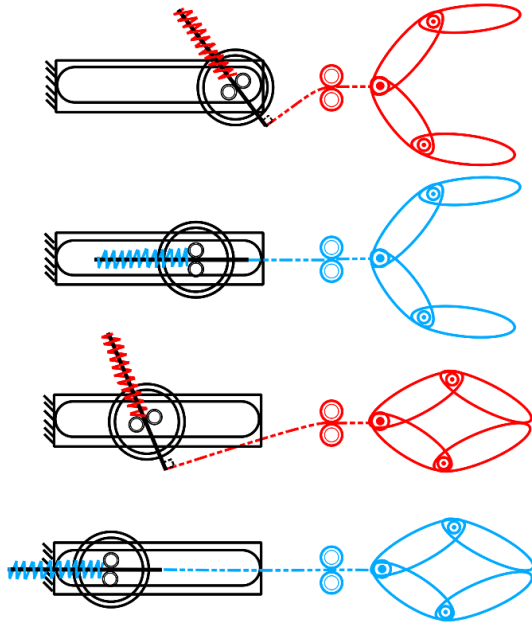


Figure 3.17: VSG₂ at **maximum** and **minimum** stiffness.

$$\sin \theta = \frac{D_0 \sin \alpha_0}{B} \quad (3.13)$$

where θ is the angle between the rod and Y-axis, B is the distance between the centre of the shaft of M_1 and wrist point of the gripper, and α_0 is the angle between the tendon and rod in their initial positions. After applying the force, and by using Eq. 3.13, we can write:

$$\frac{\sin \alpha_1}{B} = \frac{D_0 \sin \alpha_0}{BD_1} \quad (3.14)$$

Assuming that the tendon is perfectly inelastic, we can write:

$$D_1 = D_0 - d \quad (3.15)$$

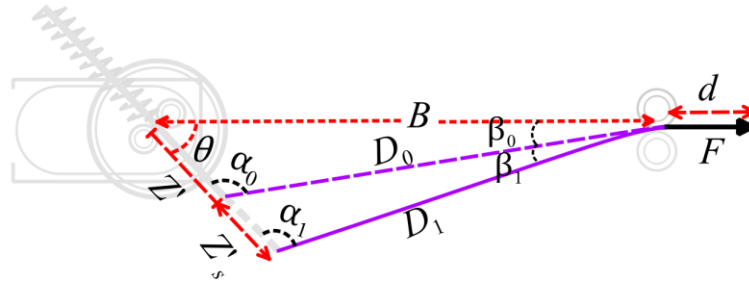


Figure 3.18: Position of the rod and tendon before and after application of force F .

Using Eq. 3.14 and 3.15 we have:

$$\alpha_1 = \sin^{-1} \frac{D_0 \sin \alpha_0}{(D_0 - d)} \quad (3.16)$$

And by again using the sine law and Eq. 3.15, we can get:

$$\frac{\sin(\beta_0 + \beta_1)}{z' + z'_s} = \frac{\sin \theta}{D_0 - d} \quad (3.17)$$

where β_0 and β_1 are shown in Figure 3.18. By simple calculation, we get:

$$\beta_1 = \alpha_0 - \alpha_1 \quad (3.18)$$

substituting Eq. 3.18 into Eq. 3.17 we obtain:

$$z'_s = \frac{(D_0 - d) \sin(\beta_0 + \alpha_0 - \alpha_1)}{\sin \theta} - z' \quad (3.19)$$

Finally, from Eq. 3.16 and Eq. 3.19 we can conclude:

$$z'_s = \frac{(D_0 - d) \sin\left(\beta_0 + \alpha_0 - \sin^{-1}\left(\frac{D_0 \sin \alpha_0}{(D_0 - d)}\right)\right)}{\sin \theta} - z' \quad (3.20)$$

Also, from Figure 3.16 we have:

$$F' = -F \cos \alpha_1 = K z'_s \quad (3.21)$$

where F' is the decomposed element of F along the rod axis. Adding Eq. 3.16 and Eq. 3.20 to Eq. 3.21 we can write:

$$F = \frac{K \frac{(d - D_0) \sin\left(\beta_0 + \alpha_0 - \sin^{-1}\left(\frac{D_0 \sin \alpha_0}{(D_0 - d)}\right)\right)}{\sin \theta} + z'}{\cos\left(\sin^{-1}\left(\frac{D_0 \sin \alpha_0}{(D_0 - d)}\right)\right)} \quad (3.22)$$

Where:

$$\begin{cases} D_0 = \sqrt{B^2 + z'^2 - 2Bz' \cos \theta} \\ \beta_0 = \sin^{-1}\left(z' \left(\frac{\sin \theta}{D_0}\right)\right) \end{cases} \quad (3.23)$$

Eq. 3.22 and 3.23 formalize the relationship between the applied force F and d for different θ , which entails the nonlinearity of the output stiffness δ_o . The set of curves in Figure 3.19 shows how F changes when d varies over a discrete range of θ (from 0 to 40°) in two different views. In these figures, the lowest line shows the stiffness of the gripper when $\theta = 0$. As expected, and due to the linear spring used in the actuator, there is a plateau in the force-displacement relationship for this angle, and the slope of this line is equal to the stiffness of the spring, K . From this figure, and entirely as expected, the slopes of the curves increase with increasing θ as the highest line, the red curve, is associated to the greatest angle $\theta = 40^\circ$.

In more generic terms, the stiffness of a grasp can be modelled by a relationship between the applied force and the displacement due to this force (92):

$$\delta_o^\theta = \left. \frac{\partial F}{\partial d} \right|_\theta \quad (3.24)$$

where the term δ_o^θ highlights the dependence of the gripper's stiffness on the angle θ . As

shown in Figure 3.19, this stiffness increases with increasing θ . It is worth noting that from Eq. 3.22 and 3.23, the fingers' stiffness, δ_o , is also dependent on the stiffness of the spring K and the variable B . Figure 3.20 shows the effect of different values of K and B on the output stiffness of the gripper. As can be noted from this figure, the output stiffness of the gripper increases with increasing K and/or B .

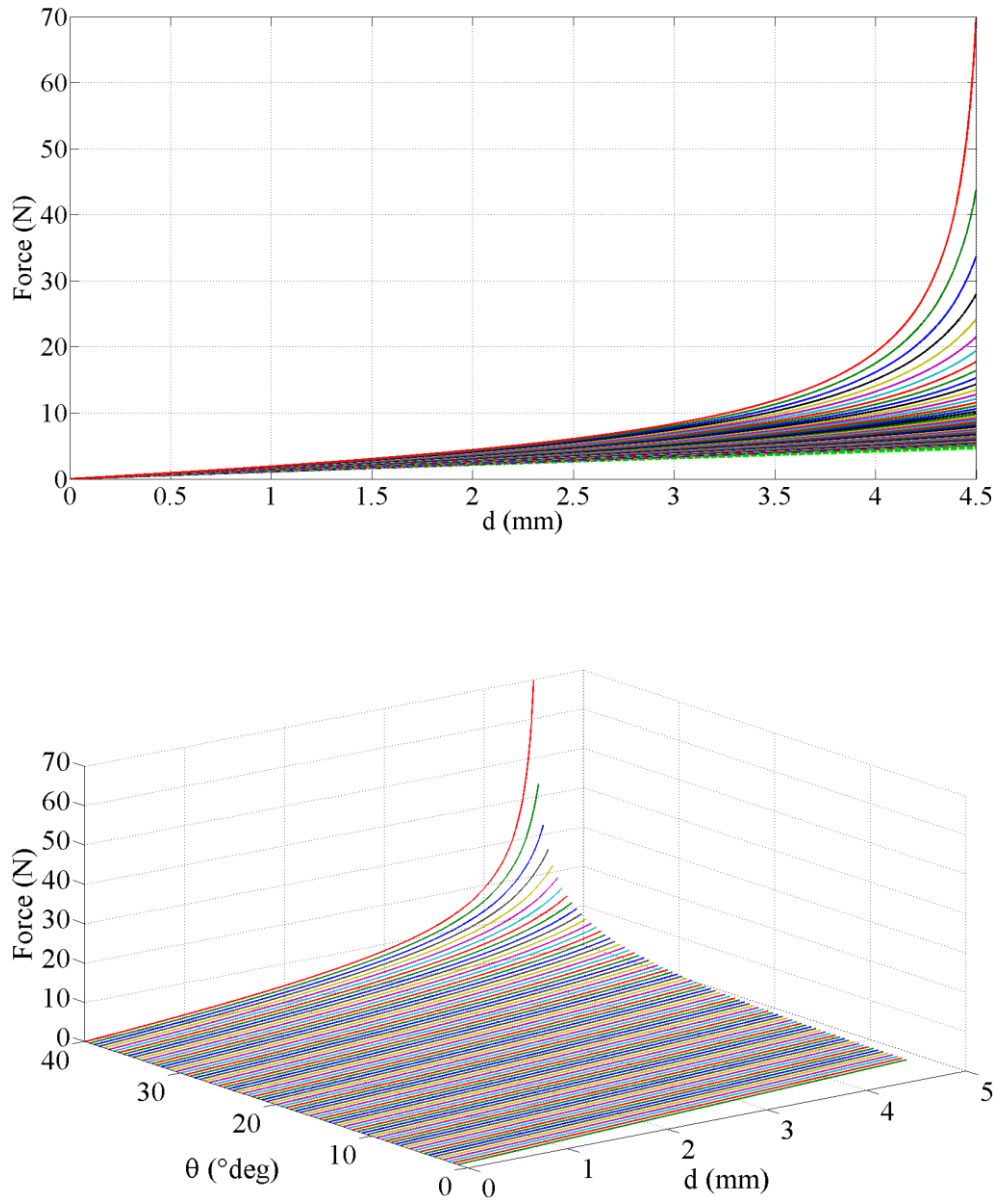


Figure 3.19: Stiffness of the gripper δ_o for different values of θ .

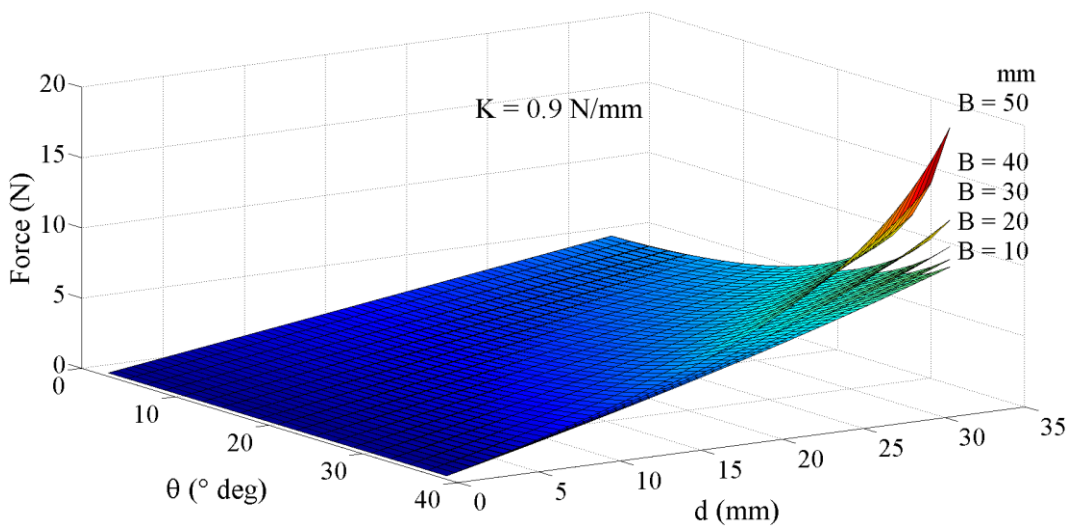
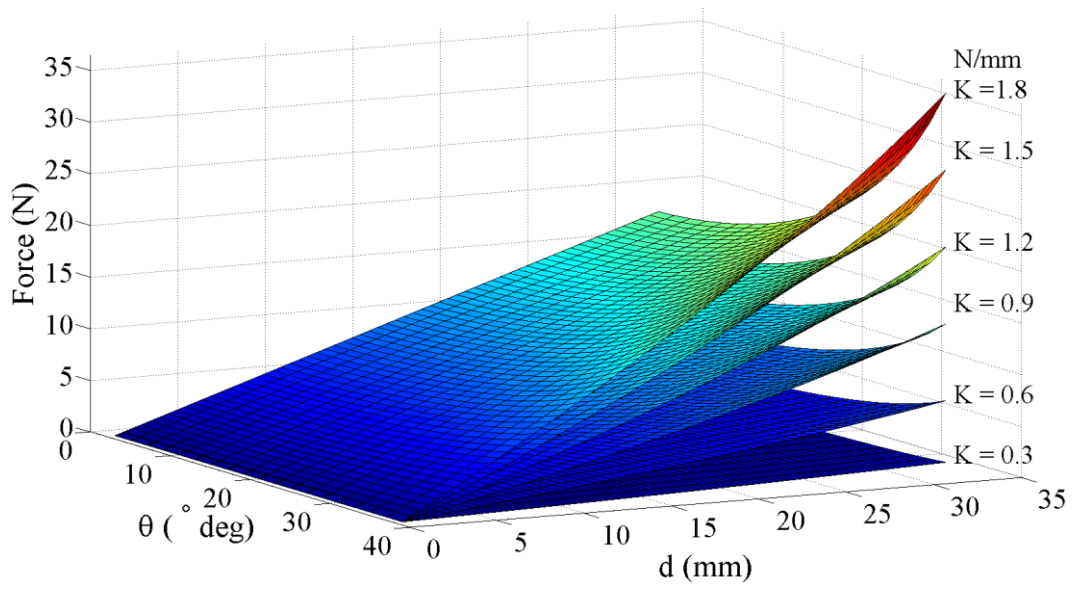


Figure 3.20: Stiffness of the gripper δ_o for different values of K and B .

3.3.3 Experimental results

To demonstrate the concept of the variable stiffness gripper, VSG₂, a tendon-driven gripper prototype has been fabricated (Figure 3.21), as characterized by three fingers and six joints (two joints per finger). This figure shows the gripper and its ability to grasp objects of different stiffnesses and weights. Figure 3.22, reports actual measurements of the displacement d for different values of applied force and rod angles ($\theta = 5^\circ, 10^\circ, 15^\circ, 20^\circ, 25^\circ, 30^\circ, 40^\circ$ and 55°). The experimental curves are shown by solid lines. Similar to VSG₁, to collect these results, the gripper has been removed from the actuation system and, by hanging different weights on the tendon, the associated elongation of the tendon, d has been measured. The stiffness coefficient of the spring used in this experiment was 0.3 N/mm. The dashed lines in this figure were calculated from the stiffness model described by Eq. 3.22 and 3.23. The fact that the overlap of the two curves are showing better coincidence compared to the results shown in Figure 3.8 illustrates the reduced friction and unmodeled features in VSG₂ compared to VSG₁. To evaluate the response of the gripper and the gripper's compliance to a sinusoidal input a trajectory tracking experiment has been performed, similar to the one shown in Figure 3.9, and the results of which are shown in Figure 3.23. In this test the angle θ has been set to $0^\circ, 10^\circ, 20^\circ, 30^\circ$ and 40° . Then the second motor, M₂, has been actuated with a sinusoidal motion input $\text{Sin}(5t)$ and with a rigid fire brick placed in the way of the fingers. This brick was used to stop the fingers in their movement at a certain position. An FSR (Force Sensitive Resistor) sensor was mounted on this brick to measure the grip force.



Figure 3.21: Different objects with different sizes and flexibilities lifted by VSG₂.

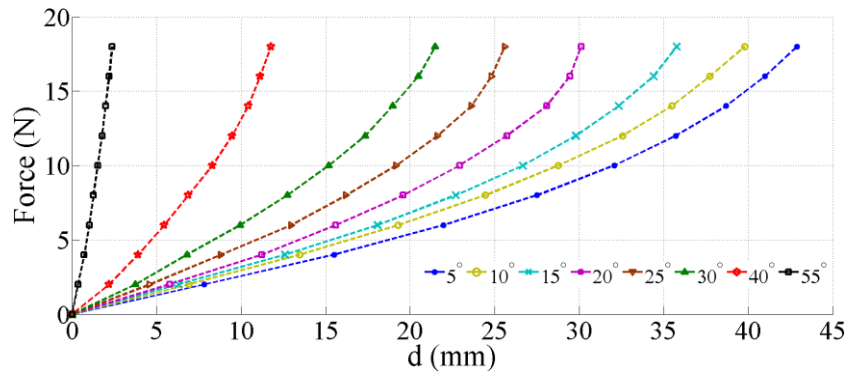


Figure 3.22: Experimental measurements of the displacement d for different values of applied force and rod angles ($\theta = 5^\circ, 10^\circ, 15^\circ, 20^\circ, 25^\circ, 30^\circ, 40^\circ$)

In Figure 3.23.a, b, c and d, the solid red lines show the actual motion of the fingers whilst the dashed green lines show the reference motion. Figure 3.23.e corresponds to the force applied by the fingers on the rigid brick, as measured through a force sensor. As expected, the figure shows that the applied force increases with increasing value of θ and, consequently, the gripper stiffness.

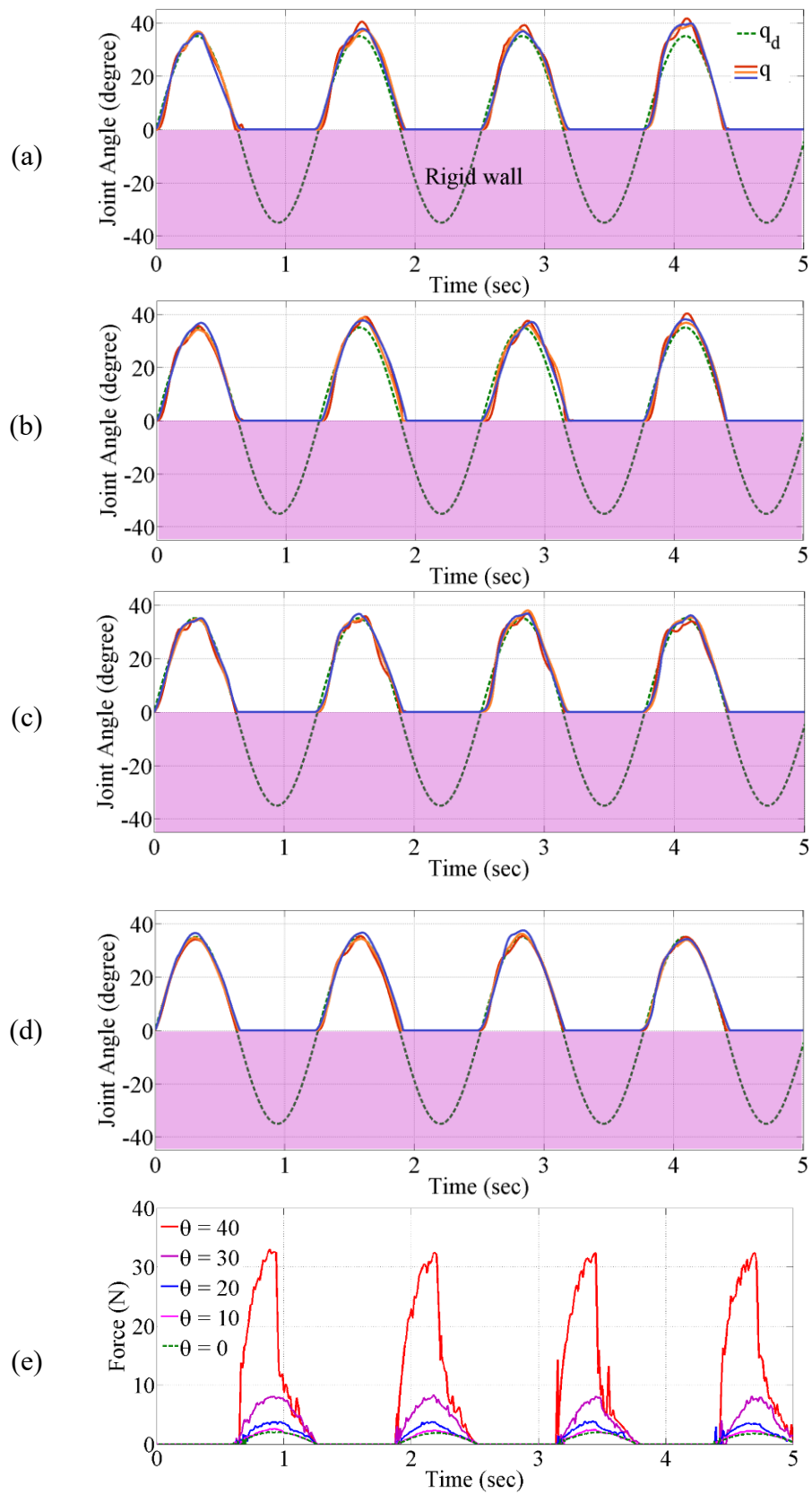


Figure. 3.23: Trajectory and force tracking for a stiffness-controlled gripper colliding with a physical rigid brick for $\theta = 0^\circ, 10^\circ, 20^\circ$ and 30° respectively.

Figure 3.24 shows the stiffness hysteresis curves for different values of the rod angle, θ , obtained by gradually applying an external force and measuring the associated displacement, d (as previously undertaken for the force-displacement curves) and then gradually removing this force. To allow comparison the hysteresis curve of VSG1 is also plotted. To perform this experiment, a spring with a constant of 0.55 N/mm has been used. Comparing these results with the hysteresis curves obtained from VSG₁, it is evident that VSG₂ shows better performance as per the smaller hysteresis band (maximum reduction = 74%, average reduction = 43%) observed. Clearly this hysteresis could be further narrowed through a better gripper design aimed at reducing friction and damping in mechanical couplings.

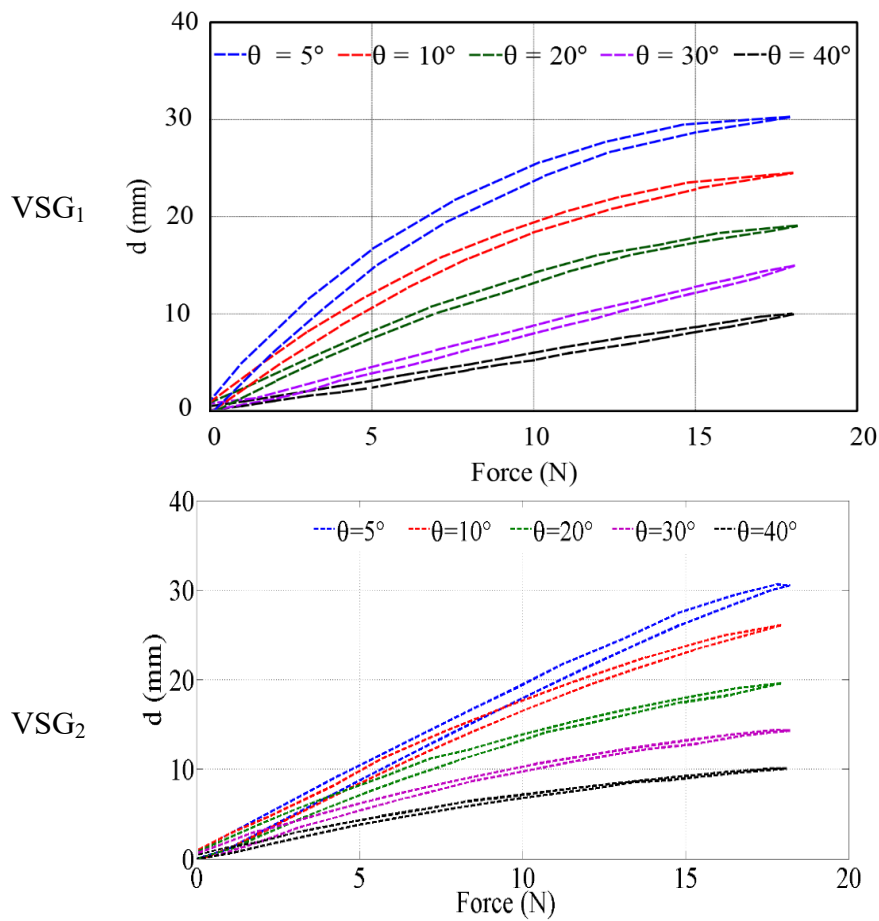


Figure 3.24: The spring hysteresis curves for different rod angles.

Finally Figure 3.25 depicts the magnitude bode plot of the fingers' motion for different values of θ . As expected, it can be seen that the peak magnitude decreases with increasing θ , consequently increasing the stiffness of the finger.

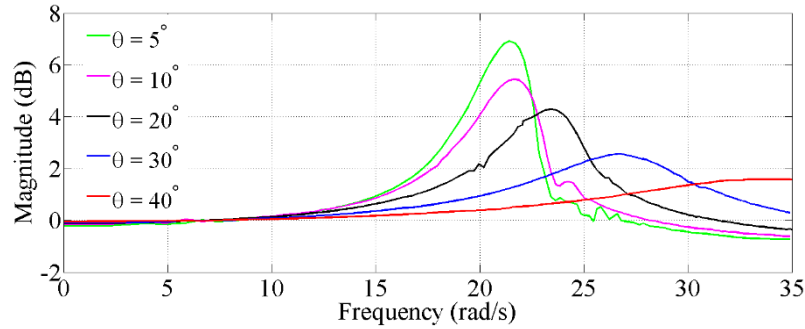


Figure 3.25: Magnitude bode plot for VSG₂ for $\theta = 5^\circ, 10^\circ, 20^\circ, 30^\circ$ and 40° .

3.4 Discussion

Two novel variable stiffness mechanisms have been presented in this chapter. The mechanisms introduced provide a driving force for the tendon-driven grippers with an ability to control the position and stiffness of the fingers. The designs consisted of two rotational servo motors. One of the servo motors, along with a linear compression spring, was used to control the stiffness of the fingers whereas the other motor was responsible for changing the fingers' position. In order to control the apparent stiffness in the fingers, a mathematical model of the stiffness as a function of the shaft angle has been derived. The stiffness has to be tuned manually and is based on prior knowledge of the objects that will be handled. The experimental results confirmed the effectiveness of the proposed variable stiffness mechanism. The gripper designs introduced were characterized by a large variability in stiffness, which is an essential requirement for a highly flexible handling system, and is particularly useful in food industry scenarios. The grippers are also characterized by their fast response and small hysteresis band. The simplicity of their design, besides providing a low-cost solution, guarantees the inherent reliability and robustness of these mechanisms. It should be mentioned that in performing the grasping task with both of the grippers, the apparent output stiffness needs to be manually adjusted but this does not need to be done for every product. Any stiffness setting will have a range of products that can be grasped.

Chapter 4

ROBUST GRASP CONTROL

4.1 Introduction

In the previous chapter, two novel variable stiffness gripper designs has been proposed. The mechanisms introduced can be used to control the grip force applied through simple control of the stiffness and compression of the integrated spring. Moreover, as explained in chapter one, these increase the robustness of the fixed gain controllers when dealing with objects with uncertain stiffness. Note that the uncertainty in the object's stiffness is not the only uncertainty in the grasp. In the design of any control system, and more specifically grasp control, there are always mismatches between the actual system and its dynamical model. These mismatches arise for various reasons such as external disturbances, linearization of nonlinear parameters, neglected and/or unmeasurable parameters (such as friction). In the presence of such uncertainties during grasping tasks and due to unknown external disturbances, utilising any ordinary control methods will be difficult if not impossible. Robust control methods, and more specifically sliding mode control, however, are an alternative solution to overcoming such difficulties (141,145, 146). The second contribution of this work is to realise a robust control method capable of performing a stable grasp in the presence of all the mentioned uncertainties. To do so, first, this section will explain the theory and concept of sliding mode control (SMC), which as mentioned is a particular method of robust controller theorem. It will be shown how, in the presence of unknown external disturbances, an SMC can robustly and in a finite time converge the state variables to the reference point. The main advantages of SMC, including robustness, insensitivity to the external disturbance and finite time convergence, are discussed in numerous examples and simulation plots. More specifically, the advantages of using this control law to control the grasp will be discussed in depth.

4.2 Gripper test platform

Figure 4.1 shows one of the grippers designed and developed as part of this research. The gripper used for the tests and results reported in this chapter was mounted on a KUKA KR10

with a 10 kg payload. The gripper consists of two fingers connected to the shaft of two servo motors through joints J_1 and J_2 . A simplified schematic model of this gripper is shown in Figure 4.2. To model the fingers' motions and grasping task, two coordinate frames are used, as shown in this same figure, a reference coordinate frame $OXYZ$ fixed on the base of the robot, and a finger coordinate frame $o'x'y'z'$, which is parallel to the reference coordinate frame. The gripper is designed such that the fingers are always parallel and move in the XZ -plane. However, for simplicity, it will be assumed that the displacement of the fingers is linear along X axis. This means that according to Figure 4.2, the fingers' actuation force F_a , will always be applied along the X -axis. For clarity, only one actuation force is shown in this figure. $f_d(x,t)$ and $\Gamma(x_f, v_f)$ in this figure represent an external disturbance and any unmodeled resistance force such as dry and viscous friction, respectively, whilst a constant M_F denotes the fingers' mass.



Figure 4.1: The two-finger gripper mounted on the KUKA robot.

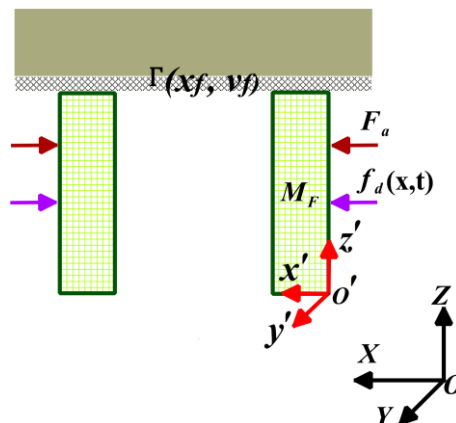


Figure 4.2: Schematic model of the gripper and the coordinate frames used.

The state variables of the fingers are chosen as below:

$$X_1 = x_f \quad (4.1)$$

$$X_2 = \dot{X}_1 = v_f$$

where x_f and v_f denote the fingers' displacement and velocity along the X-axis, respectively.

By assuming a unit mass for the fingers and from Figure 4.2 and Eq. 4.1 we can write:

$$\dot{X}_2 = F_a + f_d(x_f, t) + \Gamma(x_f, v_f) \quad (4.2)$$

The disturbance and uncertain resistance forces can be rewritten as a single force, as per below:

$$F_{du}(X_1, X_2, t) = f_d(x_f, t) + \Gamma(x_f, v_f) \quad (4.3)$$

From Eq. 4.3 and 4.2 we can write:

$$\dot{X}_2 = F_a + F_{du}(X_1, X_2, t) \quad (4.4)$$

The aim of this section is to design a control law that asymptotically drives the fingers to the desired position in the presence of a bounded F_{du} Eq. 4.5.

$$|F_{du}(X_1, X_2, t)| \leq D \quad D > 0 \quad (4.5)$$

where D in this equation is the boundary limit of F_{du} .

4.3 Proportional-Derivative position control

It is worth noting that, as explained in Section 1.1.1 of chapter one, any external disturbance and uncertainty of the model makes an asymptotic convergence of the state variables a challenging task for conventional controllers. As an example, let us assume a conventional proportional-derivative feedback control for the gripper design shown in Figures 4.1 and 4.2. Eq. 4.6 shows this control law:

$$F_a = -G_p X_1 - G_D X_2 \quad (4.6)$$

In an isolated situation ($F_{du} = 0$), this controller can drive the states variables to the origin (or any desired state). Figure 4.3 illustrates this convergence. However, in the presence of a

bounded external force and uncertainty (Eq. 4.5), the above-mentioned controller can only drive and keep the state variables X_1 and X_2 inside a bounded area.

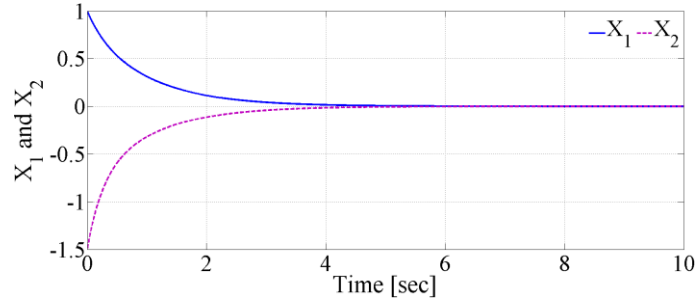
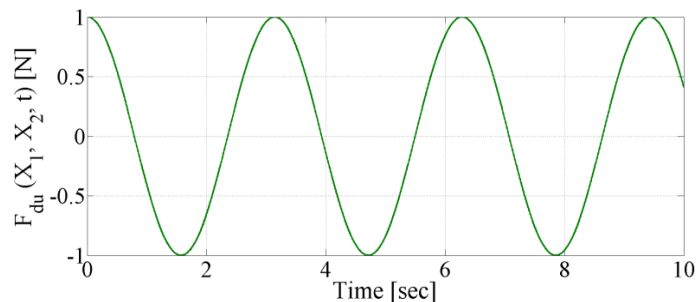


Figure 4.3: When the gripper is isolated from the environment, the conventional proportional-derivative position control will drive the state variables to the origin in a finite time.

As an example, the response of the gripper with the same controller and in the presence of a bounded external force: $F_{du}(X_1, X_2, t) = \cos(2t)$ and a square pulse wave are shown in Figure 4.4 and Figure 4.5, respectively. It is worth noting that, the frequencies were chosen as they are representative of the speeds that a task may be performed at by a human in an industrial application. From these two figures it can be noted that, unlike the isolated condition, the controller is very sensitive to the model uncertainty and unknown external disturbances, and it can only maintain the state variables inside a bounded domain in the presence of a bounded external force. To conclude, despite the convenience of utilising conventional control methods to control the isolated systems, there is an inherent disadvantage to them; they are very sensitive to model uncertainties and unknown external disturbances. To overcome this disadvantage, in the following section it will be explained an alternative control method, Sliding Mode Control (SMC). After an in-depth discussion about the concept of this approach as applied to robust control, it will be shown the response of the SMC designed for the examples discussed above, which will demonstrate the capability of this control method to overcome associated uncertainties and unknown external forces.



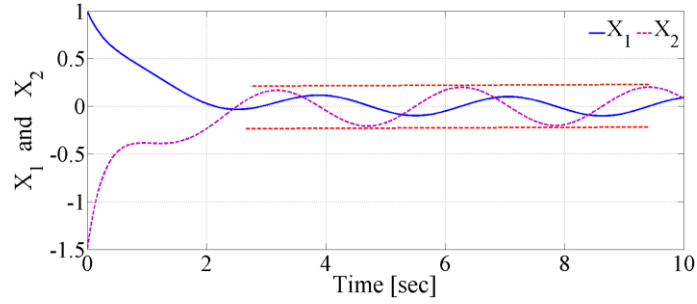


Figure 4.4: System response for a bounded disturbance $F_{du}(X_1, X_2, t) = \cos(2t)$ in the presence of a proportional-derivative control law.

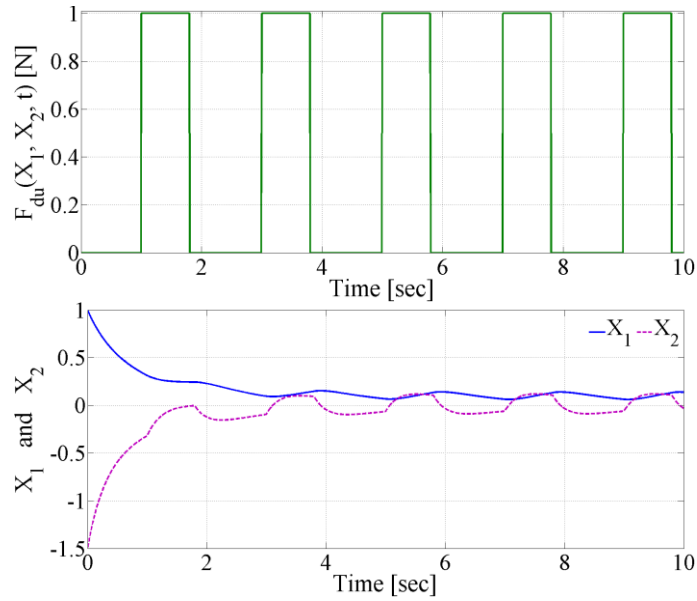


Figure 4.5: System response for a bounded square wave disturbance in the presence of a proportional-derivative control law.

4.4 First-Order Sliding Mode Control Design

This section explains the concept of sliding mode control and the way in which this controller can achieve an asymptotic stability in the presence of an undesired external force and unknown parameters of the system model. To do so, and assuming the system shown in Eq. 4.1, let us first define a linear equation for the first state variable X_1 , as below:

$$\dot{X}_1 + \eta X_1 = 0 \quad \eta > 0 \quad (4.7)$$

where the general solution for this differential equation is:

$$X_1(t) = X_1(0) e^{-\eta t} \quad (4.8)$$

From Eq. 4.1 and 4.8 we can write:

$$X_2(t) = -\eta X_1(0) e^{-\eta t} \quad (4.9)$$

From Eq. 4.8 and 4.9 we can write:

$$\lim_{t \rightarrow \infty} X_1(t), X_2(t) = 0 \quad (4.10)$$

Eq. 4.10 illustrates an asymptotic convergence of the state variables to the origin. Now we need to design a control law that provides such a compensated response for the state variables. To do so, a new variable, the so-called sliding variable, has to be designed in the state space as below.

$$\sigma(X_n) : R^n \rightarrow R \quad (4.11)$$

$$\sigma = \sigma(X_1, \dot{X}_1, \ddot{X}_1, \dots, X_1^n) = \sigma(X_1, X_2, \dots, X_n)$$

As shown in Eq. 4.11, the sliding variable, σ , is a scalar function of the state variables. A common form chosen for the sliding variable is given as per below, which as shown in this equation is a function of state variables and the scalar value η .

$$\sigma = \left[\frac{d}{dt} + \eta \right]^\lambda X$$

$$\lambda = 1 \quad \sigma = X_2 + \eta X_1 \quad (4.12)$$

$$\lambda = 2 \quad \sigma = X_3 + 2\eta X_2 + \eta^2 X_1$$

Considering the sliding variable as below:

$$\sigma(X_1, X_2) = \dot{X}_1 + \eta X_1 = X_2 + \eta X_1 \quad \eta > 0 \quad (4.13)$$

From Eq. 4.13 it can be noted that driving the sliding variable to zero (Eq. 4.14) in a finite time will cause an exponential decrease (with the convergence rate of η) and eventually an asymptotic converge to the state variables.

$$\sigma(X_1, X_2) = X_2 + \eta X_1 = 0 \quad \eta > 0 \quad (4.14)$$

It should be noted that equation (Eq. 4.14) represents a straight line in the state spaces, and is called a sliding surface. In short, to achieve an asymptotic convergence for X_1 and X_2 , it should be found a way to drive the sliding variable to the sliding surface in a finite time.

From Eq. 4.1, 4.3 and 4.13 we can write:

$$\dot{\sigma}(X_1, X_2) = \eta X_2 + F_a + F_{du}(X_1, X_2, t) \quad (4.15)$$

Eq. 4.16 and 4.17 illustrate a candidate for Lyapunov function and its relevant stability condition about the sliding surface, respectively.

$$\Lambda_\sigma = \frac{\sigma^2}{2} \quad (4.16)$$

$$\dot{\Lambda}_\sigma < 0 \text{ if } \sigma \neq 0 \quad (4.17a)$$

$$\lim_{|\sigma| \rightarrow \infty} \Lambda_\sigma = \infty \quad (4.17b)$$

Clearly from Eq. 4.16, the condition Eq. 4.17.b is always satisfied. Rewriting the condition Eq. 4.17.a as:

$$\dot{\Lambda}_\sigma \leq -\xi \sqrt{\Lambda_\sigma(t)} \quad (4.18)$$

where ξ is a positive constant. From Eq. 4.18, in a finite time, T_s , the selected Lyapunov function, will reach zero. Where:

$$T_s \leq \frac{2\sqrt{\Lambda_\sigma(0)}}{\xi} \quad (4.19)$$

From Appendix A, The control force F_a in Eq. 4.20, 4.21 and 4.22 which satisfies condition Eq. 4.17 drives the sliding manifold to the origin in a finite time, T_s .

$$F_a = -\eta X_2 - \Omega \text{sign}(\sigma) \quad (4.20)$$

where:

$$\text{sign}(\sigma) = \begin{cases} 1 & \sigma > 0 \\ \in [-1, 1] & \sigma = 0 \\ -1 & \sigma < 0 \end{cases} \quad (4.21)$$

and:

$$\Omega = D + \frac{\xi}{\sqrt{2}} \quad (4.22)$$

The constant D in Eq. 4.22 is responsible for compensating the external disturbance shown in Eq. 4.5, whilst the term $\frac{\xi}{\sqrt{2}}$ determines the reaching time to the sliding surface ($\sigma = X_2 + \eta X_1 =$

0); clearly this reaching time can easily be calculated by inputting ζ into Eq. 4.19. The control law shown in Eq. 4.20 is called the first-order sliding mode control. More information about first-order sliding mode control can be found in (141,145,146)

Figures 4.6 and 4.7 depict the results of the gripper system explained in Section 4.2 as controlled by an SMC in the presence of a sinusoidal and a pulse wave external disturbance. These unit threshold external disturbances are also shown in these figures. To perform the test, η and Ω have been set to 1 and 1.5, respectively, and the initial condition of the state variables have been set to $X_1 = 1$ and $X_2 = -1.5$. As shown in these figures, the controller satisfactorily derived the sliding variable σ toward the sliding surface ($\sigma = 0$) and kept the sliding variable at the sliding surface thereafter. Consequently, starting from initial conditions, the state variables have vanished to zero after only a short transient period, as illustrated in these figures. Comparing the results from the conventional PD controller shown in Figure 4.4 and Figure 4.5, the results shown in these two figures demonstrate the robustness of the sliding mode controller in compensating for external bounded disturbances.

The phase plot of the state variables are shown in Figure 4.6.d and Figure 4.7.d. As these figures depict, there are two distinct phases in these plots. These two phases are called the Reaching phase and Sliding phase, shown by R_{ph} and S_{ph} in the figures, respectively, where R_{ph} corresponds to the time taken for the controller to drive the sliding variable to the origin and S_{ph} represents when the controller drives the state variables toward the reference point along with the sliding surface.

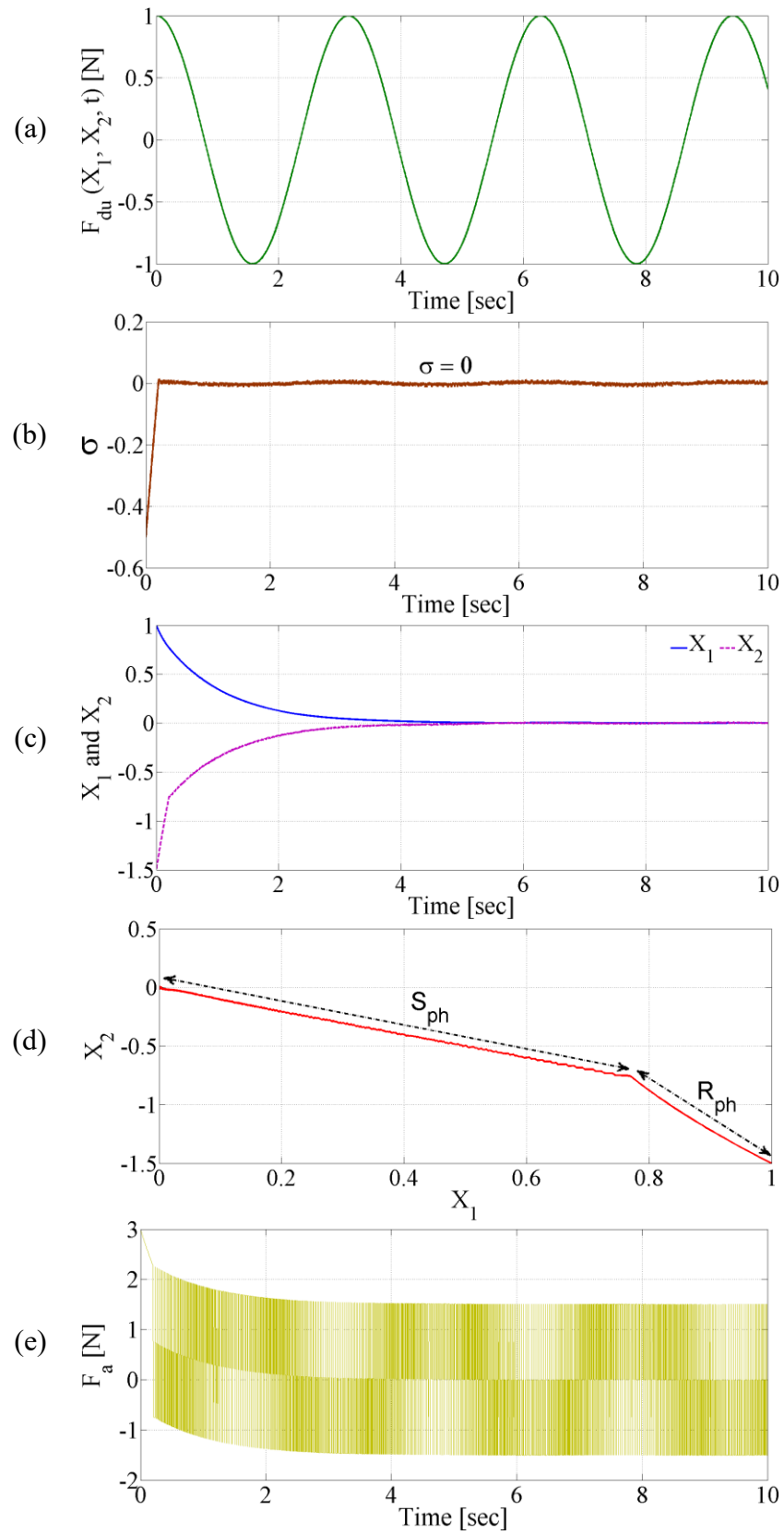


Figure 4.6: Results of the gripper system controlled by a first-order sliding mode controller in the presence of a sinusoidal external disturbance.

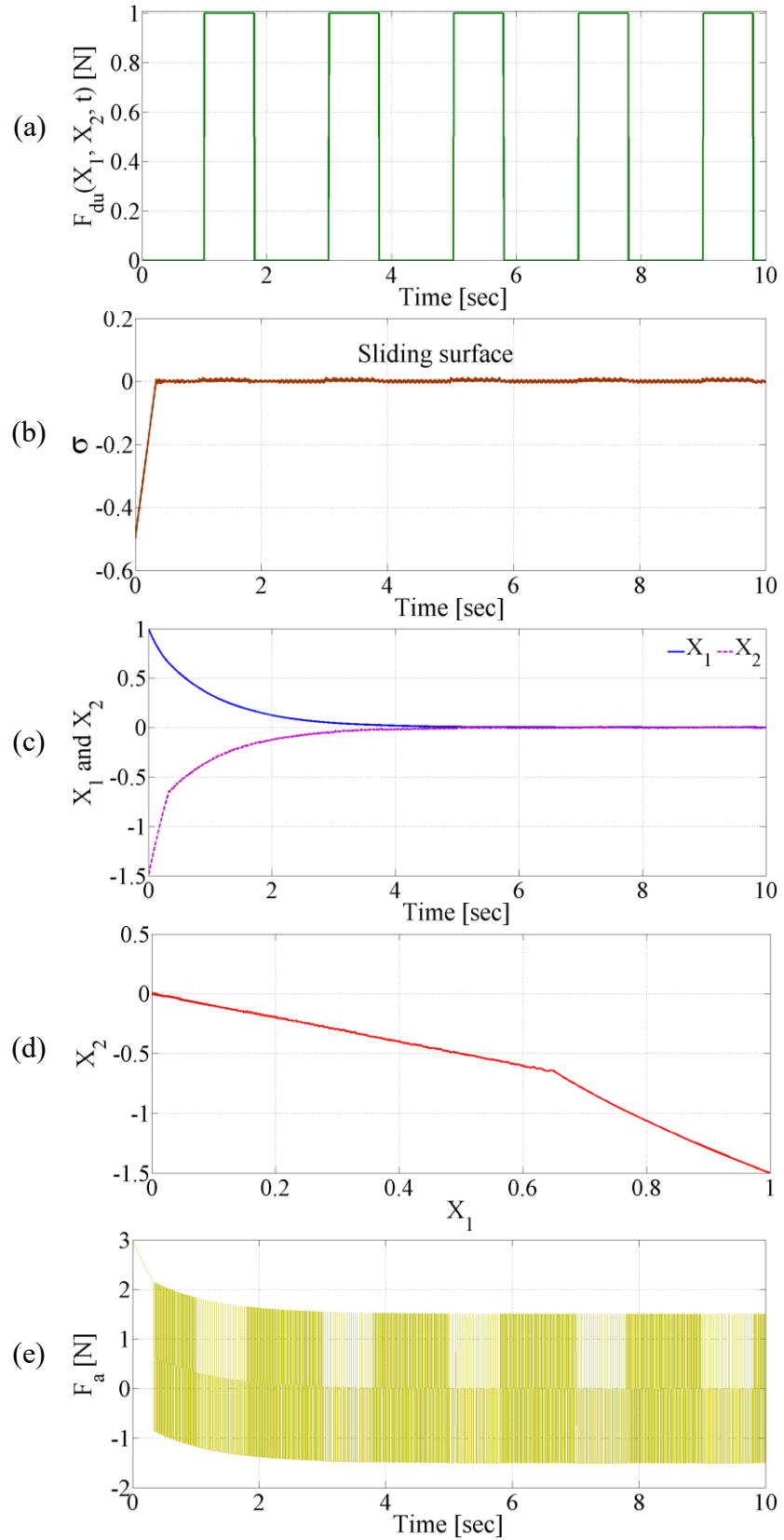


Figure 4.7: Results of the gripper system controlled by a first-order sliding mode control in the presence of a square wave pulse external disturbance.

As already described, the scalar constant η in Eq. 4.13 corresponds to the convergence rate of the state parameters where the larger the value of η the faster the convergence of the state variables. Figure 4.8.a illustrates the effects of η on the gripper system. The solid lines in this figure correspond to the response of the first state variable X_1 (position of the finger) whilst the dashed lines show the response of the second state variable X_2 (velocity of the finger). To perform this test, the above-mentioned sinusoidal disturbance has been applied. The blue, red, green and violet lines in this figure correspond to the convergence rates $\eta = 0.5, 1, 1.5,$ and $2,$ respectively.

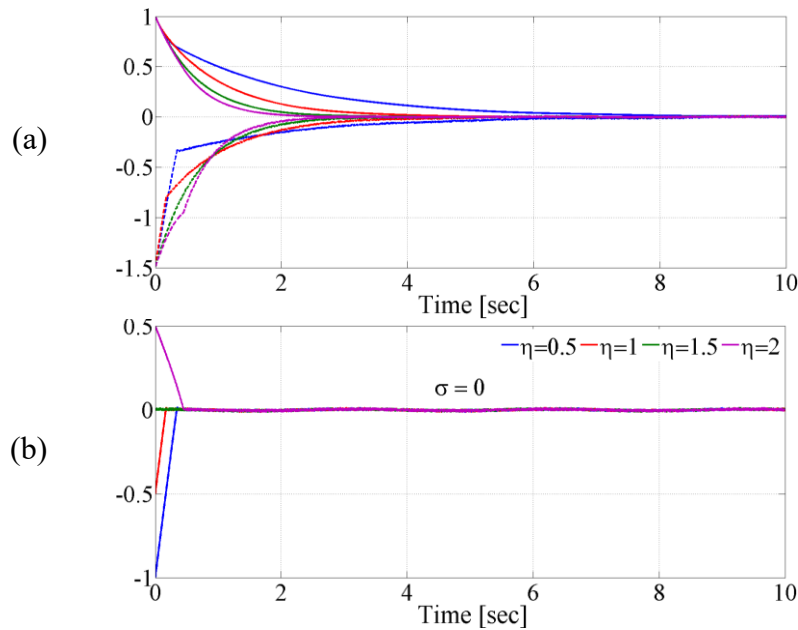


Figure 4.8: The effect of convergence rate on the response of the gripper controlled by an SMC.

The results of the sliding variable for the different convergence rates are also shown in subplot (b) of this figure. This figure clearly illustrates the consistency of the controller's performance in driving the sliding variable from its initial condition to the origin for all of the convergence rates tested. It is worth noting that from Eq. 4.13 the initial condition of σ can be written as below:

$$\sigma(0) = X_2(0) + \eta X_1(0) \quad (4.23)$$

Where $X_1(0) = 1$ and $X_2(0) = 1.5$ for the state variables, equation Eq. 4.23 clearly explains why the initial condition of σ changes from -1 to 0.5 when changing the convergence rate. Figure 4.9 depicts the effects of different Ω for the above-explained gripper system. Subplot (a) of this figure corresponds to the states' responses whilst subplot (b) depicts the sliding

variable. The solid lines in this figure represent the position of the fingers and the dashed lines correspond to the fingers' velocity. As shown in this figure, the sensitivity of the controller to the external disturbance decreased by reducing Ω such that the controller cannot keep X_1 , X_2 and σ at zero in the presence of the unit amplitude external force when Ω is smaller than 1.

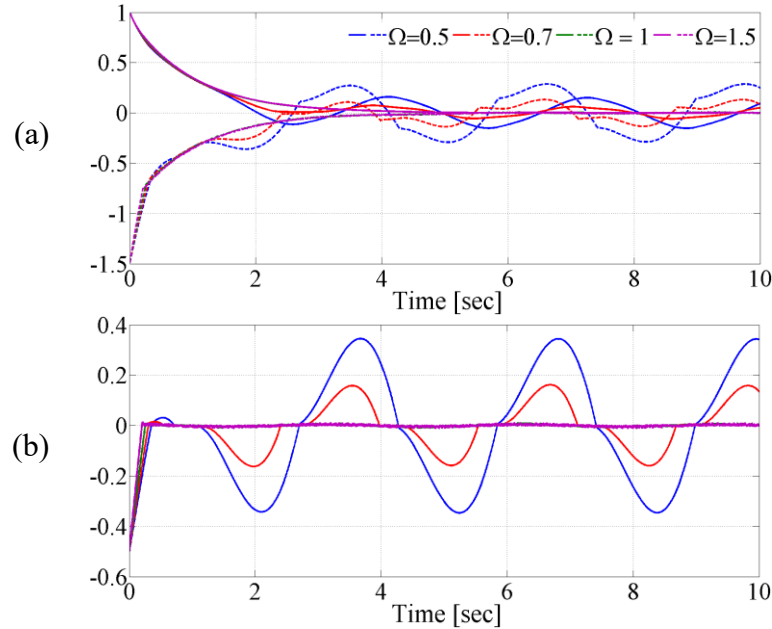


Figure 4.9: Effect of different values of Ω on the (a) states' responses and (b) sliding variable.

It is worth noting that despite the robustness of the first-order sliding mode control to overcoming unknown bounded disturbances, and in spite of insensitivity of this control architecture to any uncertainty in the model, there is nevertheless an inherent disadvantage to the FSMC. Due to the discrete behaviour of the sign function shown in Eq. 4.20 and 4.21, the outputs of the systems controlled by an FSMC have a tendency to oscillate; this behaviour is referred to as the chattering phenomenon, CHPH (141, 145, 146), as demonstrated by Figure 4.10. As shown in this figure, in the chattering mode that occurs in the steady-state phase, the control force F_a and the sliding variable σ fluctuate with very high frequency between $F_a = -\Omega$ and $F_a = \Omega$. The small amplitude, zigzag shape and high frequency behaviour of X_1 , X_2 and σ which correspond to the chattering phenomenon can be observed by zooming in on Figure 4.6.b, d and e; where Figure 4.9.a, b and c, respectively, show zoomed and cropped plots. It should also be noted that, theoretically, the chattering frequency of the sliding mode control should be infinite; however, in reality, due to control boards' limited clock pulse, the maximum

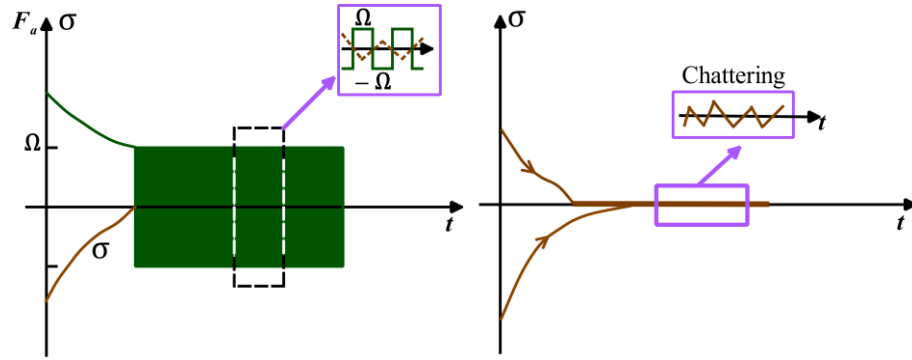


Figure 4.10: Chattering phenomenon in a system controlled by an FSMC.

frequency of the chatter will be equal to control board's clock pulse. The sample time for this example has been set to 1 KHz.

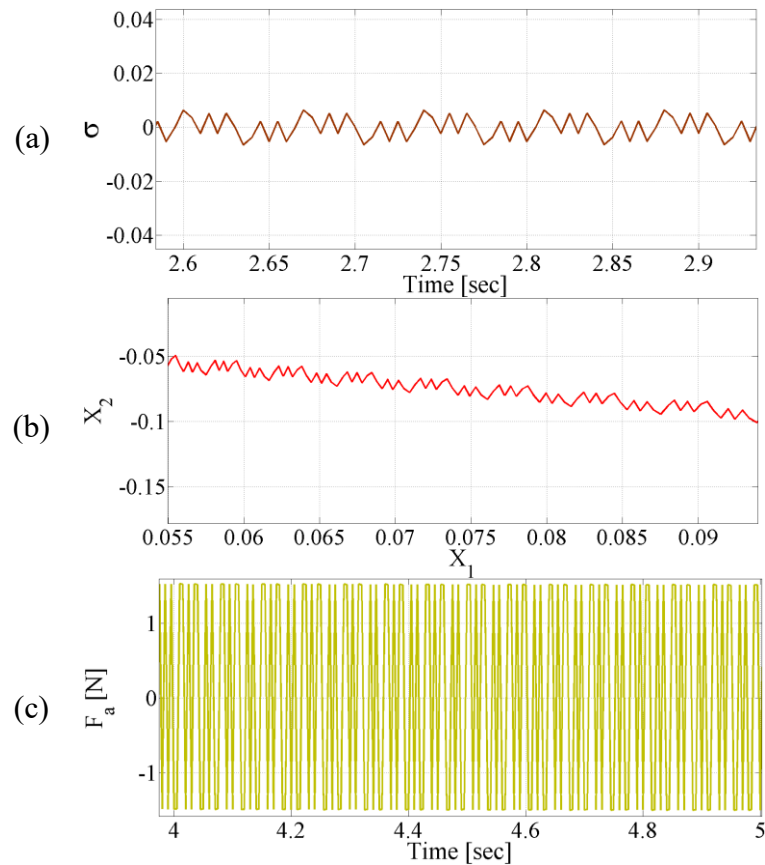


Figure 4.11: Zoomed plot of the Figure 4.6.

4.4.1 Disturbance rejection

To qualify the robustness of the first-order sliding mode control, it has been developed a more realistic case study as illustrated in Figure 4.12. As shown in this figure, the above mentioned

gripped has been used in this test to grasp and lift a T-shaped object from its thinner end. The inertial properties of the object are $[M_b \ I_{xx} \ I_{yy} \ I_{zz}] = [1.1 \ 1.3 \ 1.3 \ 0.4]$ kg, respectively, where M_b and $I_{xx}I_{yy}I_{zz}$ are the object's mass, and diagonal terms of the inertia tensor, respectively. To perform the test, an appropriate grip force has to be found in a way that the gripper can lift the object firmly and in such a way that the object does not fall; this is called a secure grasp. Clearly the appropriate grip force for a secure grasp is dependent on the friction coefficient between the fingertips of the gripper and the object's contact surface. In this test, the secure grip force has been found by trial and error. After securely lifting the object, the robot moves linearly along the X-axis of the base frame OXYZ, where this movement provides a linear displacement for the gripper and held object. To provide an adequate disturbance, a sinusoidal velocity has been set for the robot that creates an accelerated and decelerated motion. This motion is shown by a_g in Figure 4.12. A schematic model of the gripper and grasped object is also shown in Figure 4.13. According to this figure, and due to the law of conservation of angular momentum, the object exerts an external disturbance on the gripper in the presence of the accelerated motion. As shown in this figure, if the applied grip force is not sufficient to compensate this disturbance, the held object will swing between the fingers. The objective of this case study is to test the stability of the embedded FSMC as well as to evaluate the robustness of this controller to overcome the external disturbance. In short, the successful controller must hold the object firmly. Recall that from Section 1.1.1 in the first chapter, any proportional-integral (PI) motion control that satisfies Eq. 1.6 can overcome the mass of the grasped object. However, that is not the case for this test, as in this experiment the control task is to overcome the effect of the manipulator's disturbing force (as the result of the manipulator's accelerated motion). Note that the effect of the manipulator disturbing force in this example can be considered equivalent to F_b in equation Eq. 1.8 of chapter 1. As was discussed in that chapter, in the presence of the object's resistive force F_b , the PI motion control is not a good candidate for the grasp control as it leads to a steady-state error on the fingers (Please recall Figure 1.5).

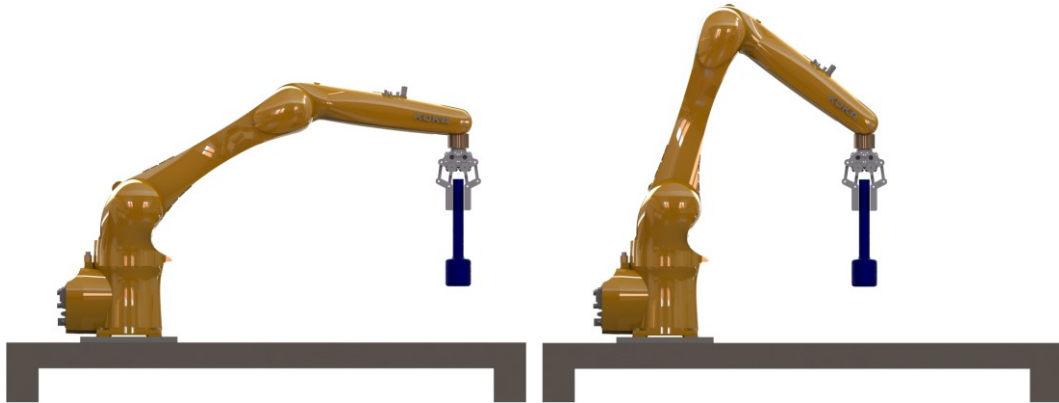


Figure 4.12: A grasp case study to test the robustness of the embedded FSM in the gripper.

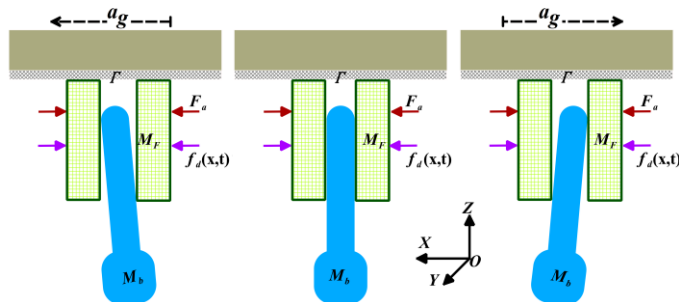


Figure 4.13: Schematic model of the gripper and held object moving together in an accelerated and decelerated manner.

Figure 4.14 represents a schematic model of the first-order sliding mode control architecture explained in this section, whilst Figure 4.15 shows the behaviour of the controlled gripper in the presence of the manipulator disturbing term.

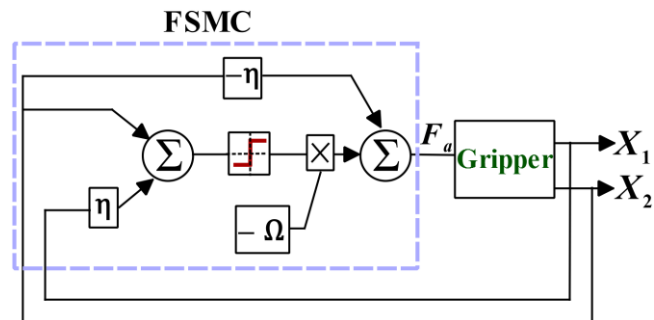


Figure 4.14: Schematic model of the gripper-FSMC system used in this test.

In Figure 4.15.a, the zero value in the X-axis represents the initial position of the fingers before the manipulator starts its motion. This position is defined as a reference. As this figure shows, by choosing a value larger than 35 for Ω ($\Omega \geq 35$), the FSMC could robustly overcome the manipulator's disturbing force as from the figure the state variables remain at origin for the test where Ω is equal to 35. This means that the sliding variable for this value of Ω will

stay at zero, as shown in Figure 4.15.b. Finally, subplot (c) of this figure demonstrates the actuation grip force controlled by the FSMC. As shown in this figure, and as already discussed, there is a high-frequency chattering behaviour in this actuation force which comes from the natural behaviour of the first-order sliding mode control.

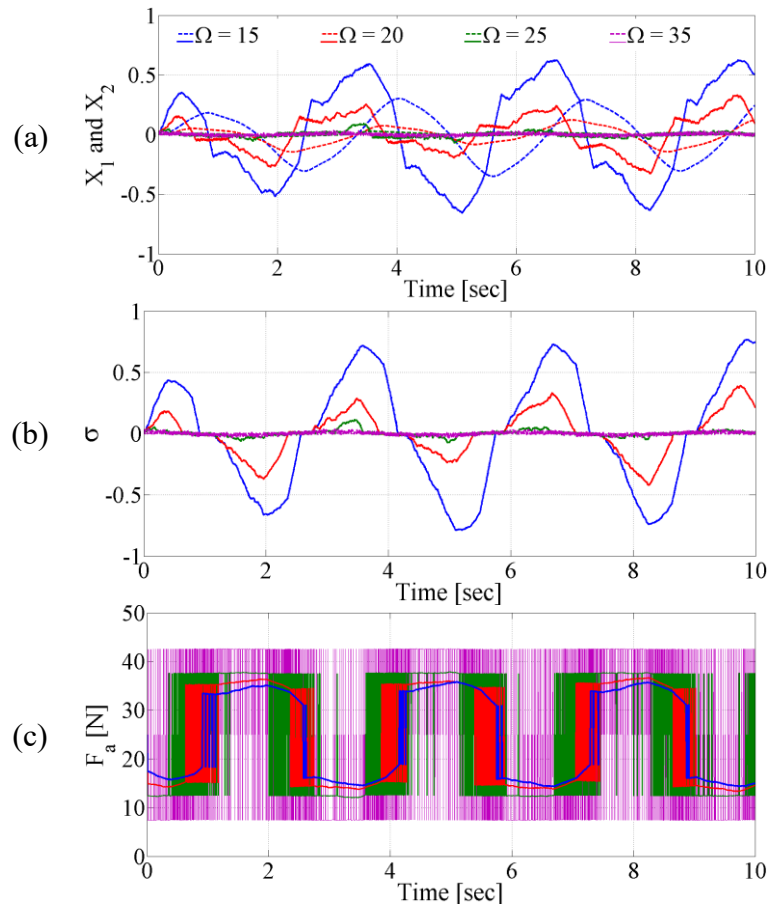


Figure 4.15: Experimental results for the T-shaped object lifted by the gripper.

4.4.2 Quasi-Sliding Mode Control Design

As discussed earlier in this chapter, the discontinuous nature of the $\text{sign}(\sigma)$ function in Eq. 4.20 lead to high-frequency zigzag response, or the so-called chattering phenomenon. Although this phenomenon has no influence on the robustness of the controller, it might shorten the lifespan of the gripper's mechanical parts. This discontinuous sign function, however, can be replaced by a continuous function in order to reduce the chatter. Equation Eq. 4.24 depicts two alternative continuous functions (a sigmoid function and a hyperbolic tangent function) that could replace the sign function.

$$F_a = -\eta X_2 - \Omega \text{Sigm}(\sigma, \varepsilon) = -\eta X_2 - \Omega \frac{\sigma}{|\sigma| + \varepsilon} \quad (4.24)$$

$$F_a = -\eta X_2 - \Omega \text{Tanh}(\sigma, \varepsilon) = -\eta X_2 - \Omega \text{Tanh}\left(\frac{\sigma}{\varepsilon}\right)$$

Where ε in this equation is a positive small constant. Figure 4.16 shows the $\text{sign}(\sigma)$ $\text{Sigm}(\sigma, \varepsilon)$ and $\text{Tanh}(\sigma, \varepsilon)$ for different values of ε respectively. As may be noted from Eq. 4.24, for these two smoother functions we can write:

$$\lim_{\varepsilon \rightarrow 0} \text{Sigm}(\sigma, \varepsilon) = \lim_{\varepsilon \rightarrow 0} \text{Tanh}(\sigma, \varepsilon) = \text{sign}(\sigma) \quad (4.25)$$

To select a value for ε there must be a compromise between control accuracy and any smoothing effect so that the value selected for ε must be a trade-off between retaining the appropriate accuracy and reducing the chatter from the control response.

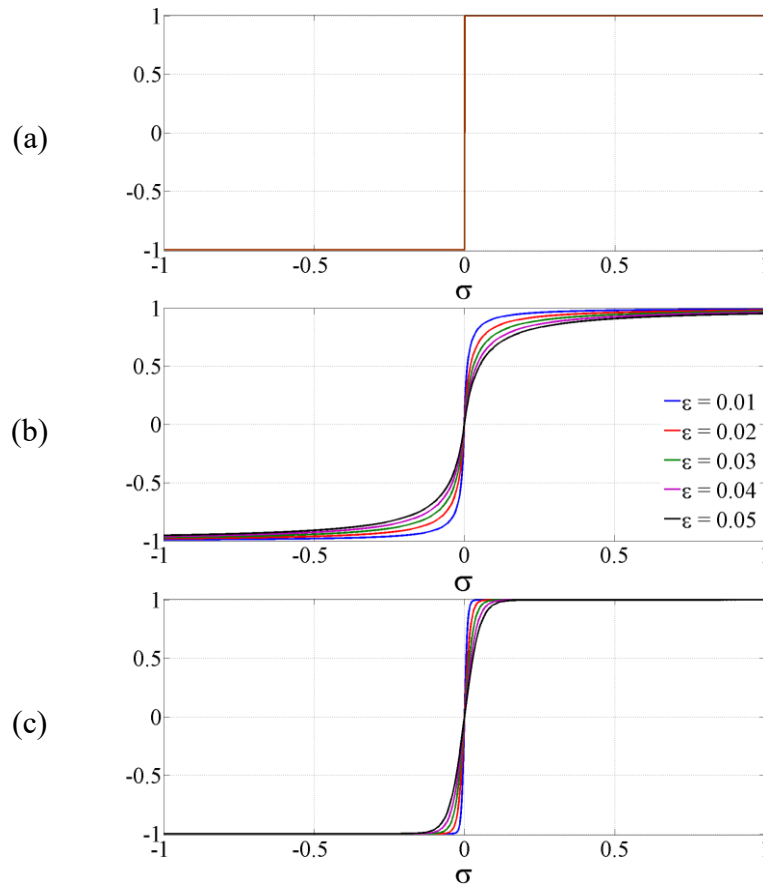


Figure 4.16: (a) $\text{sign}(\sigma)$ (b) $\text{Sigm}(\sigma, \varepsilon)$ and (c) $\text{Tanh}(\sigma, \varepsilon)$ for different values of ε .

Figure 4.17 represents a schematic model of the Quasi-FSM (sigmoid function) control architecture explained in this section, whilst Figure 4.18 shows the behaviour of the

controlled gripper in the presence of a sinusoidal external disturbance. As can be noted from Figure 4.18, unlike the FSMC, the sliding variable σ and the state variables X_1 and X_2 in quasi-SMC do not converge to zero in the presence of the bounded external force $F_{du}(X_1, X_2, t) = \cos(2t)$; instead, they converge to a bounded interval about zero. In other words, unlike the FSM, using Q-FSM will lead the system to reduced accuracy, which is the price the controller is paying to eliminate the chatter from the mechanical system (146). Recall that, technically, in order to achieve an asymptotic convergence of the state variables to the origin, the sliding variable must converge to zero in finite time.

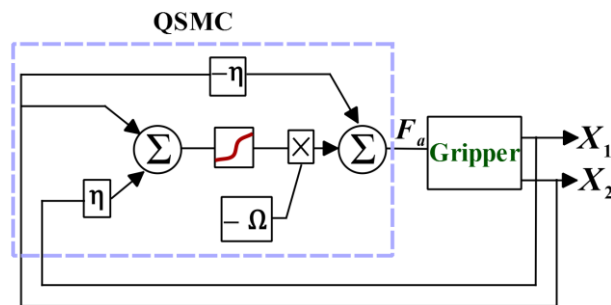


Figure 4.17: Schematic model of the gripper-QSMC system used in this test.

But, as explained above, the sliding variable never converges to zero, but rather to a bounded domain about zero instead. This bounded convergence provides a relatively similar performance for the Q-FSM, as compared to FSM. Figure 4.18 also depicts the effects of increasing the value of ε on the accuracy of the controller. The blue, red and green lines in this figure correspond to ε equal to 0.001, 0.01 and 0.1, respectively. As this figure shows, the accuracy of the controller with regards to the external disturbance decreased with increasing ε . On the other hand, although smaller ε led to higher accuracy with the control response, it also reduced the capability of the Q-FSMC in removing the chatter. Figure 4.18.c depicts the control force, F_a , for small ε . As you can see from Figure 4.18.c, there is still some chatter remaining in the system response due to the very small value of ε .

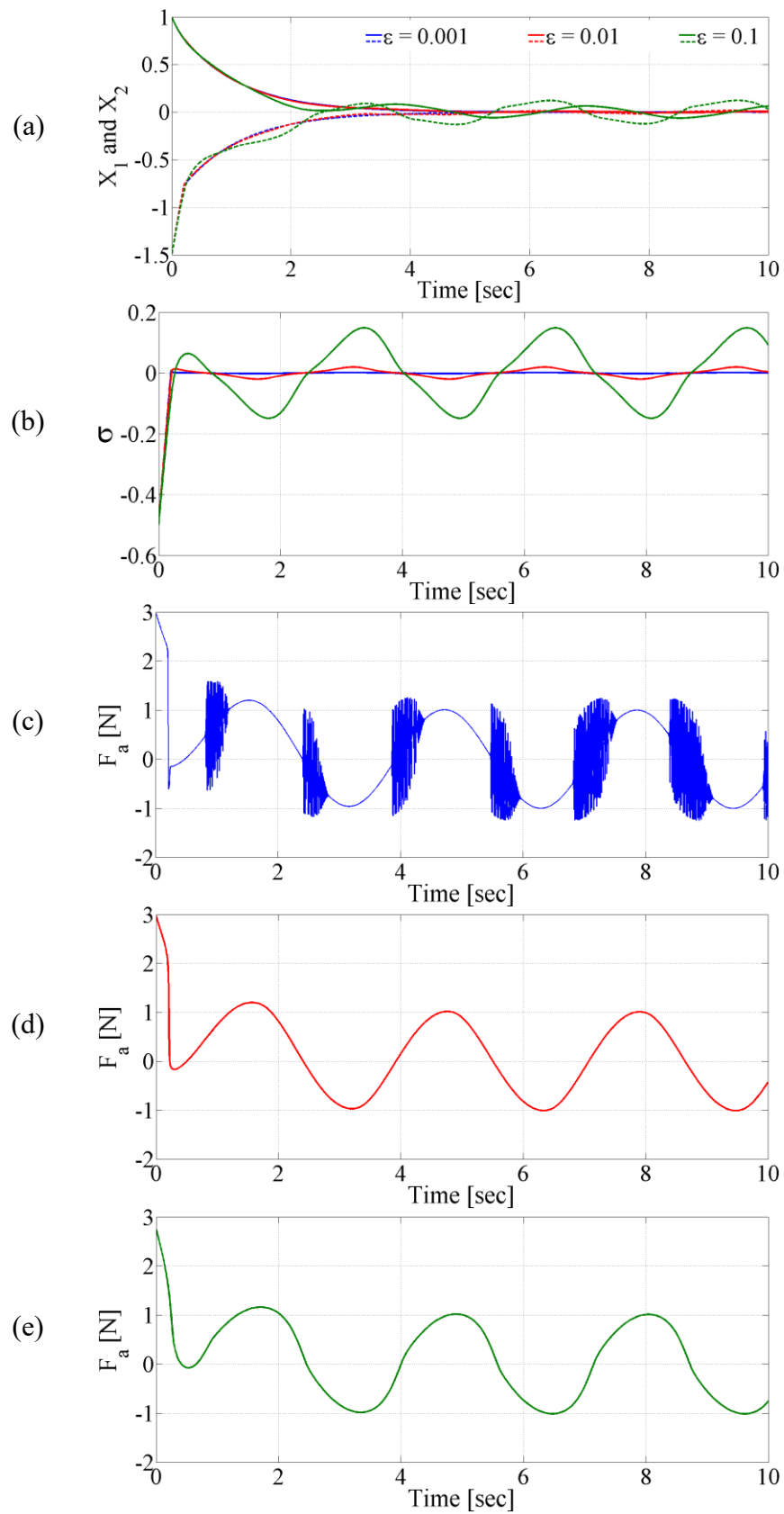


Figure 4.18: Results of the gripper system controlled by a Quasi-FSMC (sigmoid function) controller in the presence of a sinusoidal external disturbance.

Figure 4.19 depicts the reaction of the Q-FSMC for the test, as explained in Section 4.2. The X-axis in Figure 4.19.a, represents the reference for the state values of the fingers before the gripper is destabilised by the manipulator. As this figure shows, by choosing a suitable value for ε , the Q-FSMC could completely eliminate the chatter while overcoming the manipulator's disturbing force. From the figure it may be noted that the state variables in this controller do not converge to the zero but instead remain within a bounded interval in the vicinity of zero.

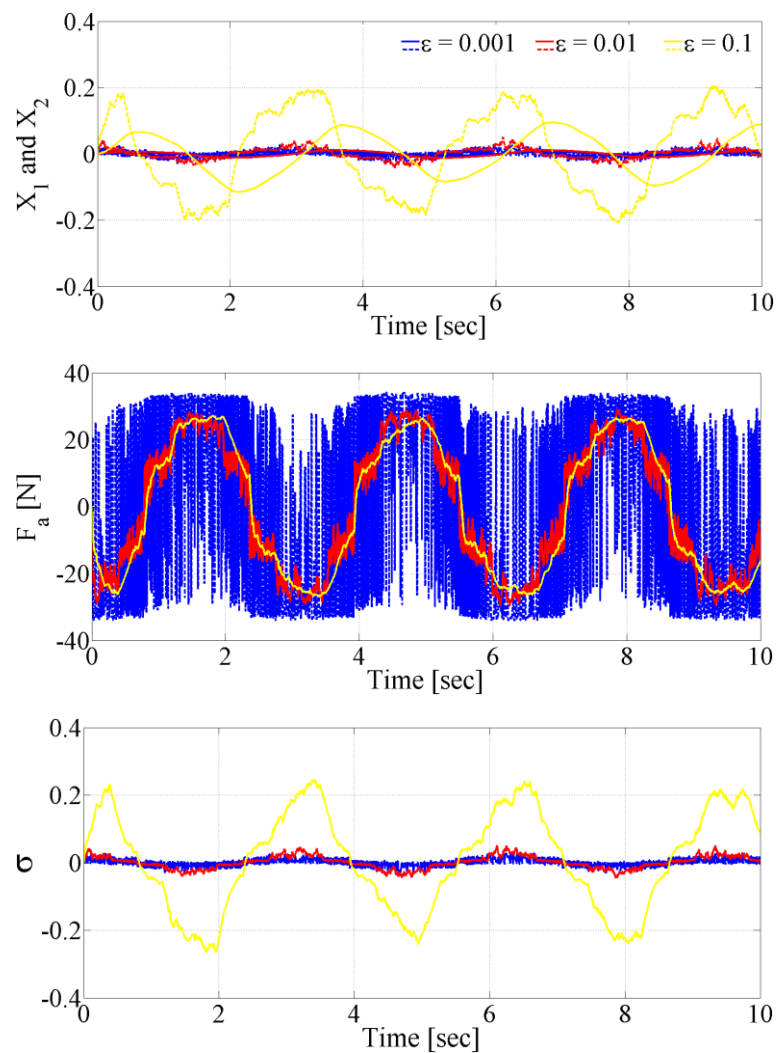


Figure 4.19: Results for the gripper system controlled by a Quasi-FSMC (sigmoid function) controller for the test, as explained in Section 4.3.

4.4.3 Error space-based sliding mode control

The sliding mode control laws that have been developed so far have been used to asymptotically converge the state variables to zero. Despite the robustness of these controllers towards overcoming unknown external disturbances, their range of applications is very narrow. As in most control problems, it should be found a control algorithm capable of driving the state variables along a desired trajectory which is not necessary zero. Recall the gripper system explained in Eq. 4.1-4.4.

$$\begin{cases} X_1 = x_f \\ \dot{X}_1 = X_2 \\ \dot{X}_2 = F_a + F_{du}(X_1, X_2, t) \end{cases} \quad (4.26)$$

where the state variables, X_1 and X_2 , denote the fingers' displacement and velocity along the X-axis, respectively; F_a and F_{du} are the fingers' control force and an external unknown disturbance force, respectively. This external force is assumed to be bounded as shown in Eq. 4.5. Let us assume that the output of the system is the position of the gripper's fingers, $y = X_1$. The SMC explained in the previous sections was able to asymmetrically drive the finger's position and velocity to zero in the presence of a bounded disturbance. Now let us to move forward and design a control law that makes the fingers (output of the system) follow a desired trajectory in the presence of the external bounded disturbance (that is, unlike the previous examples where the controller was pushing the finger to stay at its origin, here the fingers should always follow a desired trajectory. In the following sections, it will be shown how this control method can be used to control the grip force). In order to develop a control law for this task, as previously explained a sliding variable has to be defined. To do so, from Eq. 4.12, 4.13 and 4.14 we can write:

$$\sigma_{(e,\dot{e})}^t = \dot{e} + \eta e, \quad \eta > 0 \quad (4.27)$$

where $\sigma_{(e,\dot{e})}^t$ in this equation is the error-based sliding variable and e is the error of the finger in following the desired trajectory. For the error we can write:

$$e_t = y_d - y \quad (4.28)$$

where η is the convergence rate of the error, and is a positive constant. From Eq. 4.27 any control law that drives the sliding variable to zero in a finite time will asymptotically drive the error to zero. From Eq. 4.26 and 4.27, for the sliding variable we can write:

$$\dot{\sigma}_{(e,\dot{e})} = \ddot{y}_d + \eta\dot{y}_d - F_{du}(y, \dot{y}, t) - \eta\dot{y} - F_a \quad (4.29)$$

where for clarity Eq. 4.29 can be written as below:

$$\dot{\sigma}_{(e,\dot{e})} = \mathcal{F}(y, \dot{y}, t) - F_a \quad (4.30)$$

assuming that the disturbance term is bounded as below:

$$|\mathcal{F}(y, \dot{y}, t)| \leq \widehat{D} \quad (4.31)$$

From the Lyapunov function stability condition about the sliding surface Eq. 4.18, we can write:

$$\dot{\Lambda}_\sigma \leq -\xi\sqrt{\Lambda_\sigma(t)} \quad (4.32)$$

where this condition is equivalent to:

$$\sigma\dot{\sigma} \leq -\frac{\xi}{\sqrt{2}} |\sigma| \quad (4.33)$$

Condition Eq. 4.33 is called the sliding mode existence condition.

From Eq. 4.30 and 4.31 we can write:

$$\sigma\dot{\sigma} = \sigma(\mathcal{F}(y, \dot{y}, t) - F_a) \leq |\sigma|\widehat{D} - \sigma F_a \quad (4.34)$$

Now let us to choose the control law as below:

$$F_a = -\Omega \text{sign}(\sigma) \quad (4.35)$$

By substituting this control law into Eq. 4.34 and from Eq. 4.33, we have:

$$\sigma\dot{\sigma} \leq |\sigma|(\widehat{D} - \Omega) = -\frac{\xi}{\sqrt{2}} |\sigma| \quad (4.36)$$

And, finally, we can write:

$$\Omega = \widehat{D} + \frac{\xi}{\sqrt{2}} \quad (4.37)$$

Equation Eq. 4.35 and 4.37 is called the error space-based sliding mode control. Figure 4.20 represents a schematic model of this controller.

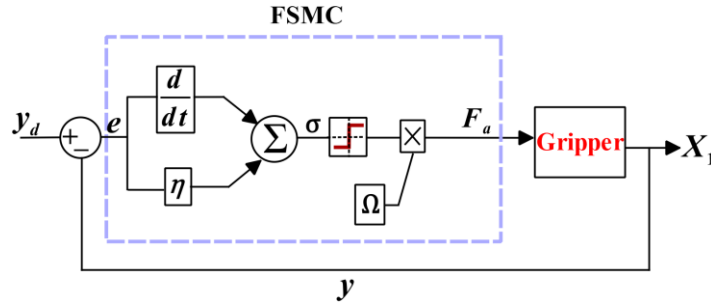


Figure 4.20: Schematic model of the gripper-SMC.

4.4.4 Impedance control for the VSGs

In this section will explain a force control method for the proposed variable stiffness grippers (VSG₁ and VSG₂) explained in Chapter 3. A schematic model of the grippers is illustrated in Figure 4. 21. For clarity, the mechanical connections for only one finger and the actuation system are shown in this figure. Two masses, M_F and M_R , depict the mass of the finger and rotor mass of the DC motor, respectively. The spring and damper, K_v and B_v , in this figure are used to model the variable stiffness mechanism. The two dampers, B and B_R , are used to model the friction between the fingers and palm and the friction between the rotor and stator of the DC motor (the friction of the shaft bearings and friction between the commutator and brushes), respectively. As shown in the figure, the rotor is driven by the motor magnetic field force, F_a , which is the control force. Let us assume that the fingers are subject to a bounded disturbance force F_{du} . As shown in Figure 4.21, the controlled output, y , is the distance between the rotor and the finger. The objective of this test is to control the output, y , to follow the desired trajectory in the presence of the external disturbance force. Please note that by controlling the length of y the grip force applied can be controlled as $F_{grip} = K_v y + B_v \dot{y}$.

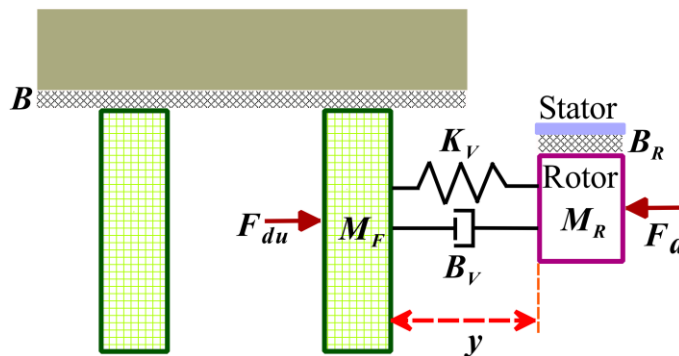


Figure 4.21: Schematic model of the gripper-SMC.

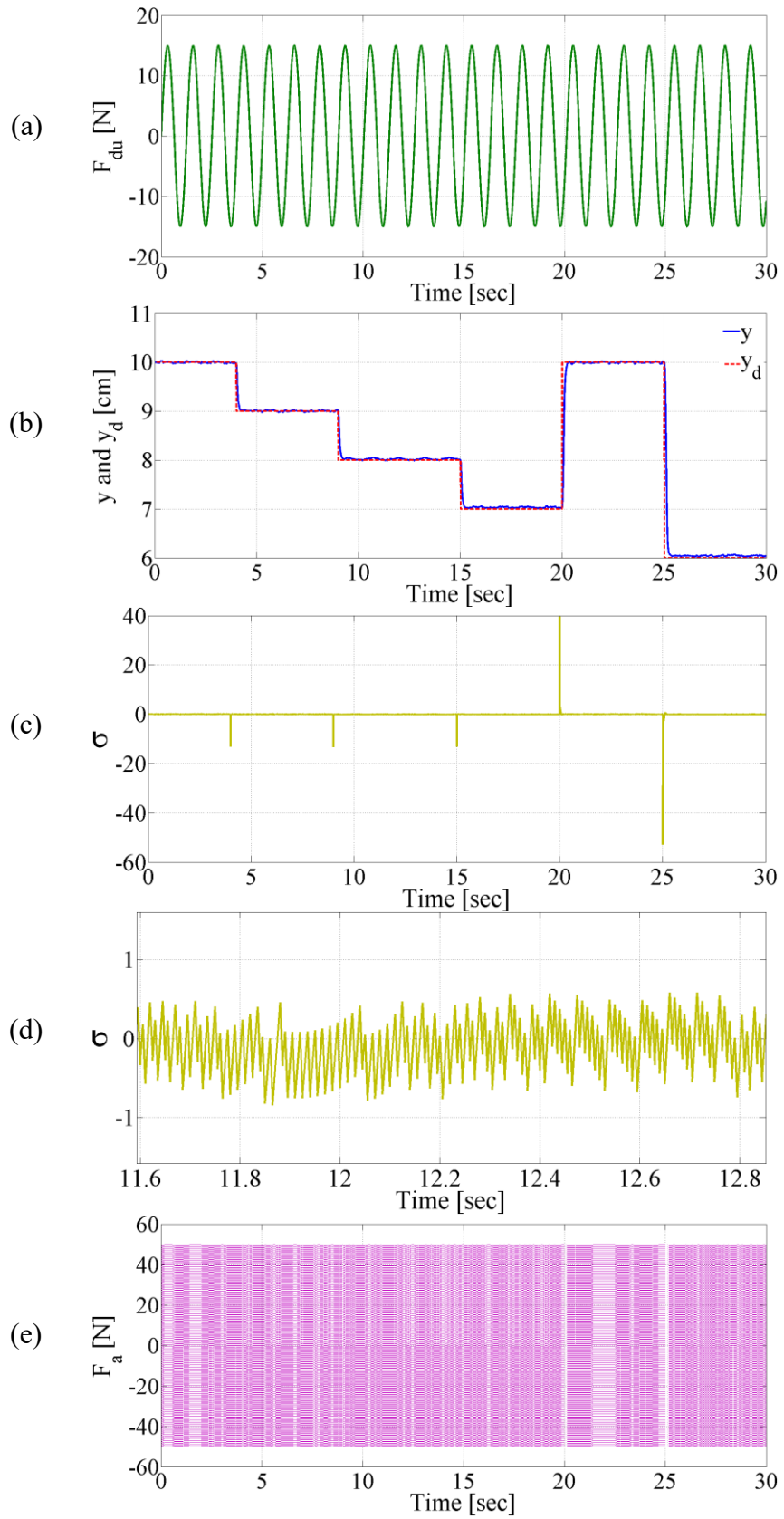


Figure 4.22: Reference trajectory tracking.

Figure 4.22 depicts the results of this test for the control law explained by equations Eq. 4.28 , 4.35 and 4.37. The control gain and the error convergence rate in this test were $\Omega = 50$ and $\eta = 20$. Figure 4.22.a depicts the external disturbance force $F_{du} = 10\sin(5t)$ applied to the fingers in this test, whilst Figure 4.22.b shows that the controller has always been robustly overcoming this disturbance and successfully controlling the distance between the finger and rotor to reach the desired distance, y_d . The error-based sliding variable $\sigma(e, \dot{e})$ for this test is shown by Figure 4.22.c and Figure 4.22.d, where the latter is a zoomed and cropped plot of Figure 4.22.c. The figure has been zoomed in to show the system chatter. As these two figures show, the sliding variable always remains at zero except at the moment when the desired distance, y_d , changes. At the time that y_d changes, the sliding variable jumps above or below zero for a very short period before the controller drove it to zero. Finally, and as expected, the high frequency chatter of the control force is shown in Figure 4.22.e.

4.5 Super-Twisting Sliding Mode Control (STSMC)

In Section 4.4.3, an error space-based sliding mode control is designed. From the results of this section, as per Figure 4.22 it is demonstrated that the controller was able to satisfactorily drive the errors to zero within a finite time. However, as Figure 4.22.e depicts, there is nevertheless a high frequency chatter in the control force F_a . As explained in Section 4.4.2, this high frequency zigzag shape behaviour makes this controller impractical for use in certain systems, such as a gripper with mechanical moving parts. In Section 4.5, it has been explained that this chatter can be eliminated from the response by replacing the discontinuous $\text{sign}(\sigma)$ function with a smoother function such as sigmoid or hyperbolic tangent function. This section will explain an alternative approach to the chatter-free sliding mode control, the so-called super twisting sliding mode control (STSMC). In order to eliminate the chatter, let us change the discontinuous ($\text{sign}(\sigma)$) function used in Eq. 4.35 with a continuous one, as below:

$$F_a = \hat{\Omega} \sqrt{|\sigma_{(e, \dot{e})}^t|} \text{sign}(\sigma_{(e, \dot{e})}^t) \quad (4.38)$$

where $\hat{\Omega}$ is a positive constant. In the absence of the disturbance term, from equations Eq. 4.30 and 4.38 we can write:

$$\dot{\sigma}_{(e,\dot{e})}^t = \frac{\partial \sigma_{(e,\dot{e})}^t}{\partial t} = -F_a = -\hat{\Omega} \sqrt{|\sigma_{(e,\dot{e})}^t|} \text{sign}(\sigma_{(e,\dot{e})}^t) \quad (4.39)$$

and from this equation we can write:

$$\sigma_{(e,\dot{e})}^t = \int_0^t \dot{\sigma}_{(e,\dot{e})}^t = \sqrt{|\sigma_{(e,\dot{e})}^t|} - \sqrt{|\sigma_{(e,\dot{e})}^0|} = -\frac{\hat{\Omega}}{2} t \quad (4.40)$$

Where from this equation the time to reach the sliding variable, T_s , can be calculated as below:

$$T_s = \frac{2}{\hat{\Omega}} \sqrt{|\sigma_{(e,\dot{e})}^0|} \quad (4.41)$$

From Eq. 4.41 we can conclude that in an isolated situation, $\mathcal{F}(y, \dot{y}, t) = 0$, the control law Eq. 4.38, can robustly drive the sliding variable $\sigma_{(e,\dot{e})}^t$ to zero in a finite time T_s , and as a result the error will converge to zero asymptotically as $\lim_{t \rightarrow \infty} e_t, \dot{e}_t = 0$. However, assuming the gripper to be an isolated system is entirely unrealistic as it is supposed to have continual interaction with environment. So, from Eq. 4.30, for the grasping task equation Eq. 4.39 should be rewritten as below:

$$\dot{\sigma}_{(e,\dot{e})}^t = \mathcal{F}(y, \dot{y}, t) - \hat{\Omega} \sqrt{|\sigma_{(e,\dot{e})}^t|} \text{sign}(\sigma_{(e,\dot{e})}^t) \quad (4.42)$$

Clearly in the presence of the disturbance term $\mathcal{F}(y, \dot{y}, t)$ shown in Eq. 4.42, the control law Eq. 4.38 should be modified in such a way as to compensate for this disturbance term. To do so, we can rewrite this control law as below:

$$\begin{aligned} F_a &= \tilde{\Omega} \sqrt{|\sigma_{(e,\dot{e})}^t|} \text{sign}(\sigma_{(e,\dot{e})}^t) + Y \\ \dot{Y} &= w \text{sign}(\sigma_{(e,\dot{e})}^t) \end{aligned} \quad (4.43)$$

with the following tuning role:

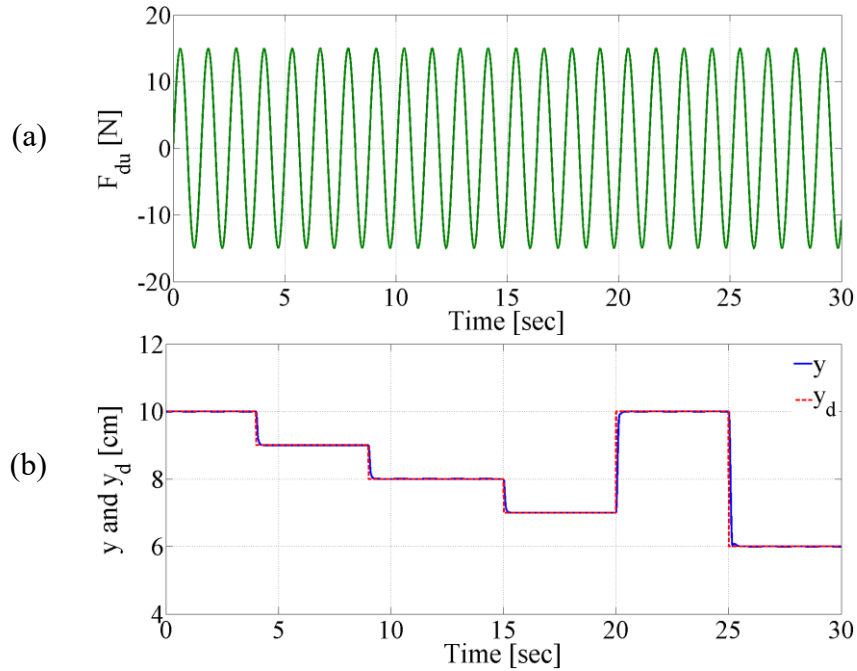
$$\tilde{\Omega} = \sqrt{U} \quad ; \quad w = 1.1U \quad (4.44)$$

where U is a positive constant. From Eq. 4.43 we can write:

$$\dot{\sigma}_{(e,\dot{e})}^t + \tilde{\Omega} \sqrt{|\sigma_{(e,\dot{e})}^t|} \text{sign}(\sigma_{(e,\dot{e})}^t) + Y = \mathcal{F}(y, \dot{y}, t) \quad (4.45)$$

$$\dot{Y} = w \text{sign}(\sigma_{(e,\dot{e})}^t)$$

From Eq. 4.45, it may be noted that in a finite time, \mathcal{T} will follow the disturbance term. The term \mathcal{T} is called the disturbance follower. Using a disturbance follower will make Eq. 4.45 become Eq. 4.39. Therefore, it can be concluded that the control laws Eq. 4.43 and 4.44 are capable of driving the sliding variable to zero in a finite time in the presence of the disturbance term. This control law is called a super-twisting sliding mode control (141, 145). The upcoming sections, will explain how this control can be used in the grippers in order to achieve a stable grasp. Figure 4.23 depicts the results of VSG₂ gripper system explained in Chapter 3 as controlled by STSMC with the following gains set: $U = 95$, $\tilde{\Omega} = 9.75$, $w = 104.5$. As shown in this figure, in the presence of a bounded disturbance $F_{du} = 15\sin(4t)$, this controller could satisfactorily drive the DC motor to reach the desired distance between the rotor and finger in order to control the distance between the rotor and the finger and consequently control the grip force.



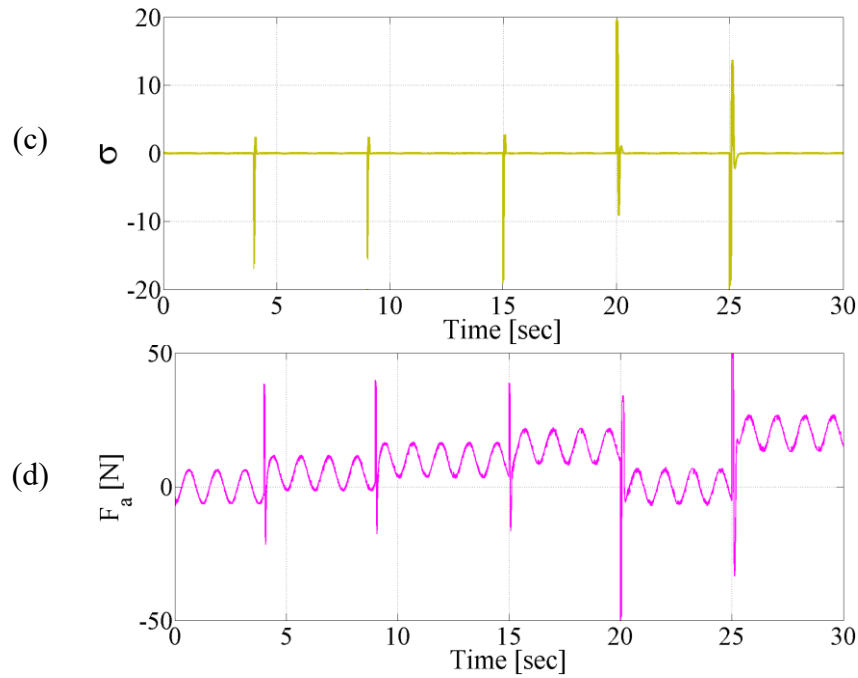


Figure 4.23: Reference trajectory tracking.

4.6 Robust Interaction Control for Robotic Grasping

In order to design a stable grasp control, the grasp model is required. This model must include the dynamical parameters of the gripper/hand, as well as the mechanical properties of the object and external environmental forces. Unfortunately, in reality, and in an optimistic scenario, only the gripper can be modelled; there is no solution to obtain the mechanical properties of the object before establishing a mechanical interaction with it. The external disturbance forces are also stochastic the majority of the time. In the previous sections of this chapter, the concept of the sliding mode control has been explained. The large number of examples provided in this chapter illustrated the robustness of this type of control in the presence of uncertainties and disturbances. Two novel grasp control designs are presented in this section. The controllers are based on the first-order and super-twisting sliding mode controls discussed above.

One of the main challenges of robotic grasping is to prevent slippage while manipulating objects. Slippage can cause the grasped object to fall and break; this is clearly undesirable, especially if the object being handled is expensive or contains a hazardous substance. A human can rather easily cope with slippage, and will counteract such by either regulating the mechanical impedance of their muscles or by changing the applied grip force on the object.

Various studies of the human hand's grasp perturbation (150) have shown that starting from a stable grasp, the shear force on the fingertips starts to increase until it reaches the upper bound of the static friction limit, at which point the object starts sliding. Since dynamic friction is generally lower than static friction, the minimum grip force required to keep the object in place suddenly increases. Therefore, to prevent slippage, the grip force is increased until the object stops sliding. Afterwards, the fingertips' normal force gently goes back towards the original safety zone, which is the range in which the normal force incurs no deformation on the held object.

As stated by Yoshida et al. (151), human mechanoreceptors' sensitivity is not limited to the magnitude of the applied shear forces but is also sensitive to the forces' rates of change, in a similar manner to the Proportional-Derivative (PD) feedback used in control theory. Countering slippage, and with a latency of 60-100 ms, a human's central nervous system receives sensory information, and then compensates for perturbations by updating the grip force, as shown in (152-154). Flanagan et al. (155) have shown that the dynamics of object grasping are learned by the central nervous system to prevent object slippage, thus building an internal model of that action.

A transient spike of neural activity while performing actions dealing with shear forces has been shown from averaged neural cuff readings on the median nerve (156). Birznieks et al. (157) demonstrated that the magnitude of this transient signal is relative to the changes in shear force, which in turn is relative to the texture change on a grasped object's contact surfaces; in-depth discussions of human grasping can be found in (150-159).

The adaptive grasp problem in robotic hands requires a grasp control scheme to exert optimal grip force in order to retain a static grasp with the held object. As influenced by the dexterity as well as adaptability of the human hand, there has been increased research in the field of adaptive grasp, in-hand manipulation and re-grasping which in chapter two some of the most recent work in this area was reviewed.

The main objective of the work presented in the following sections is the evaluation of robotic grasping performance using an HSMC with feedback on gripping force and slippage. More specifically, a Hybrid Super Twisting Sliding Mode Control (STSMC) is compared with a Hybrid First-Order Sliding Mode Control (HSMC). Force and slip feedback are provided by low-cost off-the-shelf components. The gripper used is characterised by two fingers: the force sensor is mounted on one finger and the slip sensor on the other. The rest of this chapter is organized as follows: Section 4.6.1 provides a brief explanation of the gripper design and

grasp platform used in this chapter. In Section 4.6.2 and 4.6.3, a simplified dynamic model of the gripper, force closure and grasped object and a mathematical model of the grasp are derived, respectively. Section 4.6.4 describes the two novel controllers (HSMC and HSTSMC) which were designed with the aim of preventing slippage. The performance of the two controllers were compared through an experiment which is presented in section 4.6.5 with related results. Finally, section 4.7 concludes the chapter.

4.6.1 Gripper Test Platform

Figure 4.24 shows one of the grippers designed and developed as part of this research as mounted on an ABB IRB 1200 with a 7 kg payload. The gripper consists of two fingers connected to the shaft of a servo motor by a thread with negligible stretch. The feedback is provided by a force and a slip sensor. The former is obtained from a 1D Force Sensing Resistor (FSR) mounted on the right fingertip, whereas the slip sensor is consists of a membrane potentiometer mounted on the left fingertip. The costs of the two sensors are, respectively, £9 and £6. The main technical specifications of the two sensors are reported in Table 4.1 and Table 4.2.

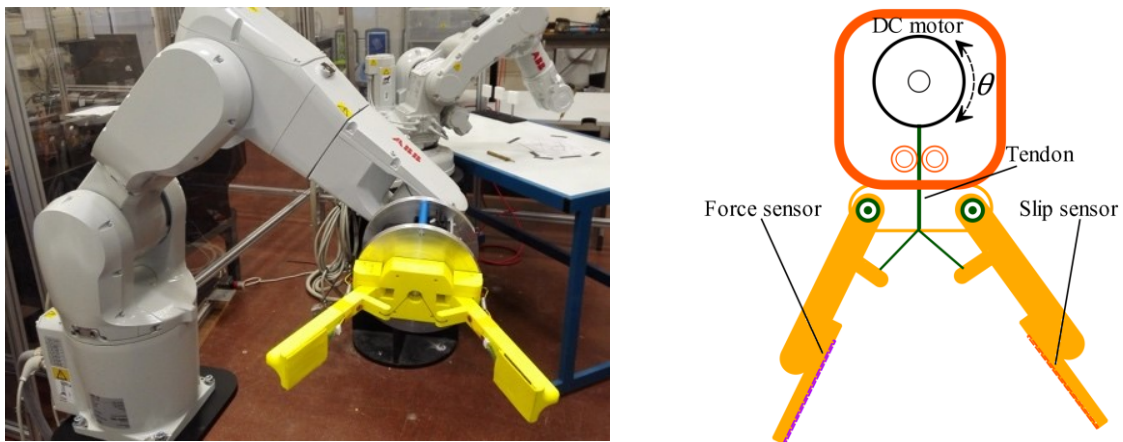


Figure 4.24: The two-finger gripper mounted on the ABB robot.

The sensors (shown in Figure 4.25) provide an analogue output as a variable resistance. There is a voltage divider circuit to transform the value of the resistance to a voltage value, which is readable by the control system. Both force and slip feedback are sent using serial communication to a Core i7, 16 Gb windows machine.

Resistance, standard	10 k Ω
Resistance tolerance	$\pm 4\%$
Resolution	Theoretical-infinite, dependent on contact wiper, thickness and construction

Sensor cover	Ethylene-vinyl acetate adhesive foam (0.45 mm thickness)
--------------	--

Table 4.1: Specification of the slip sensor used in the gripper.

Force sensitivity range	< 20 g to > 10 kg
Pressure sensitivity range	< 1.5 psi to > 150 psi
Force resolution	5 g
Sensitivity to noise/vibration	Not significantly affected

Table 4. 2: Specification of the force sensor used in the gripper.

The connection between the PC and servomotors is realised through a USB to TTL adapter. The overall rate of the control loop is about 1.5 ms.

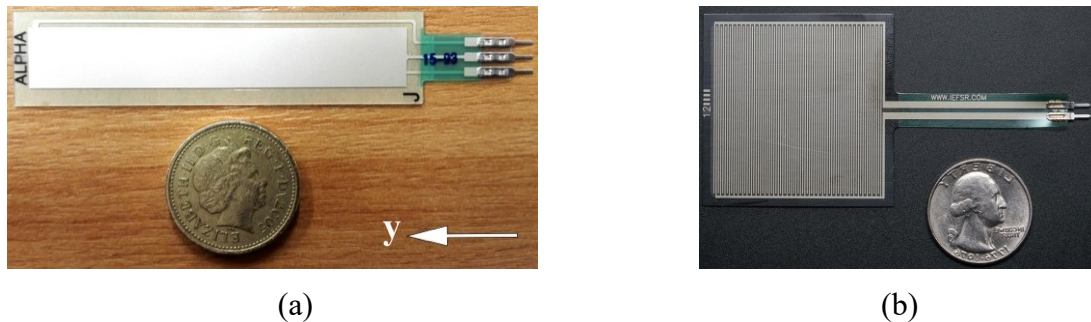


Figure 4.25: (a) Flexible absolute potentiometer (b) Force Sensing Resistor used for the tests.

The gripper prototype used a DC servomotor (whose mechanical and electrical details can be found in Table 3.1) as the actuation system, but any other less expensive servo motor with similar characteristics can be used without affecting system performance. To emulate objects of different mechanical stiffness, a variable stiffness object (VSO) was designed, wherein springs with different stiffness can be exchanged. As shown in Figure 4.26, the VSO consists of a spring in the centre which can be replaced to alter the stiffness of the object. The VSO also consists of a linear potentiometer to measure the deformation of the VSO. This data is then measured using an Arduino Mega, and sent via serial communication to the windows machine using a baud rate of 9600 bps. There are two compression springs with stiffness coefficients $K_1 = 0.6$ N/mm and $K_2 = 1.25$ N/mm. To apply a disturbance, a slide rod is connected to the base of the VSO which measures 30 cm. Three weights of 100, 200 and 300 grams are used that, as shown in Figure 4.27, are dropped from a distance of 20 cm onto the base of the slide rod to simulate different disturbance intensities.

Figure 4.26: VSO, Variable Stiffness Object used in this chapter (left).

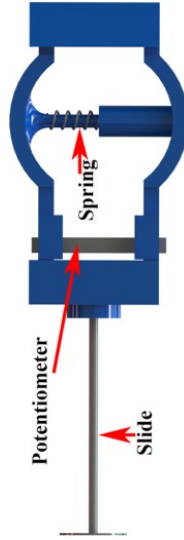


Figure 4.27: Dropping weights on the base of the slide to simulate disturbance (right).



4.6.2 Gripper Model

Eq. 4.46 depicts a second-order system that models the gripper and its DC motor.

$$I\ddot{\theta}_f + B\dot{\theta}_f + K\theta_f + F_{du} = k_T \left(\frac{V_s - V_{CEMF}}{R_{armature}} \right) = k_T I_m = T_m \quad (4.46)$$

where I is the equivalent moment of inertia for the fingers and the motor armature. The damping term B is used in order to model the frictional losses in the fingers' joint, rotor-stator ball bearings, and the friction between the tendon and pulley. K represents the system's stiffness and F_{du} is the disturbance-uncertainty term which includes the environmental disturbance force acting upon the fingers as well as un-modelled parameters of the system. k_T , V_s , V_{CEMF} and $R_{armature}$ are the DC motor's torque constant, operating voltage, counter-electromotive force (CEMF) and terminal resistance (ohms), respectively. I_m and T_m are the DC motor's operating current (the current through the motor's windings) and the motor's output torque, respectively. The counter-electromotive of the DC motor can be written:

$$V_{CEMF} = K_e \dot{\theta}_f \quad (4.47)$$

where K_e is counter-electromotive force constant of the motor. Using equation Eq. 4.47, Eq. 4.46 can be written as per below:

$$I\ddot{\theta}_f + \tilde{B}\dot{\theta}_f + K\theta_f + F_{du} = k_{TR}V_s \quad (4.48)$$

where

$$\tilde{B} = B + k_T \frac{V_{CEMF}}{R_{armature}} \quad (4.49)$$

$$k_{TR} = k_T / R_{armature}$$

From Eq. 4.49, the state space model of the system can be written as per below:

$$\begin{aligned} X_1 &= \theta_f \\ \dot{X}_1 &= X_2 = \dot{\theta}_f \\ \dot{X}_2 &= \tilde{k}_{TR} V_s - A_{I, \tilde{B}, K, D}(X_1, X_2) \end{aligned} \quad (4.50)$$

where X_1 and X_2 are the state variables which, as shown in this equation, are equal to the fingers' rotational angle and velocity ($\theta_f, \dot{\theta}_f$), respectively. $A_{I, \tilde{B}, K, D}$ in this equation is a function of state variables and contains the I, \tilde{B}, K and F_{du} terms, whereas \tilde{k}_{TR} is the quotient of I and K . It is worth noting that an accurate model of the grasp is hard to determine for several reasons. For instance, let us assume the grasp task in Figure 4.28. As shown in this figure, the gripper should grasp an object with the stiffness and damping of K_{OBJ} and B_{OBJ} . Before the fingers touch the object, the stiffness of the system (K in Eq. 4.48) has no effect on the grasp model and hence it is negligible. However, as soon as the fingers start touching the object, the stiffness of the system and the stiffness of the object should be considered in the grasp model. Unfortunately, there is no way to calculate the stiffness of the unknown objects to be grasped. This makes the grasp model inaccurate.

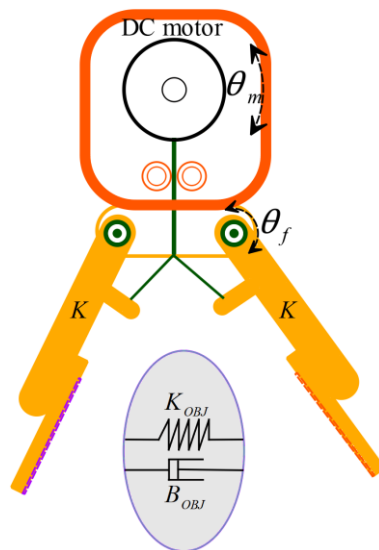


Figure 4.28. Uncertainty about the mechanical properties of the object to be grasped makes the grasp model inaccurate.

4.6.3 Grasp Model

In the previous section the gripper and its actuator were modelled. As explained above and in the previous sections, this model cannot be considered an accurate grasp model as it doesn't model the mechanical parameters of the grasped object. A simplified dynamic model of the gripper and grasped object will therefore be developed and presented in this section. Figure 4.29 shows a schematic model of the gripper with a grasped object. To model the grasping task, there are used two coordinate frames, a reference coordinate frame OXYZ at the palm of the gripper, and an object coordinate frame $O_oX_oY_oZ_o$ which is parallel to the reference coordinate frame, in such a way that O_o is fixed to the geometric centre of the object as depicted in Figure 4.29. The figure also shows the contact coordinate frames $O_cX_cY_cZ_c$ where O_c is connected to the contact point and is moving with the contact point c ; the X_c axis shows the direction of the grip force F_n . One of the contact coordinate frames is shown in the figure. Figure 4.30 shows an approximated model of the grasped object through a parallel spring-damper characterized by the stiffness constant K_{obj} , the damping coefficient B_{obj} and mass m . From Figure 4.29 and 4.30, a second-order equation can be derived as below:

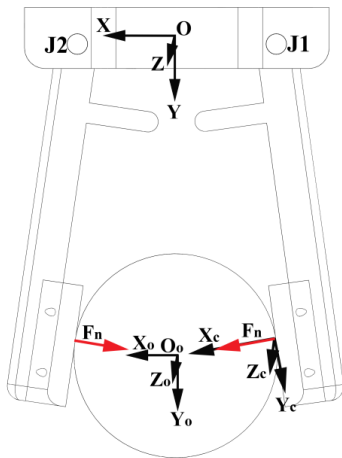


Figure 4. 29. Schematic model of the gripper with the held object and the coordinate frames used.

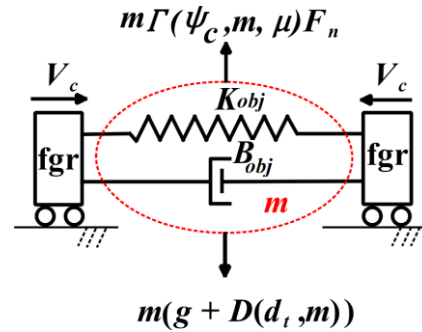


Figure 4.30. Schematic model of the object and fingers.

$$\ddot{y} = g - \Gamma(\psi_c, m, \mu)F_n + D(d_t, m) \quad (4.51)$$

where y indicates the displacement caused by the slippage of the object with respect to the reference frame in the direction of the Y-axis, \ddot{y} is its acceleration, m the weight of the object,

g the acceleration due to gravity and ψ_c is the yaw angle of $O_cX_cY_cZ_c$ around Z. F_n and μ are the normal force (grip force) along X_c and the coefficient of kinetic friction, respectively. Γ is a function of ψ_c , m and μ . The variable d_t represents the time-based disturbance acting upon the object in the form of an externally applied load. D is the disturbance term which is a function of d_t and m . Note that Eq. 4.51 is a simplified treatment of force closure and point contact with friction. Using \tilde{X}_1 and \tilde{X}_2 as the state values we can write:

$$\begin{aligned}\tilde{X}_1 &= y \\ \dot{\tilde{X}}_1 &= \tilde{X}_2 \\ \dot{\tilde{X}}_2 &= u\end{aligned}\tag{4.52}$$

$$u = g - \Gamma(\psi_c, m, \mu)F_n + D(d_t, m)$$

where u is the input to the system and is characterised by a controllable value F_n (the gripping force), a constant value g and a disturbance D . Let us assume that ψ_c does not change for small, linear slippages along Y. In this case, $\Gamma(\psi_c, m, \mu)$ can be considered a constant and represents a model uncertainty if no previous knowledge of the grasped object is available. The disturbance term D can be associated with a wide range of causes as might arise from the surrounding environment, and as such must also be dealt with as an uncertainty. F_n can be controlled through gripper motors. The kinematic model of the fingers can be written as follows:

$$\begin{aligned}V_c &= \Omega(\omega_f), & \omega_f &= \dot{\theta}_f \\ \dot{\theta}_f &= f(\omega_m), & \omega_m &= \dot{\theta}_m\end{aligned}\tag{4.53}$$

where V_c is the velocity of the contact point along the X_c axis and ω_f the angular velocity of the fingers around their joints J_1 and J_2 , which, in turn, is a function of the rotational velocity of the motor ω_m , as shown in Eq. 4.53. For simplicity, it is assumed that the object has isotropic and homogeneous density, stiffness and damping properties. It is also assumed that the deformation of the object, when grasped, is within the elastic range of the material to not cause any damage. Under these assumptions K_{obj} is constant, and from Figure 4.30 the relationship between the grip force and the velocity of the contact point is given by:

$$F_n = K_{obj} \int V_c dt + B_{obj} V_c \quad (4.54)$$

4.6.4 Control Design

This section starts by presenting an implementation of a hybrid first-order sliding mode cascade controller, with the aim of prevent slippage whilst simultaneously minimising any deformation of the grasped object. The results presented in (157, 158) show that friction plays a significant role in determining the grip force. Thus, having a rough estimation of the object's surface's friction coefficient, along with the object's weight and stiffness, can significantly reduce the chances of slippage and deformation while grasping an object. Consequently, the grip force must be modified according to the frictional properties of the object and/or its mechanical characteristics. In order to achieve the desired force, that stops the object from slipping while incurring minimum deformation, a hybrid first-order sliding mode controller (HFSMC) was designed as shown in Figure 4.31.

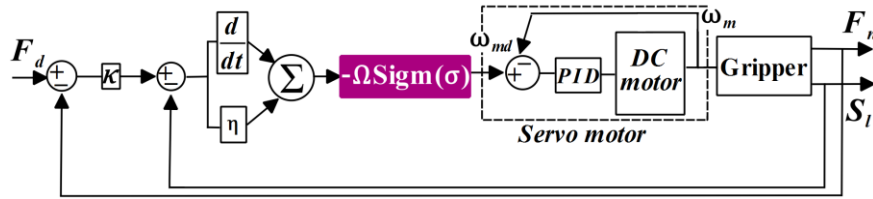


Figure 4.31. Block diagram of HFSMC.

The motor speed is driven by a desired value of the motor shaft speed ω_{md} which can be calculated by the control law explained below. The control of the servo motor used in the gripper accepts rpm values as control input.

To overcome slippage from an initial stable grasp with minimal deformation of the object, an error function is defined as:

$$e(F, S_l) = \kappa(F_n - F_d) - S_l \quad (4.55)$$

where e depends on applied force and slippage, and κ is a constant related to the stiffness of the grasped object. With respect to the reference frame, F_n is the actual (measured) grip force of the fingers, F_d the desired force of the fingers in order to stop any slippage, and S_l the slippage or displacement of the object, which is acquired through the slip sensor (the flexible absolute potentiometer shown in Figure 4.25.a). It is worth noting that from Eq. 4.55 the role

of the controller is to minimize the applied force and consequently minimize object deformation following a slippage event. If the value of F_d is known, by knowing the object's frictional constant, μ , and the object's weight, m , the controller will achieve a stable grasp while lifting the object. If F_d is not known, it should be set to a small positive initial value. In the instance where the gripper has to handle different objects, the value of F_d should correspond to the lightest object to be handled. In this scenario, the gripper will adjust F_n while lifting the heavier objects, preventing lighter objects from being crushed. From Eq. 4.12 we remember that:

$$\sigma_{(e,\dot{e})}^t = \left[\frac{d}{dt} + \eta \right]^\lambda e \quad (4.56)$$

$$\sigma_{(e,\dot{e})}^t = \dot{e} + \eta e, \quad \eta > 0 \quad (4.57)$$

where, as explained in previous sections, an arbitrary positive constant η guarantees the exponential decay of the error. Clearly, the next step is finding a control action that drives the sliding variable to the sliding surface in finite time, which means that the error states will converge to zero asymptotically. Eq. 4.58 shows the quasi-first-order control law with the sigmoid function used in the designed controller, where Ω as explained is a sufficiently large positive constant, and $\varepsilon = 0.001$.

$$\omega_{md} = -\Omega \text{Sig}(\sigma, \varepsilon) = -\Omega \frac{\sigma}{|\sigma| + \varepsilon} \quad \varepsilon > 0 \quad \varepsilon \approx 0 \quad (4.58)$$

Choosing a sufficiently large value for the controller variable, Ω , guarantees robustness of the controller. The resulting control diagram is shown in Figure 4.31. As discussed earlier, despite the robustness of this controller's design, there is an inherent disadvantage to first-order slide mode controllers. The outputs of the FSMCs have the tendency to oscillate, resulting in the chattering phenomenon (please see Figure 4.10 and 4.11). Although, as explained, chattering doesn't affect the outcome of the controller, it increases power consumption in the motor and by doing so reduces its lifetime. Alternatively, and as depicted in Figure 4.32, in order to solve the above-mentioned inconvenience of FSMCs, a hybrid super twisting second-order sliding mode controller (HSTSMC) was designed, which can completely eliminate this drawback without compromising the effectiveness of the controller. According to Eq. 4.43 and 4.44, in designing the control model we have:

$$\omega_{md} = \tilde{\Omega} \sqrt{|\sigma_{(e,\dot{e})}^t|} \text{sign}(\sigma_{(e,\dot{e})}^t) + \dot{Y} \quad (4.59)$$

$$\dot{Y} = w \text{sign}(\sigma_{(e,\dot{e})}^t)$$

$$\tilde{\Omega} = \sqrt{U} \quad ; \quad w = 1.1U$$

where U is a sufficiently large constant that has been tuned by trial and error.

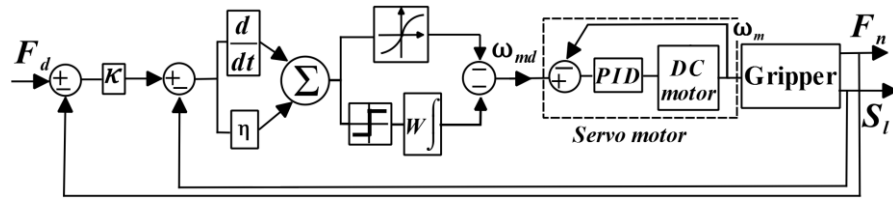


Figure 4.32: Block diagram of HSTSMC.

As explained before, thanks to the continuous algebraic function, the discontinuous oscillating output is eliminated. To quantify the performance of both control designs (HSMC and HSTSMC) more accurately, It has been carried out a four-stage experiment aimed at measuring force and slippage for the two values of stiffness, K_1 and K_2 , as defined in pervious section. The next section describes the experiment and discusses the related results.

4.6.5 Experimental Results and Discussion

Both controllers have been tested with the purpose of evaluating their performance in terms of preventing grasped objects from slipping. A four-stage experiment on both controllers was performed. The stages of the experiment were undertaken in the following order: first, at stage 1, the gripper grasped the VSO and the VSO was lifted by the gripper. In the remaining three stages, to test the controller robustness, three disturbances were applied by dropping three different weights on to the bottom of the rod hanging from the VSO. Figure 4.33 depicts these stages. The weights were dropped successively to resemble three external disturbances. Figure 4.34 shows the results of slippage, applied force and the sliding variable σ from three experiment trials on the FSMC, using the VSO with spring stiffness K_1 . The four stages of the experiment are shown in the slippage plot. As depicted in Figure 4.34.a, at stage 1, when the gripper starts lifting the VSO, the force applied by the gripper on the object starts rising due to

the slippage S_1 . After the slippage is cancelled out by the gripper's force, it proceed to stage 2 by applying the first weight, which causes slippage S_2 .

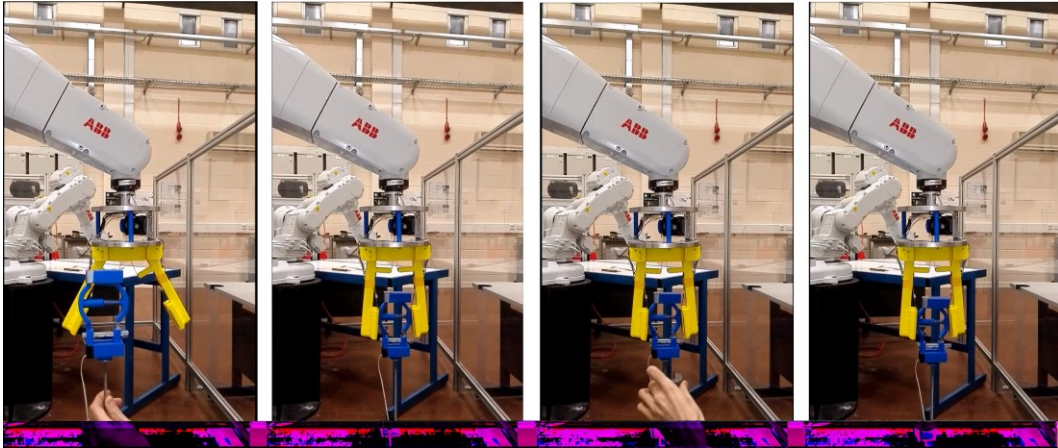


Figure 4.33: Four-stage experiment used to evaluate the performance of the designed controllers.

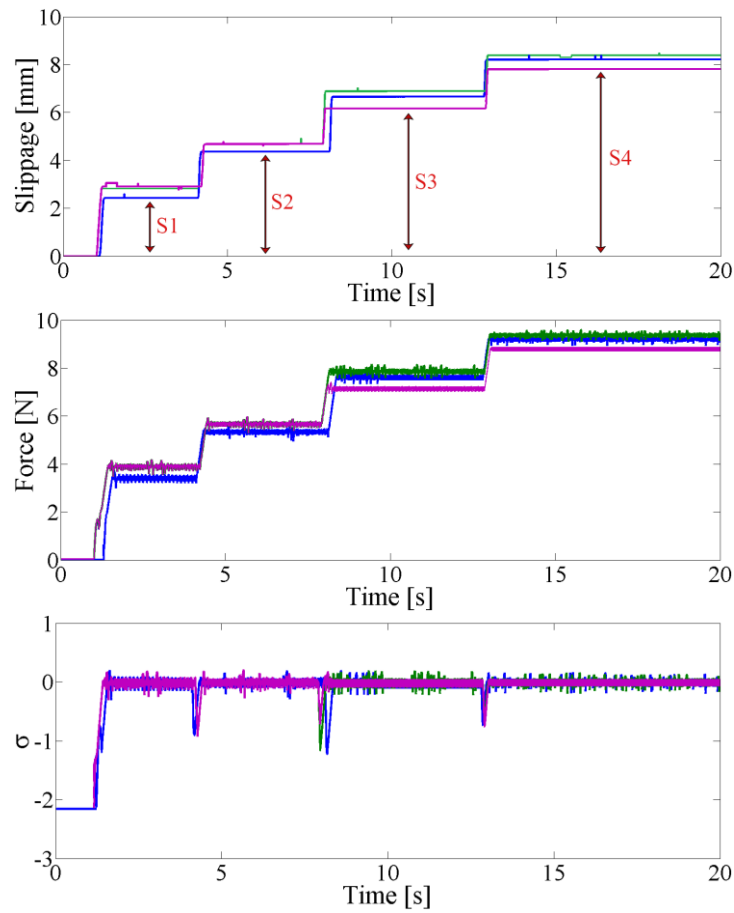


Figure 4.34: Experimental results of the FSMS for the VSO with stiffness K_f .

The controller reacts by increasing the applied force, counteracting the increased weight. The same procedure is repeated in phases 3 and 4 (with slippages S_3 and S_4 , respectively) by adding further weights. The reaction of the controller is similar to that observed in stage 2: the applied grasping force increases after applying the disturbances. From Figure 4.34 it is also possible to see how the value of σ continues fluctuating around zero after a short transient. The isolated, larger peaks in the ripple occur at the times when the weights (external disturbances) are applied, confirming the robustness of the designed FSMC in the presence of unexpected disturbances. In all cases (FSMC and STSMC with different stiffness) the experiment was repeated three times (blue, green and magenta lines in the diagrams) to test the repeatability and consistency of the results. Figure 4.35 shows the same variables as Figure 4.34 (slippage, gripping force and σ) using the VSO with spring stiffness K_2 . The increased amplitude of the ripple on F_n and σ as a result of the greater value of K_2 is quite evident in this case. The average amplitude of the ripple ranges from about 0.25 N for F_n and 0.15 for σ in the first case to about 0.5 N and 0.45, respectively, in the second case. Figures 4.36 and 4.37 show the experimental results using the STSMC for K_1 and K_2 respectively.

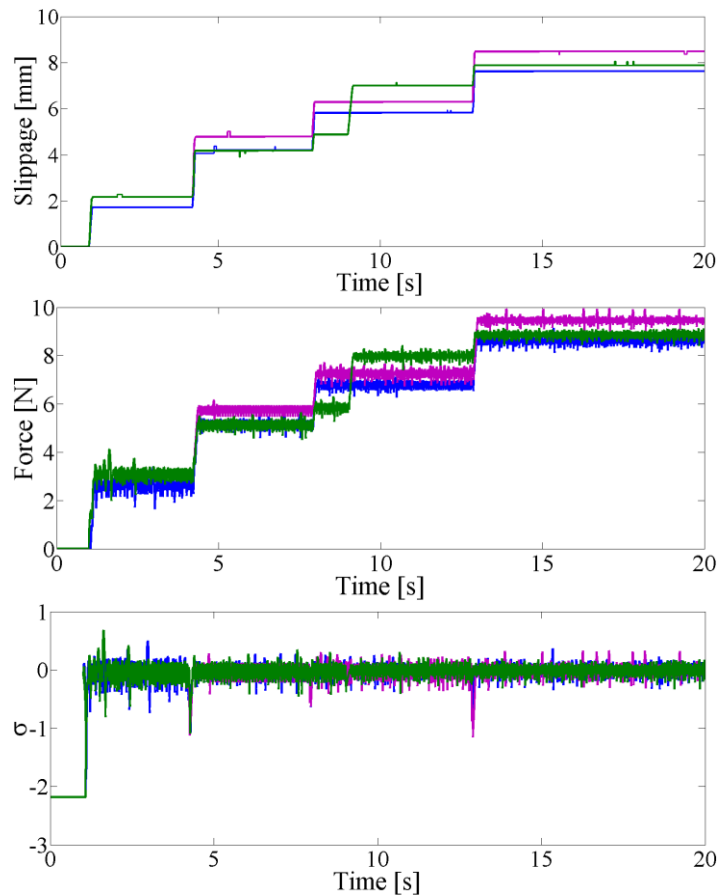


Figure 4.35: Experimental results for the HSMS with a VSO of stiffness K_2 .

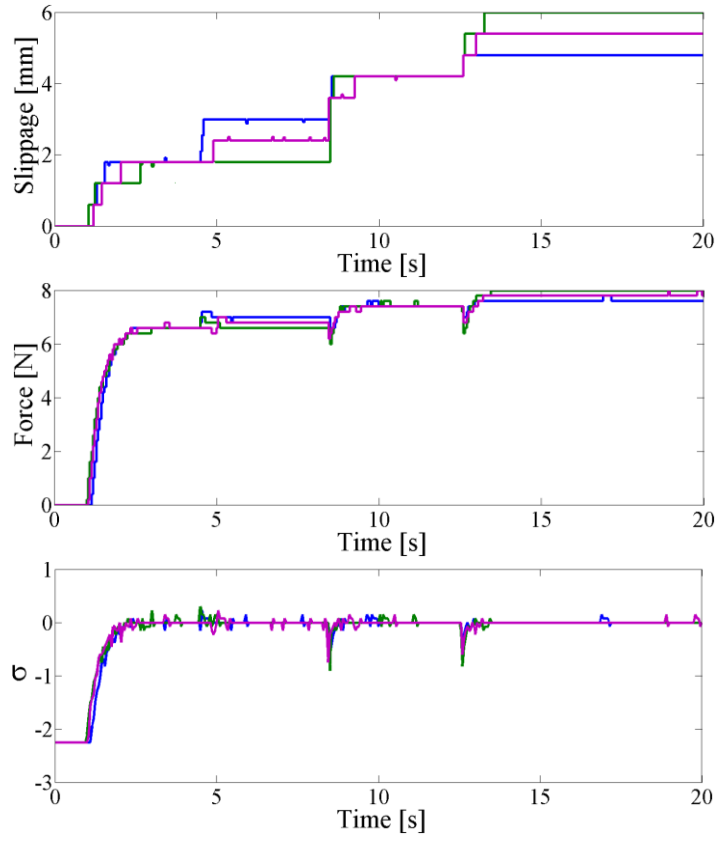


Figure 4.36: Experimental results for the HSTSMC with a VSO of stiffness K_1 .

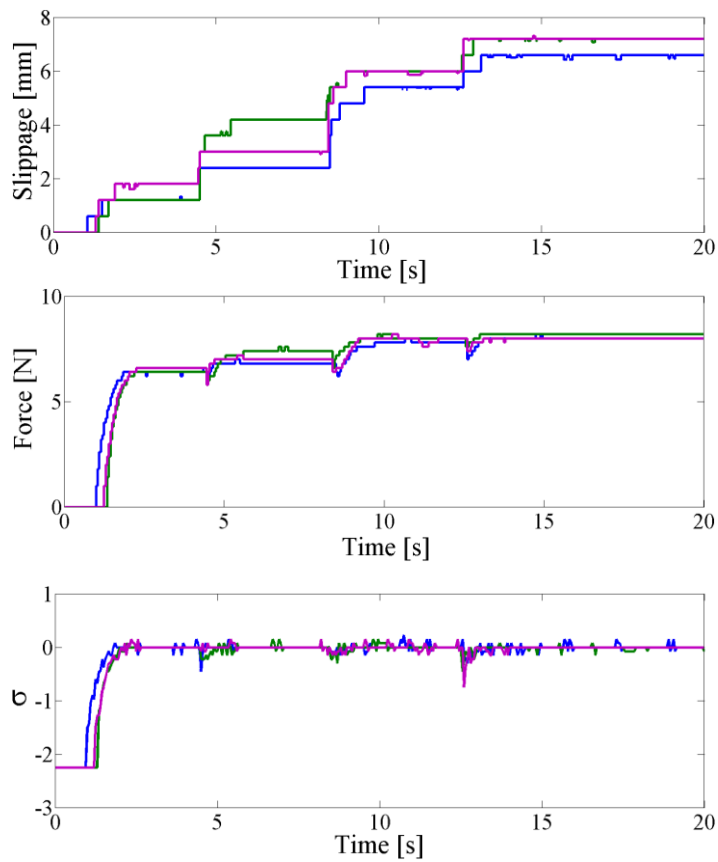


Figure 4.37: Experimental results for the HSTSMC with a VSO of stiffness K_2 .

The behaviour in terms of response times and compensation for disturbance is similar to the first controller. However, the ripple in the sliding variable σ around zero is much lower than with the FSMC and, as the diagrams show, independent of the stiffness of the grasped object. As a consequence, the chattering of the angular velocity of the motor ω_m is also reduced.

Figure 4.38 shows ω_m for both controllers in one of the experimental trials (yellow line for HSMC, purple line for HSTSMC). As discussed in Section 4.4, the chattering phenomenon is one of the major disadvantages of SMC. This figure illustrates how the proposed HSTSMC can satisfactorily eliminate the chatter from the controlled response.

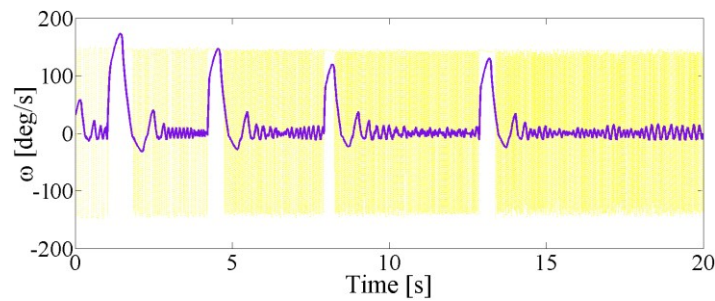


Figure 4.38: Angular velocity of the motor ω_m . The yellow line is the related velocity for HSMC whilst the purple line is the velocity for HSTSMC.

Finally, Figure 4.39 shows a practical test in which the robot, equipped with the gripper and controlled by the STSMC, grasped and lifted objects of different materials (tomato, green paper, bread, orange, coffee canister, tissue) and placed them in a target box. Because of the different weights and friction coefficients of the objects in this demo, there has been set a small initial value of F_d , so that softer and lighter objects were not squeezed during grasping. For heavier objects, the grip force was enhanced through the control action caused by the initial slippage. This is shown in Figure 4.40 in the case of an apple and an egg. In this figure, the blue, red and green lines show slippage, applied grip force and σ , respectively. The dashed lines correspond to the apple, while the solid lines correspond to the egg.

As shown in the figure, the grip force applied to the apple is, relatively, larger than the one applied to the egg, which comes from the fact that the apple is heavier and incurs more slippage. As far as σ is concerned, as expected, the values converge to zero just after lifting the objects. It is worth noting that the VSO and grasped objects were never crushed or dropped in any of the experiments.

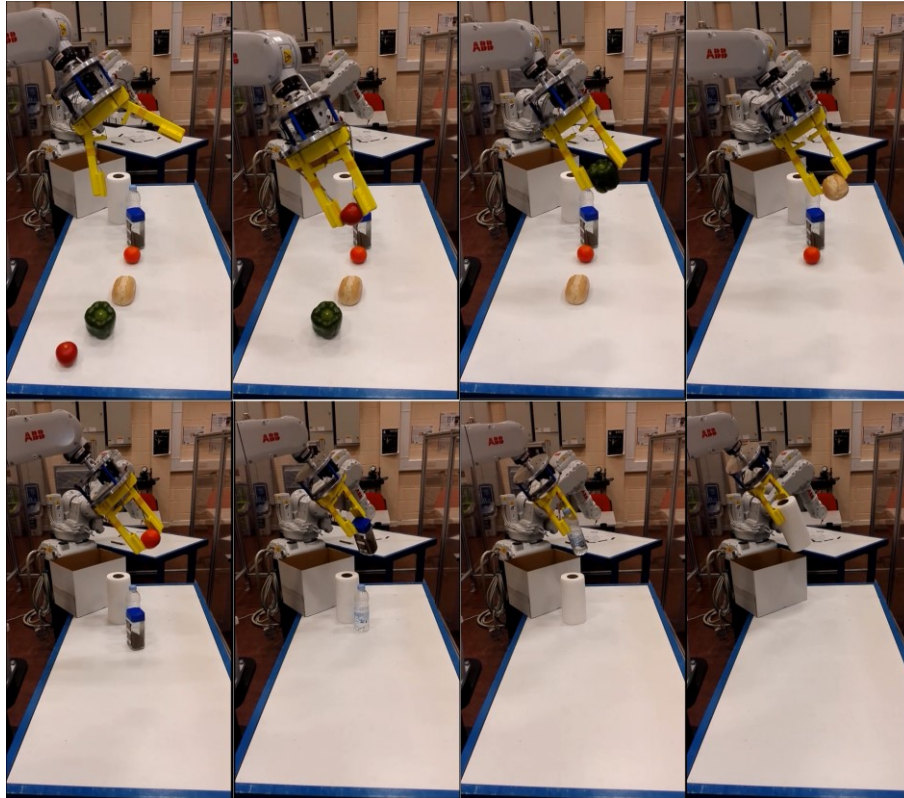


Figure 4.39: Using the gripper and HSTSMC design, the robot was able to grasp and lift objects of different mechanical properties.

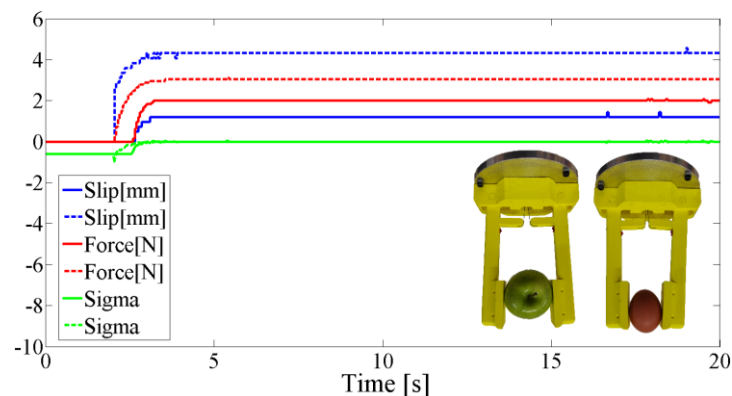


Figure 4.40: The gripper increases the applied force on the egg and apple to stop them from slipping after lifting. Dashed lines refer to the apple.

Thanks to the robustness of the controllers in preventing slippage they can be integrated with some higher-level control methods, such as the in-hand manipulation controllers presented in (160) in order to achieve more complex manipulation tasks than relatively straightforward pick and place. Indeed, including the proposed slip prevention controllers within in-hand/re-grasping algorithms allows them to outperform these algorithms by themselves, as the

controllers can stop the slippage of the object while the object is still moving between the fingers. Although such tasks (in-hand manipulation and re-grasping) are outside the scope of this work, to evaluate the possibility of this idea, a four finger,

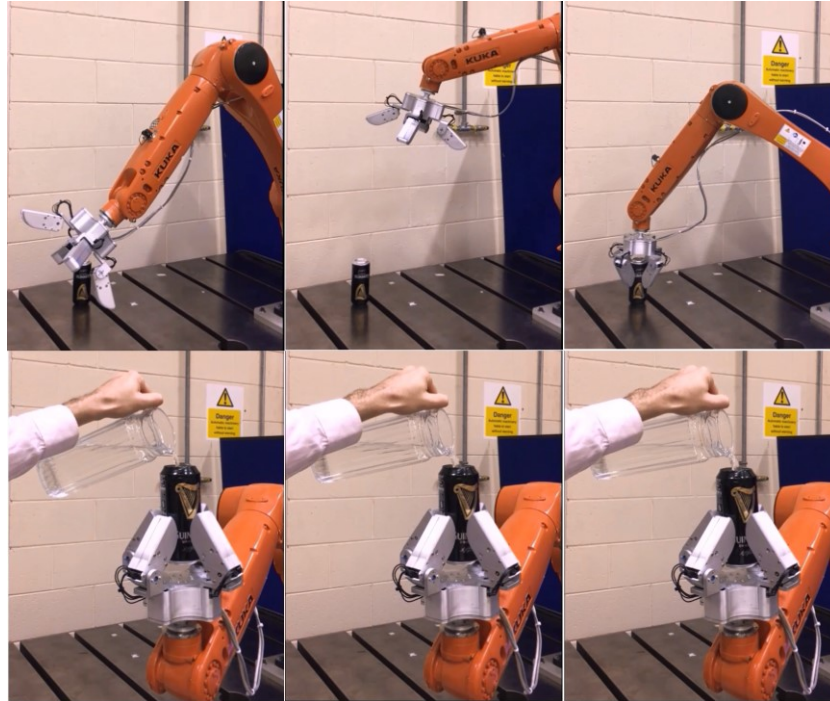


Figure 4.41: A four finger, 8 DOF hand designed and developed as part of this research in order to evaluate the possibility of integrating the slip prevention control designs with high-level, in-hand manipulation algorithms.

8 DOF direct drive robotic hand has been designed and fabricated, as shown in Figure 4.41. Similar to the tendon-driven gripper presented in the previous sections, in this hand, the applied grip force and slippage is measured using an FSR and membrane potentiometer both integrated into each finger.

Figures 4.41 and 4.42 depict two of the experiments performed by this hand (amongst many). As shown Figure 4.41, the gripper first grasps and lifts an empty beer can. Afterward, the can has been filled with water. Should the robot detects slippage at any time due to due to weight of the water, it starts to increase the grip force until the can stops slipping. Clearly, as explained before, the grip force required to stop the can from slipping is always kept to minimum using the proposed controller. Some primary experiments accomplished by this hand are currently showing great potential for the use of such a hand for the in-hand manipulation tasks that is considered as part of the future work.

Finally, Figure 4.42 depicts one of the experiments accomplished using this hand. As this figure shows, the robot grasps and lifts an egg and starts to move along a pre-programmed trajectory in an accelerating and decelerating manner. Using the proposed super twisting control, the egg never fell, or was crushed or smashed.

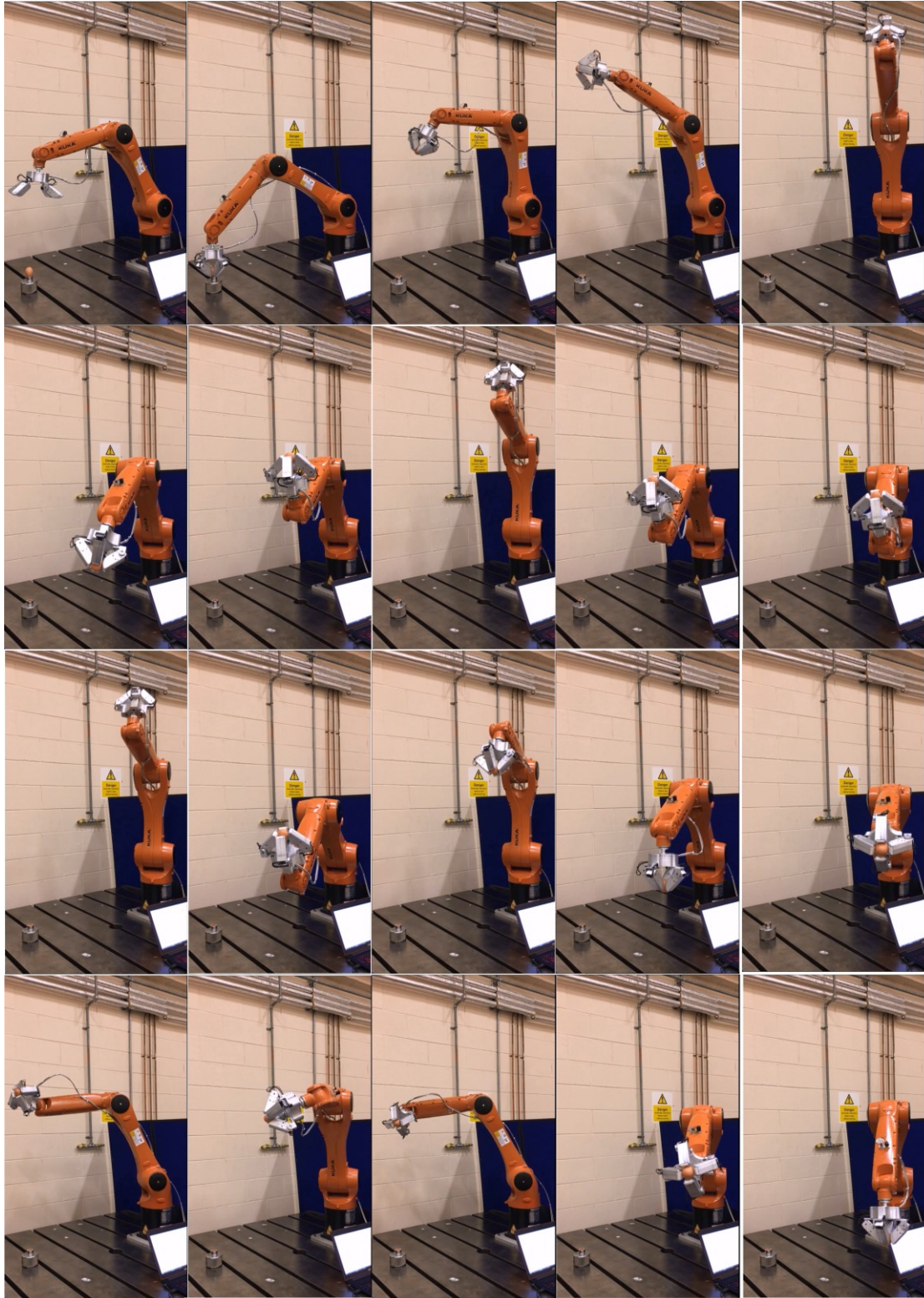


Figure 4.42: The robot grasps and lifts different objects (an egg in this figure) and starts to move along a pre-programmed trajectory in an accelerating and decelerating manner in order to test the robustness of the designed HSTSMC.

4.7 Discussion

In order to design a stable grasp control, there is an inevitably need for grasp model. This model must include the dynamical parameters of the gripper/hand, as well as the mechanical properties of the object and external environmental forces. Unfortunately, in reality, and in an optimistic scenario, only the gripper can be modelled; there is no solution by which to obtain the mechanical properties of the object before establishing a mechanical interaction with it. The external disturbance forces are also stochastic the majority of the time. In this chapter, the concept of the sliding mode control was explained. The large number of examples provided in this chapter illustrated the robustness of this type of control in the presence of uncertainties and disturbances

The main problem of grasping is that of the estimation of the exact gripping force to needs to be applied to prevent slippage without damaging or deforming the object. This chapter presented a new prototype of a two-finger gripper fitted with low-cost and yet reliable and durable force and slip sensors. To overcome external disturbances and gripper model uncertainties, two novel controllers, Hybrid SMC and STSMC, have been tested in this chapter. It is well known that the main drawback of an SMC is the chattering phenomenon. Furthermore, in the presented tests, it was found that the performance of the HSMC is also worsened by the fact that the amplitude of the chattering depends on the object's mechanical properties, more specifically its stiffness; the greater is the stiffness, the higher the chattering amplitude. The HSTSMC, while providing the same robustness to the model and external load uncertainties as the FOSMC, eliminates chattering and shows a consistent performance for any grasped object. For the sake of testing the gripper in more realistic situations, it was fitted it to an industrial robot and used to grasp a range of products of varying size and mass. The controller had no prior knowledge of the objects to be grasped. The tests performed demonstrated that the gripper has the ability to successfully grasp a wide range of objects, irrespective of shape, weight and stiffness. The gripper was able to achieve a stable grasp on each of the objects and complete the pick-and-place task without damaging them. A thorough statistical analysis of the gripping behaviour will be carried out in the future work to provide a more accurate evaluation of the reliability and performance of the grasping with different objects in presence of variable disturbances (i.e., velocity and acceleration of the robot arm).

Chapter 5

HIGH-PERFORMING ADAPTIVE GRASP CONTROL

5.1 Introduction

In the previous chapter, it has been shown how a sliding mode control can robustly overcome uncertainty/disturbance problems, which are intrinsic to the nature of robotic grasping tasks. Based on the information provided therein, this chapter will propose two novel adaptive grasp control methods for the purpose of controlling parallel jaw grippers with different payloads, which were designed and developed as part of this research.

In various industrial applications, there is a growing need for the use of robots for pick-and-place tasks in which different objects with completely different shapes, weights and stiffnesses must be handled with high accuracy during the execution of a given task. This is relevant in the food industry, for instance, as well as in nuclear decommissioning. Particularly in the case of the latter, where teleoperation is involved, these tasks can be more effectively accomplished (reducing time and cost) if no previous knowledge of the object to be grasped is assumed and a robust control, which is able to compensate for any uncertainties regarding the object model and unknown external disturbances, is implemented for the gripper. This is because there is either no real accurate information on the objects to be handled, or pre-programming the gripper for the range of different grasps required for a large number of known objects is impracticable and overly time-consuming.

This chapter addresses these challenges by evaluating the performance of a 8kg and a 45kg payload parallel jaw grippers (designed and developed as part of this research) which use the proposed novel Adaptive Super Twisting Sliding Mode Control (ASTSMC) and an Adaptive First-Order Sliding Mode Controller (ASMC) that are designed to prevent slippage whilst minimising any deformation of the grasped object. Similar to the tendon-driven gripper discussed in the previous chapter, both the controllers use force and slip feedback to counteract any slippage; slip detection is provided by off-the-shelf components. The performance of the designed ASTSMC is evaluated against the ASMC. Similar to the tendon-driven gripper, the two grippers in this chapter utilise the concept of the sliding mode control in their control system. However, the main difference between the controllers introduced in this chapter than to those in Chapter 4 is that the former control the grip force directly in order

to achieve a robust grasp, whereas the latter regulated the rotational velocity of the servomotors to control the grasping task. One of the main drawbacks of available force/torque sensors is that their resolution varies by changing the sensors' capacity. To eliminate the need for the use of a force sensor, unlike in the previous chapter, here a current-based estimation force feedback is used. This helps us to grasp a heavier payload.

The experimental results presented in this chapter show that when grasping unknown objects, the controllers are sufficiently robust to overcome external nonlinear disturbances and inaccuracies in the system model, preventing slippage and minimising any deformation of the objects. Furthermore, the ASMC and ASTSMC, as expected, eliminate the major drawback of the SMC (which is called the Chattering Phenomenon (CHPH)), whilst preserving the robustness of the control.

This chapter is organised as follows: Section 5.2 provides a brief explanation of the two grippers designed and fabricated as part of this work. In Section 5.3, the dynamical model of the grasp is modelled mathematically. Section 5.4 describes the architecture of the controllers and explains the control laws in detail. The performance of the controllers is evaluated through several experiments which are presented in Section 5.5 with their associated results. Finally, the conclusions and discussion can be found in Section 5.6.

5.2 Gripper Design Explanation

As you might recall from chapter four, there was an underactuated tendon-driven gripper as the test platform by which to assess the grasp control designs. Despite its simplicity, one of the main drawbacks of tendon-driven grippers is that the maximum payload they can lift is relatively restricted. In order to solve this problem, two direct-drive fully actuated grippers have been designed whose design description is given in the following sections.

5.2.1 The 8 kg payload gripper

Figure 5.1 shows the direct drive, fully actuated 8 kg payload parallel jaw gripper as mounted on a KUKA KR10 10 kg payload arm. The gripper in both the open and closed states is also shown in Figure 5.2. The gripper consists of two fingers connected to the shafts of two servo motors through joints J_1 and J_2 , as shown in Figure 5.3; a grasped object is also shown in this figure.

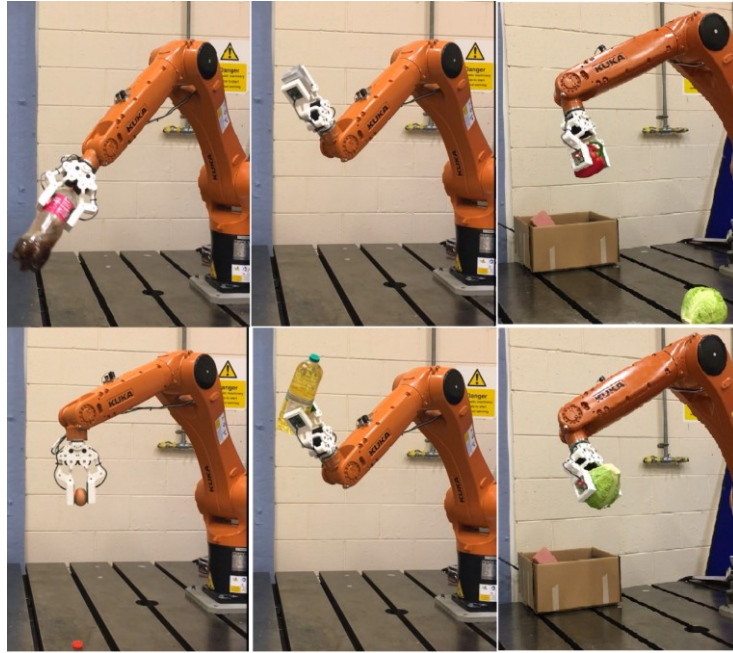


Figure 5.1: The 8 kg payload gripper mounted on the KUKA KR10 robot.

To model the grasping task, there are two coordinate frames used, as shown in this figure; a reference coordinate frame, $OXYZ$, at the palm of the gripper, and an object coordinate frame, $O_oX_oY_oZ_o$, which is parallel to the reference coordinate frame such that O_o is at the geometric centre of the object. According to the chosen reference frames, the gripping force, F_n , will always act along the X -axis of the reference coordinate frame. For clarity, only one gripping force is shown in this figure. As mentioned above, the gripper consisted of two servo motors. Each motor drives one finger of the gripper in an independent manner (i.e., there is no mechanical linkage between the two fingers).

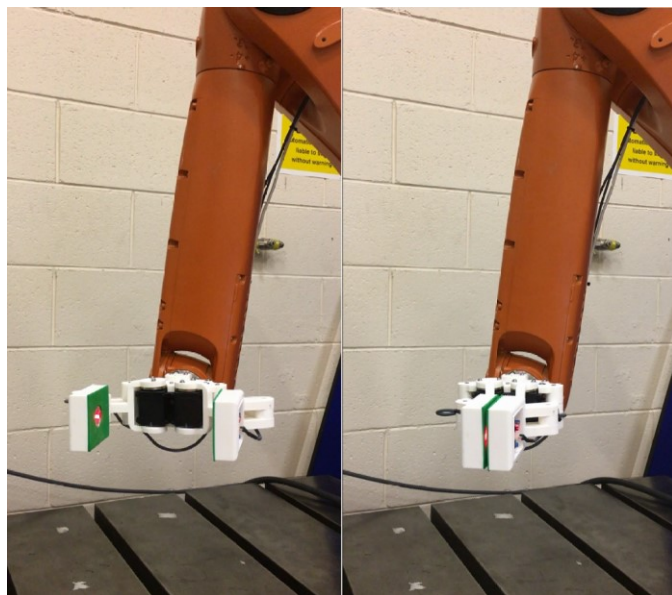


Figure 5.2: The 8 kg payload gripper in its open and closed states.

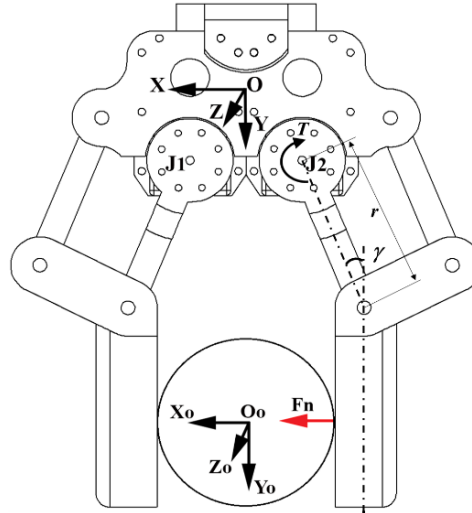


Figure 5. 3: Schematic model of the gripper illustrating a held object and the coordinate frames used.

Figure 5.3, the gripping force applied to the grasped object is linked to the motor torque by a nonlinear relationship as below:

$$F_n(t) = T(t) \cdot r \cdot \cos(\gamma(t)) \quad (5.1)$$

where γ , as shown in Figure 5.3, is the angle between the gripping link and the link connected to the motor, and $T(t)$ is the torque of the motor. For simplicity, friction is neglected in this equation. As highlighted in Eq. 5.1, F_n is a function of both T and γ .

As will be explained in the following sections, the controller's architecture relies on two feedback signals: force and slippage. The former is provided by the torque reading available as the output of the servomotors. The servo motors used in the 8 kg payload gripper provide a maximum torque of 7.3 Nm in stall conditions when supplied with a voltage of 14.8 V. The connection between the PC and servomotors is realised through a USB-TTL adapter. The motors' baud rate was set to 57,600 bps. For the slip sensor, two ADNS-9800 optical flow sensors have been used, assembled on each gripper finger. The most important features of the servo motors and slip sensors are reported in Table 5.1 and Table 5.2, respectively. The sensors were directly connected to the USB port (5 V power supply) of a PC Intel Core i7, 16 Gb RAM, Windows 10 OS.

DC Motor	Maxon
Gear Reduction Ratio	200 : 1
Max. stall torque	7.3 Nm (at 14.8 V, 5.2 A)
Control algorithm	PID
Resolution (rotation)	0.088°
No load speed	63 RPM at 12 V
Network	TTL/RS-232
Output torque values	0~1023
Resolution	0.088°
weight	135g
Dimension	40mm×61mm×41mm

Table 5.1: Specification of the servo motors

Dual power selection	3 V or 5 V
Frame rate	Up to 3000 fps
Resolution	Up to 400 cpi
Object detection distance	1 ÷ 5 mm
Motion detection	Up to 150 ips and acceleration up to 30 g

Table 5.2: Specifications of the slip (optical flow) sensor.

Specification	Value	
Dimension (mm)	54×54×126	
Weight	855 g	
Nominal Voltage	24 V	
No Load Speed	33.1 RPM	
No Load Current	1.08 A	
Continuous Operation	Speed	29.0 RPM
	Torque	44.7 Nm
	Current	9.505 A
Resolution Angle (Step/turn)	502,000	
Gear Ratio	502:1	
Backlash	3.5 arcmin	
Network Interface	RS-485	
Operating Temperature	5~55° C	
Output	200 W	

Table 5.3: Specification of the servo motors used in the 45kg payload gripper.

Specification	Value
Model	SRF05
Input voltage	5 V
Current	30 ~ 50 mA
Digital output	0 V low, 5 V High
Working temperature	-15°C to 70° C
Sensing angle	30° Cone
Ultrasonic frequency	40 kHz
Sensing range	2cm to 400 cm
Dimensions	43×20×17 mm

Table 5.4: Specification of the ultrasonic distance sensor used to measure the slippage of the object in the 45 kg payload gripper.

5.2.1.1 Optical flow-based slip sensor

As explained above, for the purposes of the slip measurement in the 8 kg payload gripper, the gripper utilises two optical flow sensors (Figure 5.4) mounted in the fingers. The main technical specifications of the slip sensors are reported in Table 5.2. An optical flow sensor is a device that provides feedback regarding the displacement using an embedded low-resolution high-speed video camera. The embedded camera is used to take low quality black and white images from the surface of the objects on which the sensor operates. The sensor consists of an LED which illuminates the object's surface. Afterwards, an embedded optical lens focuses reflected light from the surface in order to form an image (from the surface) on the sensor.

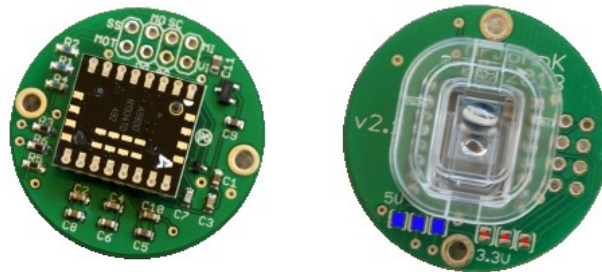


Figure 5.4: Optical flow sensor used in the 8 kg payload gripper in order to measure the grasped objects' slippages.

The right side of Figure 5.5 shows a photo taken by the optical flow sensor's internal camera. The sensor's camera continuously takes 3000 similar photos per second in order to track the displacements of the pixels.

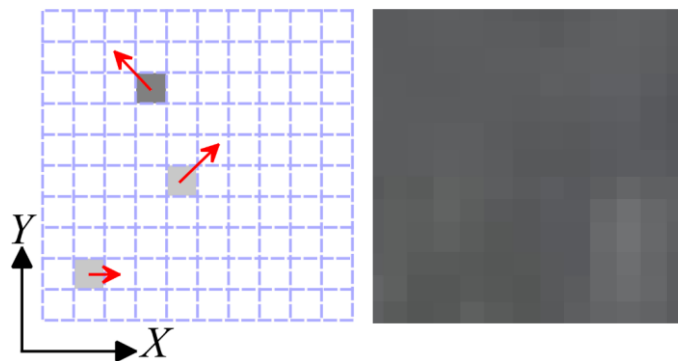


Figure 5.5: Operation explanation of the optical flow sensor.

In brief, the sensor provides (2D) feedback about the average movement of any distinct features in the pictures. It assigns a (+5) value to the features which move along the positive direction of the X and Y axes and a (-5) value for the features which move in negative direction along these axes. As an example, the output of the sensor for the movement shown on the left side of Figure 5.5 will be $x = 1.67$ and $y = 5$.

5.2.2 The 45 kg payload gripper

In order to test the performance of the designed controllers in grasping a range of industrial objects a 45 kg payload direct-drive parallel jaw gripper is designed and fabricated, as shown in Figure 5.6. As shown in this figure, the gripper is mounted on a KUKA KR180 with a 180 kg payload. Figure 5.7 depicts a CAD model and a side view of the gripper in both open and closed states. As shown in this figure, and similar to the 8 kg payload gripper, this gripper consists of two fingers and two servo motors, the latter being shown as M_1 and M_2 in this figure. To actuate a finger a servo motor is used. The gripper is made of aluminium and steel and it weighs 8.9 kg including the actuators. The motors utilise the RS-485 network communications protocol. A USB to RS-485 adapter is used to send commands from controller to the servo motors. A side view of the servo motors, as well as their most important features, are shown in Figure 5.8 and Table 5.3, respectively.

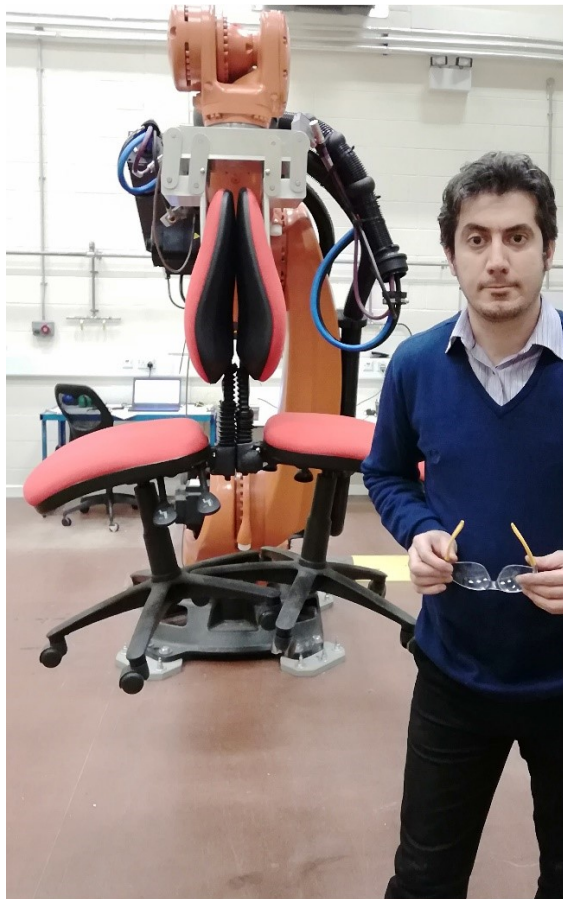


Figure 5.6: The 45 kg payload gripper mounted on a KUKA robot.

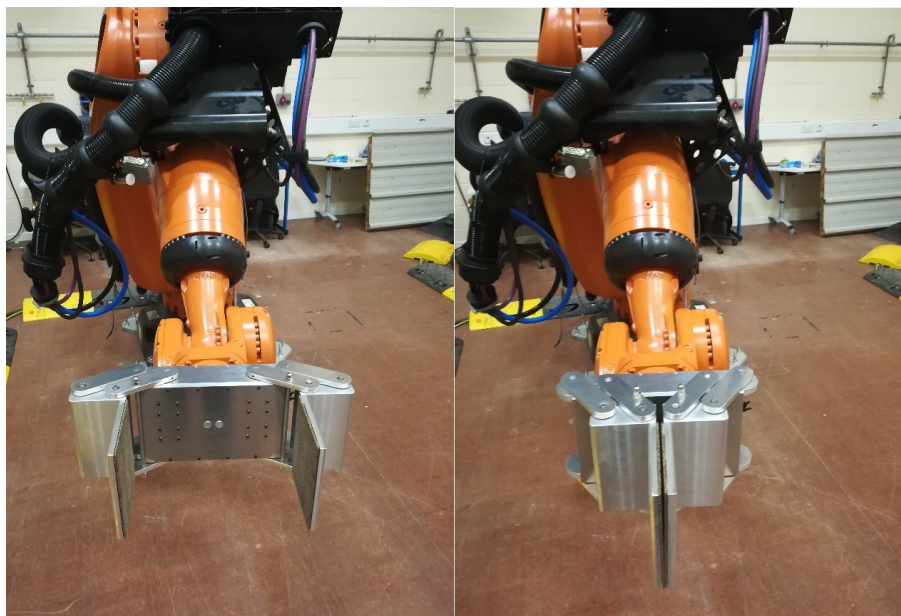
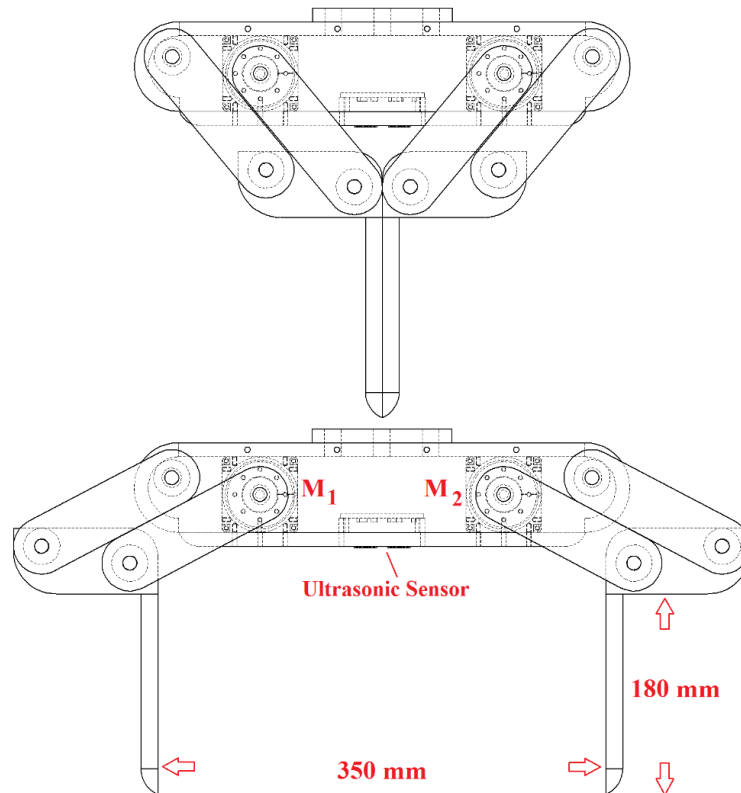


Figure 5.7: A Cad model and the side view of the 45 kg payload gripper in both open and closed states.



Figure 5.8: The servo motor used in the 45 kg payload gripper.

5.2.2.1 Ultrasonic-based slip sensor

As might be noticed from Figure 5.7, there is an ultrasonic distance sensor (shown in Figure 5.9) in the 45 kg payload gripper to measure the slippage of the grasped object. The main technical specifications of the sensor are reported in Table 5.4. Although the optical flow sensor could be used in the manner explained in the previous section for the 45 kg payload gripper, due to the larger fingertips in the 45 kg payload gripper, it needed more optical sensors to cover the entire surface of the fingertips, which would clearly increase the associated cost. Alternatively, in order to keep costs to a minimum, the gripper used an ultrasonic sensor as the slip sensor.



Figure 5.9: Front and back view of the ultrasonic sensor used in the 45 kg payload gripper.

An ultrasonic sensor is a device that provides feedback as to the object's distance by using sound waves in the ultrasound frequency range. Figure 5.10 depicts the frequency ranges of the ultrasound wave, whereas Figure 5.11 shows a schematic diagram of the ultrasonic sensors' operation.



Figure 5.10: Frequency range used for the ultrasonic sensors.

As shown in Figure 5.11, the sensor measures distance by emitting an ultrasound wave to the object and collecting the reflected wave. By measuring the elapsed time to transmit and receive a sound wave (the so-called Time-of-Flight (TOF)), and by knowing the speed of the sound wave, the distance between the sensor and object, d_{so} , can be accurately calculate as shown in Eq. 5.2.

$$d_{so} = \frac{\text{Speed of sound} \times \text{TOF}}{2} \quad (5.2)$$

In this equation, the speed of sound (in dry air) is equal to 340 m/s and the TOF includes the time taken for the sound wave to reach the object and return to the sensor. Simply, to find the distance between the sensor and object, as shown in Eq. 5.2, the round-trip time needs to be divide by two. In order to activate the SRF05 ultrasonic module, an Atmega 2560 8-bit microcontroller is used in the gripper. The sensor module has 5 pins, V_{CC} , Trig, Echo and Ground where the V_{CC} and Ground pins need to be connected to the 5 V and ground pins of the microcontroller. The Trigger and Echo pins are connected to the two Digital input/output pins of the microcontroller. In order to generate the ultrasonic wave, the Trigger pin of the sensor must receive a high value for 10 μ s. This, as shown in Figure 5.12, will generate an 8-cycle sonic burst. The generated sonic pulse then will travel at the speed of sound. The reflected pulse will be shown in the Echo pin as the time in microseconds.

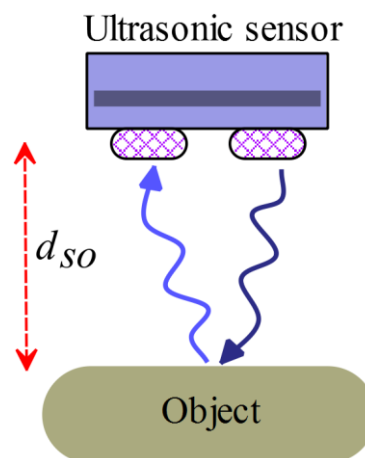


Figure 5.11: Diagram of the ultrasonic sensor operation.

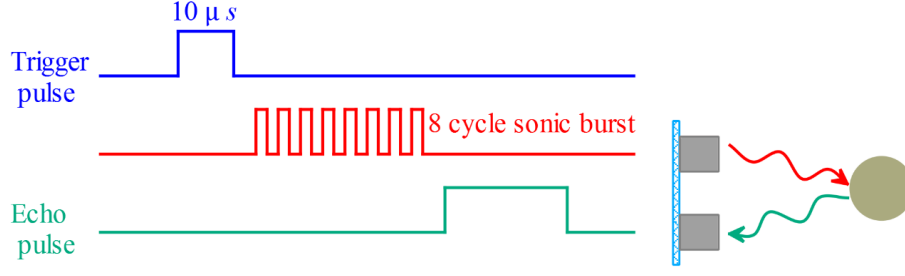


Figure 5.12: Diagram of the send and receive comments of the ultrasonic sensor.

As an example, assume that there is an object 25 cm away from the sensor; knowing the speed of the sound as being 340 m/s, which is equal to 0.034 cm/ μ s, the wave's travelling time will be 735 μ s. However, as explained before, the Echo pin will show the double value (in this case 1470) where from Eq. 5.2 it should be divided by 2.

5.3 Grasp Model

Eq. 5.3 depicts a second-order system that is used to model the gripper and its DC motors.

$$I\ddot{\theta}_f + B\dot{\theta}_f + K\theta_f + F_{du} = k_T \left(\frac{V_s - V_{CEMF}}{R_{armature}} \right) = k_T I_m = T_m \quad (5.3)$$

where I is the equivalent moment of inertia for the fingers and the motor armature. The damping term B is used in order to model the all frictional losses in the system. K represents the system's stiffness and F_{du} is the disturbance-uncertainty term which includes the stochastic environmental perturbation acting upon the fingers, as well as un-modelled parameters of the system. k_T , V_s , V_{CEMF} and $R_{armature}$ are the DC motor's torque constant, operating voltage, counter-electromotive force (CEMF) and terminal resistance (ohms), respectively. I_m and T_m are the DC motor's operating current (the current through the motor's windings) and the motor's output torque, respectively. From chapter four, Eq. 5.3 can be rewritten as per below:

$$I\ddot{\theta}_f + \tilde{B}\dot{\theta}_f + K\theta_f + F_{du} = k_{TR}V_s \quad (5.4)$$

where

$$\tilde{B} = B + k_T \frac{V_{CEMF}}{R_{armature}} \quad (5.5)$$

$$k_{TR} = k_T / R_{armature}$$

From Eq. 5.4, the state space model of the system can be written as per below:

$$X_1 = \theta_f$$

$$\dot{X}_1 = X_2 = \dot{\theta}_f \quad (5.6)$$

$$\dot{X}_2 = \tilde{k}_{TR} V_s - A_{I,\tilde{B},K,D}(X_1, X_2)$$

where X_1 and X_2 are the state variables which, as shown in this equation, are equal to the fingers' rotational angle and velocity ($\theta_f, \dot{\theta}_f$), respectively. $A_{I,\tilde{B},K,D}$ in this equation is a function of state variables and contains the I , B , K and F_{du} terms, whereas \tilde{k}_{TR} is the quotient of I and K . Figure 5.13 shows a position, velocity and force feedback control with an anti-windup layout used to control the fingers' position, velocity and grip force. In this figure, G_p , K_p , K_I , and K_{aw} are the proportional gain for the position control, the proportional gain for the velocity control, the integral gain for the velocity control and anti-windup gain, respectively. The feedback gain K_β is a conversion constant of the shaft's position and angular velocity.

To evaluate the response of the gripper to the step force inputs appropriate tests have been performed, the results of which are shown in Figure 5.14. In these tests, a chain of step functions with increasing amplitudes 5, 10, 15, 20, 25, 30, 35, 40 N has been sent as the desired force input function of the gripper. The servo motors have been actuated with these reference force inputs and with an object placed between the fingers. The objects used in this test were a foam block, a piece of wood and a RSJ steel beam. The green dashed lines in the figure depict the explained desired input force function whereas the solid blue lines are the measured grip force applied to the foam, wood and RSJ steel beam, respectively. From this figure, it may be noted that the force controller failed to reach the desired force in most of the steps and there are some steady-state errors in most of the times. Apart from the steady-state errors, there are also some overshoots in the response of the controller for the wood and steel beam, where these overshoots increased by increasing the amplitudes of the steps. The maximum overshoot took place for the input with the maximum amplitude of 40 N.

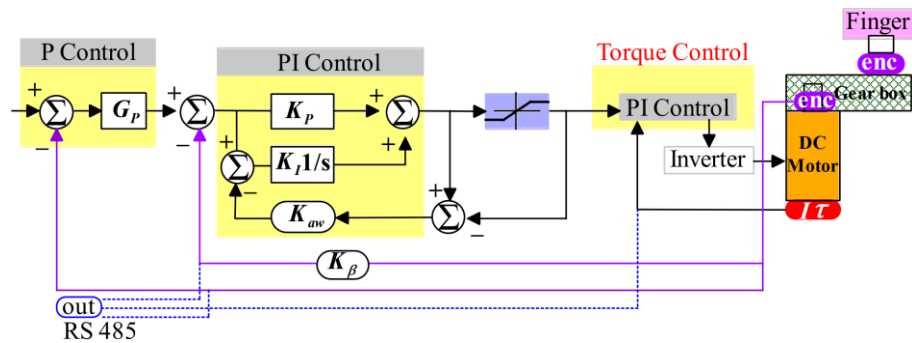


Figure 5.13: Position, velocity and force feedback control with an anti-windup layout.

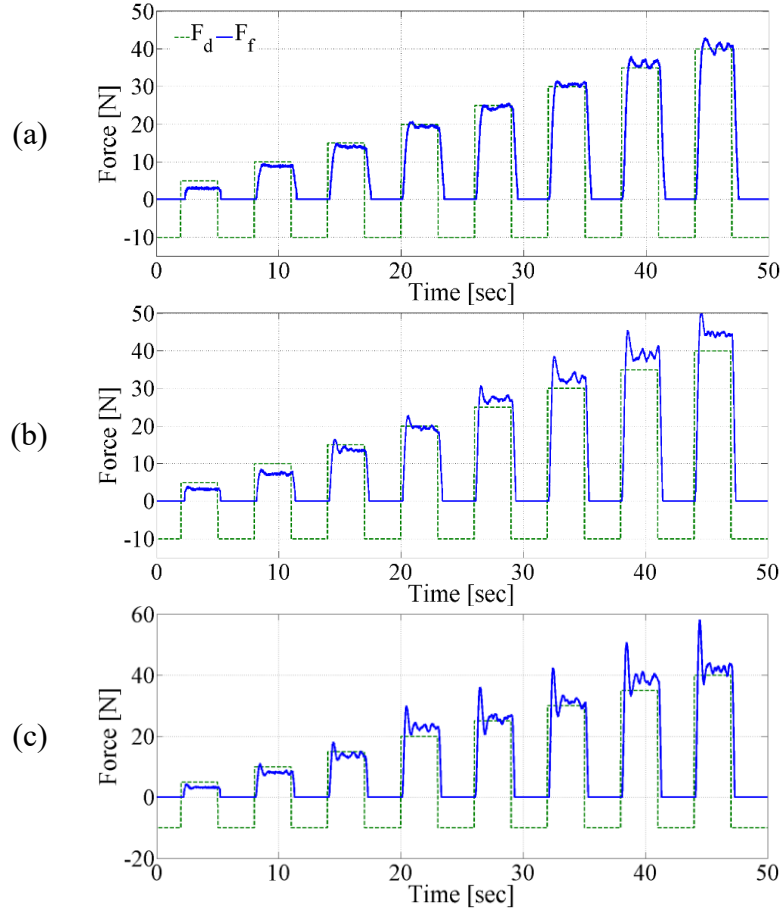


Figure 5. 14: Grasp response of the gripper controlled by the hybrid position-force controller to the step inputs with increasing amplitude (dashed green curve).

Recalling Section 4.3, it is worth noting that an accurate model of the grasp is hard to determine for several reasons. For instance, consider the grasp task shown in Figure 5.15. As shown in this figure, the gripper should grasp an object with the stiffness and damping of K_{OBJ} and B_{OBJ} . Before the fingers touch the object, the stiffness of the system (K in Eq. 5.4) has no effect on the grasp model and hence is negligible. However, as soon as the fingers start touching the object, the stiffness of the system and the stiffness of the object should be considered in the grasp model. Unfortunately, in reality, it is impractical to calculate the stiffness of the unknown objects to be grasped. This makes the grasp model inaccurate. To solve the uncertainty problem explained above, a hybrid sliding mode PI controller is designed, as shown in Figure 5.16.

As explained previously in chapter 4, the sliding mode controller will increase the robustness of the proportional integral control to the uncertainty of the object's mechanical impedance (K_{OBJ} and B_{OBJ}) and hence reduce the undesired steady-state error and response overshoot.

Figure 5.17 depicts the force tracking test performed to evaluate the performance of the designed hybrid control.

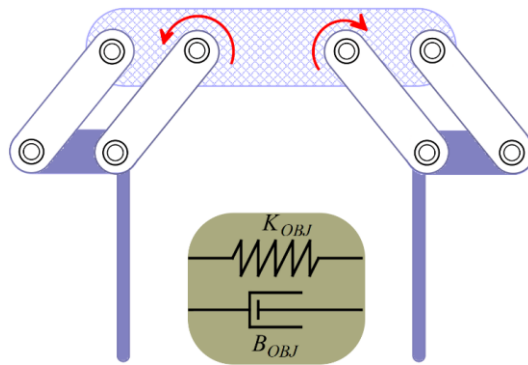


Figure 5.15: Uncertainty about the mechanical properties of the object to be grasped makes the grasp model inaccurate.

The 45 kg payload gripper is used in this test with the same objects as those used in the previous test (a foam block, a piece of wood and a RSJ steel beam) as the objects to be grasped. The dashed blue lines in this figure are the force trajectory used as the desired input, whereas the solid orange and solid red lines show the output grip force for the PI and hybrid sliding mode-PI controllers, respectively. As can be seen from this figure, the fixed gain PI controller is suffering from steady-state error and overshoot, whereas the hybrid sliding mode-PI controller can robustly remove the steady-state errors and overshoots from the PI controller.

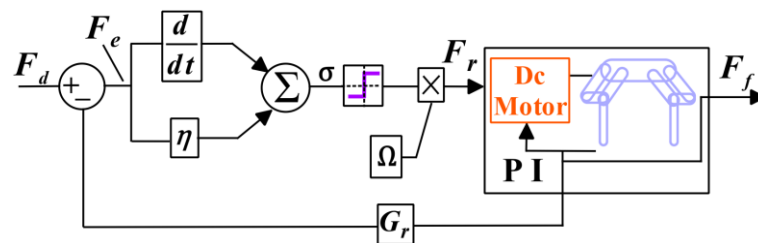


Figure 5.16: Hybrid sliding mode-PI force controller design.

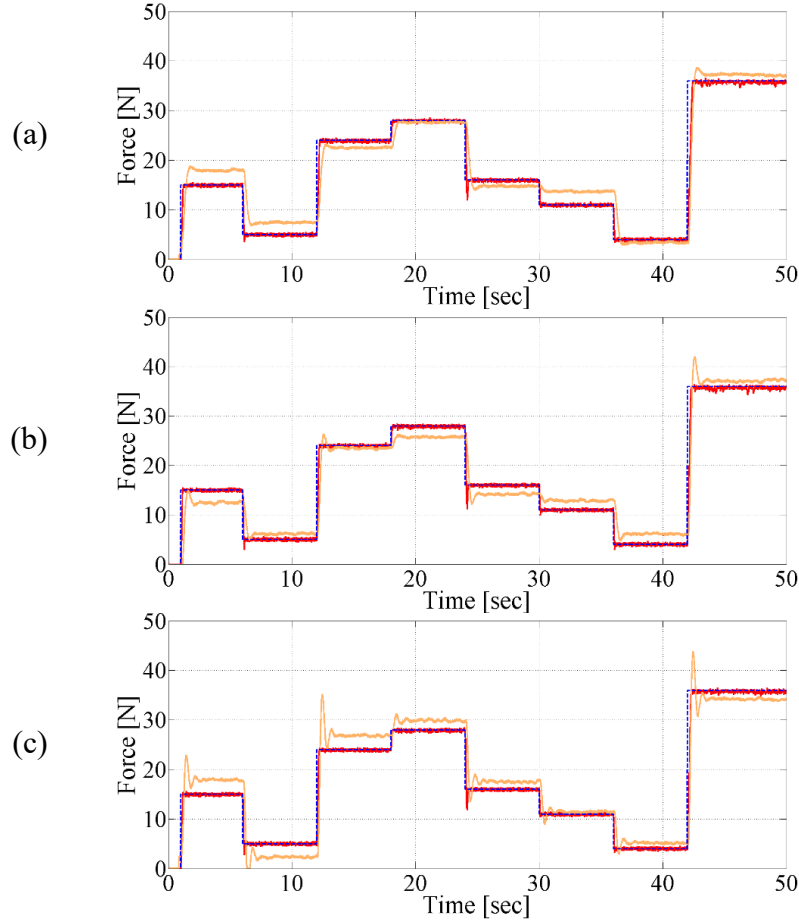


Figure 5.17: Force tracking test with the 45 kg payload gripper for (a) foam block (b) piece of wood and (c) RSJ steel beam. The dashed blue lines, solid orange and solid red lines are the reference trajectory, the response of the fixed gain PI control and the response of hybrid sliding mode-PI controller to the reference trajectory input, respectively.

5.4 Hybrid SMC-PI Control Design

In this section, an adaptive sliding mode control law is designed to control the grasp in the designed grippers. Assuming an error function as below:

$$e_{x,S_l}(t) = S_l - (x_f - x_0) \quad (5.7)$$

where S_l is the slippage of the object, the magnitude of which is acquired through the slip sensor. x_f is the position of the fingers, and x_0 is the position of the fingers when they make contact with the object's surface without applying any force to it. As can be remembered from chapter 4, the next step in designing a sliding mode control is defining a sliding variable. The sliding variable for the above error state is given by:

$$\sigma(e, \dot{e}) = \dot{e} + \eta e \quad (5.8)$$

where η is the convergence rate and any arbitrary positive constant as this guarantees the exponential decay of the error states. In order to achieve asymptotic convergence of the error state variables $e(t)$ and $\dot{e}(t)$ to zero, $\lim_{t \rightarrow \infty} e(t), \dot{e}(t) = 0$ with a convergence rate η , in the presence of a bounded disturbance $|D(d_t, m)| \leq D$, the variable σ has to be driven to zero in a finite time. The following two subsections, will explain the two different control designs used to achieve this task.

5.4.1 Quasi-sliding Mode grasp control

Recall Section 4.5 from chapter 4, the quasi sliding mode control law, QSMC, Eq. 4.24 can be used to drive σ to zero in a finite time.

$$F_{grip} = -\text{SAT}(\sigma, \varepsilon) \quad (5.9)$$

$$\text{SAT}(\sigma, \varepsilon) = -\Omega \frac{\sigma}{|\sigma| + \varepsilon} \quad \varepsilon \approx 0 \quad \varepsilon > 0$$

Where, from Eq. 4.22 we have:

$$\Omega = D + \frac{\xi}{\sqrt{2}} \quad (5.10)$$

Where the role of the D term in Eq. 5.10 is to compensate for the external bounded disturbance and any uncertainty of the system $|D(d_t, m)| \leq D$, whilst the term $\frac{\xi}{\sqrt{2}}$ determines the reaching time to the sliding surface; choosing a larger value for ξ will lead to the shorter reaching time T_s . From Eq. 4.19, the sliding manifold reaching time can be calculated as:

$$T_s \leq \frac{2\sqrt{\Lambda_\sigma(0)}}{\xi} = \frac{\sqrt{2}|\sigma(0)|}{\xi} \quad (5.11)$$

Now assume the grasp and lift scenarios shown in Figure 5.18. In the grasp mode shown on the left side of this figure, as the object is on the ground, the slip feedback from the slip sensor will show zero slippage, $S_l = 0$. In order to drive the error function (Eq. 5.7) to zero, the gripper will close the fingers until contact between the fingers and object occurs, $x_f = x_\theta$. As shown in this figure, in the grasp mode the fingers applied force will be zero.

It is evident that as the gripper's applying force is zero, the object will start sliding as soon as the gripper tries to lift the object in the lifting mode, $S_l > 0$. This means that the error is not equal to zero anymore. In this case, in order to bring the error to zero, the controller will increase x_f (and hence increase the grip force) until the object stops slipping. Figure 5.19 depicts the control diagram explained by Eq. 5.7, 5.8 and 5.9.

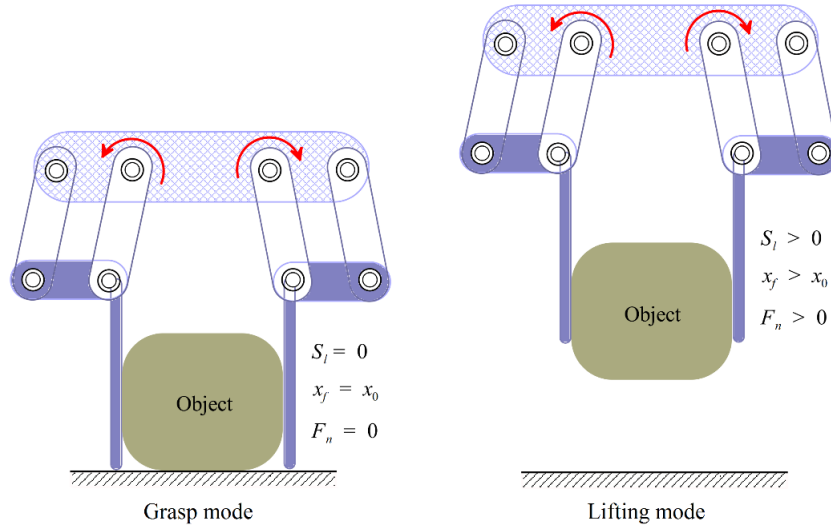


Figure 5.18: A schematic model of the gripper and object in its grasp (left) and lift (right) mode.

In this figure, status 1, 2 and 3 represent the gripper in its open, grasp and lifting modes. In this diagram, F_p is a fixed negative force which keeps the gripper in its open status as long as the system is receiving an open command from the operator. F_g is a small, positive force which slowly closes the gripper. As the controller does not have any prior knowledge about the size of the object, this small force ensures that the gripper slowly closes its fingers until the grasp takes place. As soon as the observer (OBS) receives a close command, it sends a status command 2 to the control switch, S_w . Consequently, the gripper control command will be changed to F_g . Sending F_g commands to the servomotors will cause the gripper to start slowly closing its fingers until contact between fingers and object is accomplished. As soon as the fingers establish this contact, the observer will receive a non-zero force feedback ($F_m > 0$) from the servos. Afterwards, the observer will send status command 3 to the switch and the sliding mode control will start its operation. It is worth noting that, from chapter four, in order to guarantee the robustness of the system in overcoming large disturbances, a relatively large value is chosen for the control variable, Ω .

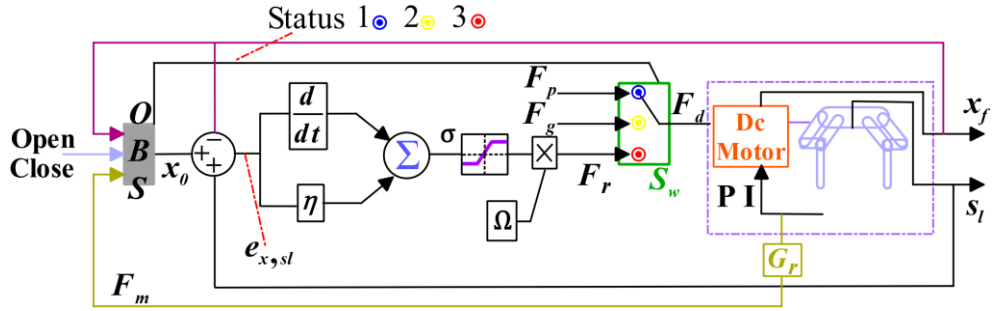


Figure 5.19: Block diagram of HSMC.

5.4.2 Control Design and Robustness Analysis

Figure 5.20 shows a schematic model of the gripper with a grasped object. From this figure, the state variable equation of motion can be obtained as below:

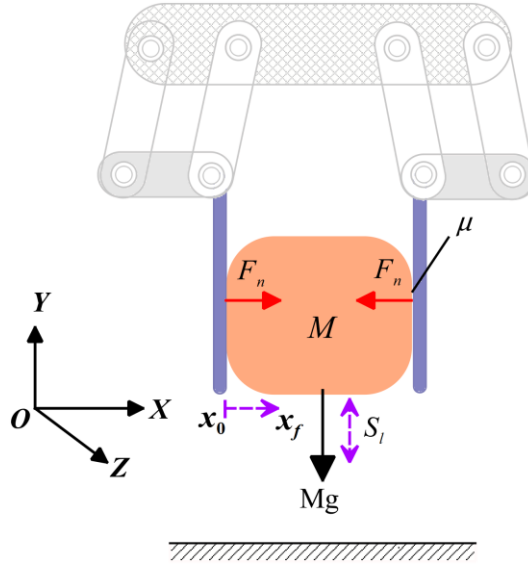


Figure 5.20: Schematic model of the gripper with the held object

$$\begin{cases} X_1 = S_l \\ \dot{X}_1 = X_2 \\ \dot{X}_2 = g - \frac{\mu}{M} F_n + f_d(X_1, X_2, t) + \Gamma(X_1, X_2) \end{cases} \quad (5.12)$$

where X_1 and X_2 are the held object's slippage and the velocity of the slippage, and F_n is control force (grip force). $f_d(X_1, X_2, t)$ and $\Gamma(X_1, X_2)$ in this equation represent an external disturbance and any uncertainty in the model, respectively, whilst the constant M denotes the object's mass. As from Eq. 4.3, the disturbance and model's uncertainty can be rewritten as a single force, as per below:

$$F_{du}(X_1, X_2, t) = f_d(X_1, X_2, t) + \Gamma(X_1 + X_2) \quad (5.13)$$

where F_{du} is assumed to be bounded as below:

$$|F_{du}(X_1, X_2, t)| \leq D \quad D > 0 \quad (5.14)$$

By substituting Eq. 5.13 into Eq. 5.12 we can write:

$$\begin{cases} X_1 = S_l \\ \dot{X}_1 = X_2 \\ \dot{X}_2 = g - \frac{\mu}{M}F_n + F_{du}(X_1, X_2, t) \end{cases} \quad (5.15)$$

From Eq. 5.7 the error function is defined as below:

$$e_{x, S_l}(t) = S_l - (x_f - x_0) \quad (5.16)$$

A sliding mode control law $F_n = F_n(X_l, X_2, t)$ has to be designed to drive the error to zero in a finite time. Using this error function, the error-based sliding variable will be:

$$\sigma_{(e, \dot{e})}^t = \dot{e} + \eta e \quad (5.17)$$

From Eq. 5.15, 5.16 and 5.17 we can obtain:

$$\dot{\sigma} = -\ddot{x}_f - \eta\dot{x}_f + \eta\dot{S}_l + g + F_{du}(X_1, X_2, t) - \frac{\mu}{M}F_n \quad (5.18)$$

where for F_n we can write:

$$\frac{\mu}{M}F_n = \frac{\mu}{M}F_n - F_n + F_n = F_n \left(\frac{\mu}{M} - 1 \right) + F_n \quad (5.19)$$

Substituting Eq. 5.19 into Eq. 5.18 we can write:

$$\begin{aligned} \dot{\sigma} &= \underbrace{\ddot{x}_f + \eta\dot{x}_f - \eta\dot{S}_l - g - \tilde{F}_{du}(X_1, X_2, \mu, M, t)}_{A(X_1, X_2, \mu, M, t)} - F_n \\ &\Rightarrow \dot{\sigma} = A(X_1, X_2, \mu, M, t) - F_n \end{aligned} \quad (5.20)$$

Where \dot{S}_l is the speed of the slippage which is measurable using the slip sensor. $A(X_1, X_2, \mu, M, t)$ is called the system's cumulative uncertainty-disturbance. It is assumed that

the cumulative uncertainty-disturbance $A(X_1, X_2, \mu, M, t)$ parameter is bounded, $|A(X_1, X_2, \mu, M, t)| \leq D_A$.

Recall the sliding mode existence condition Eq. 4.33. For convenience, the condition is rewritten as per below:

$$\sigma \dot{\sigma} \leq -\bar{\xi} |\sigma|, \quad \text{where} \quad \bar{\xi} = \frac{\xi}{\sqrt{2}} \quad (5.21)$$

Consequently:

$$\sigma \dot{\sigma} = \sigma(A(X_1, X_2, \mu, M, t) - F_n) \leq |\sigma|D_A - \sigma F_n \quad (5.22)$$

and selecting:

$$F_n = \Omega \text{sign}(\sigma) \quad (5.23)$$

Substituting Eq. 5.23 into Eq. 5.22 we obtain:

$$\sigma \dot{\sigma} \leq |\sigma|(D_A - \Omega) = -\bar{\xi} |\sigma| \quad (5.24)$$

From Eq. 5.24 it can be concluded that the sliding mode gain should satisfy the reachability condition shown by Eq. 5.25 in order to guarantee the robustness of the control law for the bounded disturbance-uncertainty, $A(X_1, X_2, \mu, M, t)$.

$$\Omega \geq D_A + \bar{\xi} \quad (5.25)$$

The term D_A in Eq. 5.25 is used to overcome $A(X_1, X_2, \mu, M, t)$, whilst the second term, $\bar{\xi}$, determines the reaching time to the sliding surface; this reaching time can be calculated by substituting $\bar{\xi}$ into Eq. 5.11.

5.4.3 Adaptive SMC grasp control

The previous section, talked about the condition in which the robustness of the controller can be guaranteed. From Eq. 5.25, it is realised that choosing any value for Ω that is greater than $D_A + \bar{\xi}$ can guarantee the robustness of the controller. However, despite the fact that choosing a large value for Ω increases the robustness of the system to unknown disturbances, as well as decreasing the response time of the controller (by reducing the reaching time), there is, however, a disadvantage inherent to the large value of Ω ; it increases the tendency of the

system towards chatter. Although, as explained before in chapter 4, this phenomenon does not affect the outcome of the controller, but increases the power consumption of the motor and reduces the lifespan of the associated mechanical parts. In order to reduce the CHPH from the control response a new adaptive sliding mode controller, the ASMC, is introduced by adding a rectifier feedback loop to the control law explained in the previous section. To do so, a small value, \tilde{D} , is selected for the bounded disturbance term, D_A , which reduces any unnecessary CHPH when the disturbance is small. The new value for Ω is given by:

$$\Omega = \tilde{D} + \frac{\xi}{\sqrt{2}} + H_1 \frac{d}{dt} S_l + H_2 = \hat{\Omega} + H_1 \dot{S}_l + H_2 K_{RC4} \quad (5.26)$$

$$K_{RC4} = \begin{cases} 1 & \text{if } V_{arm} > 0 \\ 0 & \text{if } V_{arm} = 0 \end{cases}$$

where H_1 and H_2 are constant gains. Including a time derivative slippage within the control loop can guarantee the robustness of the controller to external disturbances greater than \tilde{D} , as any unexpected disturbance will cause the grasped object to slip. As the result, this undesired slippage will increase the control gain, Ω .

There is also a feedback from the manipulator's control cabinet (K_{RC4}) to the sliding gain. The gain H_2 in this loop will become greater than zero 60 ms (or any value greater than reaching time, T_s) before the manipulator starts moving. This will help the controller to eliminate the destabilizing effect of the manipulator's movement. This gain, however, will become zero, 1 s after the manipulator stops its movement.

Figure 5.21 shows the block diagram for this controller. The experimental results reported in the next section will show how the proposed AHSMC can reduce the undesired CHPH from the control response.

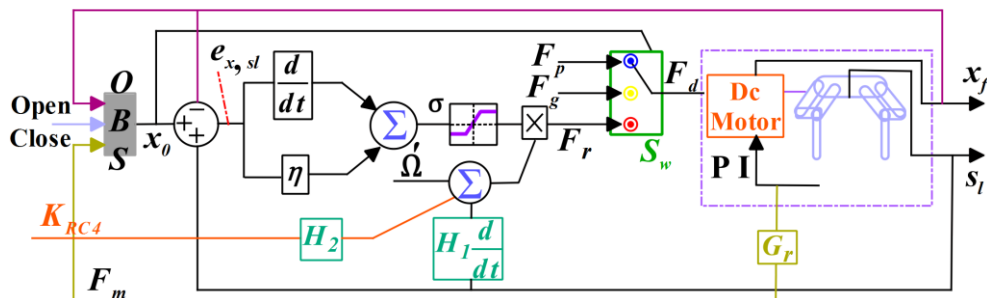


Figure 5.21: The control block diagram of the designed ASMC.

5.5 Super Twisting Sliding Mode Control

Alternatively, and as depicted in Figure 5.22, in order to solve the above-mentioned inconvenience inherent to FSMCs, an adaptive hybrid super twisting sliding mode controller (ASTSMC) is designed. The designed controller can eliminate CHPH without compromising the robustness of the controller. From chapter 4, the STSMC is a particular type of second-order sliding mode control. The great advantage of STSMC compared to other 2-SMC is that only measurements of the sliding variable σ need to be used to guarantee the condition $\sigma = \dot{\sigma} = 0$. In other words, the STSMC can be used for systems of relative degree 1 instead of a standard 1-sliding mode controller in order to avoid CHPH.

According to equation Eq. 4.43 from chapter 4, the control function for a STSMC must be provided in the form:

$$F_n = \tilde{\Omega} \sqrt{|\sigma_{(e,\dot{e})}^t|} \text{sign}(\sigma_{(e,\dot{e})}^t) + \Upsilon \quad (5.27)$$

$$\dot{Y} = w \text{sign}(\sigma_{(e,\dot{e})}^t)$$

with the following tuning relationships:

$$\tilde{\Omega} = \sqrt{U} \quad ; \quad w = 1.1U \quad (5.28)$$

where U is a positive constant which is used to eliminate the uncertainty/disturbance term. There is also a gained feedback from the manipulator's control cabinet (K_{RC4}) and a time derivative slippage to the sliding gain, U , in order to guarantee the reachability condition and hence stability of the system.

Thanks to the continuous algebraic function, unlike the SMC, any discontinuous oscillating output is eliminated in this controller.

To quantify the performance of the proposed ASTSMC more accurately, a number of experimental tests have been carried out consisting of a pick-and-place task where objects were moved between pick and place points through fast accelerations and decelerations. Due to the high dynamic trajectory, grasped objects could in principle slip through the fingers of the gripper or even drop out of it. The next section describes this experiment and discusses the related results.



Figure 5.23: The robot grasps and lifts different objects (a Coca-Cola bottle) and starts to move along a pre-programmed trajectory in an accelerating and decelerating manner.

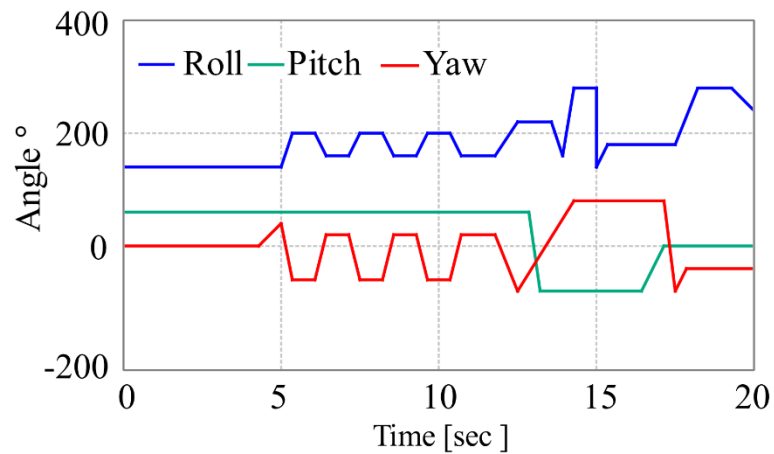


Figure 5.24: Motion trajectory profile of the gripper used in the experiment.

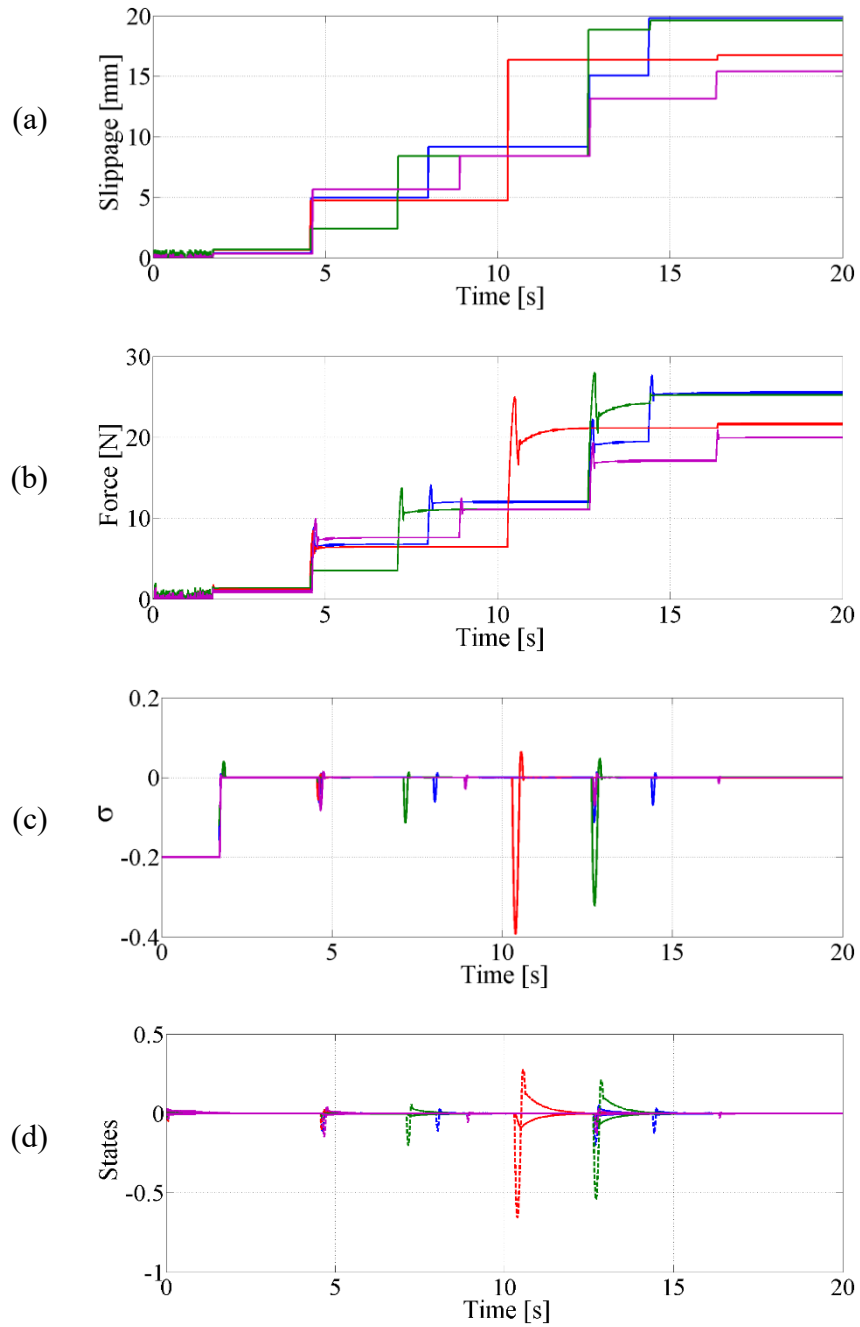


Figure 5.25: Experimental results using the ASMC for the Coca-Cola bottle

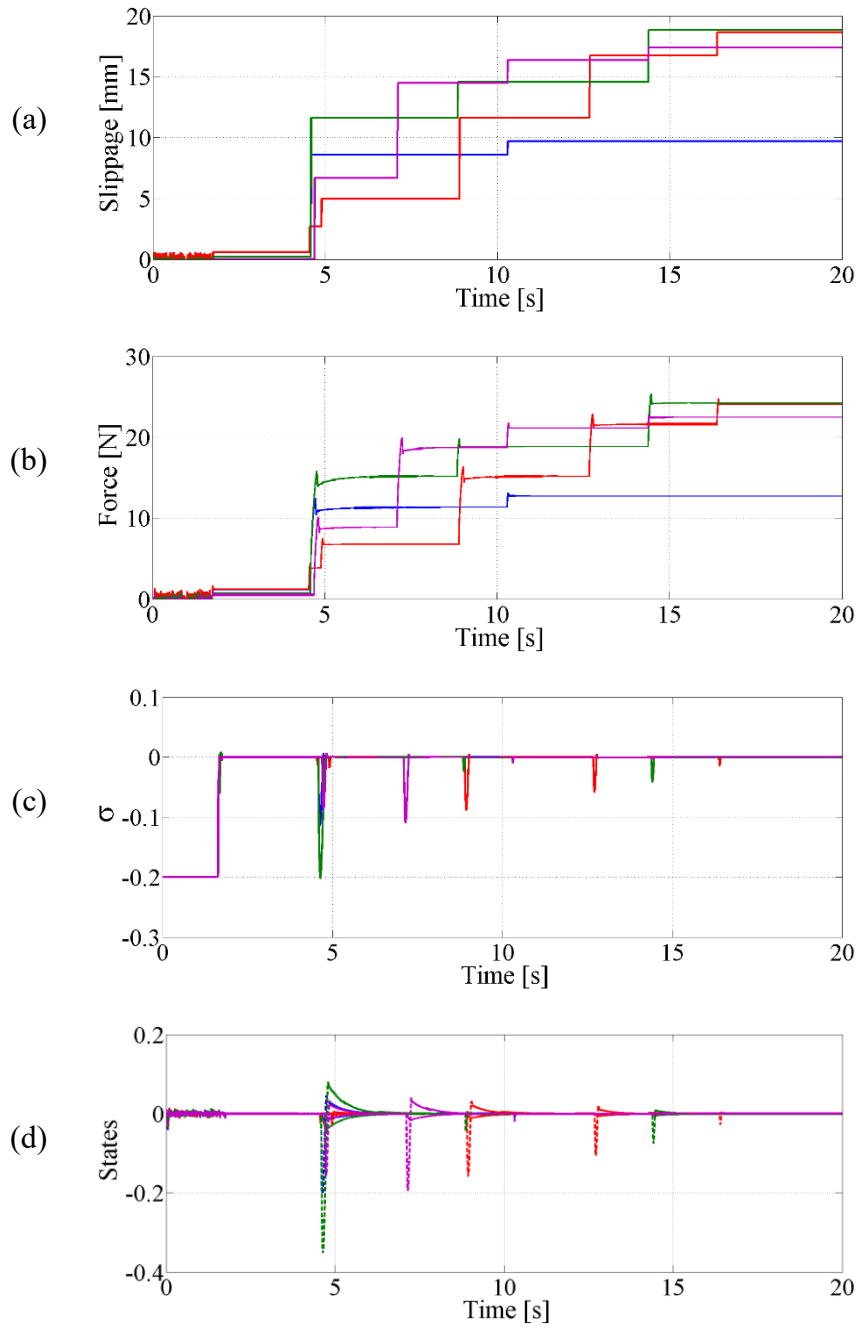


Figure 5.26: Experimental results using the ASMC for the metal block.

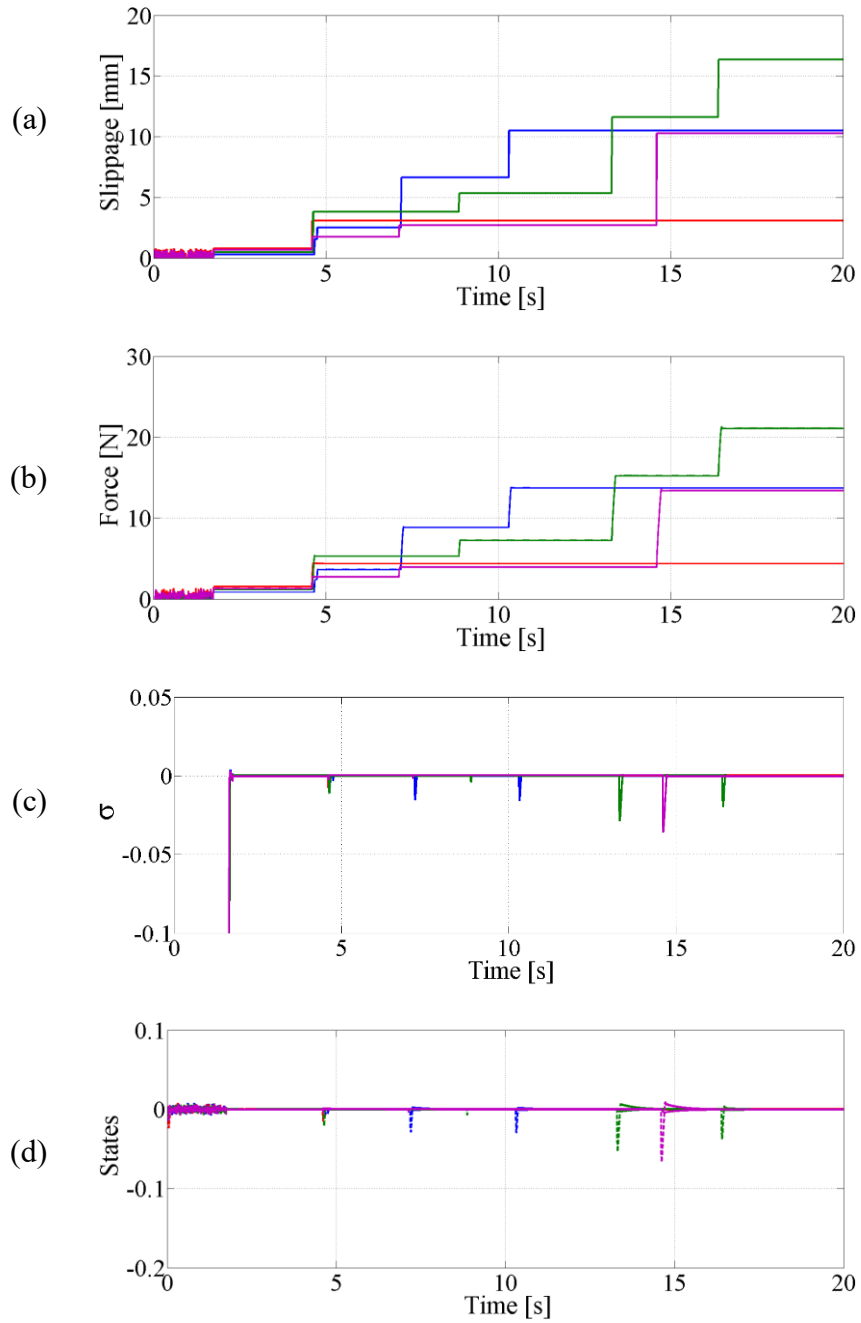


Figure 5.27: Experimental results using the ASMC for the wood.

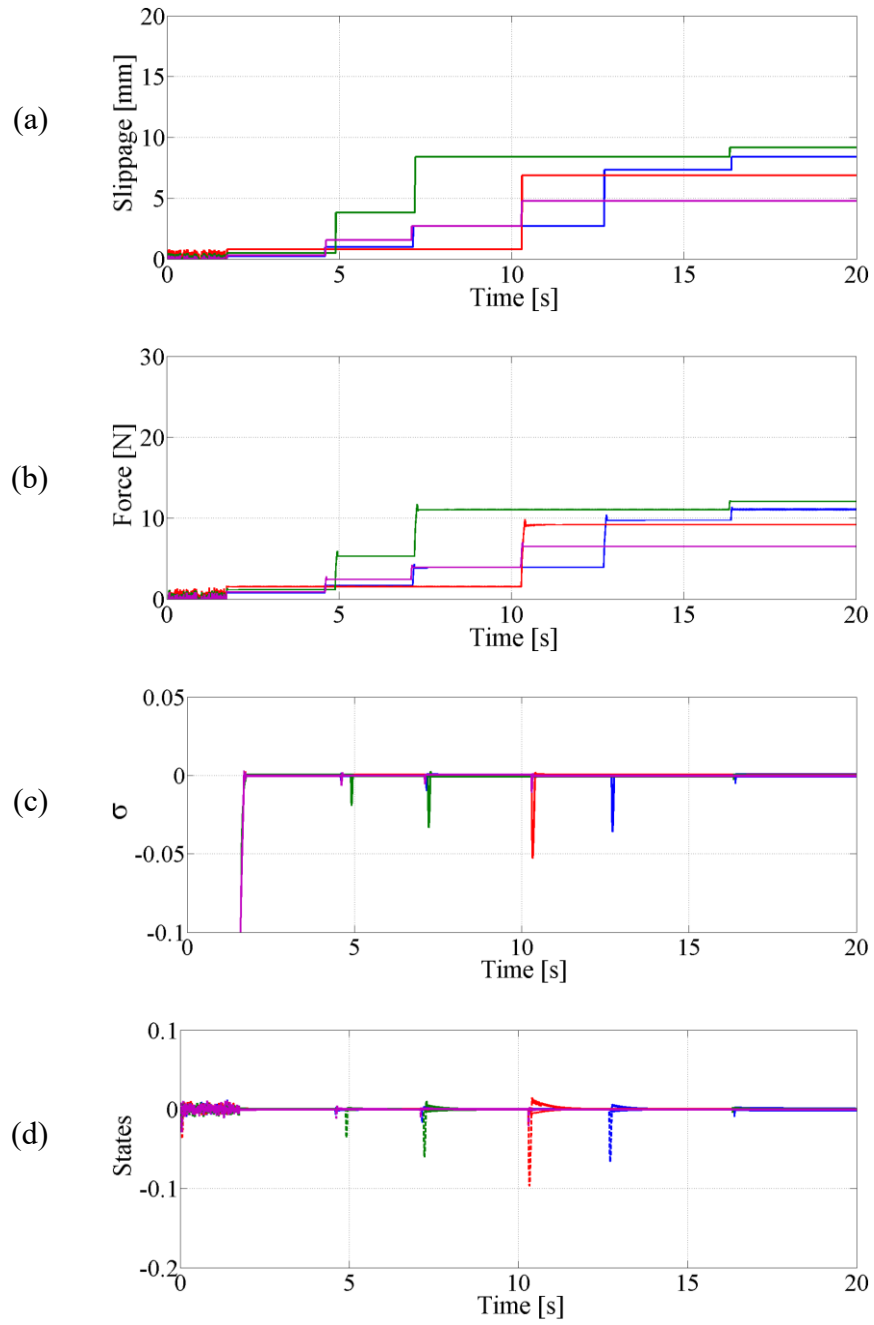


Figure 5.28: Experimental results using the ASMC for the egg.

Figures 5.25, 5.26, 5.27 and 5.28 show the recorded slippage, applied force, sliding variable σ and error states e and \dot{e} from four experimental trials using the ASMC with the four objects: a partially filled soda bottle, a block of metal, a piece of wood and an egg. As depicted in this figure, for all the results, at $t = 4.5$ s when the gripper starts lifting the objects, the force applied to the objects by the gripper starts to rise due to the slippage. For the remaining time, the controller reacts by increasing the applied force when slippage occurs. From these figures, it may also be noted that the controller maintains the value of σ at zero and consequently the error states converge to zero after only a short transient period. The isolated, larger peaks in the ripple occur when the object slips, confirming the robustness of the designed ASMC in the presence of the unexpected disturbances which result in undesired slippages. For all tests, and with all objects, the experiment has been repeated four times (blue, red, green and magenta lines in the diagrams) to test the repeatability and consistency of the results.

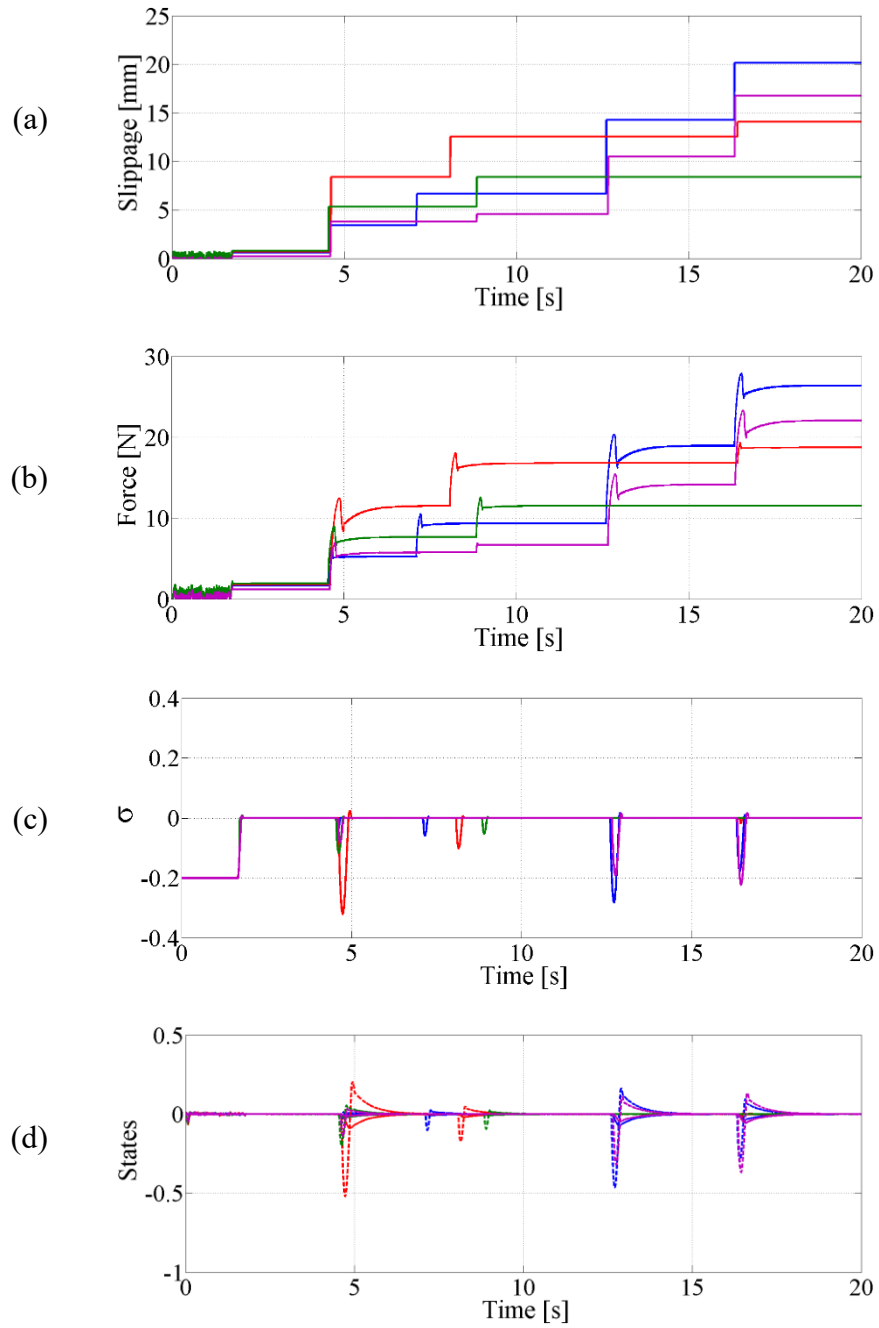


Figure 5.29: Experimental results using ASTSMC for the Coca-Cola bottle.

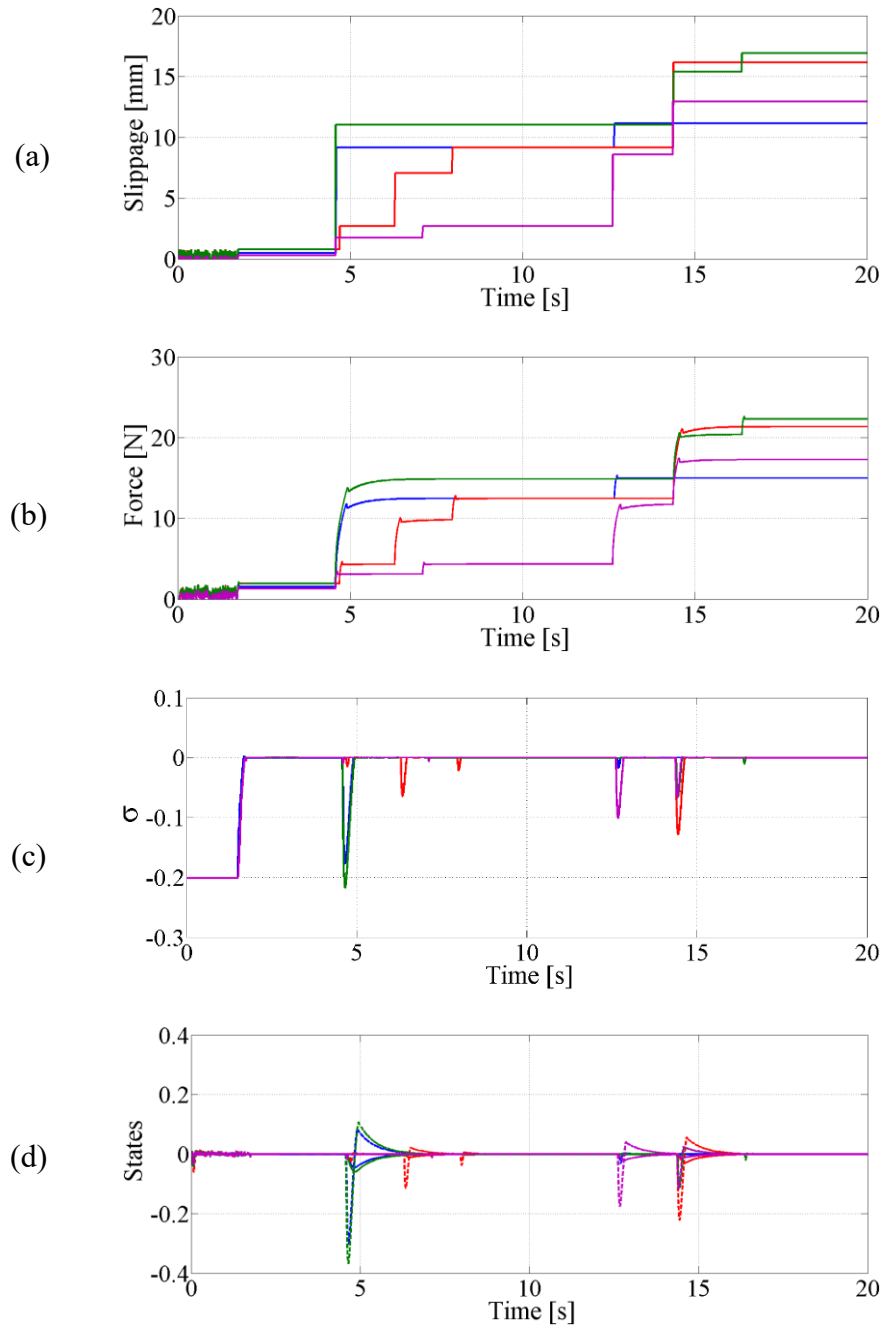


Figure 5.30: Experimental results using ASTSMC for the metal block.

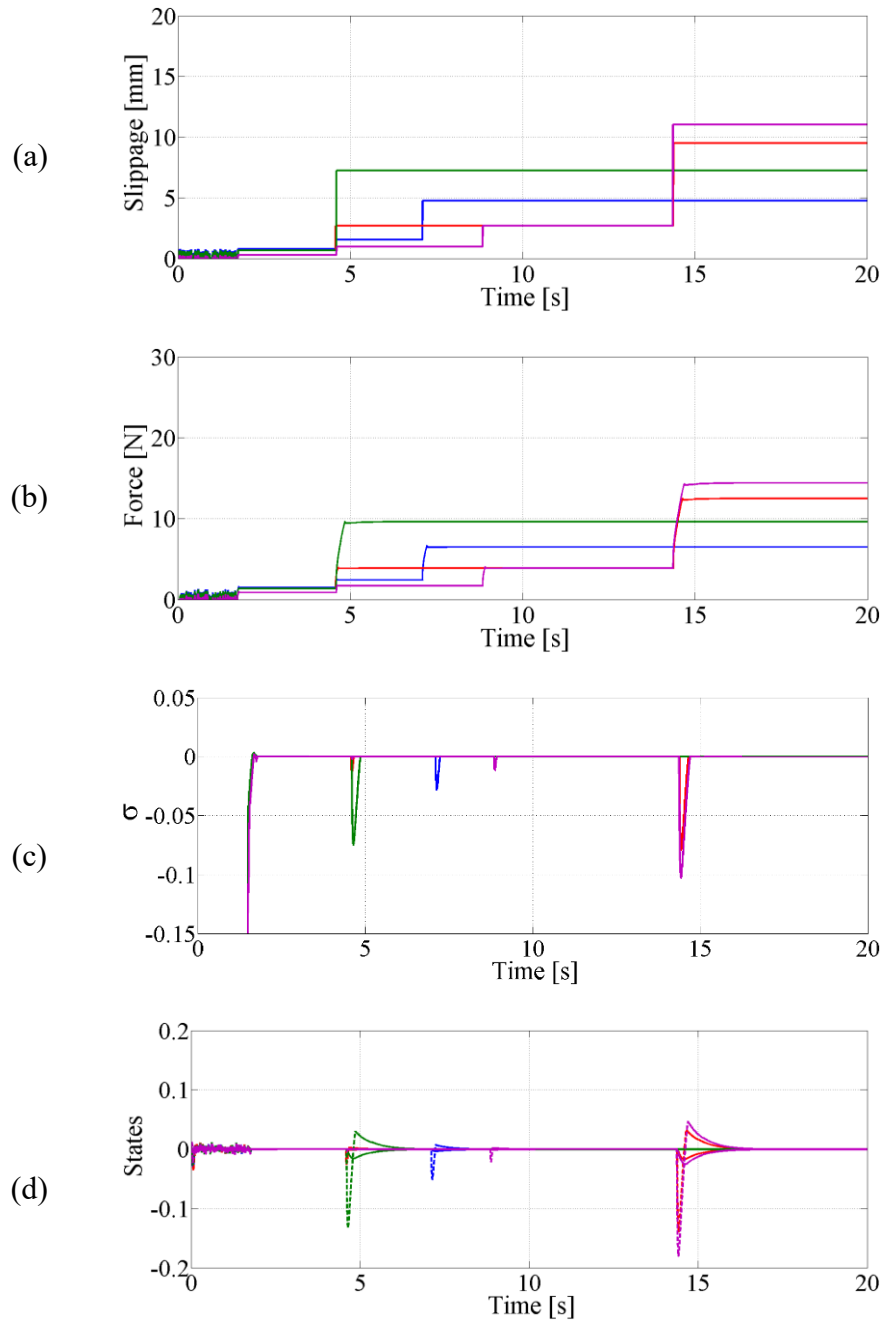


Figure 5.31: Experimental results using ASTSMC for the wood.

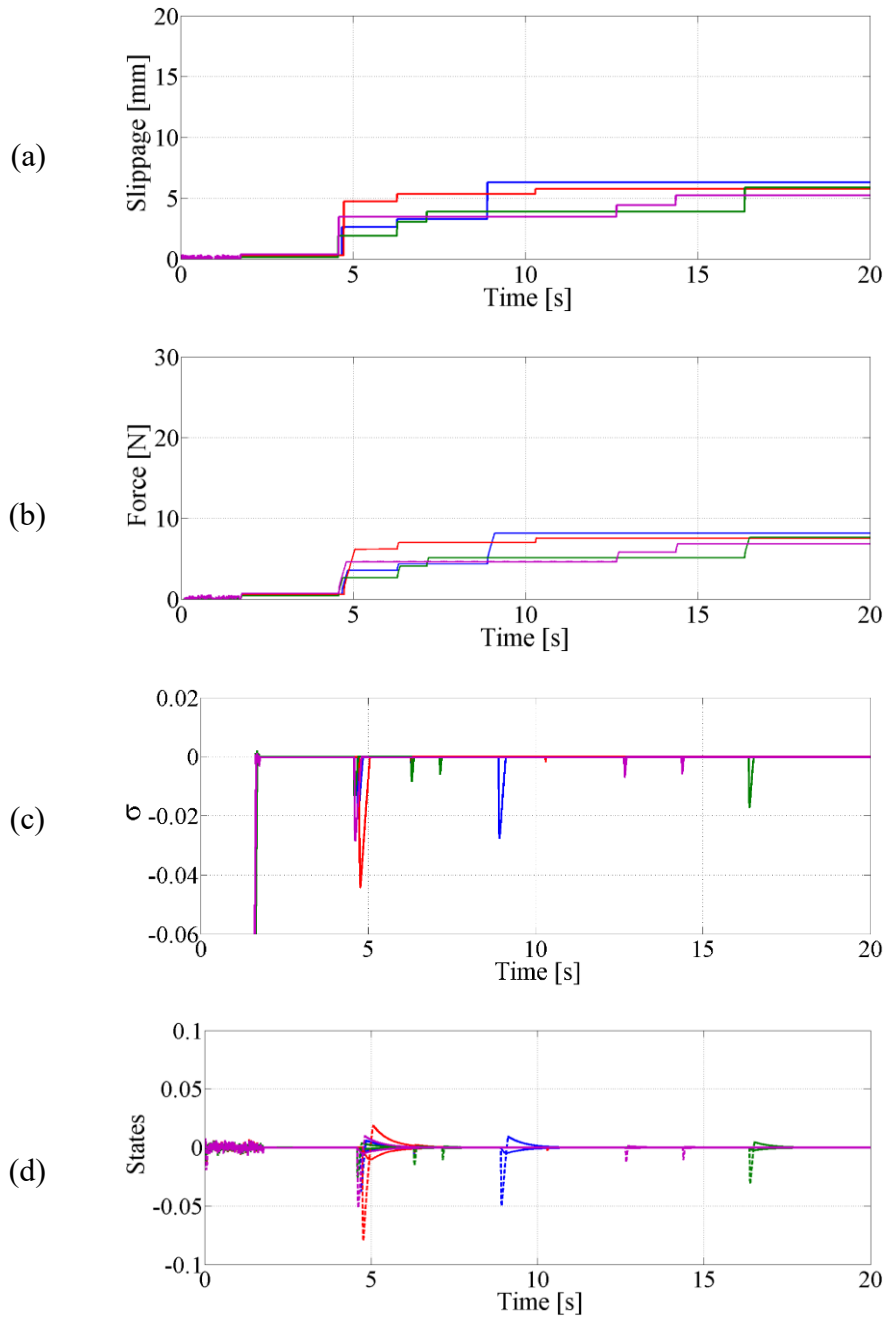


Figure 5.32: Experimental results using ASTSMC for the egg.

Figures 5.29, 5.30, 5.31 and 5.32 show the results of using designed ASTSMC for the four objects. The reaction of the controller in terms of response times and compensation for disturbance is similar to the first controller. However, CHPH is reduced dramatically, regardless of the stiffness of the grasped objects. It is worth noting that all the curves reported above evidence the random nature of the slippage, since the four tests performed for each given object do not have exactly the same outcomes. However, in spite of these random variations, it is possible to note a number of more deterministic features by comparing the results gained for the different objects. Because the objects are characterised by having significantly different weights, frictional characteristics and stiffness, for heavier objects the gripping force is initially enhanced through the control action caused by the initial slippages. This could explain the slightly different behaviour in the slippage and increasing gripping force in the first part of the movement for heavier objects. However, after about 5 seconds, all objects show similar behaviour, with the gripping force clearly being able to cope with the highly variable profile of the trajectory acceleration. The average value of the gripping force remains the same (no slippage is evident) until a further slippage occurs at around 15 seconds for all objects. The only exception is that of the partially filled bottle, where perhaps unsurprisingly the variable CM causes further intermediate slippages.

Figures 5.33, 5.35 and 5.37 depict some of the experiments have been performed with the 45 kg payload gripper, as controlled by the proposed adaptive hybrid super twisting sliding mode controller, the experimental results of which can be found in Figures 5.34 and 5.36 respectively. Figure 5.33 depicts a pick and place task in which different objects (a concrete block, a wooden beam and a pipe) with different shapes, weights and stiffnesses must be picked with high accuracy and placed in a predefined place. As shown in this figure, regardless of the diversity of the shape and mechanical properties of the objects, the robot can satisfactorily grasp and lift the objects and place them in the specified place. In addition to the theoretical stability analysis that explained above, and in order to reassure the performance of the controller and grippers in real-world scenarios, several lifting tests with many different objects have been performed. Figures 5.35 and 5.37 depict only some of these tests. As shown in this figure, thanks to the robustness of the controller to any uncertainty in its grasp, the gripper can grasp and lift different objects with different weights. As shown in this figure, the gripper first lifted a light weight and delicate glass of wine, whereas afterwards it lifted two chairs and a 20 kg steel pipe.

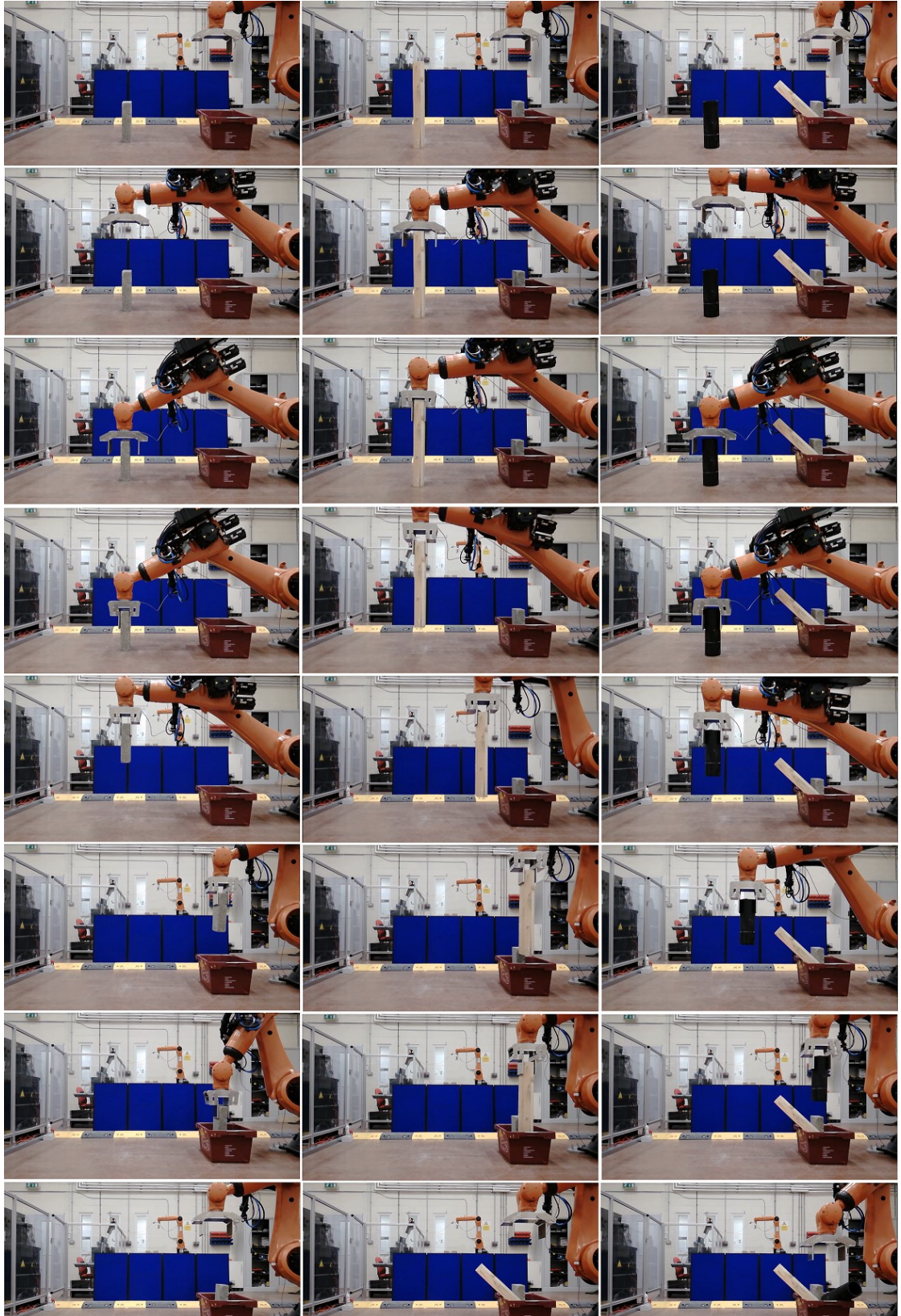


Figure 5.33: Pick and place tasks with the 45 kg payload gripper and ASTSMC.

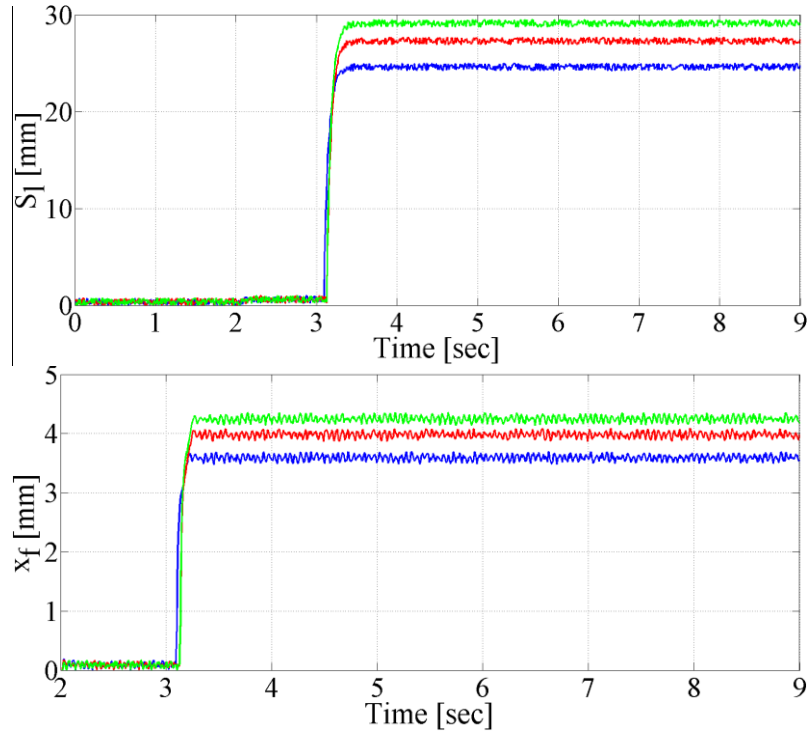


Figure 5.34: Experimental results for the Pick and place tests shown in Figure 6.33.

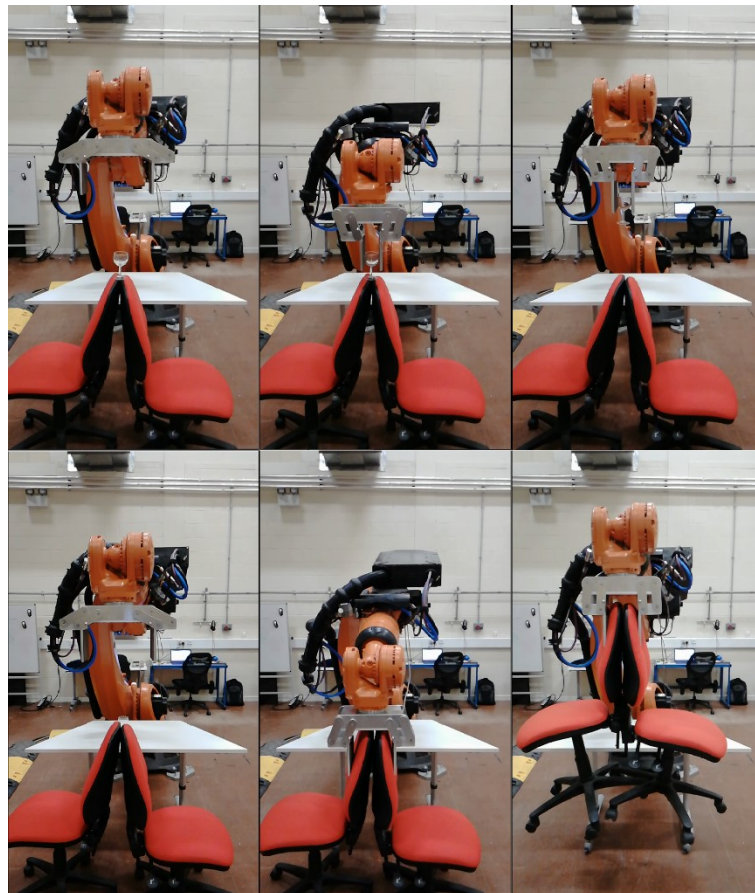


Figure 5.35: Many lifting tests with several different objects have been performed in order to test the robustness of the system in real-world scenarios.

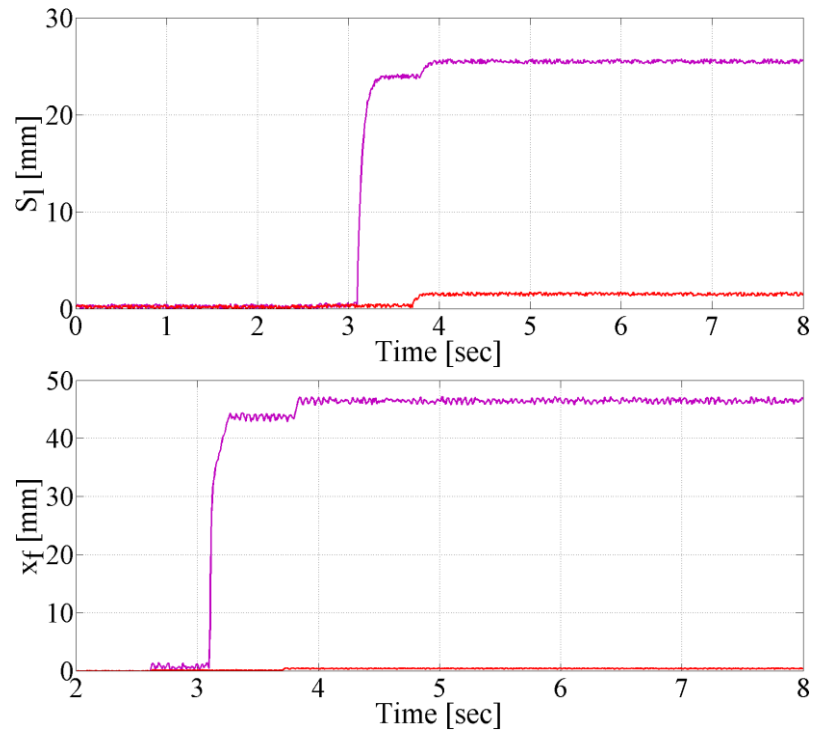


Figure 5.36: Experimental results for the test shown in Figure 6.35. Purple curves for chairs and red curves for glass of wine.

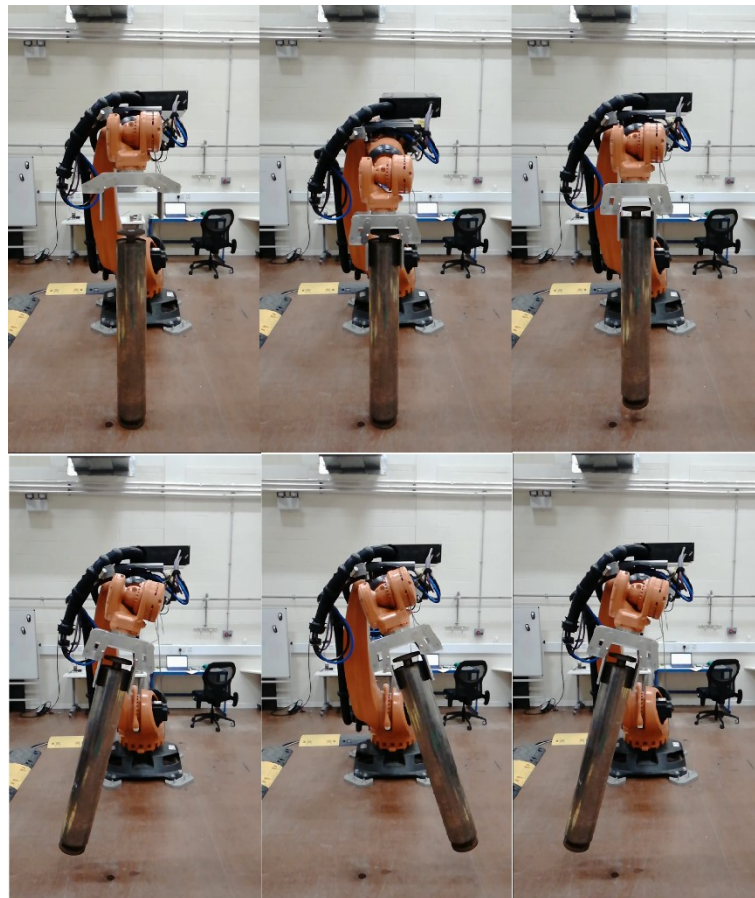


Figure 5.37: Using the designed gripper and ASTSMC the robot performs very robust grasp.

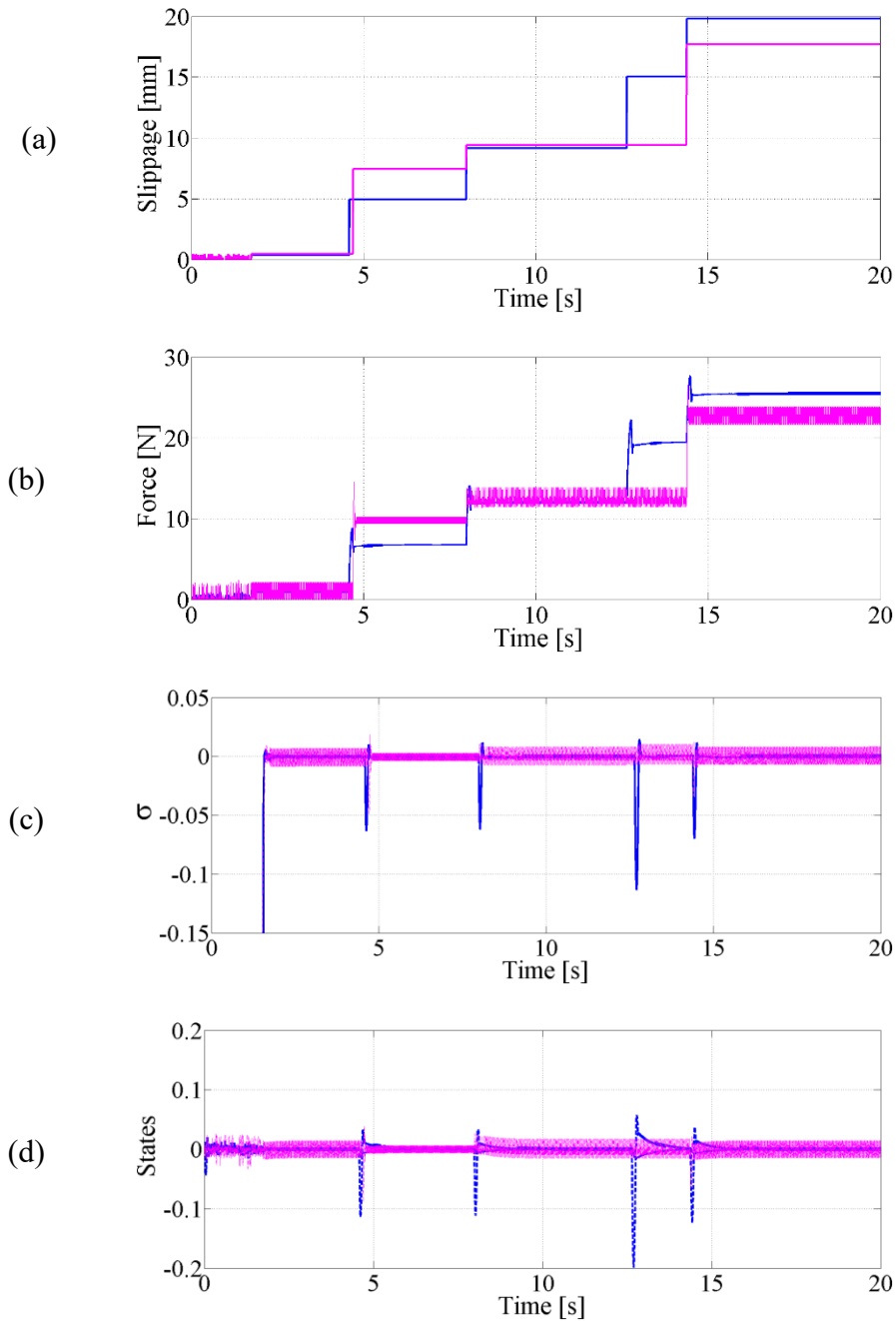
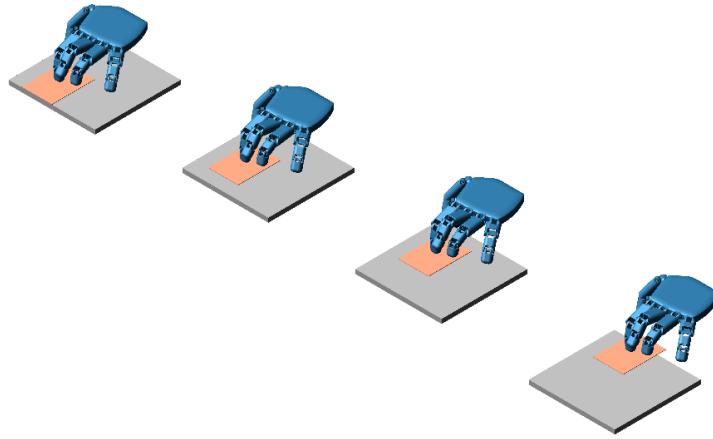


Figure 5.38: Experimental results of the ASMC (blue line) and FSMC (pink line) for the Coca-Cola bottle.

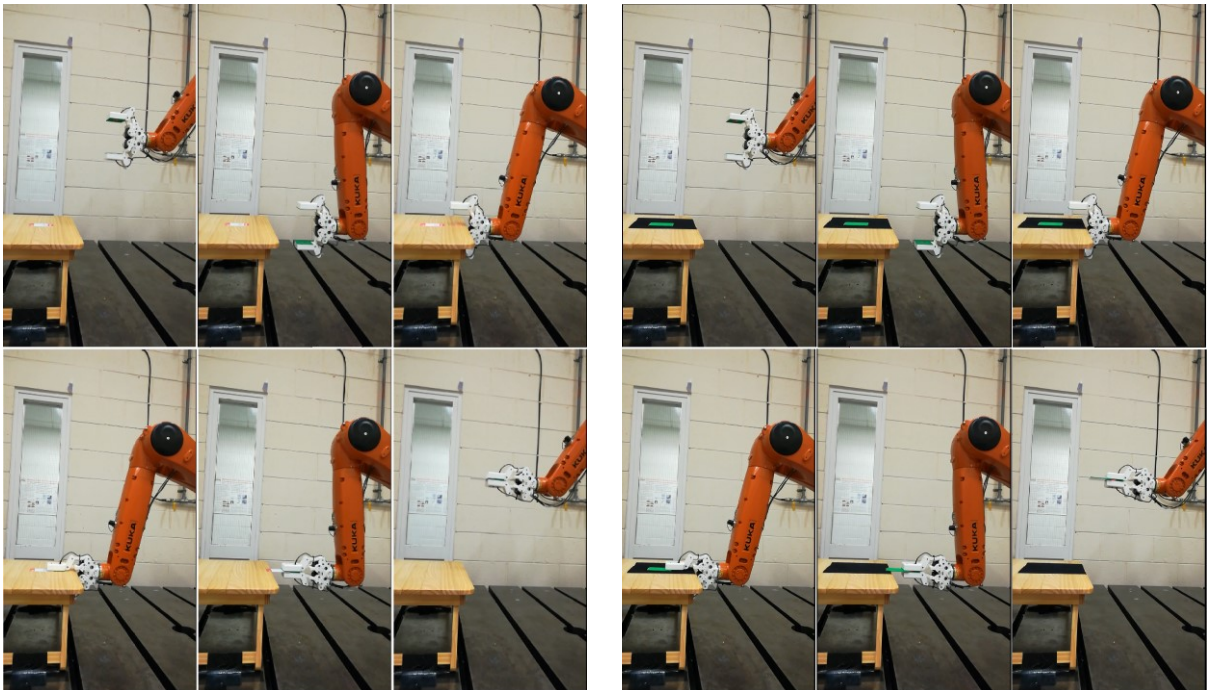
Finally, as discussed earlier, CHPH is a disadvantage of FSMC which the designed AHSMC can remove. Figure 5.38 shows the slippage, applied gripping force, F_n , σ , and the error states for both controllers in one of the experimental trials (pink line for SMC, blue line for ASMC). This figure shows that the designed ASMC can reduce CHPH without affecting controller robustness. In addition to the experimental results explained above, and as a case study, a new task for the controller was designed which is similar to certain daily tasks such as sanding or

picking up a business card from a desk. In these kinds of tasks, the goal is to keep the sliding object in the hand by applying an absolute minimum force on it. In the sanding task for instance, the goal is to keep the sandpaper in the hand by applying the minimum force to it. If the sandpaper receives too large a force from the carpenter's hand it will not move across the surface of the wood, whilst if the applied normal force is not sufficient, the sandpaper will just slide out of his hand. As another example, when sliding a business card across the surface of a desk, the shear force between the fingers and card should only be slightly greater than the friction between the card and the surface of the desk. The gripper used the STSMC to perform this task, as shown in Figure 6. 34. Figure 6. 34. a depicts the way in which a human picks up a business card or any thin object from a desk. To do so, as shown in this figure, due to the low thickness of the card, he first needs to slide the card across the surface of the desk toward the edge of the desk; afterwards, he can grab and lift the card from the edge of the desk. Figure 6. 34. b shows the implementation of such a task in the experimental platform. This figure depicts the way that the robot slides the card across the surface using ASTSMC.

In this experiment, only one of the fingers (the finger above the table) was controlled by the proposed controller, whereas the other one only received open force command (F_p) from the controller. The robot starts to slide the card across the surface of the table by applying a small amount of force while the controller increases the force when the card starts to slip out of the finger. Figure 5.39 demonstrates three results from this experiment. Four thin objects (1 mm, 1.5 mm, 1.8 mm, 2.3mm) with different friction coefficients have been used in this test. As shown in the figure, the controller was able to robustly stop the objects when they started to slip. It should be noted that significant work on this type of grasping and manipulation has been reported in the literature and this experiment has been performed not to advance the state of the art but rather to demonstrate the additional abilities of the gripper and controller.



(a)



(b)

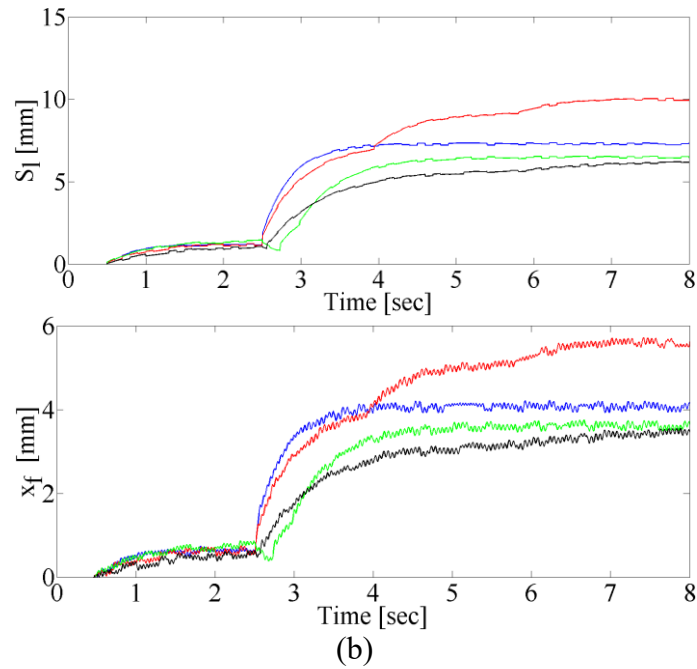
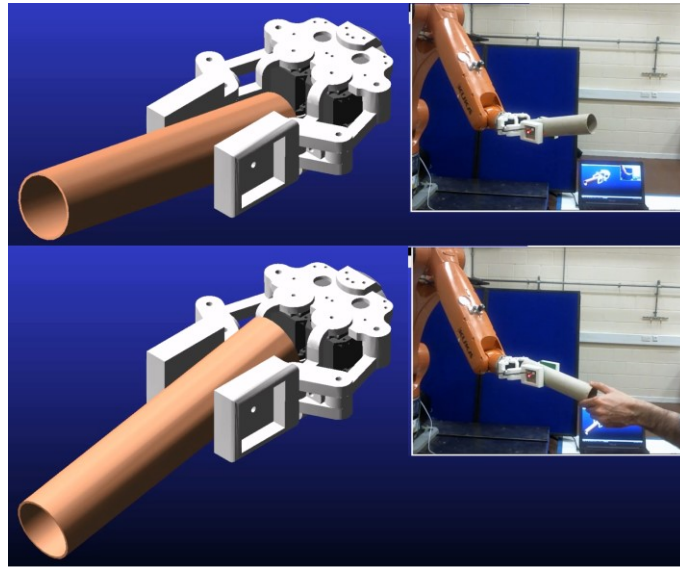
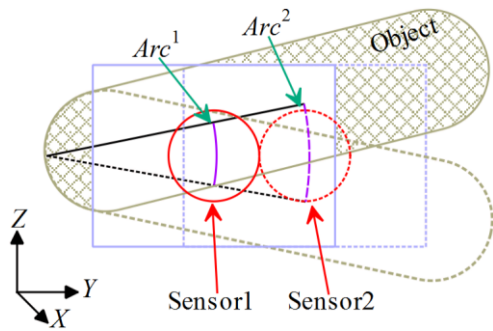


Figure 5.39: (a) The way in which a human picks up a business card or any thin object from a desk by sliding it across the surface of the desk (b) The way that the robot slides the card across the surface using ASTSMC (c) behaviour of the robot to the slippage of the object.

It is worth noting that despite the fact that only one optical flow sensor is sufficient to measure the slippage along the X- and Z, as shown in Figure 5.40.a, incorporating the second sensor into the gripper design provides the additional capability to measure the deviation of the object. In this figure, the deviation of the held object in the real gripper is measured and displayed in a simulated model in real time. This deviation (which is about the x_o axis in the $o_o x_o y_o z_o$ frame) can be calculated simply by subtracting the length of the displacement arc measured by the left sensor from that measured by the right sensor. Figure 5.40.b depicts the associated arcs measured by the two sensors. As shown in this figure, in order to measure the deviation of the object, the fingers are intentionally misaligned. This misalignment provides different displacement arc in the sensors. Also the data from the optical flow sensors has been used to re-calculate the end effector target position on the fly to compensate for grasped object displacements.



(a)



(b)

Figure 5.40: Using two sensors provides the capability to measure the deviation of the object.

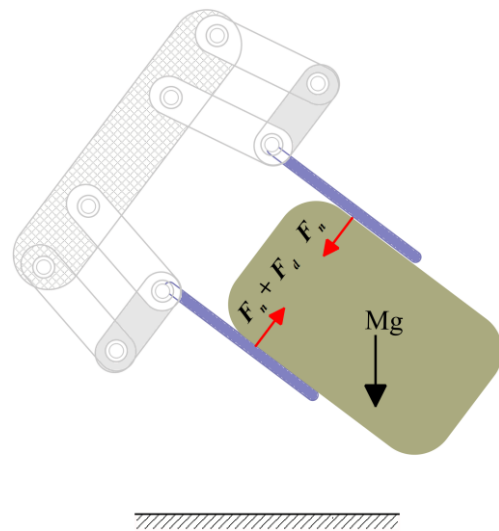


Figure 5.41: Rotation of the gripper about z_0 axis generates an extra force, F_d acting on the fingers. However, the designed controllers can satisfactorily compensate this force.

Finally, it is worth noting that in some experiments such as the one shown in Figure 5.37 and 5.41 due to rotation of the gripper around z_0 axis, one of the fingers receives an extra force, F_d due to the weight of the object. In this case, the controller will increase the desired force of the left finger in order to compensate the disturbance term, F_d .

5.7 Discussion

Grasping and lifting an unknown object in the presence of external stochastic perturbations represents a significant challenge. The main challenge is one of estimating the exact gripping force required to prevent slippage whilst avoiding any damage to, or deformation of, the object. This challenge has been addressed by initially looking for a control architecture that can guarantee any external disturbances and unmodeled/unknown characteristics of the grasped objects are properly compensated for. It has been illustrated that the proposed adaptive hybrid SMC and STMSC, in combination with feedback for the gripping force and slippage, can provide the robustness required. In the work presented, the optical flow sensors and the ultrasonic sensor were used to detect slippage, and the current-based torque measurement allowed the system to perform well with a wide variety of grasped objects in pick-and-place tasks characterised by trajectories with steep acceleration and deceleration ramps. In this chapter, experimental results for different objects with significantly different mechanical properties have been presented. During the experiments, the controllers were given no prior knowledge of these objects. The gripper was able to achieve a stable grasp on each of the objects and complete the pick-and-place task several times without damaging them.

Chapter 6

CONCLUSIONS AND FUTURE WORK

6.1 Summary

Arguably, robot interaction with the environment is one of the most challenging tasks in Robotics. Robotic grasping is one of the fields of Robotics which always needs to deal with such interactions. The difficulties of the grasping task can, in essence, be attributed to the following three reasons:

- 1) Any mechanical interaction between the gripper and object, as shown in chapter one, can potentially move the system's poles to the right side of the real axis in the locus zero-poles plot, meaning that such an interaction has the potential to destabilise the interaction port (fingers) of the gripper system (see Figure 1.7).
- 2) The mechanical properties of the object to be grasped can easily change the behaviour of the gripper in the presence of conventional control algorithms. Any interaction with an unknown object can result in a steady-state error in the presence of a fixed gain position control and/or an undesired large overshoot in the responses of conventional force control methods (see Figure 1.5 and Figure 5.14).
- 3) Even if the robot could satisfactorily grasp and lift an object, any external stochastic perturbation can destabilise the gripper and, consequently, result in the grasped object either being crushed, or falling and breaking (see Figure 4.4 and Figure 4.5).

Recalling Section 1.2, one of the low-cost solutions to stabilising a robot's mechanical port as controlled by an active force controller can be approached by adding a serial elastic element between the interaction port and actuator. This is also true in the human body, as it has been demonstrated that passive nonlinear properties of the capsular ligaments and muscle tendon units plays a vital role in providing a stable interaction with the environment.

Inspired by the metacarpophalangeal joints in the human hand, and with the aim of controlling the grip force and enhancing the stability of the grasp, two novel industrial variable passivity gripper designs have been proposed and examined in this work.

The proposed gripper designs provided a sufficiently larger interval of stiffness variability than similar existing systems. The grippers use two servomotors and one linear spring in their actuation system, which provide a relatively simple manufacturing process. Having just a single spring in the design also helped us to achieve a very small hysteresis band and a fast stiffness control.

As has been discussed in the design of a grasp controller, certain miscalculations in the system model are almost inevitable. These miscalculations arise for several reasons such as unpredictable disturbances (which is not considered in the model) as well as having to deal with objects with unknown parameters. It has been observed that this uncertain model creates difficulties when using conventional control methods for grasping tasks; however, it also has been shown that robust control methods represent an alternative solution to overcoming such difficulties.

Grasping and lifting an object with unknown friction and weight and in the presence of unpredictable external forces and/or the lack of a good estimation of the geometry and mass distribution of the object itself represent significant challenges. The main problem lies in the estimation of the exact gripping force that needs to be applied to maintain the grasp without damaging or deforming the object.

With the aim of preventing slippage whilst simultaneously minimising any deformation of the grasped object, a novel MIMO active slip prevention controller has been presented and evaluated. A two-finger tendon-driven gripper equipped with a novel arrangement of low-cost flexible force and slip sensors has been presented. This gripper was used to evaluate the performance of the proposed controllers in overcoming any undesired slippage of the grasped object.

The main shortcoming of the conventional sliding mode control that has been addressed in this work is its tendency to oscillate due to its discrete sign function.

Furthermore, it has been found that the performance of the first-order sliding mode control is also worsened by the fact that the amplitude of the chattering depends on the object's mechanical properties, more specifically its stiffness; the greater the stiffness, the higher the

chattering amplitude. The designed hybrid super-twisting mode control satisfactorily eliminated chattering in the tests and provided consistent performance for any grasped object with different stiffness, friction and weights.

Finally, a 8 kg and a 45 kg payload gripper have been proposed. The grippers were designed and fabricated as part of this work. The grippers used a novel adaptive super-twisting mode and adaptive first-order sliding mode controllers that have been designed to prevent slippage whilst minimising any deformation of the grasped object and undesired chatter. Similar to the tendon-driven gripper, both these controllers used force and slip feedback to counteract any slippage; in order to measure the slip, the gripper used a pair of optical flow sensors in the 8 kg payload gripper and an ultrasonic sensor in the 45 kg payload gripper, whereas the force feedback was measured through estimating the motor current.

The performance of the designed adaptive super-twisting mode controller has been evaluated against the proposed adaptive sliding mode control. The main difference between these controllers compared to those used to control the first tendon-driven gripper was that the former controls the grip force directly in order to achieve a robust grasp, whereas the latter regulated the rotational velocity of the servomotors to control the grasping task. The experimental results collected from the grippers showed that the controllers were sufficiently robust to overcome external nonlinear disturbances and inaccuracies in the system model when they were grasping and lifting unknown objects.

The results showed that both controllers satisfactorily prevented slippage and minimised any deformation of the objects. Furthermore, the proposed controllers eliminated the above-mentioned chattering phenomenon of the conventional sliding mode control whilst preserving its robustness.

6.2 List of contributions

The two primary contributions of this thesis are:

❖ Direct impedance modulation for stable grasping in tendon driven, angular grippers:

- ✓ Design and development of a novel variable stiffness gripper, capable of grasping unknown objects mainly intended for use by agricultural and food companies.

- ✓ Design development and validation of a novel force control algorithm that passively controls the grip force in variable stiffness grippers. Due to the passive nature of the controller, it completely eliminates the necessity for any force sensor. The combination of both the proposed variable stiffness gripper and passivity based control, provides a unique solution for the stable grasp and force control problem in tendon driven, angular grippers.

❖ **Active MIMO slip prevention grasp control for direct drive parallel jaw grippers:**

- ✓ Design, development and validation of a novel active multi input-multi output slip prevention algorithm. The algorithm provides a robust control solution to endow direct drive parallel jaw grippers with the capability to stop held objects from slipping while incurring minimum deformation; this can be achieved without any prior knowledge of the object's friction and weight. This means that unknown objects can be grasped without the need for the grasp to be pre-programmed in advance.

6.3 Design and developments

To achieve the contributions detailed above the thesis resulted in the following scientific developments:

- Design, development and modification of a novel variable compliance mechanism for industrial grippers.
- Mathematical modelling of the stiffness function of the proposed variable stiffness mechanisms with respect to the control parameters.
- Design and development of a new hybrid PI-SMC, and a hybrid PI-STSMC speed-control for robotic grasping tasks.
- Design and fabrication of a tendon-driven gripper and a four-finger direct drive hand equipped with a new combination of force-slip sensors.

- Design and development of an innovative adaptive SMC and STSMC robust grasp controller.
- Development and fabrication of a direct-drive 8 kg payload gripper and a 45 kg payload gripper with two different slip-sensing mechanisms.

6.3 Limitations and Future Work

Although all the pre-planned aims and objectives of this work have been successfully accomplished, nevertheless improvements to these works can be conducted.

1. To evaluate the performance of the proposed variable stiffness grippers and collect the experimental data, the stiffness had to be adjusted manually, as based on previous knowledge of the objects being handled. Therefore, the next phase of this work will consist of integrating a visual object recognition method for automatic adjustment of stiffness values.
2. The proposed variable stiffness designs used a tendon pulley mechanism to actuate an underactuated two-finger and three-finger grippers. Although the 3D printed prototypes presented were sufficient to verify the proposed concept of the variable stiffness mechanism, they could nevertheless be modified for used as the actuation system for grippers with more degrees of freedom.
3. In the variable stiffness grippers, there is an extra payload on the shaft of the second motor M2. This extra payload comes from the weight of the first motor M1. Clearly this extra payload can cause excessive power consumption and reduce the efficiency of the system. This problem will be addressed in future work by modifying the design in a way so as to remove this payload from the sliding mechanism.
4. Future work on these mechanisms could include an attempt to reduce friction and to make the system more compact.
5. The grippers presented in this work use only one type of slip sensor per gripper (i.e., membrane potentiometer, optical flow and ultrasonic sensor). Although these sensors

- have showed remarkable accuracy in measuring object slippage, a sensor fusion/combination method might further be considered in order to increase the accuracy of the data feedback received from the slip sensors.
6. On the 45 kg payload gripper, the dexterity could be improved by increasing the degrees of freedom (increasing the number of fingers and joints) to achieve more complex tasks such as in-hand manipulation and re-grasping of objects rather than just pick and place.
 7. Creating a modular and scalable design will be considered in future work. Such a design will allow for further adaptability through the addition/removal of additional fingers easily and quickly.
 8. Incorporating a low-cost vision system with the gripper will be considered in future work to provide an approximate position for the objects to be grasped.
 9. Further work on AI learning methods to assess and optimise the grasp will be used for the next version of the grippers, which will have more degrees of freedom.
 10. An environmental protection will be designed for the gripper to allow it to work in environments where water/liquids might well be encountered (e.g., nuclear decommissioning or under water in the oil and gas sector).
 11. The possibility of using the control designs in a prosthetic hand or exoskeleton actuated by pneumatic artificial muscles will be evaluated.
 12. The grippers and controllers presented were designed to be used in KUKA platforms. However, they could be further improved through the development of an embedded control system, allowing the grippers to be used with any type of industrial robot manipulator.
 13. Finally, as suggested in chapter four, integrating the proposed controllers with in-hand control methods can allow them to outperform the current performance associated

with in-hand manipulation tasks. To investigate this idea, an AI-sliding mode cascade control will be designed for the four-finger hand.

APPENDIX A

$$\dot{\Lambda}_\sigma = \sigma \dot{\sigma} = (\eta X_2 + (-\eta X_2 + \varrho) + F_{au})\sigma \quad \text{A1}$$

Where $\varrho = -\Omega \text{sign}(\sigma)$

$$\dot{\Lambda}_\sigma \leq |\sigma|D + \sigma\varrho \quad \text{A2}$$

$$\dot{\Lambda}_\sigma \leq -|\sigma|(\Omega - D) = -\frac{\xi}{\sqrt{2}}|\sigma| \quad \text{A3}$$

$$\Omega = D + \frac{\xi}{\sqrt{2}} \quad \text{A4}$$

$$F_a = -\eta X_2 - \Omega \text{sign}(\sigma) \quad \text{A5}$$

REFERENCES

- [1] Kurfess, T.R. ed., 2004. *Robotics and automation handbook*. CRC press.
- [2] Hogan, N., 1985. Impedance control: An approach to manipulation: Part II—Implementation. *Journal of dynamic systems, measurement, and control*, 107(1), pp.8-16.
- [3] Hogan, N., 1988. On the stability of manipulators performing contact tasks. *IEEE Journal on Robotics and Automation*, 4(6), pp.677-686.
- [4] Colgate, J.E. and Hogan, N., 1988. Robust control of dynamically interacting systems. *International journal of Control*, 48(1), pp.65-88.
- [5] Buerger, S.P. and Hogan, N., 2007. Complementary stability and loop shaping for improved human–robot interaction. *IEEE Transactions on Robotics*, 23(2), pp.232-244.
- [6] Siciliano, B. and Khatib, O. eds., 2008. *Springer handbook of robotics*. Springer Science & Business Media.
- [7] Kaneko, M., 1990. A realization of stable grasp based on virtual stiffness model by robot fingers. In *Proceedings of IEEE International Workshop on Advanced Motion Control, Yokohama* (Vol. 156).
- [8] Hanafusa, H., 1977. Stable prehension by a robot hand with elastic fingers. In *Proc. 7th Int. Symp. on Industrial Robots, Tokyo, 1977* (pp. 361-368).
- [9] Ott, C., Albu-Schaffer, A., Kugi, A. and Hirzinger, G., 2008. On the passivity-based impedance control of flexible joint robots. *IEEE Transactions on Robotics*, 24(2), pp.416-429.
- [10] Dohring, M. and Newman, W., 2002. Admittance enhancement in force feedback of dynamic systems. In *Robotics and Automation, 2002. Proceedings. ICRA'02. IEEE International Conference on* (Vol. 1, pp. 638-643). IEEE.
- [11] Ozparpucu, M.C. and Haddadin, S., 2014, June. Optimal control of elastic joints with variable damping. In *Control Conference (ECC), 2014 European* (pp. 2526-2533). IEEE.
- [12] Kashiri, N., Laffranchi, M., Caldwell, D.G. and Tsagarakis, N.G., 2016. Dynamics and control of an anthropomorphic compliant arm equipped with friction clutches. *IEEE/ASME Transactions on Mechatronics*, 21(2), pp.694-707.

- [13] Kashiri, N., Caldwell, D.G. and Tsagarakis, N., 2017, May. A self-adaptive variable impedance actuator based on intrinsic non-linear compliance and damping principles. In *Robotics and Automation (ICRA), 2017 IEEE International Conference on* (pp. 1248-1254). IEEE.
- [14] Petit, F. and Albu-Schäffer, A., 2011, May. State feedback damping control for a multi dof variable stiffness robot arm. In *Robotics and Automation (ICRA), 2011 IEEE International Conference on* (pp. 5561-5567). IEEE.
- [15] Kehoe, B., Matsukawa, A., Candido, S., Kuffner, J. and Goldberg, K., 2013, May. Cloud-based robot grasping with the google object recognition engine. In *Robotics and Automation (ICRA), 2013 IEEE International Conference on* (pp. 4263-4270). IEEE.
- [16] Mahler, J., Pokorný, F.T., Hou, B., Roderick, M., Laskey, M., Aubry, M., Kohlhoff, K., Kröger, T., Kuffner, J. and Goldberg, K., 2016, May. Dex-net 1.0: A cloud-based network of 3d objects for robust grasp planning using a multi-armed bandit model with correlated rewards. In *Robotics and Automation (ICRA), 2016 IEEE International Conference on* (pp. 1957-1964). IEEE.
- [17] Calli, B., Caarls, W., Wisse, M. and Jonker, P.P., 2018. Active Vision via Extremum Seeking for Robots in Unstructured Environments: Applications in Object Recognition and Manipulation. *IEEE Transactions on Automation Science and Engineering*.
- [18] Chen, S., Li, Y. and Kwok, N.M., 2011. Active vision in robotic systems: A survey of recent developments. *International Journal of Robotics Research*, 30(11), pp.1343-1377.
- [19] Asif, U., Bennamoun, M. and Sohel, F.A., 2017. Rgb-d object recognition and grasp detection using hierarchical cascaded forests. *IEEE Transactions on Robotics*, 33(3), pp.547-564.
- [20] Sun, F., Liu, C., Huang, W. and Zhang, J., 2016. Object classification and grasp planning using visual and tactile sensing. *IEEE Transactions on Systems, Man, and Cybernetics: Systems*, 46(7), pp.969-979.
- [21] Okamura, A.M. and Cutkosky, M.R., 1999. Haptic exploration of fine surface features. In *Robotics and Automation, 1999. Proceedings. 1999 IEEE International Conference on* (Vol. 4, pp. 2930-2936). IEEE.
- [22] Chitta, S., Piccoli, M. and Sturm, J., 2010, May. Tactile object class and internal

- state recognition for mobile manipulation. In *Robotics and Automation (ICRA), 2010 IEEE International Conference on* (pp. 2342-2348). IEEE.
- [23] Schmitz, A., Bansho, Y., Noda, K., Iwata, H., Ogata, T. and Sugano, S., 2014, November. Tactile object recognition using deep learning and dropout. In *Humanoid Robots (Humanoids), 2014 14th IEEE-RAS International Conference on* (pp. 1044-1050). IEEE.
- [24] Dahiya, R.S., Metta, G., Valle, M. and Sandini, G., 2010. Tactile sensing—from humans to humanoids. *IEEE transactions on robotics*, 26(1), pp.1-20.
- [25] Allen, P.K., 1988. Integrating vision and touch for object recognition tasks. *The International Journal of Robotics Research*, 7(6), pp.15-33.
- [26] Jamali, N. and Sammut, C., 2010, May. Material classification by tactile sensing using surface textures. In *Robotics and Automation (ICRA), 2010 IEEE International Conference on* (pp. 2336-2341). IEEE.
- [27] Wu, L., de Andrade, M.J., Saharan, L.K., Rome, R.S., Baughman, R.H. and Tadesse, Y., 2017. Compact and low-cost humanoid hand powered by nylon artificial muscles. *Bioinspiration & biomimetics*, 12(2), p.026004.
- [28] Jeong, S.H., Kim, K.S. and Kim, S., 2017. Designing anthropomorphic robot hand with active dual-mode twisted string actuation mechanism and tiny tension sensors. *IEEE Robotics and Automation Letters*, 2(3), pp.1571-1578.
- [29] Lovchik, C.S. and Diftler, M.A., 1999. The robonaut hand: A dexterous robot hand for space. In *Robotics and Automation, 1999. Proceedings. 1999 IEEE International Conference on* (Vol. 2, pp. 907-912). IEEE.
- [30] Sugio, N., Kinouchi, Y. and Shirai, F., 1997. Grasping Control of Robot Hand by Autonomous Learning Algorithm. *IFAC Proceedings Volumes*, 30(25), pp.233-238.
- [31] Maekawa, H., Yokoi, K., Tanie, K., Kaneko, M., Kimura, N. and Imamura, N., 1992. Development of a three-fingered robot hand with stiffness control capability. *Mechatronics*, 2(5), pp.483-494.
- [32] Okada, T., 1982. Computer control of multijointed finger system for precise object-handling. *IEEE Transactions on Systems, Man, and Cybernetics*, 12(3), pp.289-299.
- [33] Dai, J.S. and Wang, D., 2007. Geometric analysis and synthesis of the metamorphic robotic hand. *Journal of mechanical design*, 129(11), pp.1191-1197.
- [34] Ide, S. and Nishikawa, A., 2016. Bioinspired control of a multifingered robot hand

- with musculoskeletal system. In *Smart Textiles and their Applications* (pp. 185-195).
- [35] Gosselin, C., Pelletier, F. and Laliberte, T., 2008, May. An anthropomorphic underactuated robotic hand with 15 dofs and a single actuator. In *Robotics and Automation, 2008. ICRA 2008. IEEE International Conference on* (pp. 749-754). IEEE.
- [36] Jacobsen, S., Iversen, E., Knutti, D., Johnson, R. and Biggers, K., 1986, April. Design of the Utah/MIT dextrous hand. In *Robotics and Automation. Proceedings. 1986 IEEE International Conference on* (Vol. 3, pp. 1520-1532). IEEE.
- [37] Venkataraman, S.T. and Iberall, T. eds., 2012. *Dextrous robot hands*. Springer Science & Business Media.
- [38] Wu, C.H., Houk, J.C., Young, K.Y. and Miller, L.E., 1990. Nonlinear damping of limb motion. In *Multiple muscle systems* (pp. 214-235). Springer, New York, NY.
- [39] Esteki, A. and Mansour, J.M., 1996. An experimentally based nonlinear viscoelastic model of joint passive moment. *Journal of biomechanics*, 29(4), pp.443-450.
- [40] Shrivastava, N., Koff, M.F., Abbot, A.E., Mow, V.C., Rosenwasser, M.P. and Strauch, R.J., 2003. Simulated extension osteotomy of the thumb metacarpal reduces carpometacarpal joint laxity in lateral pinch1. *Journal of Hand Surgery*, 28(5), pp.733-738.
- [41] Minami, A., An, K.N., Cooney III, W.P., Linscheid, R.L. and Chao, E.Y., 1985. Ligament stability of the metacarpophalangeal joint: a biomechanical study. *The Journal of hand surgery*, 10(2), pp.255-260.
- [42] Tamai, K., Ryu, J., An, K.N., Linscheid, R.L., Cooney, W.P. and Chao, E.Y.S., 1988. Three-dimensional geometric analysis of the metacarpophalangeal joint. *Journal of Hand Surgery*, 13(4), pp.521-529.
- [43] Kuo, P.H. and Deshpande, A.D., 2012. Muscle-tendon units provide limited contributions to the passive stiffness of the index finger metacarpophalangeal joint. *Journal of biomechanics*, 45(15), pp.2531-2538.
- [44] Qin, J., Lee, D., Li, Z., Chen, H. and Dennerlein, J.T., 2010. Estimating in vivo passive forces of the index finger muscles: Exploring model parameters. *Journal of biomechanics*, 43(7), pp.1358-1363.
- [45] Carrozza, M.C., Cappiello, G., Stellin, G., Zaccone, F., Vecchi, F., Micera, S. and Dario, P., 2005, April. A cosmetic prosthetic hand with tendon driven under-

- actuated mechanism and compliant joints: ongoing research and preliminary results. In *Robotics and Automation, 2005. ICRA 2005. Proceedings of the 2005 IEEE International Conference on* (pp. 2661-2666). IEEE.
- [46] Carozza, M.C., Cappiello, G., Stellin, G., Zaccone, F., Vecchi, F., Micera, S. and Dario, P., 2005, August. On the development of a novel adaptive prosthetic hand with compliant joints: experimental platform and EMG control. In *Intelligent Robots and Systems, 2005.(IROS 2005). 2005 IEEE/RSJ International Conference on* (pp. 1271-1276). IEEE.
- [47] Tondu, B., Boitier, V. and Lopez, P., 1994, October. Naturally compliant robot-arms actuated by McKibben artificial muscles. In *Systems, Man, and Cybernetics, 1994. Humans, Information and Technology., 1994 IEEE International Conference on* (Vol. 3, pp. 2635-2640). IEEE.
- [48] Carrozza, M.C., Massa, B., Micera, S., Zecca, M. and Dario, P., 2001, November. A wearable artificial hand for prosthetics and humanoid robotics applications. In *Proceedings of the 2001 IEEE-RAS International Conference on Humanoid Robots*.
- [49] English, C.E. and Russell, D., 1999. Mechanics and stiffness limitations of a variable stiffness actuator for use in prosthetic limbs. *Mechanism and machine theory*, 34(1), pp.7-25.
- [50] Christensen, R.J., CHRISTENSEN ROLAND J AS OPERATING MANAGER OF RJC DEVELOPMENT LC GENERAL PARTNER OF ROLAND J CHRISTENSEN FAMILY LP, 2003. *Prosthetic foot with energy transfer medium including variable viscosity fluid*. U.S. Patent 6,663,673.
- [51] Pratt, G.A. and Williamson, M.M., 1995, August. Series elastic actuators. In *Intelligent Robots and Systems 95.'Human Robot Interaction and Cooperative Robots', Proceedings. 1995 IEEE/RSJ International Conference on* (Vol. 1, pp. 399-406). IEEE.
- [52] Robinson, D.W., Pratt, J.E., Paluska, D.J. and Pratt, G.A., 1999, September. Series elastic actuator development for a biomimetic walking robot. In *Advanced Intelligent Mechatronics, 1999. Proceedings. 1999 IEEE/ASME International Conference on* (pp. 561-568). IEEE.
- [53] Pratt, Gill A. and Matthew M. Williamson "Series Elastic Actuators", presented at *IROS 95*, Pittsburgh, PA, 1995.
- [54] Robinson, D.W. and Pratt, G.A., 2000. Force controllable hydro-elastic actuator. In *Robotics and Automation, 2000. Proceedings. ICRA'00. IEEE International*

Conference on (Vol. 2, pp. 1321-1327). IEEE.

- [55] Tsagarakis, N.G., Laffranchi, M., Vanderborght, B. and Caldwell, D.G., 2009, May. A compact soft actuator unit for small scale human friendly robots. In *Robotics and Automation, 2009. ICRA'09. IEEE International Conference on* (pp. 4356-4362). IEEE.
- [56] Tsagarakis, N.G., Sardellitti, I. and Caldwell, D.G., 2011, September. A new variable stiffness actuator (CompAct-VSA): Design and modelling. In *Intelligent Robots and Systems (IROS), 2011 IEEE/RSJ International Conference on* (pp. 378-383). IEEE.
- [57] Kong, K., Bae, J. and Tomizuka, M., 2012. A compact rotary series elastic actuator for human assistive systems. *IEEE/ASME transactions on mechatronics*, 17(2), pp.288-297.
- [58] Woo, H., Na, B. and Kong, K., 2017, May. Design of a compact rotary series elastic actuator for improved actuation transparency and mechanical safety. In *Robotics and Automation (ICRA), 2017 IEEE International Conference on* (pp. 1872-1877). IEEE.
- [59] Sugar, T.G., 2002. A novel selective compliant actuator. *Mechatronics*, 12(9-10), pp.1157-1171.
- [60] Tonietti, G., Schiavi, R. and Bicchi, A., 2005, April. Design and control of a variable stiffness actuator for safe and fast physical human/robot interaction. In *Robotics and Automation, 2005. ICRA 2005. Proceedings of the 2005 IEEE International Conference on* (pp. 526-531). IEEE.
- [61] Bicchi, A., Tonietti, G., Bavaro, M. and Piccigallo, M., 2005. Variable stiffness actuators for fast and safe motion control. In *Robotics Research. The Eleventh International Symposium* (pp. 527-536). Springer, Berlin, Heidelberg.
- [62] Robinson, D.W., 2000. *Design and analysis of series elasticity in closed-loop actuator force control* (Doctoral dissertation, Massachusetts Institute of Technology).
- [63] Inoue, T., Miyata, R. and Hirai, S., 2016, October. Force control on antagonistic twist-drive actuator robot. In *Intelligent Robots and Systems (IROS), 2016 IEEE/RSJ International Conference on* (pp. 3830-3835). IEEE.
- [64] Van Ham, R., Vanderborght, B., Van Damme, M., Verrelst, B. and Lefeber, D., 2006, May. MACCEPA: the mechanically adjustable compliance and controllable

- equilibrium position actuator for 'controlled passive walking'. In *Robotics and Automation, 2006. ICRA 2006. Proceedings 2006 IEEE International Conference on* (pp. 2195-2200). IEEE.
- [65] Van Ham, R., Vanderborght, B., Van Damme, M., Verrelst, B. and Lefeber, D., 2007. MACCEPA, the mechanically adjustable compliance and controllable equilibrium position actuator: Design and implementation in a biped robot. *Robotics and Autonomous Systems*, 55(10), pp.761-768.
- [66] Vanderborght, B., Tsagarakis, N.G., Semini, C., Van Ham, R. and Caldwell, D.G., 2009, May. MACCEPA 2.0: Adjustable compliant actuator with stiffening characteristic for energy efficient hopping. In *Robotics and Automation, 2009. ICRA'09. IEEE International Conference on* (pp. 544-549). IEEE.
- [67] Wolf, S. and Hirzinger, G., 2008, May. A new variable stiffness design: Matching requirements of the next robot generation. In *Robotics and Automation, 2008. ICRA 2008. IEEE International Conference on* (pp. 1741-1746). IEEE.
- [68] Chalvet, V. and Braun, D.J., 2017. Algorithmic Design of Low-Power Variable-Stiffness Mechanisms. *IEEE Transactions on Robotics*, 33(6), pp.1508-1515.
- [69] Kim, B.S. and Song, J.B., 2012. Design and control of a variable stiffness actuator based on adjustable moment arm. *IEEE Transactions on Robotics*, 28(5), pp.1145-1151.
- [70] Choi, J., Hong, S., Lee, W. and Kang, S., 2009, May. A variable stiffness joint using leaf springs for robot manipulators. In *Robotics and Automation, 2009. ICRA'09. IEEE International Conference on* (pp. 4363-4368). IEEE.
- [71] Grebenstein, M. and van der Smagt, P., 2008. Antagonism for a highly anthropomorphic hand–arm system. *Advanced Robotics*, 22(1), pp.39-55.
- [72] Grebenstein, M., Chalon, M., Friedl, W., Haddadin, S., Wimböck, T., Hirzinger, G. and Siegwart, R., 2012. The hand of the DLR hand arm system: Designed for interaction. *International Journal of Robotics Research*, 31(13), pp.1531-1555.
- [73] Grebenstein, M., Chalon, M., Hirzinger, G. and Siegwart, R., 2010, December. Antagonistically driven finger design for the anthropomorphic DLR hand arm system. In *Humanoid Robots (Humanoids), 2010 10th IEEE-RAS International Conference on* (pp. 609-616). IEEE.
- [74] Schulte, H.F., 1961. J., "The characteristics of the mckibben artificial muscle," in [The Application of External Power in Prosthetics and Orthotics], Washington, DC:

Nat. Acad. Sci.-Nat. Res. Council.

- [75] Shin, D., Yeh, X. and Khatib, O., 2014. A new hybrid actuation scheme with artificial pneumatic muscles and a magnetic particle brake for safe human–robot collaboration. *The International Journal of Robotics Research*, 33(4), pp.507-518.
- [76] Chou, C.P. and Hannaford, B., 1996. Measurement and modeling of McKibben pneumatic artificial muscles. *IEEE Transactions on robotics and automation*, 12(1), pp.90-102.
- [77] Kobayashi, H., Ishida, Y. and Suzuki, H., 2004, September. Realization of all motion for the upper limb by a muscle suit. In *Robot and Human Interactive Communication, 2004. ROMAN 2004. 13th IEEE International Workshop on* (pp. 631-636). IEEE.
- [78] Chou, C.P. and Hannaford, B., 1994, May. Static and dynamic characteristics of McKibben pneumatic artificial muscles. In *Robotics and Automation, 1994. Proceedings., 1994 IEEE International Conference on* (pp. 281-286). IEEE.
- [79] van der Linde, R.Q., 1999. Design, analysis, and control of a low power joint for walking robots, by phasic activation of McKibben muscles. *IEEE transactions on robotics and automation*, 15(4), pp.599-604.
- [80] Kang, B.S., Kothera, C.S., Woods, B.K. and Wereley, N.M., 2009, May. Dynamic modeling of Mckibben pneumatic artificial muscles for antagonistic actuation. In *Robotics and Automation, 2009. ICRA'09. IEEE International Conference on* (pp. 182-187). IEEE.
- [81] Tondu, B. and Lopez, P., 1997. The McKibben muscle and its use in actuating robot-arms showing similarities with human arm behaviour. *Industrial Robot: An International Journal*, 24(6), pp.432-439.
- [82] Takuma, T., Nakajima, S., Hosoda, K. and Asada, M., 2004, August. Design of self-contained biped walker with pneumatic actuators. In *SICE 2004 Annual Conference* (Vol. 3, pp. 2520-2524). IEEE.
- [83] Davis, S., Canderle, J., Artrit, P., Tsagarakis, N. and Caldwell, D.G., 2002. Enhanced dynamic performance in pneumatic muscle actuators. In *Robotics and Automation, 2002. Proceedings. ICRA'02. IEEE International Conference on* (Vol. 3, pp. 2836-2841). IEEE.
- [84] Yeh, T.J., Wu, M.J., Lu, T.J., Wu, F.K. and Huang, C.R., 2010. Control of McKibben pneumatic muscles for a power-assist, lower-limb

orthosis. *Mechatronics*, 20(6), pp.686-697.

- [85] Ouanezar, S., Jean, F., Tondu, B., Maier, M.A., Darlot, C. and Eskiizmirli, S., 2011, May. Biologically inspired sensory motor control of a 2-link robotic arm actuated by McKibben muscles. In *Robotics and Automation (ICRA), 2011 IEEE International Conference on* (pp. 2785-2791). IEEE.
- [86] Meller, M.A., Bryant, M. and Garcia, E., 2014. Reconsidering the McKibben muscle: Energetics, operating fluid, and bladder material. *Journal of Intelligent Material Systems and Structures*, 25(18), pp.2276-2293.
- [87] Tondu, B., 2012. Modelling of the McKibben artificial muscle: A review. *Journal of Intelligent Material Systems and Structures*, 23(3), pp.225-253.
- [88] Vitale, F., Accoto, D., Turchetti, L., Indini, S., Annesini, M.C. and Guglielmelli, E., 2010, May. Low-temperature H₂O₂-powered actuators for biorobotics: Thermodynamic and kinetic analysis. In *Robotics and Automation (ICRA), 2010 IEEE International Conference on* (pp. 2197-2202). IEEE.
- [89] Fite, K.B., Withrow, T.J., Shen, X., Wait, K.W., Mitchell, J.E. and Goldfarb, M., 2008. A gas-actuated anthropomorphic prosthesis for transhumeral amputees. *IEEE Transactions on Robotics*, 24(1), pp.159-169.
- [90] Hurst, J.W., Chestnutt, J.E. and Rizzi, A.A., 2004, April. An actuator with physically variable stiffness for highly dynamic legged locomotion. In *Robotics and Automation, 2004. Proceedings. ICRA'04. 2004 IEEE International Conference on* (Vol. 5, pp. 4662-4667). IEEE.
- [91] English, C.E. and Russell, D., 1999. Mechanics and stiffness limitations of a variable stiffness actuator for use in prosthetic limbs. *Mechanism and machine theory*, 34(1), pp.7-25.
- [92] Catalano, M.G., Grioli, G., Garabini, M., Bonomo, F., Mancini, M., Tsagarakis, N. and Bicchi, A., 2011, May. Vsa-cubebot: A modular variable stiffness platform for multiple degrees of freedom robots. In *Robotics and Automation (ICRA), 2011 IEEE International Conference on* (pp. 5090-5095). IEEE.
- [93] Mancini, M., Grioli, G., Catalano, M.G., Garabini, M., Bonomo, F. and Bicchi, A., 2012, May. Passive impedance control of a multi-DOF VSA-CubeBot manipulator. In *Robotics and Automation (ICRA), 2012 IEEE International Conference on* (pp. 3335-3340). IEEE.

- [94] Laffranchi, M., Tsagarakis, N.G. and Caldwell, D.G., 2010, May. A variable physical damping actuator (VPDA) for compliant robotic joints. In *Robotics and Automation (ICRA), 2010 IEEE International Conference on* (pp. 1668-1674). IEEE.
- [95] Visser, L.C., Carloni, R. and Stramigioli, S., 2011. Energy-efficient variable stiffness actuators. *IEEE Transactions on Robotics*, 27(5), pp.865-875.
- [96] Visser, L.C., Carloni, R., Ünal, R. and Stramigioli, S., 2010, May. Modeling and design of energy efficient variable stiffness actuators. In *Robotics and automation (icra), 2010 ieee international conference on* (pp. 3273-3278). IEEE.
- [97] Johansson, R.S. and Westling, G., 1988. Programmed and triggered actions to rapid load changes during precision grip. *Experimental brain research*, 71(1), pp.72-86.
- [98] Tahara, K., Luo, Z.W., Ozawa, R., Bae, J.H. and Arimoto, S., 2006, May. Bio-mimetic study on pinching motions of a dual-finger model with synergistic actuation of antagonist muscles. In *Robotics and Automation, 2006. ICRA 2006. Proceedings 2006 IEEE International Conference on* (pp. 994-999). IEEE.
- [99] Deshpande, A.D., Gialias, N. and Matsuoka, Y., 2012. Contributions of intrinsic visco-elastic torques during planar index finger and wrist movements. *IEEE Transactions on Biomedical Engineering*, 59(2), pp.586-594.
- [100] Kuo, P.H., DeBacker, J. and Deshpande, A.D., 2015, May. Design of robotic fingers with human-like passive parallel compliance. In *Robotics and Automation (ICRA), 2015 IEEE International Conference on* (pp. 2562-2567). IEEE.
- [101] Niehues, T.D., Rao, P. and Deshpande, A.D., 2015. Compliance in parallel to actuators for improving stability of robotic hands during grasping and manipulation. *The International Journal of Robotics Research*, 34(3), pp.256-269.
- [102] Kajikawa, S. and Abe, K., 2012, October. Development of robot hand with multi-directional variable stiffness for human-care services. In *Intelligent Robots and Systems (IROS), 2012 IEEE/RSJ International Conference on* (pp. 2889-2894). IEEE.
- [103] Yang, Y. and Chen, Y., 2016, June. Novel design and 3D printing of variable stiffness robotic fingers based on shape memory polymer. In *Biomedical Robotics and Biomechatronics (BioRob), 2016 6th IEEE International Conference on* (pp. 195-200). IEEE.
- [104] Yap, H.K., Lim, J.H., Nasrallah, F., Goh, J.C. and Yeow, R.C., 2015, May. A soft

exoskeleton for hand assistive and rehabilitation application using pneumatic actuators with variable stiffness. In *Robotics and Automation (ICRA), 2015 IEEE International Conference on* (pp. 4967-4972). IEEE.

- [105] Odhner, L.U., Jentoft, L.P., Claffee, M.R., Corson, N., Tenzer, Y., Ma, R.R., Buehler, M., Kohout, R., Howe, R.D. and Dollar, A.M., 2014. A compliant, underactuated hand for robust manipulation. *The International Journal of Robotics Research*, 33(5), pp.736-752.
- [106] Deimel, R. and Brock, O., 2013, May. A compliant hand based on a novel pneumatic actuator. In *Robotics and Automation (ICRA), 2013 IEEE International Conference on* (pp. 2047-2053). IEEE.
- [107] Kuo, P.H. and Deshpande, A.D., 2013, October. Novel Design of a Passive Variable Stiffness Joint Mechanism: Inspiration From Biomechanics of Hand Joints. In *ASME 2013 Dynamic Systems and Control Conference* (pp. V002T28A003-V002T28A003). American Society of Mechanical Engineers.
- [108] Dollar, A.M. and Howe, R.D., 2010. The highly adaptive SDM hand: Design and performance evaluation. *The international journal of robotics research*, 29(5), pp.585-597.
- [109] Dollar, A.M. and Howe, R.D., 2006. A robust compliant grasper via shape deposition manufacturing. *IEEE/ASME transactions on mechatronics*, 11(2), pp.154-161.
- [110] Dollar, A.M. and Howe, R.D., 2005. Towards grasping in unstructured environments: Grasper compliance and configuration optimization. *Advanced Robotics*, 19(5), pp.523-543.
- [111] Meng, Q., Wang, H., Li, P., Wang, L. and He, Z., 2006, June. Dexterous underwater robot hand: HEU Hand II. In *Mechatronics and Automation, Proceedings of the 2006 IEEE International Conference on* (pp. 1477-1482). IEEE.
- [112] Zollo, L., Roccella, S., Guglielmelli, E., Carrozza, M.C. and Dario, P., 2007. Biomechatronic design and control of an anthropomorphic artificial hand for prosthetic and robotic applications. *IEEE/ASME Transactions On Mechatronics*, 12(4), pp.418-429.
- [113] Oshima, R., Takayama, T., Omata, T., Kojima, K., Takase, K. and Tanaka, N., 2010. Assemblable three-fingered nine-degrees-of-freedom hand for laparoscopic surgery. *IEEE/ASME transactions on mechatronics*, 15(6), pp.862-870.

- [114] Park, S.W., Bae, J.H., Park, J.H. and Baeg, M.H., 2012, August. Development of an anthropomorphic robot hand aimed at practical use for wide service robot application. In *Automation Science and Engineering (CASE), 2012 IEEE International Conference on* (pp. 431-435). IEEE.
- [115] Pettersson, A., Davis, S., Gray, J.O., Dodd, T.J. and Ohlsson, T., 2010. Design of a magnetorheological robot gripper for handling of delicate food products with varying shapes. *Journal of Food Engineering*, 98(3), pp.332-338.
- [116] Maekawa, H., Yokoi, K., Tanie, K., Kaneko, M., Kimura, N. and Imamura, N., 1992. Development of a three-fingered robot hand with stiffness control capability. *Mechatronics*, 2(5), pp.483-494.
- [117] Liu, H., Meusel, P., Seitz, N., Willberg, B., Hirzinger, G., Jin, M.H., Liu, Y.W., Wei, R. and Xie, Z.W., 2007. The modular multisensory DLR-HIT-Hand. *Mechanism and Machine Theory*, 42(5), pp.612-625.
- [118] Liu, H., Meusel, P., Hirzinger, G., Jin, M., Liu, Y. and Xie, Z., 2008. The modular multisensory DLR-HIT-Hand: hardware and software architecture. *IEEE/ASME Transactions on mechatronics*, 13(4), pp.461-469.
- [119] Park, Y.L., Ryu, S.C., Black, R.J., Chau, K.K., Moslehi, B. and Cutkosky, M.R., 2009. Exoskeletal force-sensing end-effectors with embedded optical fiber-Bragg-grating sensors. *IEEE Transactions on Robotics*, 25(6), pp.1319-1331.
- [120] Guglielmino, E., Zullo, L., Cianchetti, M., Follador, M., Branson, D. and Caldwell, D.G., 2012, May. The application of embodiment theory to the design and control of an octopus-like robotic arm. In *Robotics and Automation (ICRA), 2012 IEEE International Conference on* (pp. 5277-5282). IEEE.
- [121] Tramacere, F., Beccai, L., Mattioli, F., Sinibaldi, E. and Mazzolai, B., 2012, May. Artificial adhesion mechanisms inspired by octopus suckers. In *Robotics and Automation (ICRA), 2012 IEEE International Conference on* (pp. 3846-3851). IEEE.
- [122] Kier, W.M. and Smith, A.M., 2002. The structure and adhesive mechanism of octopus suckers. *Integrative and Comparative Biology*, 42(6), pp.1146-1153.
- [123] Yeung, B.H. and Mills, J.K., 2004. Design of a six DOF reconfigurable gripper for flexible fixtureless assembly. *IEEE Transactions on Systems, Man, and Cybernetics, Part C (Applications and Reviews)*, 34(2), pp.226-235.
- [124] Kang, S., In, H. and Cho, K.J., 2012. Design of a passive brake mechanism for

tendon driven devices. *International Journal of Precision Engineering and Manufacturing*, 13(8), pp.1487-1490.

- [125] Fukaya, N., Asfour, T., Dillmann, R. and Toyama, S., 2013, November. Development of a five-finger dexterous hand without feedback control: The TUAT/Karlsruhe humanoid hand. In *Intelligent Robots and Systems (IROS), 2013 IEEE/RSJ International Conference on* (pp. 4533-4540). IEEE.
- [126] Lau, C.Y. and Chai, A., 2012. The Development of a low cost pneumatic air muscle actuated anthropomorphic robotic hand. *Procedia Engineering*, 41, pp.737-742.
- [127] Rasakatla, S. and Krishna, K.M., 2013, December. RAMA-1 highly dexterous 48DOF robotic hand using magnetic spherical joints. In *Robotics and Biomimetics (ROBIO), 2013 IEEE International Conference on* (pp. 816-823). IEEE.
- [128] Karnati, N., Kent, B.A. and Engeberg, E.D., 2013. Bioinspired sinusoidal finger joint synergies for a dexterous robotic hand to screw and unscrew objects with different diameters. *IEEE/ASME Transactions on Mechatronics*, 18(2), pp.612-623.
- [129] Chu, J.U., Jung, D.H. and Lee, Y.J., 2008, May. Design and control of a multifunction myoelectric hand with new adaptive grasping and self-locking mechanisms. In *Robotics and Automation, 2008. ICRA 2008. IEEE International Conference on* (pp. 743-748). IEEE.
- [130] Dai, J.S., Wang, D. and Cui, L., 2009. Orientation and workspace analysis of the multifingered metamorphic hand—Metahand. *IEEE Transactions on Robotics*, 25(4), pp.942-947.
- [131] Chen, L., Ge, M.F., He, D.X., Guan, Z.H. and Wang, Y.W., 2014, May. Synchronization control of multi-finger dexterous hand based on iterative learning control scheme. In *Control and Decision Conference (2014 CCDC), The 26th Chinese*(pp. 1162-1166). IEEE.
- [132] Stulp, F., Buchli, J., Ellmer, A., Mistry, M., Theodorou, E.A. and Schaal, S., 2012. Model-free reinforcement learning of impedance control in stochastic environments. *IEEE Transactions on Autonomous Mental Development*, 4(4), pp.330-341.
- [133] Howe, R.D., 2010. The Highly Adaptive SDM Hand: Design and Performance Evaluation. *The International Journal of Robotics Research*, 29(5), pp.585-597.
- [134] Kemp, C.C., Edsinger, A. and Torres-Jara, E., 2007. Challenges for robot manipulation in human environments [grand challenges of robotics]. *IEEE Robotics*

& *Automation Magazine*, 14(1), pp.20-29.

- [135] Romano, J.M., Hsiao, K., Niemeyer, G., Chitta, S. and Kuchenbecker, K.J., 2011. Human-inspired robotic grasp control with tactile sensing. *IEEE Transactions on Robotics*, 27(6), pp.1067-1079.
- [136] Engeberg, E.D. and Meek, S.G., 2011, September. Adaptive sliding mode control of grasped object slip for prosthetic hands. In *Intelligent Robots and Systems (IROS), 2011 IEEE/RSJ International Conference on* (pp. 4174-4179). IEEE.
- [137] Engeberg, E.D. and Meek, S.G., 2009. Backstepping and sliding mode control hybridized for a prosthetic hand. *IEEE Transactions on Neural Systems and Rehabilitation Engineering*, 17(1), pp.70-79.
- [138] Engeberg, E.D., Meek, S.G. and Minor, M.A., 2008. Hybrid force-velocity sliding mode control of a prosthetic hand. *IEEE Transactions on Biomedical Engineering*, 55(5), pp.1572-1581.
- [139] Edwards, C. and Spurgeon, S., 1998. *Sliding mode control: theory and applications*. Crc Press.
- [140] O'Toole, M., Bouazza-Marouf, K., Kerr, D. and Vloeberghs, M., 2010. Robust contact force controller for slip prevention in a robotic gripper. *Proceedings of the Institution of Mechanical Engineers, Part I: Journal of Systems and Control Engineering*, 224(3), pp.275-288.
- [141] Drakunov, S.V. and Utkin, V.I., 1992. Sliding mode control in dynamic systems. *International Journal of Control*, 55(4), pp.1029-1037.
- [142] Sayama, K., Tamamoto, T. and Koganezawa, K., 2015, July. Multi-joint gripper-control of envelope gripping. In *Advanced Intelligent Mechatronics (AIM), 2015 IEEE International Conference on* (pp. 336-341). IEEE.
- [143] Tamamoto, T. and Koganezawa, K., 2013, November. Multi-joint gripper with stiffness adjuster. In *Intelligent Robots and Systems (IROS), 2013 IEEE/RSJ International Conference on*(pp. 5481-5486). IEEE.
- [144] Kim, B.S. and Song, J.B., 2011, May. Object grasping using a 1 dof variable stiffness gripper actuated by a hybrid variable stiffness actuator. In *Robotics and Automation (ICRA), 2011 IEEE International Conference on* (pp. 4620-4625). IEEE.
- [145] Utkin, V., Guldner, J. and Shi, J., 2017. *Sliding mode control in electro-mechanical*

systems. CRC press.

- [146] Shtessel, Y., Edwards, C., Fridman, L. and Levant, A., 2014. *Sliding mode control and observation* (Vol. 10, pp. 978-0). New York: Birkhäuser.
- [147] Young, K.D., Utkin, V.I. and Ozguner, U., 1996, December. A control engineer's guide to sliding mode control. In *Variable Structure Systems, 1996. VSS'96. Proceedings., 1996 IEEE International Workshop on* (pp. 1-14). IEEE.
- [148] Perruquetti, W. and Barbot, J.P., 2002. *Sliding mode control in engineering*. CRC Press.
- [149] Bartolini, G., Fridman, L., Pisano, A. and Usai, E. eds., 2008. *Modern sliding mode control theory: New perspectives and applications* (Vol. 375). Springer Science & Business Media.
- [150] Kourtis, D., Kwok, H.F., Roach, N., Wing, A.M. and Praamstra, P., 2008. Maintaining grip: anticipatory and reactive EEG responses to load perturbations. *Journal of neurophysiology*, 99(2), pp.545-553.
- [151] Yoshida, K., Bertram, M.J., Hunter Cox, T.G. and Riso, R., 2017. Peripheral nerve recording electrodes and techniques. In *Neuroprosthetics: Theory and Practice* (pp. 377-466).
- [152] Cole, K.J. and Abbs, J.H., 1988. Grip force adjustments evoked by load force perturbations of a grasped object. *Journal of neurophysiology*, 60(4), pp.1513-1522.
- [153] Dugas, C. and Smith, A.M., 1992. Responses of cerebellar Purkinje cells to slip of a hand-held object. *Journal of neurophysiology*, 67(3), pp.483-495.
- [154] Johansson, R.S. and Westling, G., 1987. Signals in tactile afferents from the fingers eliciting adaptive motor responses during precision grip. *Experimental brain research*, 66(1), pp.141-154.
- [155] Flanagan, J.R. and Wing, A.M., 1997. The role of internal models in motion planning and control: evidence from grip force adjustments during movements of hand-held loads. *Journal of Neuroscience*, 17(4), pp.1519-1528.
- [156] Yoshida, K. and Riso, R., 2004. PERIPHERAL NERVE RECORDING ELECTRODES AND TECHNIQUES. In *Neuroprosthetics: Theory and Practice* (pp. 683-744).
- [157] Birznieks, I., Jenmalm, P., Goodwin, A.W. and Johansson, R.S., 2001. Encoding of

- direction of fingertip forces by human tactile afferents. *Journal of Neuroscience*, 21(20), pp.8222-8237.
- [158] O’Doherty, J.E., Lebedev, M.A., Ifft, P.J., Zhuang, K.Z., Shokur, S., Bleuler, H. and Nicolelis, M.A., 2011. Active tactile exploration using a brain–machine–brain interface. *Nature*, 479(7372), p.228.
- [159] Häger-Ross, C. and Johansson, R.S., 1996. Nondigital afferent input in reactive control of fingertip forces during precision grip. *Experimental brain research*, 110(1), pp.131-141.
- [160] Ward-Cherrier, B., Rojas, N. and Lepora, N.F., 2017. Model-free precise in-hand manipulation with a 3d-printed tactile gripper. *IEEE Robotics and Automation Letters*, 2(4), pp.2056-2063.
- [161] Rothling, F., Haschke, R., Steil, J.J. and Ritter, H., 2007, October. Platform portable anthropomorphic grasping with the bielefeld 20-dof shadow and 9-dof tum hand. In *Intelligent Robots and Systems, 2007. IROS 2007. IEEE/RSJ International Conference on* (pp. 2951-2956).
- [162] Shadow Dexterous Hand Technical Specification. Retrieved from <https://www.shadowrobot.com/tag/motor-hand/>
- [163] Brown, E., Rodenberg, N., Amend, J., Mozeika, A., Steltz, E., Zakin, M.R., Lipson, H. and Jaeger, H.M., 2010. Universal robotic gripper based on the jamming of granular material. *Proceedings of the National Academy of Sciences*, 107(44), pp.18809-18814
- [164] John R. Amend, Jr., Student Member, IEEE, Eric Brown, Nicholas Rodenberg, Heinrich M. Jaeger, and Hod Lipson, Member, IEEE, A Positive Pressure Universal Gripper Based on the Jamming of Granular Material, *IEEE TRANSACTIONS ON ROBOTICS*, VOL. 28, NO. 2, APRIL 2012.
- [165] Festo flexshape and Festo adaptive gripper fingers DHAS. Retrieved from <https://www.festo.com>
- [166] Yuki OKATANI, Takeshi NISHIDA, Kenjiro TADAKUMA, Development of Universal Robot Gripper Using MR α Fluid, SCIS&ISIS 2014, Kitakyushu, Japan, December 3-6, 2014.
- [167] DLR-HIT dexterous hand. Retrieved from: <https://www.dlr.de>
- [168] Chen, W., Zhao, S. and Chow, S.L., 2014. Grippers and End Effectors. In *Handbook of Manufacturing Engineering and Technology* (pp. 1-32). Springer, London.
- [169] Flat vacuum cups for dynamic handling of oily metal sheets. Retrieved from:

https://www.fipa.com/en_GB/products/216073-vacuum-cup-series

- [170] Electromagnetic lifters for bundles. Retrieved from: <https://www.goudsmitmagnets.com>
- [171] Máximo A. Roa · Raúl Suárez, Grasp quality measures: review and performance, *Auton Robot* (2015) 38:65–88 DOI 10.1007/s10514-014-9402-3.
- [172] Berenson, D., Diankov, R., Nishiwaki, K., Kagami, S. and Kuffner, J., 2007, November. Grasp planning in complex scenes. In *Humanoid Robots, 2007 7th IEEE-RAS International Conference on* (pp. 42-48).
- [173] Bohg, J., Morales, A., Asfour, T. and Kragic, D., 2014. Data-driven grasp synthesis—a survey. *IEEE Transactions on Robotics*, 30(2), pp.289-309.
- [174] Sahbani, A., El-Khoury, S. and Bidaud, P., 2012. An overview of 3D object grasp synthesis algorithms. *Robotics and Autonomous Systems*, 60(3), pp.326-336.
- [175] Cutkosky, M.R., 1989. On grasp choice, grasp models, and the design of hands for manufacturing tasks. *IEEE Transactions on robotics and automation*, 5(3), pp.269-279.
- [176] Hsiao, K. and Lozano-Perez, T., 2006, October. Imitation learning of whole-body grasps. In *Intelligent Robots and Systems, 2006 IEEE/RSJ International Conference on* (pp. 5657-5662).
- [177] Lenz, I., Lee, H. and Saxena, A., 2015. Deep learning for detecting robotic grasps. *The International Journal of Robotics Research*, 34(4-5), pp.705-724.
- [178] Shimoga, K.B., 1996. Robot grasp synthesis algorithms: A survey. *The International Journal of Robotics Research*, 15(3), pp.230-266.
- [179] Howard, W.S. and Kumar, V., 1996. On the stability of grasped objects. *IEEE transactions on robotics and automation*, 12(6), pp.904-917.
- [180] [Cutkosky, M.R., 1989. On grasp choice, grasp models, and the design of hands for manufacturing tasks. *IEEE Transactions on robotics and automation*, 5(3), pp.269-279.
- [181] Bruyninckx, H., Demey, S. and Kumar, V., 1998, May. Generalized stability of compliant grasps. In *Robotics and Automation, 1998. Proceedings. 1998 IEEE International Conference on* (Vol. 3, pp. 2396-2402).
- [182] Bicchi, A., 1995. On the closure properties of robotic grasping. *The International*

Journal of Robotics Research, 14(4), pp.319-334.

- [183] Rimon, E. and Burdick, J., 1996, April. On force and form closure for multiple finger grasps. In *Robotics and Automation, 1996. Proceedings., 1996 IEEE International Conference on*(Vol. 2, pp. 1795-1800).
- [184] Liu, Y., Lam, M., & Ding, D. (2004c). A complete and efficient algorithm for searching 3-D form closure grasps in the discrete domain. *IEEE Transactions on Robotics*, 20(5), 805–816.
- [185] Rimon, E., & Burdick, J. (1996). On force and form closure for multiple finger grasps. In *Proceedings of IEEE International Conference on Robotics and Automation—ICRA* (pp. 1795–1800).
- [186] Bicchi, A. and Kumar, V., 2000, April. Robotic grasping and contact: A review. In *ICRA* (Vol. 348, p. 353).
- [187] Rus, D., 1999. In-hand dexterous manipulation of piecewise-smooth 3-D objects. *The International Journal of Robotics Research*, 18(4), pp.355-381.
- [188] Donald, B., Jennings, J., and Rus, D. 1993. Information invariants for cooperating autonomous mobile robots. *Proc. of the Intl. Symp. on Robot. Res.*
- [189] Donald, B., Jennings, J., and Rus, D. 1997. Information invariants for cooperating autonomous mobile robots. *Intl.J. Robot. Res.* 16(5):673–702.
- [190] Salisbury, J.: *Kinematics and force analysis of articulated hands*. Ph.d. thesis, Stanford University (1982)
- [191] León, B., Morales, A. and Sancho-Bru, J., 2014. *From robot to human grasping simulation*. Springer International Publishing.
- [192] Bicchi, A.: On the problem of decomposing grasp and manipulation forces in multiple whole limb manipulation. *Int. J. Robot. Auton. Syst.* 13, 127–147 (1994)
- [193] Prattichizzo, D., Trinkle, J.: *Springer Handbook of Robotics*, pp. 671–700. Springer, Berlin (2008).
- [194] Olsson, H., Astrom, K., de Wit, C., Gafvert, M., Lischinsky, P.: Friction models and friction compensation. *Eur. J. Control* 4(3), 176–195 (1998).
- [195] Ciocarlie, M., Miller, A., Allen, P.: Grasp analysis using deformable fingers. In: *IEEE/RSJ International Conference on Intelligent Robots and Systems, In (2005). (IROS 2005)*. pp. 4122–4128 (Aug 2005)

- [196] Zheng, Y., Lin, M., Manocha, D.: On computing reliable optimal grasping forces. *IEEE Trans. Robot.* 28(3), 619–633 (June 2012)